Site-controlled quantum dots integrated with photonic crystal waveguides and cavities

THÈSE N^{O} 8304 (2018)

PRÉSENTÉE LE 9 MARS 2018

À LA FACULTÉ DES SCIENCES DE BASE
LABORATOIRE DE PHYSIQUE DES NANOSTRUCTURES
PROGRAMME DOCTORAL EN PHYSIQUE

ÉCOLE POLYTECHNIQUE FÉDÉRALE DE LAUSANNE

POUR L'OBTENTION DU GRADE DE DOCTEUR ÈS SCIENCES

PAR

Bruno Marie Dominique RIGAL

acceptée sur proposition du jury:

Prof. V. Savona, président du jury
Prof. E. Kapon, directeur de thèse
Prof. P. Lodahl, rapporteur
Prof. D. Gershoni , rapporteur
Prof. N. Grandjean, rapporteur

ÉCOLE POLYTECHNIQUE
FÉDÉRALE DE LAUSANNE

Suisse
2018

To see a World in a Grain of Sand

And a Heaven in a Wild Flower

Hold Infinity in the palm of your hand

And Eternity in an hour

W. Blake, *Auguries of Innocence*

À ma fiancée, à mes parents

Remerciements

Ce travail fut une épreuve de longue haleine, jalonnée d'illuminations passionnées et de moments de doute, de réussites gratifiantes mais aussi d'erreurs et d'échecs. Aucune de ces réussites n'aurait été envisageable sans le concours de toute l'équipe du LPN. Et bien au-delà des succès, ma passion pour la recherche n'aurait pu durer sans le soutien de tous ceux qui m'ont entouré et que je souhaiterais remercier.

Ma gratitude va tout d'abord au professeur Elyahou Kapon qui a supervisé ces quatre années de recherche au sein de son laboratoire. Le professeur Kapon a été pour moi un exemple de patience et d'honnêteté intellectuelle, qui m'a inspiré lorsqu'à mon tour j'ai eu à encadrer des étudiants en stage. Ses conseils et son expertise ont été une aide cruciale pour aller au bout des publications dont cette thèse fait l'objet.

Je souhaiterais aussi remercier les membres du jury, Peter Lodahl, David Gershoni et Nicolas Grandjean pour leur relecture attentive et leurs nombreuses questions lors de la soutenance.

Ce travail de thèse a été le fruit d'une collaboration de mes collègues du LPN, une collaboration technique et scientifique bien sûr, mais aussi de multiples moments de partage. A ce titre, je tiens à remercier Clément Jarlov qui m'a appris de nombreux aspects du travail au LPN, mais qui a également été un interlocuteur précieux pour élaborer des idées ou corriger des erreurs. Merci à Benjamin Dwir pour toutes ces discussions qui nous ont permis de penser les expériences présentées dans cette thèse et celles que nous nous sommes contentés de rêver. Un grand merci aussi à Alok Rudra, pour son expertise des croissances et pour nos innombrables discussions au niveau géopolitique, économique, culturelle, philosophique... Je remercie également Alexey Lyasota qui m'a enseigné les bases du travail en salle blanche et Andrei Caliman dont les conseils ont été précieux pour renforcer ce savoir. Merci aux membres du LPN qui m'ont soutenu ces quatre années: Antoine Delgoffe qui reprend courageusement le flambeau des boites en cavités et avec qui j'ai beaucoup échangé, Pascal Gallo dont l'enthousiasme débordant m'a bien inspiré, Mikhaïl Lazarev, Alessio Miranda, Irina Kulkova, Fredrik Karlsson, Marc-André Dupertuis, Moshe Judelewicz, Alexandru Mereuta, Vladimir Iakoviev, Milan Calic. Je remercie aussi Jakob Rosenkrantz de

Lasson qui m'a été d'une aide précieuse pour lancer le projet sur des bases numériques solides. Enfin, un grand merci à Gabriella Fuchs pour sa présence joyeuse au sein du LPN.

Au-delà de l'équipe du LPN, il me faut remercier l'équipe des salles blanches qui nous a bien soutenus dans la maintenance de nos expériences: Nicolas Leiser, Damien Trolliet, Yoan Trolliet, Jonathan Delaloye.

Je tiens aussi à remercier tous les étudiants qui ont participé à ces recherches, que ce soit à travers des simulations ou des mesures de photoluminescence: Thomas Produit, Kristoffer Joanesarson, Monika Zimmermann, Achraf Kabbabi, Manuel Deckart, Morgane Loretan.

En parallèle du doctorat, une aventure de ces derniers mois a été le lancement de Polyphys, l'association des doctorants de physique et l'organisation des pizza physics beer et particulièrement du physics day avec Clément Javerzac-Galy, Philippe Roelli, Rogerio Jorge, Anton Smirnov, Luc Testa, Patrick Gono et Alexandra Nagy pour lequel nous avons largement bénéficié du soutien de Anh Eyman, Vincenzo Savona, Harald Brune et Daniele Mari. A tous, un grand merci.

Quelles qu'aient pu être les difficultés, je me suis durant les trois première années de ma thèse très largement reposé sur ce foyer qu'était pour moi le Centre Universitaire Catholique. J'en retiens un lieu de vie chaleureux et de riches amitiés: Joseph, gardien du CUC, tant pour la propreté que dans l'accueil des nouveaux arrivant, Ombline pour son charisme joyeux et bien souvent contagieux, Marta pour ses dons artistiques dont j'ai profité avec largesse, Pierre, pour , Myriam pour son calme pacifiant, Briac pour son humour débridé, Gaia pour ses concerts virtuoses, Gaby pour nos discussions sur la nature de la liberté, Gab pour sa motivation dans l'action quel que soit le jeux ou le plat culinaire qui nous attirait, Jacques pour ses blagues recherchées, Pierre, pour sa passion dans les discussions métaphysiques, Giovanni pour ses discussions éclectiques et ses lectures approfondies de la Genèse, Graziele, Guillem, Laetitia, Christophe, Pierre, Vincent, Laure, Vérène, Justine, Nuno, Alexis, Jacques, Noémie, Alexandre, Nicolas, Caroline, Héléna, Flore, Odile, Justyna, Inès, Charlotte.

Merci à mes colocs, ermites du minicuc, qui sauront se reconnaitre: le maitre, pour nos disputatios parfois infructueuses, mais toujours orientées vers la vérité, el padre pour son souci d'une vie communautaire riche et profonde, le scout pour son engagement dans chaque service, monsieur Thibault Jean François Marie, vicomte de la Roubertie et autres... , pour la fidélité de ses engagements, Winnie, parce qu'il a fait de moi un champion, Louis, pour ses chansons à la guitare et ses chefs-d'oeuvre culinaires et Clément pour son humour piquant.

Merci à mes frères et soeurs, Marthe, Jean, Augustin, Elisabeth, Philippe et Joseph pour leurs encouragements.

Merci à mes parents, cause première de ma présence ici ce soir, mais aussi soutien

bienveillant, psychologique et logistique, quels que puissent être mes problèmes.

Enfin, je ne saurais assez remercier ma fiancée chérie, Anne, dont la bienveillante proximité et la joie m'ont comblé tout au long de ces deux dernières années.

Abstract

Quantum mechanics did not only deeply transform our world view down to a philosophical level, it is also expected to be key ingredient of future so-called quantum technologies. Indeed, quantum properties of matter such as isolated single particles or entanglement, can provide a technological resource for faster computers or perfectly secure communication protocols. In this new paradigm, arbitrary quantum states of light and matter would be deterministically controlled to perform operations that are not feasible in the realm of classical physics. When applied to photons, this new technological field is called quantum optics.

A promising platform proposed for quantum optics consists of quantum dots (QD) embedded in photonic crystal (PhC) circuits. While QDs exhibit high oscillator strengths, and are a promising solution as single photon sources, PhCs represent an ideal platform for light processing due to their capacity to enhance light matter interactions. However, such circuits require a deterministic control over the position and energy of the QDs. Most previous experiments relied on self-assembled QDs nucleating at random position, which prevents their scaling to larger systems with multiple QDs. The subject of this thesis is the study of site-controlled quantum dots and their interaction with photonic crystal systems made of cavities and waveguides.

A first challenge lies in the free propagation of light in simple PhC waveguides. Elongated PhC cavities were first harnessed to measure the mode reflectivity at the edge of the linear cavities, and the propagation losses in PhC waveguides, from which we inferred a propagation loss coefficient near the band edge increasing faster than the group index. The impact of disorder on the density of states, mode localization and dispersion in long linear PhC cavities was then investigated. The direct imaging of the modes permitted to distinguish localized modes from modes extended throughout the whole cavity. A statistical analysis of the measured group index near the band edge clarified the boundary between the diffusive and dispersive regime. The site control of the QDs permitted the selective mode excitation and the in-situ probing of the the local density of states, from which we showed experimentally that waveguide modes are strongly distorted by phase scattering in the diffusive regime but only weakly

distorted in the dispersive regime.

In a second part, the integration of five site controlled QDs in a PhC waveguide is demonstrated together with the corresponding on-chip single photon transfer over macroscopic distances. The efficiency of coupling QDs to waveguides in these structures is measured while taking into account the statistical variations of the QDs intrinsic properties. Broad fluctuations of the coupling efficiencies were observed and attributed to the formation of Fabry-Pérot modes in the waveguides. An optimal design to reach reproducibly a broadband high efficiency of coupling is proposed using a short slow light section, an optimal positioning of QDs and the suppression of Fabry-Pérot modes.

The final part focuses on a system in which a QD is embedded in a cavity, itself coupled to a PhC waveguide. First, a design for coupling light out of plane from a PhC waveguide with reduced back-reflection in the waveguide is presented. This coupler is then used for collecting light from the QD-cavity-waveguide system. The existence of a cavity to waveguide coupling which optimizes the coupling efficiency of single photons to the waveguide is then shown theoretically. The parameters controlling the coupling between the QD cavity and waveguide are measured, from which we infer a single photon collection efficiency close to its optimal value.

This work represents the first experimental implementation of site-controlled QDs in PhC circuits beyond simple cavities. It focuses on the limitations and possibilities opened by such QD systems as on-chip efficient single photon sources. These results are interesting for on-chip quantum circuits with multiple QDs, which would enable, for example, large scale linear optical quantum computing.

Keywords: Photonic crystal, site-controlled quantum dot, waveguide, optical cavity, disorder, single photon source, nanophotonic, semiconductor.

Résumé

La mécanique quantique ne s'est pas contentée de transformer notre vision du monde en profondeur, et ce jusqu'à un niveau philosophique, elle représente aussi un élément clé de technologies actuellement en développement. En effet, des propriétés quantiques de la matière, comme l'existence de particules isolées, ou l'intrication entre particules distantes, peut être un atout technologique pour la conception d'ordinateurs plus rapides ou de protocoles de communications parfaitement sécurisés. Ce nouveau paradigme technologique permet d'imaginer que des états quantiques combinant photons et électrons soient contrôlés de manière déterministe afin réaliser des opérations impossibles avec des technologies purement classiques. Lorsque des photons sont utilisés, ce nouveau champ d'investigation se nomme l'optique quantique.

Une implémentation possible pour l'optique quantique consiste à utiliser des boites quantiques intégrées dans des circuits faits de cristaux photoniques. En effet, les boites quantiques présentent des transitions électroniques avec des forces d'oscillateurs remarquablement fortes, et peuvent émettre des photons uniques. Les cristaux photoniques quant à eux sont une plateforme idéale pour contrôler des états lumineux grâce à leur capacité à augmenter la force de l'interaction lumière-matière. Cependant, de tels circuits nécessitent un degré de contrôle important sur la position et l'énergie d'émission des boites quantiques. Dans la plupart des expériences intégrant boites quantiques et cristaux photoniques, les boites quantiques étaient formées par un processus de nucléation aléatoire ne permettant pas un contrôle précis de leur position. Ces techniques ne permettent donc pas la fabrication de systèmes plus large impliquant de nombreuses boites quantiques. L'objectif de cette thèse est l'étude de boites quantiques dont la position est contrôlée, ainsi que de leur intégration dans des circuits en cristaux photoniques constitués de cavités et de guides d'ondes.

Un premier obstacle vers cet objectif provient de la propagation de photons dans de simples guides d'ondes en cristaux photoniques. Les pertes durant la propagation de lumière dans de tels guides d'ondes ont tout d'abord été mesurées à l'aide de cavités linéaires ce qui a permis d'observer une augmentation du coefficient de perte au niveau du bas de la bande du guide d'onde plus rapide que l'indice de groupe.

Dans un second temps, l'impact du désordre sur la densité d'états, la localisation de lumière et la dispersion de lumière dans des guides d'ondes a été caractérisé à l'aide de ces cavités. Par l'observation directe des modes dans ces cavités, les modes localisés par le désordre et les modes de guide d'onde se propageant dans l'ensemble de la cavité ont pu être distingués. Une analyse statistique de l'indice de groupe mesuré sur différentes cavités linéaires a mené à une identification de la frontière entre le régime diffusif et le régime dispersif du guide d'onde. Finalement, le contrôle précis de la position des boites quantiques a permis de sonder avec précision la densité d'états de lumière. Cette analyse de la densité d'états lumineux a mis en évidence les distorsions importantes induites sur les modes par le désordre dans le régime diffusif, mais aussi les faibles distorsions dans le régime dispersif.

Une seconde étape a consisté à intégrer cinq boites quantiques dans un guide d'onde en cristaux photoniques au sein duquel l'émission et la propagation de photons uniques sur des distances macroscopiques a pu être démontrée. L'efficacité de couplage des boites au guide d'onde dans ces structures a été mesurée en prenant en compte les variations statistiques inhérentes aux boites quantiques utilisées. Les larges fluctuations de couplage observées ont été attribuées à la présence de modes de Fabry-Pérot dans le guide d'onde. Une structure optimale a finalement été proposée afin d'atteindre de manière reproductible une haute efficacité de collection des photons par un positionnement adéquat des boites, par l'utilisation de lumière lente et par la suppression de ces modes de Fabry-Pérot.

La dernière étape s'est concentrée sur un système formé d'une boite quantique intégrée dans une cavité en cristaux photoniques, elle même couplée à un guide d'onde. Premièrement, un design permettant de réduire la réflexion à la sortie d'un guide d'onde tout en couplant la lumière hors du plan a été démontré. Ce coupleur a par la suite été utilisé pour collecter la lumière hors du système formé par la boite quantique, la cavité et le guide d'onde. Ensuite, à travers un modèle basé sur la théorie des modes couplés, l'existence d'une valeur du couplage entre la cavité et le guide d'onde optimisant l'extraction de photons depuis la boite a été démontré. Les paramètres contrôlant le couplage de la boite quantique à la cavité, puis de la cavité au guide d'onde ont été mesurés. De ces mesures, une efficacité totale de collection de photons proche de son optimum théorique a été déduit.

Ce travail représente la première démonstration expérimentale de boites quantiques intégrées dans des circuits en cristaux photoniques au delà de simples cavités. Il met en évidence les limites et possibilités offertes par ces systèmes pour une utilisation en tant que source de photons uniques. Ces résultats sont utiles pour la fabrication de circuits intégrés quantiques contenant de nombreuses boites quantiques et permettant par exemple la réalisation d'ordinateurs quantiques basés sur l'optique.

Mots clés: Cristal photonique, boite quantique contrôlée en position, guide d'onde, cavité optique, désordre, source de photons uniques, nano-photonique, semi-conducteur.

Contents

List of abbreviations

AFM: atomic force microscope
AM: alignment marks
APD: avalanche photo-diodes
As: arsenide
Cavity-QED: cavity quantum electrodynamics
CB: conduction band
CCD: charge coupled device
DFT: discrete fourier transform
DOS: density of states
EBL: electron beam lithography
FDFD: finite difference frequency domain
FDM: finite difference method
FDTD: finite difference time domain
FP: Fabry-PÃ©rot
FSR: free spectral range
FSS: fine structure splitting
Ga: gallium
HBT: Hambury Brown and Twiss
HF: hydrofluoric acid
ICP: inductively coupled plasma etching
In: indium
IPA: isopropanol
KLM: Knill, Laflamme and Milburn
LDOS: local density of states
MIBK: methylisobutylcetone
MOCVD: metal organic chemical vapor deposition
NA: numerical aperture
Nd:YAG: neodymium-doped yttrium yluminium garnet
PECVD: plasma enhanced chemical vapor deposition

PhC: photonic crystal
PhCW: photonic crystal waveguide
PL: photoluminescence
PML: perfectly matched layer
PMMA: poly methyl-methacrylate
QD: quantum dot
QKD: quantum key distribution
QW: quantum well
QWR: quantum wire
RF: radio-frequency
RIE: reactive ion etching
SEM: scanning electron microscope
SK: Stranski Krastanov
TE: transverse electric
TEGa: triethylgallium
TEIn: triethylindium
Ti-Sa laser: titanium-sapphire laser
TLS: two level system
TM: transverse magnetic
TMGa: trimethylgallium
TMIn: trimethylindium
TRPL: time-resolved photoluminescence
VB: valence band
X-: negatively charged trion
X: neutral exciton
X+: positively charged trion
XX: biexciton

1 Introduction

Quantum mechanics has been at the forefront of a scientific paradigm shift transforming our vision of the world, unifying light and matter in a single theoretical framework, which turned out to be essential in describing the properties of individual particles and deducing from them the properties of our daily world [1]. It also transformed our world view, shedding doubts on the now antiquated Laplacian determinism [2] and leading to a deep understanding of the inner structure of atoms and molecules [1]. The knowledge gained from quantum physics was not confined to laboratories, but it was harnessed into what was retrospectively called the first quantum revolution, with the development of pervasive technologies such as computers or lasers.

A second wave of innovations started with the idea that purely quantum properties of matter such as isolated single particles or entanglement, could be technologically useful, which was the beginning of what is now called the second quantum revolution [3]. In this new paradigm, arbitrary quantum states of light and matter would be deterministically controlled to perform operations that are not possible in the realm of classical physics.

1.1 Nanophotonics and quantum technologies

1.1.1 Quantum technologies

Quantum technologies take ground in the fundamental properties of quantum physics, the physical theory describing matter at the fundamental level of single particles. In the quantum physical paradigm, matter and light are described by quantum fields, which are exhibiting properties of both waves and particles. Quantum technologies are based on two fundamental properties of quantum physics [4]. First, the existence of well-isolated single particles such as single photons or single electrons. Second, quantum entanglement, according to which the state of a group of particles can only

be described as a linear superposition of the states of each individual particles. This effect is evidenced by the correlations of measurements made on several entangled particles [5].

The main quantum technologies currently undergoing a substantial research effort are:

- Quantum simulations: In which a quantum system is used to simulate another quantum system in a more controllable way as was foreseen by Feynman few decades ago [6]. Indeed, the size of the parameter space of quantum states grows exponentially with the number of elements simulated. Therefore, simulations of quantum phenomenon quickly become intractable on classical computers. This technology could be used for example to simulate large molecules in quantum chemistry.

- Quantum computing [7]: a new computing paradigm in which the philosophy is to use massively entangled quantum states named Qubits to perform computation on many inputs in parallel and then to obtain with a reasonable probability the required result through a suitable treatment of the entangled output state. One of the most advertised algorithms, the Shor algorithm [8] is capable of providing an exponential speedup of computation for factoring large integers, which would annihilate the security of some widely used cryptographic algorithms.

- Quantum Key Distribution [9]: which is a method to distribute cryptographic keys over quantum channels. In this method, the security is ultimately guaranteed by quantum physics laws and especially the no-cloning theorem which prevents copying arbitrary quantum states without errors.

- Quantum metrology in which quantum entanglement or quantum squeezing is harnessed to increase the sensitivity of a sensor [10, 11].

1.1.2 Experimental realizations of quantum technologies

Most implementations of these technologies are based on the control and manipulation of single quanta of light and matter, which is a major frontier in physics and the central focus of many researchers around the globe. This control is achieved by using discrete quantum states and well-defined photonic modes.

A broad variety of physical systems were proposed to achieve this challenging goal. In the first successful one, Rydberg atoms were sent through a Fabry-Pérot cavity made with superconducting mirrors, thanks to which, quantum properties of atoms interacting with quanta of light were observed [12, 13]. This field of research was further improved by the possibility to trap ensembles of atoms and cool them down

to milli-kelvin temperatures [14] and culminated with the 2012 physics Nobel prize to S. Haroche and D. J. Wineland "for ground-breaking experimental methods that enable measuring and manipulation of individual quantum systems". Although these techniques are of great interest for the fundamental study of light-matter interaction in the quantum regime, the complex requirements in terms of cooling and scalability are more easily solved in solid-state systems.

A solid-state implementation for quantum technologies which is currently obtaining remarkable results are superconducting circuits. This technology demonstrated quantum effects such as the emission of single photons [15] and the implementations of few Qubits circuits [16]. One limitation of this technology is the stringent requirement of cooling the circuit to a few tens of milli-Kelvin.

1.1.3 Nanophotonics for quantum optics

A third actively explored solution is to use solid-state materials in which quantum systems exhibiting two discrete electronic states (Two Level Systems or TLS) embedded in a solid-state matrix. It usually combines simultaneously, strongly confined electronic and photonic states.

Strong confinement of the electronic states is necessary in order to to have well isolated discrete energy levels usable as Qubits or to emit single photons. These confined states are usually realized by:

- Single atoms or defects trapped in the solid-state matrix such as nitrogen vacancy centers.
- Tailoring a dip in the energy potential of a solid-state material, thus creating a so-called artificial atoms or Quantum Dots (QD).

Strongly confined light states are used to increase the light matter interaction, which is beneficial to make these TLS interact or to increase the extraction efficiency of photons. The study of these confined light states is the domain of nanophotonics [17] which focuses on studying the confinement of a light field at nanometer scales. Such strong confinements are typically achieved using:

- Photonic crystals, which are materials exhibiting periodic dielectric constants in which a photonic bandgap is formed and prevents the light from propagating in chosen directions [18]. It can be used to guide, slow down or even confine light. Photonic crystal cavities can confine light to the smallest volumes achievable in non-lossy materials.
- Plasmonic materials in which hybridized electrons and photons oscillations called plasmons are created in metals [19]. These plasmons can be confined to volumes below the diffraction limit at the expense of significant losses.

- Other kinds of nanocavities: such as nanodisk or micropillar nanocavities[20].

This thesis is about single quantum dots embedded in photonic crystal circuits. QDs are extensively studied as a possible Qubits implementation. This work is more focused on their use as efficient on chip single photon sources. These single photon sources would represent an enabling technology for a number of quantum technologies, such as quantum key distribution [9], to create photonic entangled states necessary in some quantum metrology applications [11], and for a specific implementation of quantum computing called the Knill, Laflamme and Milburn protocol [21], which would require only deterministic single photon sources, beamsplitters and detectors to fabricate a quantum computer. We will now present the fundamental properties of the building blocks used throughout this thesis: quantum dots and photonic crystals.

1.2 Electrons in semiconductor nanostructures

In this work, the single photon emitters are quantum dots, a type of nanostructure able to confine electrons in a nanometric volume. The two most common types of QDs are colloidal QDs and epitaxial QDs [22]. The formers are spherical nanoparticles produced by heating a colloidal solution in which spherical nanocrystals nucleate [23]. The latter are fabricated through the epitaxial growth of semiconductors layers. Although colloidal QDs are useful for solar cells, light emitting diodes and displays, they exhibit a large inhomogeneous broadening and are not easily integrated in solid-state materials [23]. On the contrary, epitaxial QDs are fabricated directly in semiconductor systems and have already been used in a number of quantum optics experiments [22]. The fundamental properties of epitaxial QDs and their fabrication is summarized in this section.

1.2.1 Semiconductors

Semiconductors are a type of solid-state crystal critical in a number of modern technologies such as integrated circuits, diodes or cameras. A crystal is a periodic arrangement of atoms in which the valence states electrons hybridize into delocalized modes extended throughout the whole material. These extended states form bands of the electronic states: ranges of energies that the electrons may occupy. These bands are filled in, starting from the lowest to the upper energy levels. The energy at which electronic levels have a 50% chance of being occupied is called the Fermi level. If it lies within a band, the material is a conductor of electricity. If it is in between two bands separated by an energy gap sufficiently large to prevent the excitation of electrons between them, the material is an insulator. A last class of materials is characterized by

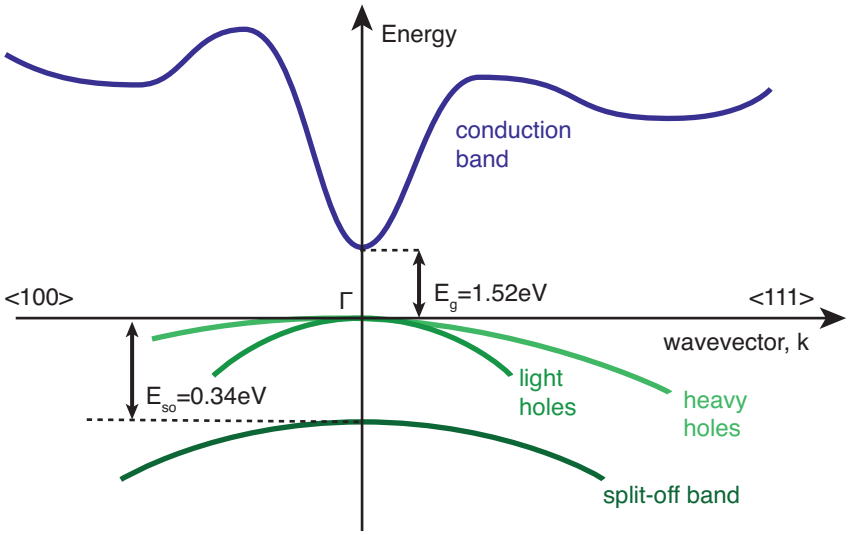

Figure 1.1 – Bandstructure of GaAs at 10K [24]

the presence of a bandgap and the possibility to control precisely the conductivity by inserting intermediate energy levels in the bandgap through a process called doping, which consist in replacing some crystal atoms with other atoms exhibiting a different number of valence band electrons. Semiconductor materials usually exhibit a non-zero energy gap which is still sufficiently small to allow for excited electrons from the lower valence band (VB) to the upper conduction band (CB). Although semiconductors behave as insulators at zero temperature, at larger temperatures, the presence of excited electrons contribute to electricity conduction.

At low temperatures, the VB is almost entirely filled with electrons. A common model to describe its physical properties is to consider the absence of an electron as a quasi-particle instead of the sea of electrons. These quasi-particles are called holes. The possibility to dynamically engineer the conductivity of a semiconductor by controlling the density of electrons and holes is the fundamental idea behind the fabrication of transistors and the avalanche of innovations that followed.

The exact band structure in a semi-conductor is determined by its symmetry and the types of atoms it is made of. In this thesis, the QDs were fabricated with gallium arsenide (GaAs) and indium gallium arsenide (InGaAs). GaAs has a zinc blende crystal structure with a lattice constant: 0.56nm. Its band gap at 10K is 1.52eV. As indicated on Fig. 1.1, the VB is made of three different hole bands: the heavy and light hole bands which are degenerate, and the split off band blue shifted from the band edge because of the spin orbit interaction. The degeneracy of the heavy and light hole bands is lifted for propagating electrons as a consequence of the larger mass of heavy holes.

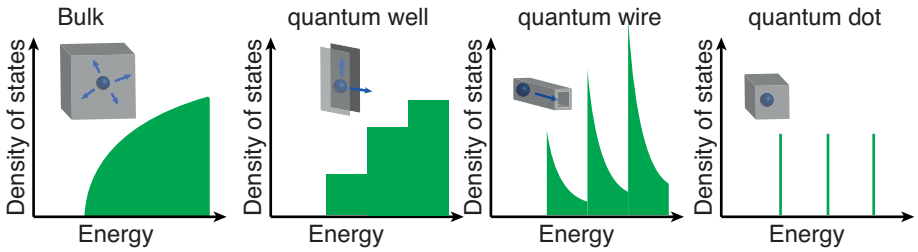

Figure 1.2 – Electronic density of states for electrons and holes in an infinite semiconductor and in the three types of quantum heterostructures.

$In_xGa_{1-x}As$ is a semiconductor with similar physical properties, in which a fraction x of the gallium sites are replaced by an indium atom. It has a smaller bandgap and a smaller lattice constant. Each of these can be approximately determined from the indium content as a linear interpolation between the known bandgap and lattice constant from pure GaAs and pure In [24].

1.2.2 Quantum Dots

1.2.2.1 Quantum heterostructures

Semiconductors with different bandgaps can be assembled together provided they have similar crystalline geometries. Such arrangements of semiconductor layers with different bandgaps are called hetero-structures. These are used to confine electrons or holes in well-defined regions of space and control their interactions or their movements. When the confinement length is of the order of the de Broglie wavelength of the particle, the typical lengths needed to have a quantum confinement, a quantum hetero-structure is formed [25]. In GaAs at 10K, the de Broglie wavelength of electrons and holes is a few tens of nanometers [25].

Quantum hetero-structures are divided in three main families. If the confinement is in only one dimension of space, it is a Quantum Well (QW), in two dimensions, it is a Quantum Wire (QWR) and if the electron is confined in all dimensions of space it is a Quantum Dot (QD) (see Fig. 1.2).

When submitted to quantum confinement electrons and holes cannot move along their confinement directions. In this case, an electron in a QW behaves as if it were living in a 2D space, in a QWR it moves freely only in one direction and in a QD it does not move at all. Quantum confinement strongly distorts the electronic density of states (DOS) as sketched on Fig. 1.2. In the bulk semiconductor, the DOS increases as the square root of the energy, while in a quantum dot, the electronic DOS is discrete. The energy and electronic configuration in quantum heterostructures can be estimated within the effective mass approximation by solving the following Schrödinger equation approximation [22]:

$$\left(-\frac{\hbar^2}{2m^*}\nabla^2 + V(r)\right)\phi(r) = E\phi(r) \tag{1.1}$$

where m* is the electronic effective mass, V is the confinement potential and E is the electron energy. In this expression, the spin degree of freedom was neglected. Including its effects is the subject of the k.p method, which was very successful in predicting the properties of quantum heterostructures [26].

1.2.2.2 Electron and hole states in quantum dots

Epitaxial QDs, i. e. QDs formed by the epitaxial growth of semi-conductor layers, are in most experiments smaller along the growth direction (z-direction) than in the plane. Thus, a reasonable model of the QDs approximates their confinement potential by two infinite barriers along the growth direction (z direction) and by parabolas along the other two directions (x and y). The energy spectrum of electrons confined in QDs according to this model is [22]:

$$E_{n,m,p} = \frac{E_g}{2} + \hbar\omega_e(n_x + n_y + 1) + \frac{\pi^2\hbar^2 n_z}{2m_e L_z^2} \tag{1.2}$$

where n_x and n_y are the quantum integers associated with the quantized spectrum along the two horizontal directions. The last term corresponds to the QW-like confinement in the z-direction. L_z is the confinement length along z and n_z is quantization number along z. As noted before, this spectrum is completely quantized because of the confinement along all directions of space. According to the Pauli exclusion rule for fermions, only two electrons (one with each spin orientation) can occupy each energy level which makes QDs artificial equivalent of atoms. This remarkable effect is crucial to obtain the isolated single electrons used as Qubits. The confinement in the z direction is usually strongest and splits the electron states in energy equidistant sets of states associated with the quantum number z. In analogy with electronic states in atoms, these sets are labelled with the letters s, p, d... However, unlike atoms, only four degenerate states occupy the p level and six occupy the d level. Within this model, the electrons can be labeled by their spin $\pm 1/2$ and their orbital angular momentum along z $n_x - n_y$ [22]. The total angular momentum of s-states electrons is therefore: $J_z = \pm 1/2$.

The description of holes in GaAs QDs is more involved because of the presence of the heavy and light hole bands near the GaAs band edge. However, the strong confinement of holes along the z direction induces strain in the crystal which results in a large splitting of the heavy and light hole bands. In this case, the heavy hole band is sufficient for describing the hole properties. This model then predicts similar sets of hole states as depicted on Fig. 1.3(a). The heavy hole electrons carry a spin $S = \pm 3/2$ and an angular momentum $n_y - n_x$, from which the total angular momentum of

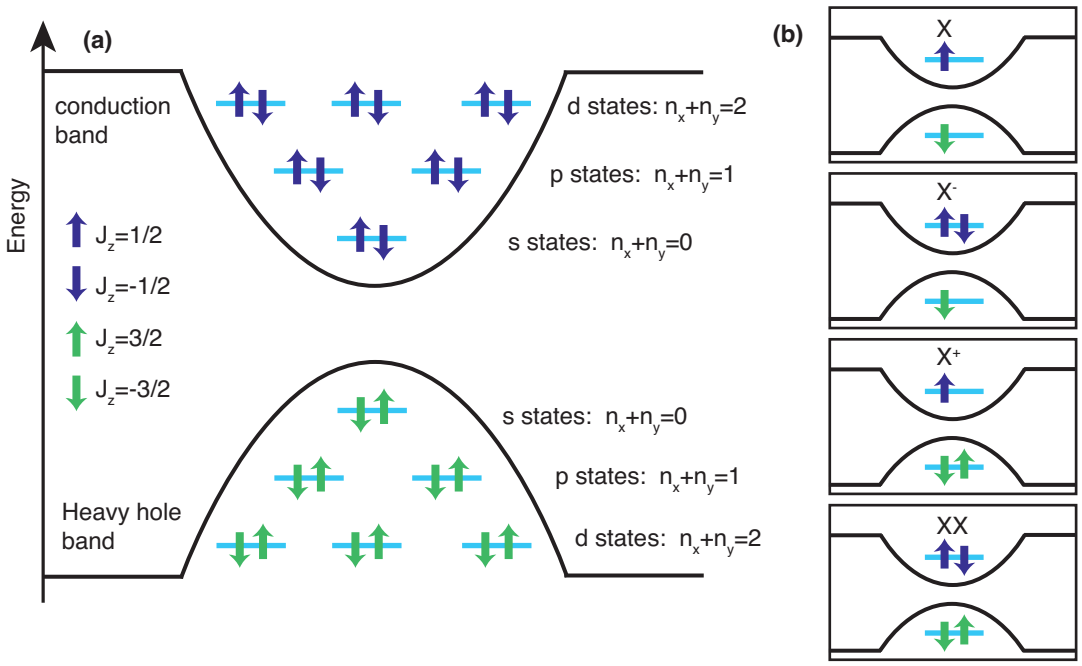

Figure 1.3 – (a) The energy level structure of QDs; (b) From top to bottom: Neutral exciton; Negative trion; Positive trion; biexciton; [22]

s-states heavy holes is derived: $J_z = \pm 3/2$.

1.2.2.3 Excitons in QDs

These electronic and hole states can be combined in a zoology of quasi-particles depicted on Fig. 1.3(b-c-d). If the QD s-state contains simultaneously an electron and a hole, it forms a quasi-particle called an exciton. If it contains two electrons and one hole or one electron and two holes, it is a (charged) trion. If it is completely filled with two electrons and two holes, it is a biexciton.

When electrons and holes are blended together in a QD their Coulomb interaction shifts the excitonic energy levels. In the strong confinement regime, the electron and holes wavefunctions are weakly distorted by their interaction and the Coulomb interaction energy can be computed perturbatively as [22] :

$$V_C^{1-2} = < \Psi_1, \Psi_2 | \frac{q_1 q_2}{4\pi\epsilon_0\epsilon_r |\hat{r}_1 - \hat{r}_2|} | \Psi_1, \Psi_2 > \tag{1.3}$$

The energies of the excitonic species are then given by:

$$E_X = E_e + E_h - V_C^{e,h} \tag{1.4}$$

$$E_{X^-} = 2E_e + E_h + V_C^{e,e} - V_C^{e,h} \tag{1.5}$$

$$E_{2X} = 2E_e + 2E_h + V_C^{e,e} + V_C^{h,h} - 4V_C^{e,h} \tag{1.6}$$

1.2.2.4 Optical transitions in QDs

Thanks to the direct bandgap of GaAs, these excitons are optically active: they can interact with light. Understanding the optical transitions between excitonic states requires a more precise description of electronic and hole states in QDs. In an infinitely large semiconductor medium, the Bloch theorem implied by the crystal periodicity permits a description of electrons or holes as Bloch functions:

$$|\Psi_{e,h}> = |u_{e,h}(k,r)> |s> e^{-kr} \tag{1.7}$$

Where $|u_{e,h}(k,r)>$ is a function of space with the same periodicity as the crystal, $|s>$ is the spin state and k is the electronic wavevector. Within the envelope function approximation, the electronic or hole states in a QD can be written as [27]:

$$|\Psi_{e,h}> = |F_{e,h}(r)> |u_{e,h}(0,r)> |s_{e,h}> \tag{1.8}$$

Where $|F_{e,h}(r)>$ is the envelope function defined by the confinement potential, $|u_{e,h}(0,r)>$ is the Bloch function at the Gamma point (where k=0) and |s> is its spin state. The optical transitions are determined by the electromagnetic interaction hamiltonian and ultimately by the momentum matrix element [27]:

$$\vec{P} = < F_h(r)|F_e(r) >< u_h(0,r)|\vec{p}|u_e(0,r) >< s_h|s_e > \tag{1.9}$$

This matrix element determines the selection rules that apply to allowed optical inter-band transitions in QDs:

- The envelope wavefunctions must share the same parity.
- The Bloch wavefunctions must have opposite parity.
- The electron spin states must not change.

We now focus on the transitions between s electron and hole states. The Bloch function of electrons in the conduction band are symmetry invariant under all transformations of the crystal lattice (orbital s symmetry), they are commonly written: $|s> |\uparrow>$ and $|s> |\downarrow>$. Where the arrows correspond to the two spin orientations. On the contrary, the heavy hole states have an orbital p symmetry and can be written as [22]:

$$|u_{h,1}(0,r)>=-\frac{1}{\sqrt{2}}|x+iy>|\uparrow> \tag{1.10}$$

$$|u_{h,2}(0,r)>=\frac{1}{\sqrt{2}}|x-iy>|\downarrow> \tag{1.11}$$

Where |x> and |y> are the p-type parts of the Bloch states which have the same symmetry as the coordinates x and y. Notice that only the heavy hole band was considered here. Within a more realistic picture, the hole states are a mixture of heavy and light holes. A more accurate description involving several hole and electron bands is possible within the k.p method [28]. The different excitonic states and their possible transitions are depicted on Fig. 1.4. From the two electrons and two holes, four different excitonic species can be formed. However, only two are optically allowed: those on which the spin of the electron is conserved; these are called the bright states. The two other excitons, the dark states, can still recombine through non-radiative transitions, although these transitions are usually very weak. In a similar way, the two trions can recombine radiatively to the simple electronic and hole states. Notice that the transition matrix elements in all the optical transitions are circularly polarized. However, in a realistic system, asymmetries of the QD can break the bright excitonic states in two linearly polarized states, separated by an energy splitting called the fine structure splitting (FSS). The trions on the contrary are made of an odd number of fermions and are thus forced to be doubly degenerate by the Kramers degeneracy theorem [29].

Transitions in a QD are typically characterized by their oscillator strength, which is related to the momentum matrix element by [27]:

$$f=\frac{2|P|^2}{\hbar\omega_0 m_e}=\frac{E_K}{\hbar\omega_0}<F_h(r)|F_e(r)> \tag{1.12}$$

Where m_e is the electron mass, ω_0 is the transition frequency and E_K is a constant characteristic of each material called the Kane energy. In GaAs, $E_K = 22eV$ [30], from which we can infer a maximal dipole strength in case of perfect overlap between the electron and the hole of $f = 16$; simulated values in typical QDs range between $f = 10$ and $f = 15$ [27]. In weakly confined QDs, the dipole strength is proportional to the QD volume and may reach much larger values [31].

1.2.2.5 Linewidth broadening in QDs

Although QDs share some of their properties with atoms, their solid-state nature is a source of additional effects not observed in atomic physics. The spectral emission of an atom is a lorentzian with a full width at half maximum (FWHM) equal to the inverse of the atomic lifetime as a consequence of the Heisenberg uncertainty principle.

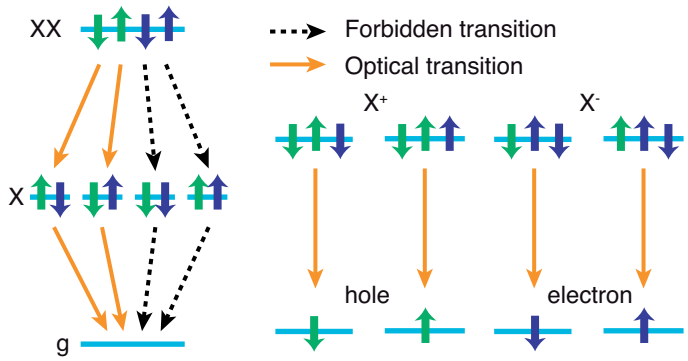

Figure 1.4 – Optical transitions in a QD. Right: Exciton, biexciton cascade; Left: transitions in positive and negative trions.

However, contrary to isolated atoms, QDs are necessarily embedded in a solid-state matrix through which the excitonic states constantly interact with their environment. These interactions are a source of decoherence, a process by which the coherence of quantum states eventually stored in excitons is lost. Another consequence is the broadening of the excitons linewidths from the $\approx 1\mu eV$ lifetime limited linewidth to the 10-100µeV values observed in experimental QDs.

A first source of broadening is caused by fluctuating charges surrounding the QDs. These moving charges induce a fluctuating electric field which shifts the emission energy of the QDs. When these fluctuations are slower than the QD decay rate, they induce spectral shifts of the excitonic line, which are known as spectral diffusion [32]. When these fluctuations are much faster, the exciton emission line is inherently broadened, this phenomenon is called pure dephasing [33] and is a source of decoherence, usually detrimental to quantum optics applications. However, in some cases, pure dephasing can be used as a resource to increase the out-of-resonance feeding of cavities by QD [34] or to increase the indistinguishability of photons [35].

Another effect of the solid-state environment results from the interaction with crystal lattice vibrations called phonons. The interaction with phonons induces a broadening of the excitonic lorentzian line caused by the scattering of phonons and similar to the pure dephasing caused by fluctuating charges. Although this broadening is negligible at low temperature, it can increase up to 50µeV at 50K [36]. The interaction with phonons is also responsible for a temperature dependent broadband emission corresponding to the emission and absorption of a photon and a longitudinal acoustic phonon simultaneously [37]. At low temperatures, the broadband emission is asymmetric and more intense at lower energy, because the phonon population is low and the QD cannot absorb, but only emit phonons. The interaction between QD and phonons and its temperature dependence have been demonstrated in several photoluminescence experiments [38, 39].

1.2.3 Fabrication of Quantum Dots

1.2.3.1 Epitaxial QDs

The first epitaxial QDs experimentally observed were naturally formed in the unavoidable monolayer defects in thin QWs [40]. However, these QDs are not suitable for most of the above-mentioned applications due to their weak confinement energy. The most popular method for fabricating QDs is based on the Stranski Krastanov (SK) technique. The fabrication relies on the heteroepitaxy of a highly strained layer (for example InAs over GaAs) [41]. When the grown thickness rises above a threshold, islands of InGaAs nucleate at random positions. These islands are the SK QDs as shown on the AFM picture of Fig. 1.5(a). To prevent the interaction of QDs with surface states, this layer is then covered by a cap of GaAs. These QDs have heights typically between 1 and 10 nm and a horizontal size between 10 and 100nm [27] and are randomly distributed over the GaAs surface. The thin layer from which the QD are formed is called the wetting layer. Such QDs were fabricated with emission wavelengths ranging from 850nm to telecom wavelengths at $1.3\mu m$. They are easy to fabricate and exhibit sharp emission linewidths close to their lifetime limit (a few μeV). However, the size of these QDs is not controlled precisely and induces an inhomogeneous broadening of QD lines usually around 50meV [42].

These QDs can be integrated within PhCs or other optical nanostructures. However, it is difficult to control the QD position in the photonic nanostructure because of their random nucleation site. In typical experiments, many structures are fabricated and the sample is scanned by photoluminescence measurements to find structures in which the QD is efficiently coupled to the optical modes. An alternative approach is to align the nanostructure directly over a selected QD [43]. However, these approaches are not applicable for integrated photonics in which arrays of many QDs would need to be placed at precise locations in photonic circuits.

1.2.3.2 Site-controlled QDs

Several approaches were proposed to fabricate arrays of position controlled QDs. These usually rely on structuring the growth surface to control their position of nucleation.

Typical methods include the fabrication of dielectric mask aperture to etch nanoholes in the substrate [44] from which average optical linewidths down to 156μeV were obtained [45]. In a different technique [46], several layers were grown to obtain stacked QDs, in which the nucleation sites of the QDs were determined by the strain induced by the presence of the lower QDs. In the upper layers, the QD quality was improved with linewidths down to 110μeV. In a different technique [47], the nanorecesses were etched directly inside the growth chamber to ensure minimal contamination. Record linewidths for such site controlled QDs were obtained down to 43μeV [48] (Fig. 1.5 (b))

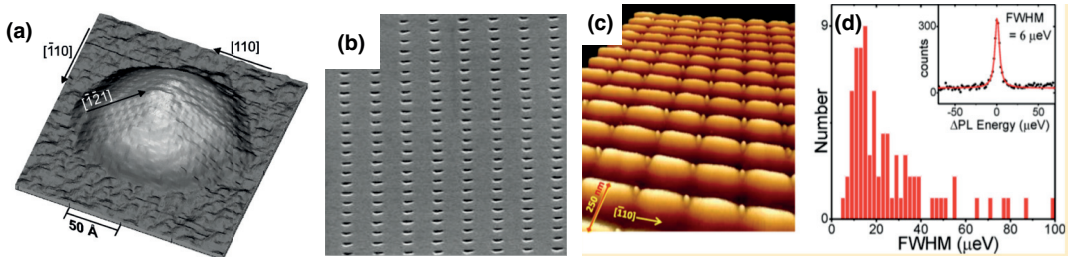

Figure 1.5 – (a) Atomic force microscopy image of an SK QDs; (b) scanning electron microscope image of an array of nanoholes used to grow site controlled QDs; (c) Atomic force microscopy image of an array of individual QDs; (d) Distribution of linewidths for site-controlled QDs; (a) Reprinted with permission from [50]. Copyright (2001) with the permission of AIP Publishing; (b) Reprinted from Publication 1.5, Copyright (2011), with permission from Elsevier. (c-d) Reprinted with permission from [49]. Copyright (2013) American Chemical Society.

and more recently [49] down to 6μeV (Fig. 1.5 (c-d). However, when using techniques based on the preferential nucleation of SK QDs, zero or more than one QD may be formed [45] which compromises their site control.

1.2.3.3 Pyramidal QDs

An alternative technique for growing site controlled QDs is based on the growth of InGaAs/GaAs or AlGaAs/GaAs QDs in arrays of pyramidal recesses. The QDs are formed at the apex of each pyramid by the interplay of growth rate anisotropy and capillarity [51]. They are called pyramidal QDs. Because the formation of these QDs is not driven by strain, only one QD is grown in each pyramid. Besides, no wetting layer is formed during the growth of QDs, although under certain conditions, QWRs are formed at the edges of the pyramids [52]. These QDs offers promising properties, including reproducible optical spectra [53] and relatively narrow linewidths down to the resolution limit of 20μeV. The inhomogeneous broadening is typically around 5-10meV, and a record value of 1.4meV [54] was observed. Thanks to the three fold symmetry of the crystal and the pyramids permitted by the symmetric (111)B orientation of the growth plane, highly symmetric QDs can be formed in which the FSS is lower than in SK QDs [55, 56, 57].

1.2.3.4 The perfect QD

All these experimental efforts aim at improving the quality of QDs to make them suitable for quantum optics experiments. The desirable properties of QDs depends on their application. We propose here a non exhaustive list of these properties [59].

Some properties aim at obtaining a high quality optical spectra. QDs exhibiting a large confinement energy are more easily protected from unwanted interaction

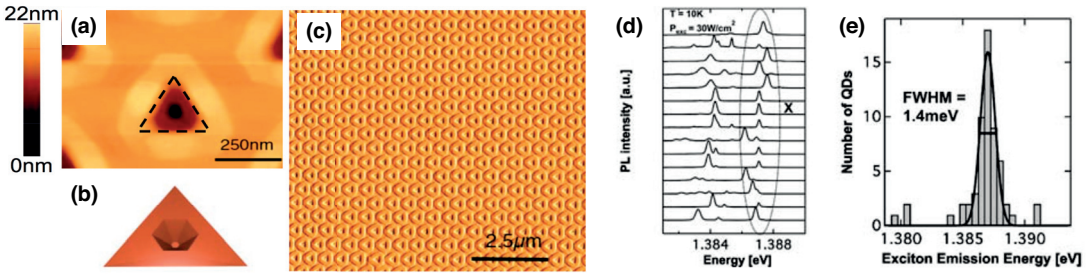

Figure 1.6 – (a) Atomic force microscopy image of one pyramidal QD intentionally not planarized; (b) 3D schematics of the growth in pyramidal QDs (c) Atomic force microscopy image of an array of pyramidal QDs; (d) Spectra of individual pyramidal QDs; (e) Distribution of the resonance energies of excitons in pyramidal QDs; (a-c) Reprinted with permission from [58], Copyright (2008), AIP Publishing LLC; (e-f) Reprinted with permission from [54] (2010) Wiley-VCH Verlag GmbH & Co. KGaA, Weinheim.

with residual defect states. Besides, deeply confined QDs are optically active at much higher temperatures. Optimally, QDs would therefore be confined deep enough for room temperature single photon emission as was demonstrated with GaN QDs [60].

Ideal QDs would also exhibit perfectly reproducible spectra including a low inhomogeneous broadening of exciton lines [54]. Although a vanishing inhomogeneous broadening would be appreciated, nanofabrication limitations will probably prevent reducing the inhomogeneous broadening much below 1meV. This issue can be circumvented by controlling the wavelength of each QD individually at the cost of additional complexity, for example by applying a strain [61], via the Stark effect [62] or the Zeeman effect [63].

High quality QDs would also exhibit narrow lifetime limited linewidths as was observed in SK QDs, and a high dipole strength [27] to attain a strong light-matter interactions and a bright emission.

Other desirable properties are more focused on fabricating QDs that are easily integrated into scalable technologies such as the position control [64] and the possibility to fabricate QD emitting over a broad energy range [65].

Last but not least, QDs are expected to play a role in quantum technologies. The two main quantum properties expected from ideal QDs are the emission of single photons with a high degree of indistinguishability [66].

Although each of these requirements was the subject of separate publications indicating promising result, achieving all of them simultaneously and reproducibly on a large array of QDs is extremely challenging. All these aspects will be considered in this thesis except for the photons indistinguishability.

1.3 Photonic crystals

1.3.1 From solid-state physics to photonic crystals

Photonic crystals (PhC) are dielectric nanostructures in which the refractive index is periodically modulated along one, two or three dimensions of space. These nanostructures affect the propagation of photons in a similar way crystal lattices affect the propagation of electrons. Their potential in controlling light-matter interaction was first noted in the nineties [67, 68]. In 1996, Krauss et al. [69] used methods from the semiconductors industry to fabricate the first photonic crystals operated at optical wavelengths, which opened new possibilities to a field which kept growing since.

The propagation of waves in a dielectric nano-structured medium is governed by the Helmoltz equation [18]:

$$(\nabla \times \nabla \times -\epsilon(r)(\frac{\omega}{c})^2)\vec{E}(r) = 0 \tag{1.13}$$

where ϵ is the dielectric function of the PhC, which has the periodicity of the material. This equation defines a linear eigenvalue problem in ω and E. Both $\nabla \times \nabla \times$ and $\epsilon(r)$ are linear, hermitian, positive semi definite operators. As a consequence, its eigenvalues ω are real, positive, and its eigenvectors with different energies abide by the following orthogonality relation:

$$\int \epsilon(r)\vec{E}_1(r) \cdot \vec{E}_2(r) dr = 0 \tag{1.14}$$

The Bloch-Floquet theorem first used to describe electrons in crystal lattices is also valid for PhCs, because the crystalline symmetry operators commute with the hermitian operators of the Helmoltz equation. This theorem states that the electric field in a PhC is:

$$\vec{E}(r,\omega) = \vec{E}_k(r,\omega)e^{i\vec{k}(\omega)\cdot\vec{r}} \tag{1.15}$$

where $\vec{E}_k(r,\omega)$ has the crystal periodicity and $\vec{k}(\omega)$ is the photonic wavevector. This relation between k and ω is called the dispersion relation. Notice that it is completely analogous to the band structure of electrons in crystals. This dispersion relation defines continuous energy ranges or photonic bands at which the photons can propagate in the PhC. In between these bands, bandgaps are formed where no propagating photonic states are allowed. Although infinite PhCs do not exist, bandgaps still persist in finite size PhC. In this case, the finite PhC acts as a mirror reflecting incident photons. An alternative interpretation is that light scattered by the periodic inhomogeneities will interfere destructively so as to prevent its propagation.

PhCs can be one, two or three dimensional. 1D PhCs can be fabricated by the

epitaxial growth of a periodic arrangement of layers. They have been massively used as Bragg mirrors or optical filters. However, 1D PhCs have a bandgap only along one dimension of space: a complete photonic bandgap requires a 3D PhCs. The first experimental 3D PhC was named Yablonovite after the name of its inventor, E. Yablonovitch[70]. It was fabricated by drilling holes along the three directions of an fcc lattice.

However, 3D PhCs require complex fabrication procedures. The most practical PhCs for photonic circuits are 2D PhCs which are more easily fabricated using conventional lithography techniques from the semiconductor industry [69]. Light propagation in 2D planes can be divided in two classes corresponding to the two polarizations of light: the transverse electric (TE) modes in which the electric field is confined in the PhC plane and the transverse magnetic (TM) modes where the magnetic field is confined in the PhC plane [18]. An example of 2D PhC: a triangular lattice of air holes drilled in a dielectric medium is shown in the inset of Fig. 1.7(a) [18]. It is entirely defined by its refractive index n, its lattice pitch a and the radius of the air holes r. The TE and TM bandgap ranges are given in blue and red as a function of the radius on Fig. 1.7(a) [18]. Designing a system based on PhCs requires first carefully choosing the right set of parameters to obtain a sufficiently large bandgap at the desired energy. However, 2D PhCs do not confine light in the third direction of space. In experimental implementations of 2D PhCs, the PhC is drilled in a dielectric slab (inset of Fig. 1.7(b)). In such a case, total internal reflection at the upper and lower interface of the slab confines the modes with an in plane wavevector: $|k_{||}| < \omega/c$. The dispersion relation for these modes is shown on Fig. 1.7(b). Modes with a larger wavevector are free to propagate into space and are part of the light cone depicted as a blue area of Fig. 1.7(b). In such PhC slabs, the bandgap is not complete and refers only to modes below the light cone. In addition, the distinction between TE and TM modes is no more valid, because the slab breaks the translation symmetry along the vertical direction [18]. However, the PhC symmetry under reflections through the plane at the center of the slab still allows for a classification: Modes even under this reflection are called TE-like and modes odd under this reflection are called TM-like.

1.3.2 PhC circuits

1.3.2.1 PhC cavities

Perturbing locally the PhC breaks its translational symmetry and creates discrete 'defect' modes inside the bandgap which are analogous to QD states. These modes are confined near the defect and are called cavity modes. A common type of PhC cavities named L_n cavities is made by leaving n holes unetched along a line (Fig. 1.8(a)). The in plane electric field of an L_3 cavity mode called M_0 mode is shown on Fig. 1.8(c). The higher order modes in cavities are usually labelled by increasing energy as M_p

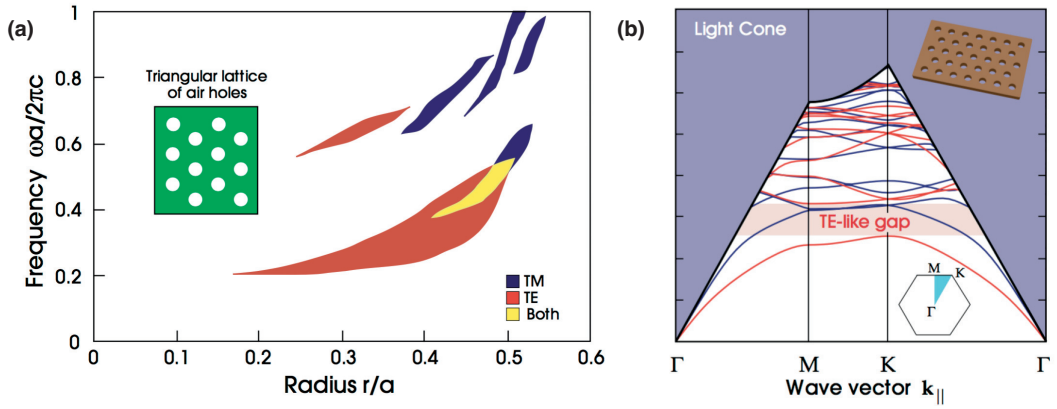

Figure 1.7 – (a) Bandgap of a triangular lattice 2D PhC (ε = 11.4); (b) Band diagrams in a triangular lattice PhC slab. The blue area is the light cone. Below the light cone, the red and blue lines are the TE and TM modes. The shaded red area indicates the TE-like bandgap. (a-b) republished with permission of Princeton University Press, from [18]; permission conveyed through Copyright Clearance Center, Inc.

modes (p=0,1,2...). The electric field is concentrated near the unetched holes and decays exponentially inside the PhC regions which act as mirrors surrounding the cavity.

A fundamental parameter of photonic cavities is their quality factor Q quantifying the energy storing time of light in the cavity. It is defined as: $Q = \tau\omega_0/2$, where ω_0 is the angular cavity frequency and τ is the time constant of the electric field amplitude exponential decay. A Fourier transform of the exponential decay yields the cavity spectrum and shows an alternative definition for the Q-factor: $Q = \Delta E/E$ where E is the cavity energy and ΔE is its FWHM, inversely proportional to the lifetime of the cavity mode.

In a finite size PhC, the electric field may leak through the PhC, but the in plane confinement increases exponentially with the number of layers surrounding the cavity [71]. This source of losses is usually negligible. Another cause of losses is out of plane scattering. In L_3 cavities, Nakamura et al. and others [72, 73, 74, 75] showed how leakage originates from scattering at the edges of the cavity and how a careful engineering of the holes permits to increase the M_0 mode Q-factor from 4000 to more than one million. However, experimental cavities suffer from two additional sources of losses: absorption by impurities or surface states of the semiconductor crystal and scattering caused by fabrication related disorder. In GaAs, the Q-factor of small cavities is usually limited to a few tens of thousands [76], although the record value of 700000 was observed at telecom wavelengths (1.5µm), where the GaAs absorption is lower [77]. In silicon, Q-factors as high as 9 million were obtained [78].

A significant advantage of photonic crystal cavities compared to other types

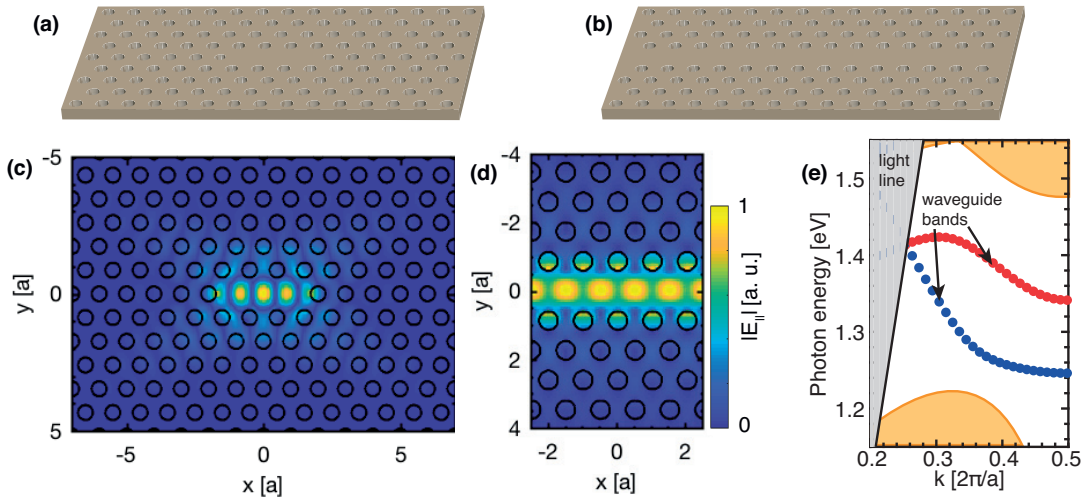

Figure 1.8 – (a) L_3 cavity and (b) W1 waveguide in a PhC slab; (c) in plane electric field of the M_0 mode in an L_3 cavity; (d) in plane electric field of the lowest energy band in W1 waveguide; (e) Dispersion relation in a W1 waveguide, the light cone shown in grey, the orange area depicts the non confined PhC bands; (These simulations were performed using the finite difference method in the frequency domain exposed in Chapter 2 with the parameters: a=225nm, r=61nm, n_{2D}=3.17)

of cavities stems from the possibility to confine light in the tiniest mode volumes achievable in non-lossy materials [17]. The mode volume in small PhC cavities is typically around $(\lambda/n)^3$, and can be as low as $0.23(\lambda/n)^3$ in the H_0 type cavities defined by shifting two adjacent holes [73]. Achieving simultaneously the highest Q-factor and the smallest mode volume is critical for enhancing light matter interaction as will be shown in the next section.

1.3.2.2 PhC waveguides

PhC cavities excel at storing light in small volumes for long times [73]. However, light propagation requires optical waveguides that may be used to connect cavities or to extract light from PhC circuits. The simplest PhC waveguide, called W1 waveguide, is realized by leaving a whole range of holes unetched (Fig. 1.8(b)). In such waveguides, photonic bands corresponding to propagating modes are trapped within the photonic bandgap. As waveguides are periodic in their propagation direction, the Bloch theorem also applies in the propagation direction (which we call here x):

$$\vec{E}(r,\omega) = \vec{E}_k(r,\omega)e^{ik(\omega)\cdot x} \tag{1.16}$$

Where $\vec{E}_k(r,\omega)$ has a period of a in the x direction and $k(\omega)$ is the mode wavevector along x which defines the dispersion relation of the waveguide band. The electric field of a waveguide mode is shown on Fig. 1.8(d) and the waveguide dispersion

relation for the two bands (in red and blue) confined in this specific waveguide is given on Fig. 1.8(e). The dispersion relation also defines the energy velocity of light in the waveguide also called group velocity [27]: $v_g = \partial\omega/\partial k$. Another equivalent quantity characterizing the energy velocity is the group index: $n_g = c/v_g$. This group velocity goes to zero when $\partial\omega/\partial k$ approaches zero as is the case of the red and blue bands near the bands edges where: $k = \pi/a$. Stopping the light in PhC waveguides induces a compression of optical pulses and an equivalent increase in the electric field intensity. As a consequence, slowing down light can dramatically increase the light-matter interaction and enhance non-linear processes, light collection or absorption [79]. Although the group indexes are usually limited to values below 100 by fabrication disorder [80], significant work was done to engineer low dispersion slow light PhC systems [81, 80] that may be used in low power optical switches, compact gas detectors or quantum circuits [79].

1.4 QDs in photonic crystals

In the last two sections, the physical properties of QDs and PhCs have been successively reviewed. We will now show how these two elements can be combined together in nanophotonic experiments and devices.

1.4.1 QDs in cavities

Systems made of an atom coupled to a cavity constitute an ideal system for understanding light matter interaction. The field interested in these systems is called cavity quantum electrodynamics (QED) [82]. cavity QED can be realized on chip by using artificial atoms (QDs) and nanocavities [83]. In this section, we will show how the presence of an optical cavity mode overlapping a QD can dramatically impact its physical properties.

1.4.1.1 The Jaynes -Cummings model

The simplest model delving into the interaction of a QD and a cavity is called the Jaynes Cummings model [84]. In this model, the QD is described as a two level system (TLS), interacting with a single optical mode. The Hamiltonian for the Jaynes Cummings model is:

$$\hat{H}_{tot} = \frac{1}{2}E_{TLS}\hat{\sigma}_z + E_c\hat{a}^\dagger\hat{a} + g(\hat{a}\hat{\sigma}_+ + \hat{a}^\dagger\hat{\sigma}_-) \tag{1.17}$$

The first two terms are the well-known Hamiltonians for a two level system (with energies $-E_{TLS}/2$ and $E_{TLS}/2$) and for an harmonic oscillator. The last term is the interaction dipole Hamiltonian in the rotating wave approximation. $\hat{\sigma}$ is the annihilation

operator for the TLS and $\hat{a}$ is the annihilation operator for the cavity mode.

The energy levels of the Jaynes Cummings hamiltonian are:

$$E_{n,\pm} = E_c n \pm \frac{1}{2}\hbar\Omega \tag{1.18}$$

where $\Omega = \sqrt{(E_{TLS} - E_c)^2 + 4g^2 n}/\hbar$ is called the Rabi frequency. On resonance, the coupling induces a splitting of each cavity level by $g\sqrt{n}$. Each splitted state is a quantum superposition of cavity and TLS states. When the system is initialized in the atomic excited state, the coupling of the QD and cavity on resonance induces Rabi oscillations through which the system state oscillates between the QD excited state and the single photon cavity state. The intermediate states are quantum superpositions of these two states. When the excitonic line is tuned through the cavity lorentzian line shape, the coupling induces an anticrossing of the two lines by $2g\sqrt{n}$, which is a hallmark of strong coupling in cavity QED systems where light and matter coherently exchange quantum states.

1.4.1.2 The strong coupling regime

A more realistic model must include interaction with the environment such as the decay rate of the cavity mode γ_c and the out of plane TLS emission γ (Fig. 1.9(a)). Analytical expression for the spectra of such quantum system can be obtained in the Linblad master equation formalism [85] or by a Langevin equation approach [86]. In the so-called strong coupling limit ($g > \gamma_c, \gamma/2$), the Rabi splitting and coherent exchange of energy is still taking place. However, the Rabi oscillations are damped by the cavity and atomic losses and the pure dephasing. Reaching this regime where coherent exchange of quantum states between light and matter are taking place is crucial for many quantum computer implementations because light may be used as a coherent link between nearby QDs. The strength of the TLS coupling to a cavity mode is determined by the coupling constant g [27]:

$$g = d \cdot E_0(x_0) \tag{1.19}$$

$$E_0(x_0) = \sqrt{\frac{E_c}{2\epsilon_r \epsilon_0 V}}\zeta \tag{1.20}$$

where d is the transition dipole matrix element between the two levels, E_0 is the electric field of one single cavity photon at the TLS position, E_c is the cavity energy, ϵ_r is the GaAs relative permittivity, ζ is the scalar product between the cavity mode polarization and the dipole orientation, and V is the cavity mode volume. The transition dipole in the envelope function approximation for a deeply confined exciton is given by [27]:

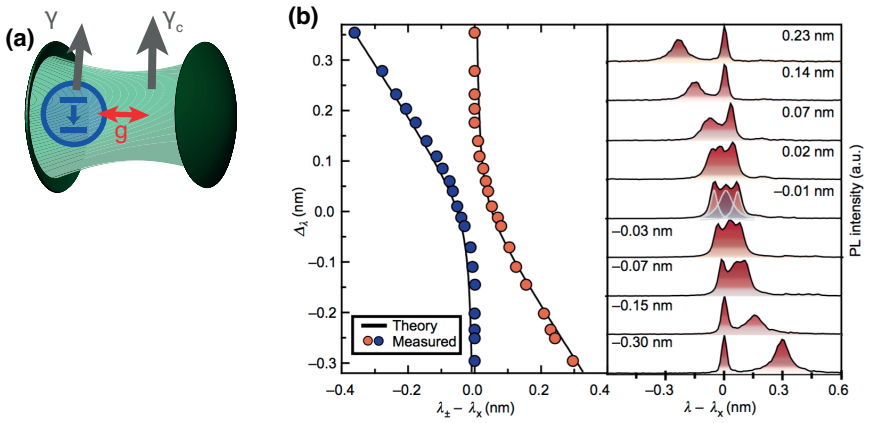

Figure 1.9 – (a) Sketch of a cavity QED system; (b) Strong coupling anticrossing for a QD in an L3 cavity; Reprinted by permission from Macmillan Publishers Ltd: Nature [91], copyright (2007)

$$d = q\sqrt{\frac{\hbar f}{2m_e\omega_{TLS}}} \tag{1.21}$$

where ω_{TLS} is the TLS angular frequency, m_e is the electron mass and f is the TLS transition oscillator strength. If we assume a cavity mode volume typical in L_3 cavities of $(\lambda/n)^3$, the maximum coupling strength achievable with deeply confined excitons in GaAs is: $g = 150\mu eV$ (with a dipole oscillator strength $f = 16$). When γ is sufficiently small, the coherence of the coupling is limited by the ratio g/γ_c, proportional to $Q/\sqrt{V}$. The coherence is therefore highest in small volume and high Q cavities, hence the advantage of PhC cavities in which the mode volumes can be reduced down to a single oscillation of the optical field [17].

Strong coupling in a QD-PhC cavity system was first observed in 2004 [87, 88]. Since then it has been observed a number of times with values of the coupling strength ranging from 40 to 106μeV [89, 63, 90, 43]. An example of anticrossing between an exciton and a cavity mode is shown on Fig. 1.9(b).

1.4.1.3 The Purcell effect

In opposition to the strong coupling regime, the regime where $\gamma, g < \gamma_c$ is called the weak coupling regime. In this regime, the photonic environment can affect the QD lifetime. This effect was first noted by Purcell [92] and arises as a natural consequence of Fermi's golden rule for the decay of a TLS to a set of optical modes[17]:

$$\Gamma = \frac{2\pi}{\hbar^2}\sum_f \left|\langle f|H_f|i\rangle\right|^2 \delta(\omega_i - \omega_f) \tag{1.22}$$

where $|i>$ and $|f>$ are initial and final states and $\hat{H}_f$ is the electromagnetics hamiltonian for a photon emission in mode f in the dipole approximation:

$$\hat{H}_f = \vec{d} \cdot \vec{E}_f \tag{1.23}$$

in the case of an isotropic transition, the transition rate is proportional to the total local optical density of states (DOS) defined as [17]:

$$LDOS(\vec{r},\omega) = \sum_f \frac{2\epsilon_0}{\hbar\omega_f} |\vec{E}_f(\vec{r},\omega_f)|^2 \delta(\omega-\omega_f) \tag{1.24}$$

where the sum is over all optical modes: $\vec{E}_k(\vec{r},\omega_k)$. Note that LDOS along each dipole polarization may also be defined analogously. In this context, PhCs offer a considerable advantage as a highly controllable photonic environment. When the pure dephasing is neglected, the Purcell factor of a QD coupled to a cavity is [17]:

$$F_{p,c} = \frac{4g^2}{\gamma_c \gamma} = \frac{3}{4\pi^2} \frac{(\lambda/n)^3}{V} Q\zeta^2 \tag{1.25}$$

where ζ accounts for the matching between the polarization of the field in the cavity and the dipole of the QD:

$$\zeta = \frac{\vec{d} \cdot \vec{E}}{|\vec{d}| \cdot |\vec{E}|} \tag{1.26}$$

The Purcell factor being proportional to Q/V, there is a considerable interest in fabricating small cavities exhibiting high Q-factors to increase the photon emission rate of QDs and thereby the communication rate of QKD protocols. However, beyond a certain value of Q, the cavity QD system enters the strong coupling regime in which photons are transferred back to the QD. A solution to further increase this emission rate is to reduce the mode volume, which is feasible using plasmons [59]. Assuming a perfect matching between the cavity mode and the dipole matrix element: (ζ = 1, Q=2000, $V = (\frac{\lambda}{n})^3$), the Purcell factor is 150. Purcell enhancements induced by cavity modes were measured by comparing the lifetime of an exciton in the bulk and in resonance with the cavity modes. The measured values range from 1.3 to 35 [91, 93, 94, 95, 96, 97]. These values are much lower than the ones expected from theory. The reasons invoked are usually a mismatch between the QD dipole moment and the cavity modes. Another possible explanation may be that QDs have a significant non-radiative coupling. The Purcell effect is not limited to decreasing the lifetime: the photonic environment can also inhibit emission with Purcell factors lower than one as is the case in the 2D photonic bandgap of a PhC slab. The measured values for QD lifetime inhibition range between 2 up to record values of 70 [98, 93, 95, 94].

1.4.2 QD in waveguides

Waveguides for guiding photons over macroscopic distances and connecting distant photonic systems are necessary components of the nanophotonic toolbox. Besides, they are an interesting alternative to cavities as efficient means of collecting photons and as light matter interaction interfaces [27], which may yield scalable quantum circuits as depicted on Fig. 1.10(a). Indeed, waveguides are by nature open systems and therefore exhibit a broadband density of states which can efficiently collect the inherently broadened emission of QD ensembles.

The Purcell effect described in the previous section also applies to waveguides. As evidenced by Rao et al. [99], the Purcell enhancement of a TLS placed in a waveguide is:

$$F_{p,wg} = \frac{3}{4\pi}\frac{(\lambda/n)^2}{A}\frac{n_g}{n}\zeta^2 \tag{1.27}$$

Where ζ accounts for the matching between the polarization of the field in the cavity and the dipole of the QD, n_g is the group velocity of the waveguide mode, n is the refractive index of the material and A is the waveguide mode area defined by:

$$A = \frac{\int dV \epsilon_r(r)|E_k|^2(r)}{a \cdot max(\epsilon_r(r)|E_k|^2(r))} \tag{1.28}$$

As noted by Rao et al. [99], this expression for the Purcell factor is analogous to the one in cavities. We can define an equivalent mode volume: V=aA and Q-factor: $Q_{eq} = \pi n_g a/\lambda$ for waveguides which traduces the interaction time between the QD and the waveguide mode. Thus, light matter interaction in a waveguide is determined by its mode area and its group index, analogous to the mode volume and Q-factor in cavities. In the same way as cavities, fabricating small mode volume waveguides with large group indexes is interesting to increase light matter interaction, hence the interest of using tiny waveguides such as the W1 waveguide presented in the last section operated near the band edge (k=π/a) of PhC waveguide modes where the group index theoretically diverge. In typical PhCW, the predicted Purcell effects are around $F_{p,wg} \approx 1$ [99], much lower than in cavities. This number can be enhanced near the band PhC band edge thanks to slow light effects, however disorder in PhCW limits achievable group indexes to values below 100, for which Purcell enhancements ≈ 20 are possible.

Tightly confined waveguides and the enhanced interaction they induce have been used to prove nonlinearities at the single photon level [101]. Besides, the directional single photon emission was demonstrated in nanophotonic waveguides combined with magnetic fields [102, 103], opening interesting perspectives to on chip quantum circuits.

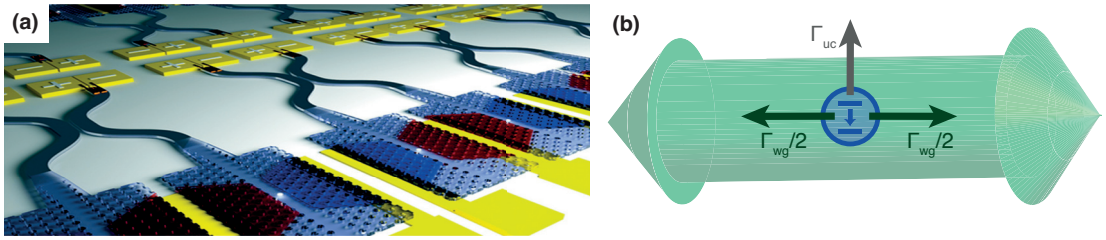

Figure 1.10 – (a) Example of GaAs based implementation of integrated quantum photonic circuit; (b) Sketch of a QD coupled to a waveguide; (a) Reprinted with permission from [100] (2016) Wiley-VCH Verlag GmbH & Co. KGaA, Weinheim.

In this work, waveguides will be studied as a mean to efficiently collect and channel QD emitted single photons. Efficient collection is necessary not only to increase the rate of collected single photon, but also to obtain a deterministic emission of single photons, which may be useful in many quantum optics experiments. Indeed, although pulsed excitation can force QDs to emit photons at a precise timing, the photon can be called deterministic only if it is efficiently collected. The figure of merit for the collection efficiency of photons is called the β factor and is defined as:

$$\beta = \frac{\Gamma_{wg}}{\Gamma_{wg} + \Gamma_{uc}} \tag{1.29}$$

where Γ_{wg} is the QD rate of emission in the waveguide mode and Γ_{uc} is all the rate of all other emission processes, such as non radiative emission rates Γ_{nr} and emission into other optical modes such as the radiation modes Γ_{rad} (see Fig. 1.10(b)).

β factors are typically measured by comparing the emission rate of a QD coupled to the waveguide to that of a QD weakly coupled or uncoupled to the waveguide mode. Measured values that have been reported range from 50 to 98% [104, 105, 106, 107]. However, estimating β factors is difficult because the QD emission into the radiation modes Γ_{rad} depends on its location [104] and because of statistical uncertainties in the values of Γ_{nr} for different QDs. Performing such experiments with site controlled QDs would both constrain these uncertainties and open a way to reproducible and scalable on chip quantum experiments. Besides, the highest β factor values were obtained near the band edge [104] where disorder and absorption are increased by the slowdown of light [79]. However, these works did not study the losses occurring inside the PhCW after the QD light emission. A simultaneous analysis of β factors and PhC related sources of loss would therefore be of great interest for the complete characterization of on chip single photon sources.

1.5 Thesis goal

This thesis focuses on the design fabrication and experimental study of systems composed of pyramidal QDs, PhC cavities and waveguides. Although similar structures were studied in the past using SK QDs, achieving reproducible and scalable experiments requires site controlled QDs.

The first results in this direction were obtained by Gallo et al., who first demonstrated the integration of a pyramidal QD inside a PhC cavity [58]. Calic et al. proved the coupling of two QDs to the same PhC cavity [108]. Jarlov et al. [96] focused on the study of QD to cavity coupling through time resolve measurements and by modeling the effect of phonons [109] as well as on systems of coupled cavities [110, 111]. Lyasota et al. demonstrated the first simultaneous coupling of 4 different QDs to L_7 cavity modes [112].

All these results were focused on cavities or systems of coupled cavities [111, 110]. This thesis describes an extension of these works aiming at the direct integration of multiple QDs in PhC circuits involving cavities and waveguides.

In chapter 2, the experimental methods and techniques used to simulate, fabricate and characterize the PhC devices are described. Both the nanofabrication techniques and the fabrication steps relevant to the pyramidal QDs [113] and PhC technology are detailed as well as the tools used to simulate our PhC structures.

Chapter 3 investigates the impact of disorder on the losses, density of modes, mode localization and dispersion in long linear PhC cavities. The site control of the QDs permits the selective mode excitation and the in-situ probing of the impact of disorder, from which we identify a diffusive edge for photon transport, below which phase scattering distorts the optical modes. These structures are also harnessed to measure both the mode reflectivity at the edge of the linear cavities, and the propagation losses in PhC waveguides [114].

Chapter 4 describes the integration of five site controlled QDs in a PhC waveguide and the corresponding on chip single photon transfer over macroscopic distances. We measure the coupling properties of QDs in these structures and give optimal conditions to reach reproducibly a broadband high efficiency of coupling.

Chapter 5 focuses on a system in which a QD is embedded in a cavity itself coupled to a PhC waveguide. We show theoretically the existence of a cavity to waveguide coupling which optimizes the coupling efficiency of single photons to the waveguide. We measure the parameters in our system, from which we infer a single photon collection efficiency close to its optimal value.

Chapter 6 summarizes the results and proposes possible research orientations to further improve the quality of fabrication and demonstrate new quantum optics effects with pyramidal quantum dots.

This work represents the first experimental implementation of site-controlled QDs in PhC systems beyond cavities. It focuses on the limitations and possibilities opened by such QD systems as on chip efficient single photon sources. These results open a path towards on chip quantum circuits with multiple QDs, which could enable large scale linear optical quantum computing [21].

2 Experimental and simulation techniques

The fabrication of systems incorporating pyramidal QDs and PhC circuits is challenging due to the nano-size of the structures, the high quality requirements at each step of the process and the large number of steps which have to be performed. In this Chapter, a detailed account of the design, fabrication and characterization of the samples studied in the thesis is given.

The process can be divided in four major steps. The first one is the design of experiments. It is partly based on numerical simulations from which we can infer target fabrication parameters and optimal designs. The second step is the substrate preparation which includes the fabrication of a membrane and the etching of alignment marks. The third and fourth steps are respectively the fabrication of pyramidal QDs and of the PhC circuits which are precisely positioned using the alignment marks fabricated in the second step. The fabrication process is summarized in the flow chart of Fig. 2.1. The growth of high purity QDs and the fabrication of weakly disordered PhC systems imposes very stringent requirements in terms of cleanliness and controllability in the fabrication. In this Chapter, all these steps will be explained in details.

2.1 Design and numerical simulations of photonic crystals

The first fabrication step is the design of each experiment. This design needs to follow the constraints imposed by pyramidal QDs and membrane PhCs. The two main constraints imposed by InGaAs/GaAs based pyramidal QDs are their emission wavelength which is currently limited between ≈ 850 and $\approx 980nm$ and the pyramid sizes. In the first demonstrations, of pyramidal QDs, the pyramids had a lateral size of few microns [115, 116]. These large pyramids allowed to grow thick buffer

layers separating the QDs from the patterned substrate, which usually suffers from defects and contaminations. However, as noted in the precedent Chapter, light matter interaction strength increases when the volume of optical modes decrease. In that context, thin PhC slabs are preferable, and significant progresses permitted the growth of high quality QD ensembles in smaller pyramids [117, 118, 53] down to 200nm [65]. Besides, thicker PhC slabs incorporate more slab modes as shown on Fig. 2.2, which can be detrimental to obtaining monomode rib or PhC waveguides.

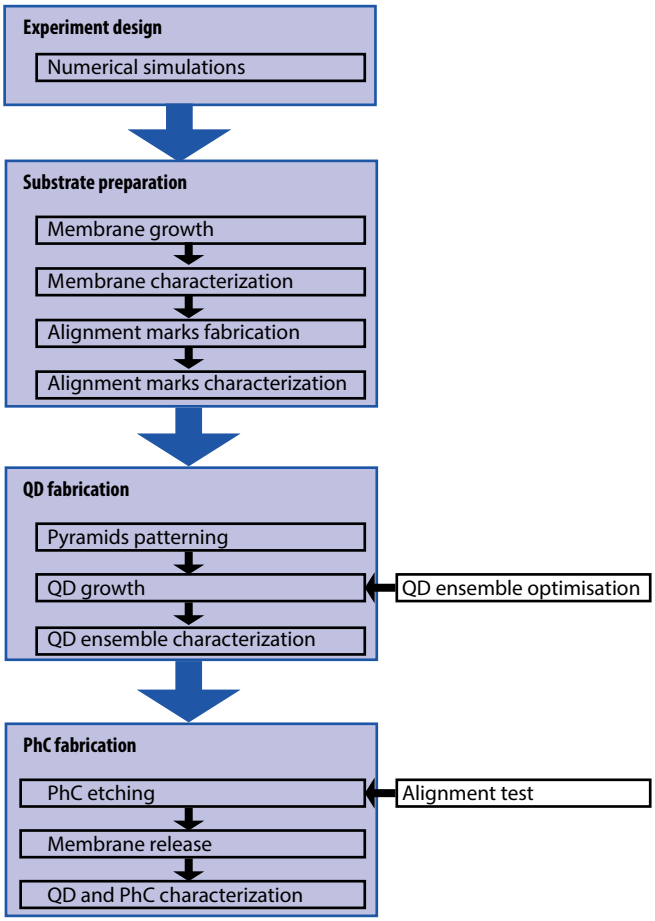

Figure 2.1 – Flow chart of the realization process

In this thesis, we are interested in using the in-plane dipole momentum of QDs, which interacts solely with the quasi-TE PhC modes. Slabs thinner than 150nm exhibit a single TE mode, justifying the use of membrane widths around 160nm in PhC experiments [104, 119]. Pyramidal QDs exhibiting good quality were obtained in pyramids with a lateral sizes as small as 200nm and 163nm height which could be integrated in slabs 180nm thick [65]. However, the best results insofar were obtained in the 260nm pyramids (with a height of 212nm) studied in this thesis. These pyramids would permit using slabs as thin as 230nm. In this work, a 20nm safety margin was

adopted with a slab thickness of 250nm.

Once the slab width and the wavelength are decided, obtaining TE photonic bandgaps requires a triangular array PhC with periodicity of the order of the wavelength of light in GaAs $\approx 260nm$. The ratio radius over PhC periodicity must lie in the range $r/a \approx 0.2-0.3$ to ensure both holes sufficiently large to be more easily fabricated and small enough to maintain a good robustness of the PhC structures. As demonstrated in the last Chapter, such r/a ratio imposes a ratio a/λ around 0.25 to ensure that our target wavelength lies within the PhC bandgap. This constraint fixes the periodicity around 238nm. In this work the PhC periodicity was a=225nm.

The exact radius is then adapted in each structure to ensure a spectral matching between the QD emission and the photonic modes.

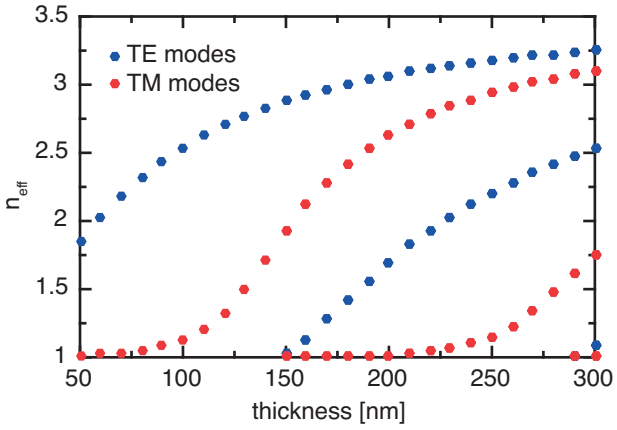

Figure 2.2 – Modes in a GaAs slab surrounded by air at 950nm wavelength (n_{GaAs} = 3.4653)

2.1.1 Solving Maxwell's equation

As emphasized in the last Chapter, optimizing the light matter interaction requires simultaneously a good spectral and spatial matching between the excitons dipole momenta and the PhC electric field, which requires to solve Maxwell's equations. However, exact analytical solutions exist in the literature for only very few problems. The design of our experiments therefore requires numerical solvers, which can be classified in two categories:

- Frequency domain solvers in which Maxwell's equations are solved for discrete frequencies.
- Time domain solver where Maxwell's equations are discretized in space and time. The numerical method implements the time evolution of the electro-magnetic field.

2.1.2 Finite difference method

The finite difference method (FDM) is very popular owing to its simple implementation [120]. It consists of discretizing Maxwell's equations along a rectangular grid and solving them in the frequency domain. It is relatively fast for 2D problems but quickly becomes intractable for larger 3D problems. In the latter case, the finite element method is a much better choice. Within the FDM, Maxwell's equations are solved as the following eigenvalue problem:

$$\vec{\nabla} \times \frac{1}{\epsilon(r)} \vec{\nabla} \vec{H}(r) = \left(\frac{\omega}{c}\right)^2 \vec{H}(r) \tag{2.1}$$

in which the squared frequency is the photonic modes eigenvalue. The derivative operators are discretized in the following way:

$$\partial_{x_i} f_k \quad = \quad \frac{f_{k+1} - f_k}{d x_i} \tag{2.2}$$

where f_k is the discretized function to be derived and x_i is the coordinate along which the derivation is performed. Through this discrete approximation, the differential operator: $\nabla \times \frac{1}{\epsilon(r)} \nabla$ becomes a large sparse matrix whose eigenvalues are the photonic modes of the PhC device. In all FDM simulations performed in this work, periodic boundary conditions were adopted. Considering the large PhC structures studied in this thesis, and the significant computational complexity of 3D FDM. The photonic modes were approximated as perfect 2D TE modes using the standard effective index approximation for the slab vertical index profile. The matlab based 2D FDM code used during this thesis was written by F. Karlson [121]. In this thesis, 2D FDM will be constantly used to obtain with a good approximation the electric field of confined modes.

2.1.3 Finite difference time domain method

Although the FDM algorithm exposed above is efficient to retrieve the modes of small PhC structures, it is restricted to the modelling of periodic waveguides or cavity modes: it can describe neither light propagation in a finite waveguide nor light sources. Besides, it cannot compute the precise resonance energies of cavity modes or the band edges of photonic waveguides. The precise design of PhC structures therefore requires a 3D solver for Maxwell's equations.

The finite difference time domain method (FDTD) that we adopted for 3D computations is an alternative numerical technique in which Maxwell's equation are discretized in space and time. It was invented by Yee et al. in 1966 [122] and is now used broadly thanks to its simplicity of implementation, its robustness, its low mem-

ory requirements (especially useful for large scale 3D simulation) and its versatility [123]. Another significant advantage is the possibility to probe a broad frequency range by simulating the transient response of a device to a broadband pulsed excitation. Its main disadvantage is the long simulation times required to simulate resonant devices such as high Q-factor cavities.

FDTD consists of discretizing Maxwell's equations using a central finite difference scheme discretized on a staggered Yee grid [123]. The electric and magnetic field are evolved in a leapfrog time stepping scheme in which the electric field is computed at time t+dt/2 from the magnetic field at time t. The magnetic field is then computed at t+dt from the magnetic field at t+dt/2.

In this thesis, two FDTD softwares were used for simulations. One is a matlab based software written by F. Karlson [110], from which we obtained the 3D photonic modes of photonic crystal cavities and their resonance energies. The other one is the open source software meep [124], which was used to compute the dispersion relations in waveguides, the Q-factor of PhC cavities or the propagation of light in large PhC structures.

2.1.3.1 L_3 cavities

The M_0 mode in optimized L_3 cavities are popular in the photonics community thanks to their small mode volume and large Q-factor, which makes them quasi-optimal solutions for obtaining strong coupling and large Purcell enhancements. In the past, these cavities have been studied as a cavity QED platform [109, 125]. In this thesis, they will be used as a figure of merit for measuring the quality of PhC fabrication. Their inherently high Purcell factor will also be employed in Chapter 5 to optimize the light extraction from pyramidal QDs in cavities coupled to waveguides.

The L_3 cavity fabricated in this work was optimized by Minkov et al. [126] with a genetic optimization algorithm to reach a theoretical Q-factor of 200000. Such a high Q-factor could be obtained by optimizing the terminations of this cavity according to the design shown on Fig. 2.3 (a). This process is equivalent to minimizing the mode coupling to the light cone [127].

The modelling of PhC cavities realized with the matlab code was performed in a two-step computation. First, the system response to a broadband Gaussian pulse was recorded in the cavity. To do such a transient analysis, the targeted cavity mode was first computed using FDM. Then the FDTD simulation was performed with an extended source placed in the center of the slab and exhibiting the distribution of the FDM computed mode. This first simulation allowed to excite only the mode of interest. The frequency of this mode was computed using the Fourier transform of the electric field recorded by a probe placed in the cavity. Once this frequency was known, the simulation was continued, and the temporal Fourier transform of the electric field at the target mode frequency was recorded during the simulation. This

Fourier transform step permits to select only the electric field emanating from the cavity and to filter out any other spurious mode. The Fourier transformed field thus obtained corresponds to the cavity mode shown on Fig. 2.3 (b-c-d). This mode has a mode volume: $V \approx 1.0(\lambda/n)^3$.

The cavity design is symmetric through the x, y and z=0 planes. Therefore, these symmetry operators commute with the eigen-operator of Maxwell's equations. Consequently, the photonic modes are eigenvectors of these symmetries for one of the two possible eigenvalues: 1 and -1, which corresponds to symmetric and anti-symmetric modes along each of these directions. As is clear from the simulations on Fig. 2.3 (b-c-d). The M_0 mode is symmetric along the y direction and anti-symmetric along the x and z direction. Besides, the E_y component of the electric field is maximal at the cavity center. An optimal design for cavity QED is therefore obtained by placing a y-oriented exciton at the cavity center, where it has a zero overlap with TM PhC modes which are not confined by the PhC and a maximum overlap with the M_0 cavity mode.

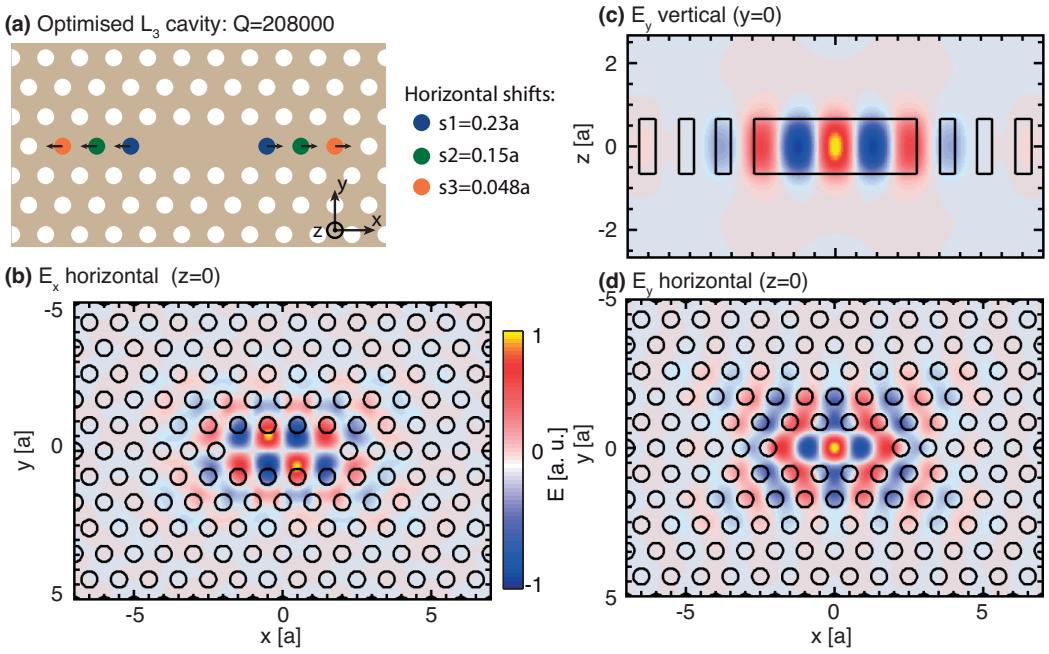

Figure 2.3 – FDTD simulation of an L_3 cavity: (a) Design of the optimized L_3 cavity; (b) E_x slice in the z=0 plane; (c) E_y slice in the y=0 plane; (d) E_y slice in the z=0 plane (n=3.46, r=61nm, a=225nm, th=250nm)

2.1.3.2 W1 waveguides

Although PhC cavities excel at enhancing light matter interactions, waveguides are required to guide light and connect elements of a photonic circuits. Optimal solutions for guiding light in on chip optical circuits consist in using rib or ridge waveguides

[128]. However, photonic crystal waveguides thanks to the slow light effect represent a promising alternative to cavities both as a mean to extract light and for enhancing light matter interaction [129]. To that end, PhC waveguides exhibiting small mode cross-sectional areas such as W_1 waveguides represent a promising option.

A simulation similar to that described for an L_3 cavity was used to obtain the band structure and the electric field of modes of an infinite waveguide. The infinitely long waveguide can be reduced to a finite simulated volume thanks to Bloch's theorem. The simulated volume is then restricted to only one period of the waveguide with Bloch boundary conditions along the waveguide direction and perfectly matched layers (pml) along the other directions. The band structure of a W1 waveguide is ontained by performing one simulation for each value of the wavevector k. The simulations were performed with meep [124], the result shows a number of guided modes extending between the air and the dielectric bands (Fig. 2.4). The target band in blue lies in the 900-980nm range. This waveguide also contains modes very close to the light line (in red). These spurious modes were not observed in our experiments. A possible explanation is that disorder prevents their guiding over large distances.

The group index n_g is straightforwardly computed from the band structure using its definition: $n_g = -c\partial k/\partial\omega = \lambda^2/(2\pi)\cdot\partial k/\partial\lambda$. It shows a monotonous increase with k going from 6 to infinity while approaching the band edge. This slow light effect was emphasized in many previous publications [130]: in a disorderless infinite waveguide at the band edge, light can be completely stopped.

The W1 target mode mode at $k = 0.6\pi/a$ is then computed using the 3D FDTD method described for the L_3 cavity. As mentioned before, this mode is anti-symmetric along z and symmetric along y. The y component of the electric field is maximal at x=y=z=0, which is where the QD has to be positioned to be optimally routed into the propagating mode.

2.1.3.3 Design of the PhC structures

Spatial matching between excitons and photonic modes is permitted by the accurate positioning of pyramidal QDs at targeted locations in the PhC structures. An efficient coupling to the light modes also requires a good spectral matching. To that end, the variations of the M_0 mode energy in L_3 cavities and the band edge in W1 waveguides with the PhC hole radius r were simulated via FDTD. They are given on Fig. 2.5. In this thesis, as will be shown later the emission wavelength of the employed QDs in the PhC devices is around 945nm. The corresponding hole radii for L_3 cavities are between 65 and 70nm. The coupling of QDs to a W1 waveguide is less stringent thanks to its (ideally) broadband nature. The main constraint is that the PhC hole radius be kept below 70nm: the radius for which the photonic band edge crosses the emission wavelength of QDs. The intersection between the waveguide band and the light line is indicated in black (Fig. 2.5). The waveguide band is sufficiently broadband to ensure a

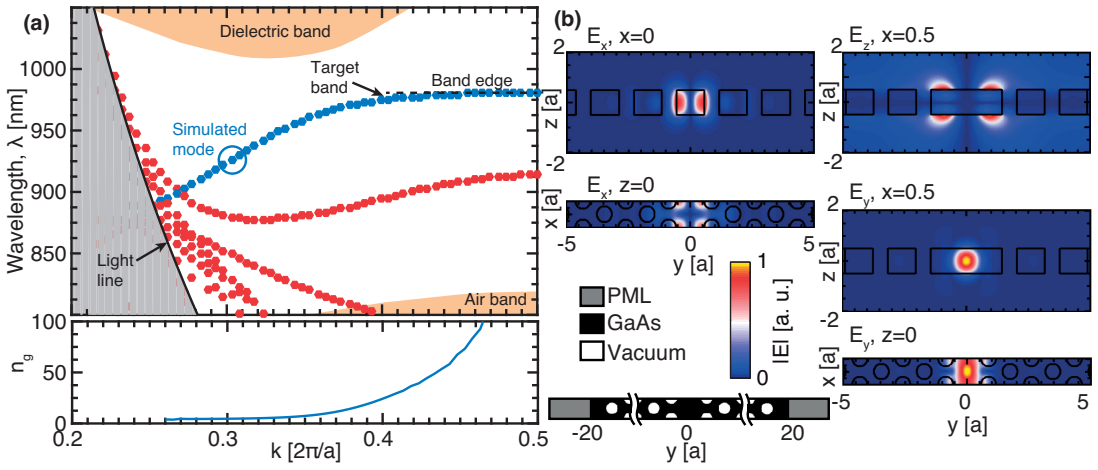

Figure 2.4 – FDTD simulations of W1 waveguide: (a) Upper panel: Band structure of an infinite W1 waveguide, the blue dots indicate the target (lowest frequency) waveguide band, the red dots are other waveguide modes; the mode simulated in (b) is indicated by a blue circle; lower panel: group index of the target mode (n=3.46, r=61nm, a=225nm, th=250nm); (b) Electric field simulations of the blue mode in a W1 waveguide: E_x in the z=0 and x=0 plane, E_y in the x=0.5a and y=0 plane,E_z in the z=0 plane (n=3.46, r=61nm, a=225nm, th=250nm, $k = 0.6\pi/a$).

coupling in PhC waveguides with hole sizes below 50nm. Besides, one major interest in PhC waveguides lies in the possibility to slow down light and thereby increase the light matter interaction. This is feasible in W1 waveguides, provided the QDs are resonant with slow light modes which is the case when the PhC hole radius is between 65 and 70nm.

2.1.4 2D Finite Difference Frequency Domain Method (FDFD) Modelling

FDTD is much more versatile than the FDM algorithm described above. However, FDTD simulations of continuous waves are very slow since they require very long simulation times to make sure all transient fields have decayed. A more efficient solution for obtaining the response of a PhC system to a continuous wave excitation is the Finite Difference Frequency Domain Method (FDFD). It consists of the simulation of frequency domain Maxwell's equation discretized on a Yee cell:

$$(\vec{\nabla} \times \frac{1}{\epsilon(r)} \vec{\nabla} \times - \left(\frac{\omega}{c}\right)^2) \vec{H}(r) = \vec{\nabla} \times \frac{\vec{J}(r)}{\epsilon_r} \tag{2.3}$$

Contrary to FDTD, this equation is solved for only one frequency. Contrary to FDM, it contains a source term. Once discretized, the wave equation becomes a linear matrix equation in the form: Ax=b. It is solved by inverting the large sparse matrix

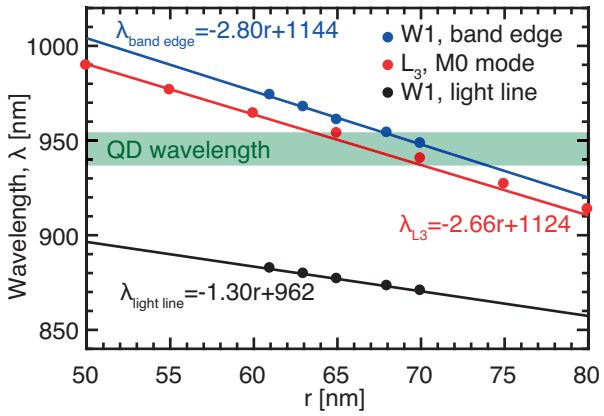

Figure 2.5 – Variations of the wavelengths of the L_3 M_0 mode, the photonic band edge and the intersection between the guided band and the light line in a W1 waveguide; the dots indicate FDTD simulations, the lines are linear fits. (FDTD simulation parameters: n=3.46, a=225nm, th=250nm)

A. The matlab 2D-FDFD code used in this work is based on the work of Rumpf et al. [120].

The sources are implemented using the total field/scattered field formalism, in which space is divided in two regions. One region contains the total field, while a second region contains only the scattered field, but not the incident field. The source is placed at the boundary between the total field and the scattered field and is implemented as an equivalent magnetic field modal source. To avoid spurious reflections, pml were implemented at the boundary of the simulated zone [123] by transforming Maxwell's equation as:

$$\nabla \times \vec{E} = -i\eta_0 k_0 s \vec{H} \tag{2.4}$$

$$-i\eta_0 \nabla \times \vec{H} = k_0 s \vec{E} \tag{2.5}$$

in which $\eta_0 = 376\Omega$ is the vacuum impedance and s is a tensor [123] :

$$s = \begin{bmatrix} \frac{s_y}{s_x} & 0 \\ 0 & \frac{s_x}{s_y} \end{bmatrix} \tag{2.6}$$

$$s_i(x) = (1 - i\eta_0 \sigma e^{1-L/x}) \tag{2.7}$$

where x is the pml coordinate, and is zero at the interface between the pml and the simulated volume. L is the pml length. In such a formulation, the s tensor introduces a gradual increase of the absorption losses, while ensuring that the reflection of incident

plane waves at any incident angle is zero in the limit of infinite resolution.

This result does not hold in inhomogeneous media such as PhCs. However, we will show that the pml absorption can still be made efficient. Notice that we did not introduce stretching of the grid as is common in pml formulations which tries to model an infinite vacuum space with a finite memory. We choose to do so because stretching induces distortions of the PhC and tends to increase unwanted reflection.

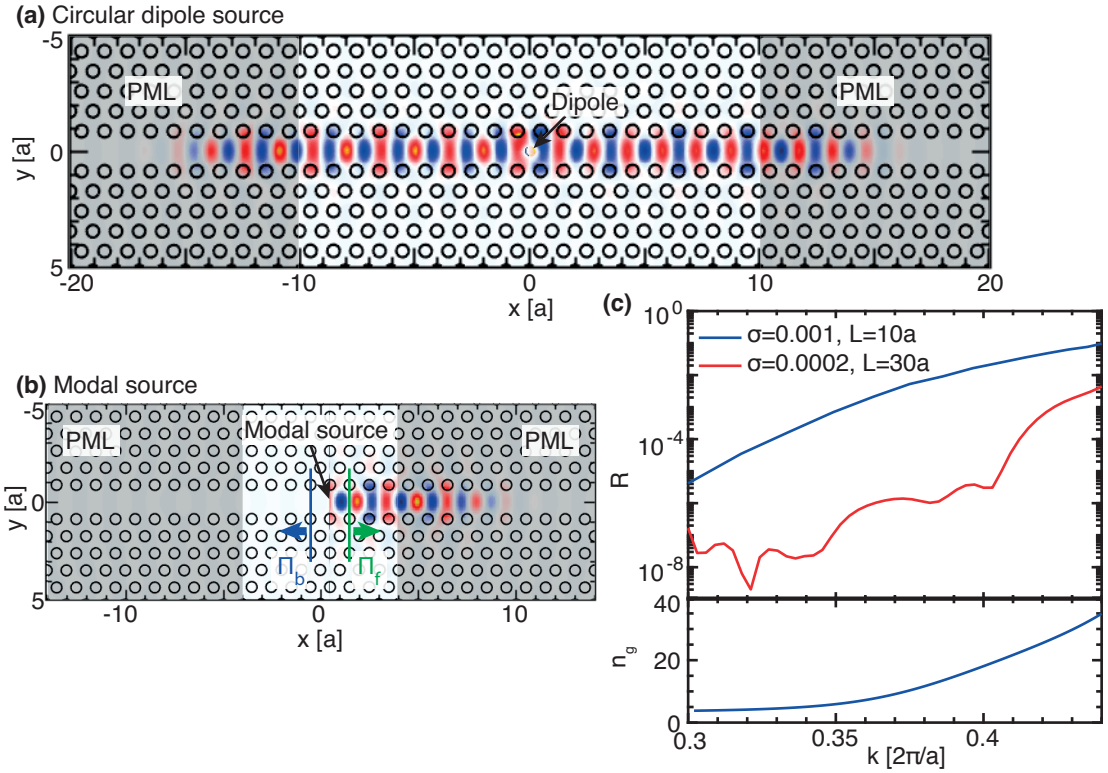

Figure 2.6 – FDFD simulations of PhC waveguides: (a) E_y component of the electric field emitted by a circularly polarized dipole placed in a PhC waveguide; (b) E_y component of the electric field emitted by a modal source placed in a PhC waveguide; (c) Upper part: Reflectivity of the PML in a PhC waveguide. Lower part: group index in a PhC waveguide. In all these simulations, the simulated PhC parameters are: a=225nm, resolution: 0.05a, r=61nm, $n_{2D} = 3.17$.

A first example of FDFD simulation is shown in Fig. 2.6(a). A circular dipole source was placed in a 20a waveguide, with L=10a pml absorbing layers at each edges, with $\sigma = 0.001$. Light is coupled to the left and right propagating waveguide modes until it reaches the pml where it is gradually absorbed.

In a second simulation in Fig. 2.6(b), the source is a modal waveguide source propagating in the right direction in which the mode was previously computed using the FDM method. The forward and backward propagating energy fluxes (Π_f and Π_b) carried by the waveguide modes were computed at the positions indicated by

the green and blue arrows. In the limit of weak reflection by the pml, the reflection coefficient of the pml is given by the ratio: $R = \Pi_f / \Pi_b$. This ratio was computed for each value of k, the wavevector of the incident waveguide mode on Fig. 2.6(b), and for two sets of pml parameters: L=10a, $\sigma = 0.001$ (in blue) and L=30a, $\sigma = 0.0002$ (in red). In the first case (blue curve), the reflection increases with the group index but is reasonably low (below 1%) up to $k = 0.39$ $[2\pi/a]$ or equivalently $n_g = 15$. In the second simulation (larger pml with lower absorption), the losses were reduced below 10^{-5} up to k=0.4 [2π/a] and below 1% up to $k = 0.45$ $[2\pi/a]$ or equivalently $n_g = 42$. However, significant reflections are still observed in the slow light regime. This issue may be solved with mode matched boundary conditions similar to those proposed in FDTD simulations [131].

FDFD will be used in Chapter 5 to simulate the propagation of light emitted by a dipole in an L_3 cavity coupled to a W1 waveguide.

2.2 Fabrication of QDs in PhC circuits

This section will now go through the fabrication process, including the etching of alignment marks, the fabrication of pyramidal QDs and finally the fabrication of PhC circuits aligned over the array of QDs.

2.2.1 Substrate preparation

Before the fabrication of pyramidal QDs and PhCs, a membrane substrate is required. Its fabrication process starts with the growth of the PhC membrane which was then characterized in a scanning Electron Microscope (SEM) and with an atomic force microscope (AFM). Once the membrane quality was validated, alignment marks used to align the QDs and PhCs were etched into the substrate. This section starts with a presentation of the tools that are used to characterize the membrane.

2.2.1.1 Scanning electron microscope

Although conventional optical microscopy is a standard tool to characterize nano-fabricated objects, it is limited by the Abbe diffraction limit to $\frac{\lambda}{2n} \approx 400 - 200nm$ in the vacuum [17] (even though super-resolution techniques, more and more popular in biology, may overcome it [17]). Electrons, instead have a de-Broglie wavelength , orders of magnitude smaller (($\lambda \approx h/(m_e v)$=38$pm$ at $1keV$ at non relativistic speed, where v is the electron speed). They can be harnessed in imaging systems reaching much higher resolution of surfaces or volumes than optical microscopes.

In a SEM, an electron beam is thermoionically (or field-induced) emitted from a metallic tip, focused and scanned on a sample using a set of magnetic lenses as shown on Fig. 2.7. The incoming electron beam ionizes the atoms, which emit secondary

electrons with a weak kinetic energy. These secondary electrons are emitted only near the surface and are used to achieve a high resolution imaging $\sim 1-10nm$ however with a large depth of focus $\sim 1mm$. The number of reflected electrons depends on the composition, the depth, the surface orientation and its chemical composition. The achievable resolution is limited by the beam waist and the topographic contrast.

Some electrons are backscattered and exhibit an energy close to that of the incoming beam. This backscattering is higher for heavy atoms which is useful to obtain information on the composition of the surface, however with a lower resolution. In this case, the resolution, is limited by the electron diffusion during the scattering process. Lower acceleration voltage usually means lower diffusion and higher resolution. When the electron beam scatters an electron from a core atomic shell, the de-excitation leads to X-ray emissions which is commonly used for atomic characterization.

We also note that Transmission Electron Microscope (TEM), in which electrons transmitted through the sample are imaged, can reach much higher resolution than SEM , $< 0.1nm$ but this technique requires a complex preparation of samples. SEM is thus the tool of choice for rapid daily imaging of nano-objects.

Throughout this work SEM pictures were taken using a JEOL (JSM-6701F), with a resolution of 1 nm at a 5 kV acceleration voltage.

2.2.1.2 Atomic force microscope

SEM provides high resolution pictures of nanometric structures. However, its horizontal resolution is still limited by the focusing of electrons, its vertical resolution is poor, and this technique is applicable only to conducting surfaces. On the contrary, very high resolution 3D imaging of surfaces is achievable with a local probe microscope called atomic force microscope (AFM) invented in 1985 by Binnig, Quate and Gerber [132]. The 3D map of a sample is obtained by scanning a metallic tip over its surface. The height is measured via the deflection of a laser beam reflected on the cantilever holding the tip as shown on Fig. 2.7. This technique doesn't need any special sample preparation, it is low cost and simple to operate, however it requires a slow scanning over a surface and is limited to surface imaging. It is broadly used for sub-micron characterization of surfaces. A piezoelectric XY stage moves the sample such that the tip can acquire the surface topology.

Most AFM instruments exhibit three modes of imaging:

- The contact mode, where the tip is in permanent contact with the surface. The cantilever is bent due to Van-der-Waals repulsive forces. The deviation of the laser beam on the detector is used to measure the height of the surface. This technique has the highest resolution. However, it can damage the surface and it is problematic in ambient air where the surface is covered with a $\approx 1nm$ adsorbed water layer which forms a meniscus around the tip and leads to a

hysteresis in the movement.

- The intermittent-contact (tapping) mode, in which the tip is oscillating in intermittent contact with the surface. To do so, the cantilever oscillates at a frequency close to its resonance frequency. The oscillation amplitude changes when the tip interacts with the Van-der-Waals force which can be used in a feedback loop to monitor the height. This is the most common mode thanks to its good compromise between high resolution and simplicity of use.

- The non-contact mode, in which the tip is oscillating without touching the surface and the feedback is obtained from the interaction of the tip with the attractive Van-der-Waals force. It is optimal to image soft surfaces albeit with a lower resolution.

In this work, an XE-100 made by PSIA was used to record AFM pictures in tapping mode with a resolution high enough to record monolayer crystallographic steps in GaAs.

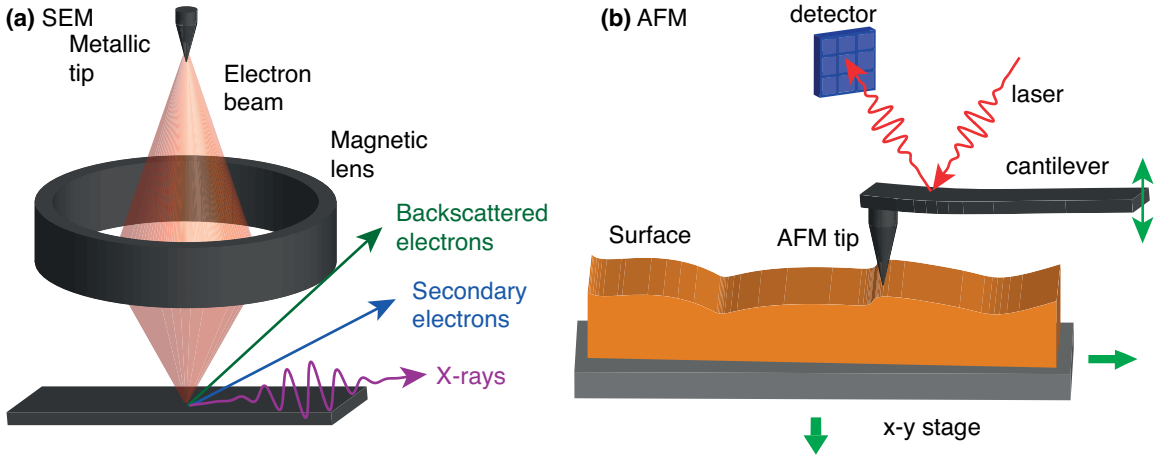

Figure 2.7 – (a) sketch of a SEM; (b) sketch of an AFM

2.2.1.3 Membrane growth

A first step towards the integration of QDs in PhC devices is the growth of a high quality membrane slab used to confine light along the direction perpendicular to the PhC plane. This growth is a crucial step to fabricate high performance PhC devices and was optimized to achieve low step bunching and low residual doping. The membranes were grown by A. Arnoult from the Laboratory of Analysis and Architecture of Systems (LAAS) by means of molecular beam epitaxy. The growth was done on a (111B) oriented undoped GaAs substrate with a 3° misorientation in the [-2 1 1]

direction. This specific misorientation is crucial to achieve the low step bunching necessary to ensure a low roughness of the photonic crystal upper and lower surface.

The grown layer sequence was:

- A 1µm $Al_{0.65}Ga_{0.35}As$ sacrificial layer.
- A 265nm $GaAs$ slab in which the QDs and PhCs are to be fabricated.

The substrate composition, dimensions and quality were measured by:

- AFM: A root mean squared roughness of 0.3nm was measured and an distance between steps of 66nm (see Fig. 2.8 (a-b)). On a 3° off misoriented GaAs substrate, monolayer steps are separated by 5.5nm. Therefore, these membranes exhibit an average step bunching of twelve monolayers.
- X-ray diffraction measurements performed by A. Rudra as shown on Fig. 2.8 d), indicating an aluminium content of 65% and a membrane height of 265nm.
- Direct SEM observation of the grown layers from a cleaved edge piece of the grown wafer as shown on Fig. 2.8 c), indicating a $991 \pm 5nm$ AlGaAs layer and a $260 \pm 5nm$ GaAs layer.

All these measurements are consistent within their error margin and confirm the suitability of this membrane for our objective.

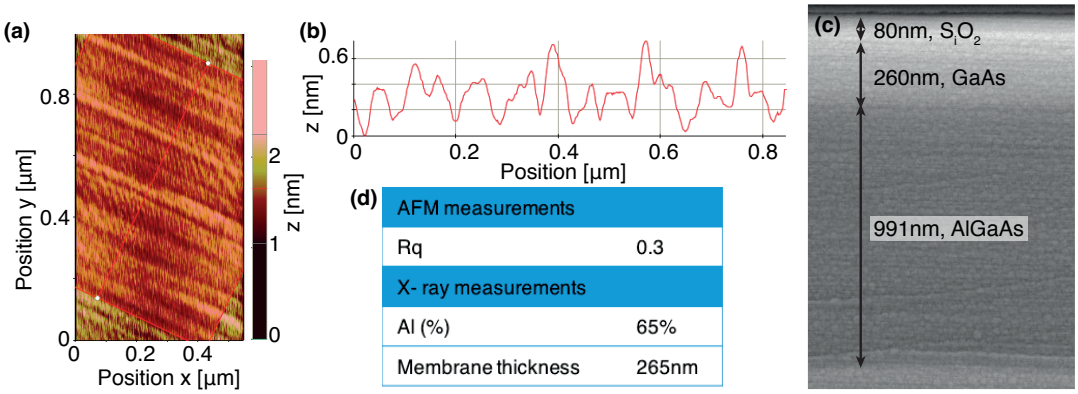

Figure 2.8 – Membrane characterization: (a) AFM picture of the surface; (b) AFM measured height averaged along the direction perpendicular to the step flow. The red transparent square in (a) indicates the surface over which this roughness was averaged; (c) SEM measurement of a cleaved edge piece of the substrate; (d) AFM and X-ray results (credits go to A. Rudra for the X-ray measurements, The work was partly supported by the French RENATECH network: we thank A. Arnoult for MBE growth of the (111)B GaAs/AlGaAs membrane wafers employed).

In a second step, integrating site controlled QDs and PhC circuits on the membrane requires the fabrication of alignment marks to ensure a good alignment between the QD and the PhCs. These alignment marks are etched using the inductively coupled plasma (ICP) etching technique using a SiO_2 mask, itself patterned with an upper polymer mask, which is defined using a technique called electron beam lithography (EBL). The SiO_2 mask is deposited with a plasma enhanced chemical vapor deposition technique (PECVD) and then etched in a Reactive Ion Etching (RIE) chamber. These four techniques are presented in the next subsections.

2.2.1.4 Electron Beam Lithography

In the same way as in SEM, EBL uses a focused electron beam to "write" a pattern in an "electron resist" layer with much higher resolution than conventional optical lithography techniques. Thanks to the high acceleration voltage, usually around 100keV, the de Broglie wavelength is very small, while the spot size is limited by electron lenses to $< 5nm$. The writing resolution is then ultimately limited by electron diffusion. This technique is very flexible as it doesn't require a fixed mask, however it is a serial process, where the electron beam writes pixels one by one. Optical lithography is therefore the method of choice for industrial mass production, when the mask resolution is not a limiting factor. EBL is best suited for writing high resolution structures. EBL resist is usually composed of long polymer chains, which are broken by the electron beam into smaller pieces, more soluble in a dedicated solvent.

The resist used for all the fabrication procedures during this thesis was polymethylmetacrylate (PMMA) permitting a resolution of $< 10nm$, and the solvent was a mixture of methylisobutylcetone (MIBK) and isopropanol (IPA), 1:3.

All EBL writings were realized by B. Dwir, using a Vistec EPBG5000+ system, permitting to write structures with a resolution down to $< 5nm$, a positioning accuracy at the nm level and the alignment over substrate marks with a precision of $< 20nm$.

2.2.1.5 Plasma Enhanced Chemical Vapor Deposition

PECVD is a nanofabrication technique where thin films of materials with controllable composition are deposited over a substrate without heating the samples at the high temperatures required for Chemical Vapor Deposition techniques. The deposition is done by introducing gases between parallel RF driven electrodes. The gas is then ionized and thin layers of the chosen material (here S_iO_2) resulting from the chemical reaction of the different reactants are deposited onto the substrate.

In this thesis work, we used a PlasmaLab system 100 PECVD made by Oxford Instruments to deposit S_iO_2 masks for the patterning of samples using a combination of SiH_4 and N_2O. The standard process used in all depositions cited subsequently had the following parameters: Temperature: $T = 300°C$, flux rates: $N/S_iH_4 = 400sccm$, $N_2O = 710sccm$, Pressure: $P = 1000mBar$, RF power: $P_{RF} = 20W$.

2.2.1.6 Reactive Ion Etching

RIE is a dry etching technique which is made directional via the use of a plasma. It is commonly used to transfer a mask pattern onto a substrate. An RIE system is usually composed of a chamber under vacuum in which some gases are injected and ionized with a strong radio-frequency electromagnetic field. The electrons are accelerated by the RF field, while the ions are weakly affected due to their larger mass. The chamber walls are electrically connected to the ground and the substrate positioned on an insulating platter becomes negatively charged and attracts the positive ions which will then etch the substrate. The etching is more chemical or mechanical depending on the composition of the plasma and the etched layer. The intensity of the RF source controls both the ions concentration and their energy.

In this work, an Oxford Instruments Plasmalab 80 was used to etch SiO2 layer masked by a PMMA layer. The process used throughout this thesis had the following parameters: flux rates: $CHF_3 = 25sccm$, $Ar = 25sccm$, Pressure:$P = 15mBar$, RF power:$P_{RF} = 50W$. The etching rate was around 10nm/min for large mask openings.

2.2.1.7 Inductively Coupled Plasma Etching (ICP)

ICP is a dry-etching nanofabrication technique used as an alternative to the more conventional RIE. It usually offers higher mask selectivity and lower damages than RIE. The ICP system is made of a chamber, in which a gas is injected and ionized by coils generating an oscillating magnetic field. An RF bias between the platter and the chamber is used to accelerate the ions onto the substrate, itself placed on a wafer holder. The RF power generating the magnetic field controls the ion density while their acceleration is controlled via the RF bias. This technique gives more freedom in setting the plasma parameters and is therefore a method of choice for the critical etching step required to make photonic crystals.

In this work we used a Sentech Plasma Etcher SI 500 ICP system, in which the temperature of the substrate was kept constant by a helium flow and a heating resistor below the platter. The ICP was used to etch GaAs with a combination of BCl_3 and N_2, using the following parameters: the gas fluxes: $7.5sccm$ of BCl_3, $12.5sccm$ of N_2, the pressure reactor of $0.18Pa$, the coil power: 600W, the RF power: 20W. The temperature was stabilized by water cooling at: $T = 29$°C. The balance between BCl_3, a chemical etchant for the GaAs surface, and N_2 which passivates the GaAs surface, permitted the etching of straight PhC holes.

2.2.1.8 Alignment marks patterning

The alignment marks consisted of $10\mu m$ squares which were not etched directly in the 260nm membrane layer, but rather in the substrate GaAs layer, below the AlGaAs sacrificial layer. This required first to etch large openings in the membrane. The alignment marks were then etched inside these openings.

The fabrication of these openings started with the deposition of a 300nm SiO_2 layer inside the PECVD machine 2.2.1.5 followed by a layer of polymethyl-methacrylate (PMMA) A8 spun coated at 6000rpm. The PMMA was then baked for 5 minutes at 160°C. The openings were written with EBL and released within a bath of MIBK:IPA 1:3 during 1min. The PMMA pattern was transferred to the SiO_2 layer with a 40 minute long RIE etching (with the etching parameters given in 2.2.1.6). The residues of the PMMA mask was stripped off by a five minutes dip in an ultrasound acetone bath followed by five minutes of O_2 plasma cleaning (power: $50W$, pressure: $60mTorr$). The same sequence was used throughout this thesis for the fabrication of all SiO_2 masks including the ones of the alignment marks, the QDs, and the PhC. The only changes in this procedure were the varying SiO_2 and PMMA thicknesses and the corresponding changes in RIE etching times.

The openings were then etched through the membrane layer by 400s of ICP with the parameters given in 2.2.1.7. The sample was then dipped into a 10% hydrofluoric acid ($HF:H_2O$) during 10s to dissolve the AlGaAs layer in the region of the openings, leaving a smooth surface for the fabrication of alignment marks. These alignment marks were fabricated with the very same process (including the same PMMA and SiO_2 layer thickness and the same RIE time), except for the longer ICP etching time of 1200s in order to obtain the $2\mu m$ deep alignment marks.

2.2.2 QD fabrication

Just as the alignment marks, the QD fabrication started with the deposition of 40nm SiO_2 and the spinning of PMMA A4 at 6000rpm (Fig. 2.10 step 1) followed by the EBL writing of an array of triangles. The written structures were developed by a 1 minute bath in MIBK:IPA 1:3 (Fig. 2.10 step 2). The PMMA mask was transferred to the SiO_2 layer through five minutes of RIE 2.2.1.6 (Fig. 2.10 step 3). PMMA was then stripped away by five minutes in an ultrasound bath in acetone followed by a five minute O_2 plasma (power: $50W$, pressure: $60mTorr$, Fig. 2.10 step 4). The inverted pyramids were etched in a process involving five steps (Fig. 2.10):

1. 30s water bath
2. 10s methanol bath,
3. 6s etching in a solution of Br:Me with 0.06% of brome prepared four hours earlier.
4. 10s rinsing in methanol
5. 2 minutes rinsing in water.

The SiO_2 layer was removed in a HF bath (Fig. 2.10 step 6). At this stage, the sample takes the form of a GaAs substrate, patterned with an array of inverted pyramids in which the QD array can be grown. Before the growth, we followed a last deoxydation and cleaning procedure, crucial to ensure the cleanest possible surface and a high QD optical quality:

1. 5 minutes O_2 plasma (power: $50mW$, pressure: $60mTorr$)
2. 5 minutes in a buffered-HF bath.
3. 2 minutes rinsing in water (more recent results showed that a 10 minutes rinsing time improved significantly the growth quality).
4. Transport of the sample in a nitrogen filled glove to the growth chamber.

2.2.2.1 Metal organic chemical vapor deposition

Pyramidal QDs are then grown using the metal organic chemical vapor deposition technique (MOCVD). MOCVD is a broadly used epitaxial technique to produce multilayer crystalline thin films. It can grow a wide variety of materials with monolayer precision, a very good uniformity over large areas and a low defect density. It is widely used both in research institutes and for industrial mass production of optoelectronic devices thanks to its uniform deposition capability permitting high throughput growth.

In MOCVD, metal-organic compounds combined with hydrides such as arsine (AsH_3) are injected into a reactor through a carrier gas (here N_2), where they are decomposed in contact with the hot substrate, resulting in the growth of a pure crystalline layer as shown on Fig. 2.9.

The substrate is rotated to ensure the growth uniformity and needs to be kept at a temperature high enough to break the bond between the Ga or In adatom and its associated ethyl or methyl radicals. In contact with the surface, the precursors adsorb to the surface, where they flow over the surface and undergo a thermal decomposition until they reach their final adsorption (crystallization) site. The organic byproducts (H, methane, ethane, ethene) desorbs and are evacuated from the reactor.

Under normal growth conditions, the flow rate of group V components is larger than that of group III. This difference is measured by the V/III ratio. A fine control over the substrate temperature, the V/III ratio, the reactor pressure, the nature of precursors and the growth rate was used to achieve a high purity growth of semiconductor heterostructures.

In this thesis, the QDs were grown in an Aixtron 200 system operated by A. Rudra, using a combination of trimethylgallium (TMGa: $Ga(CH_3)_3$), triethylgallium ($TEGa$: $Ga(C_2H_5)_3$), arsine (AsH_3), triethylindium (TEIn: $In(C_2H_5)_3$). and trimethylindium

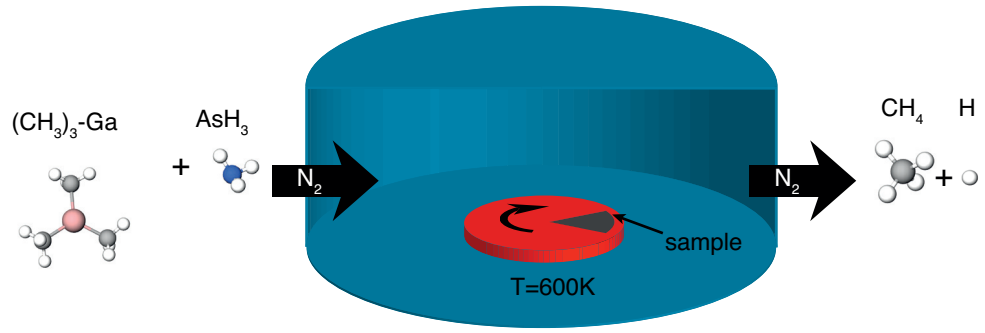

Figure 2.9 – Principle of MOCVD of GaAs

(TMIn: $In(CH_3)_3$). The carrier gas was N_2. The growths were performed at a temperature of 600°C under a pressure of 20$mBar$.

2.2.2.2 QD growth

The growth is carried out in the MOCVD chamber with the following steps (Fig. 2.10 step 7):

1. Stabilization of the sample at a thermocouple temperature of 600°C.
2. Deoxydation of the sample during 4 minutes at a thermocouple temperature of 600°C.
3. Buffer of GaAs: 5nm grown with TEGa and AsH_3.
4. 0.8nm of $In_{0.25}Ga_{0.75}As$ grown with TEGa, TMIn and AsH_3.
5. 2nm of GaAs grown with TEGa and AsH_3.
6. An 8nm thick cap of GaAs grown with TMGa and AsH_3 to planarize the surface.

During all these steps, the GaAs growth rates were stabilized in the 0.005 - 0.01nm/s range. All thicknesses and In mole fractions mentioned here are those that were measured on planar (100) GaAs. The growth rate and In mole fraction were calibrated by A. Rudra. $(Ga)InAs/GaAs$ superlattice structures were grown. X-ray diffraction rocking curves were fitted with simulated curves. Actual thicknesses are much larger due to the larger growth rates inside the inverted pyramids.

The growth of pyramidal QDs results from the interplay between several phenomena: first there is a decomposition of precursors on the gallium terminated (111)A facets as opposed to the arsenic -terminated (111)B facets. After decomposition, adatoms undergo a surface diffusion over 200-300nm. As a consequence, the layers are grown predominantly on (111)A facets, inside the pyramids. Capillarity leads to a larger thickening of the layers at the pyramid edges where QWRs are created and at

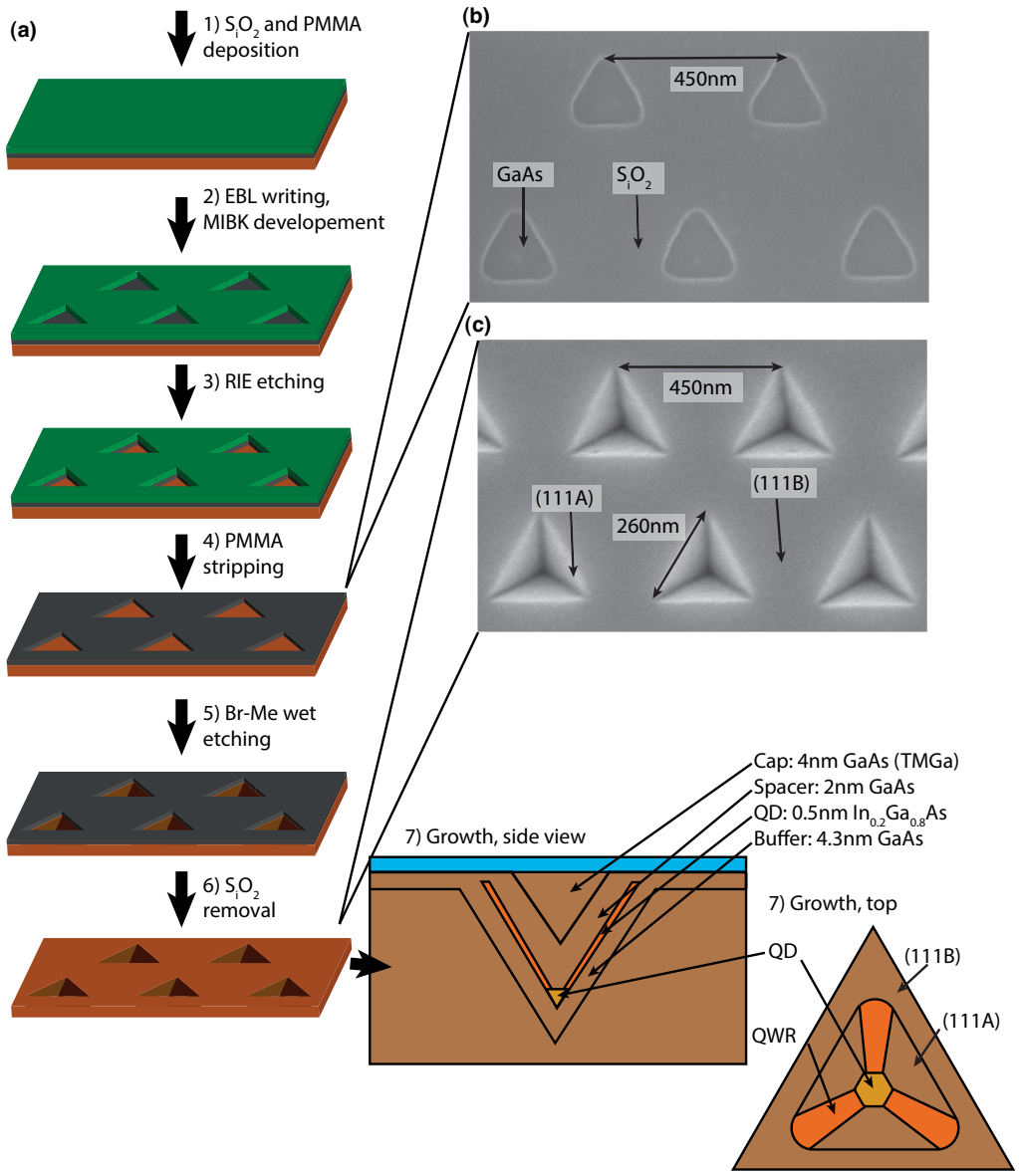

Figure 2.10 – Pyramidal QDs fabrication: (a) Step by step fabrication of the inverted pyramidal recesses; (b) SEM image of the SiO_2 mask of the array of triangles; (c) SEM image of the inverted pyramids array.

the apex of pyramids where the QD is formed [115] as shown on the sketch of Fig. 2.10 (step 7).

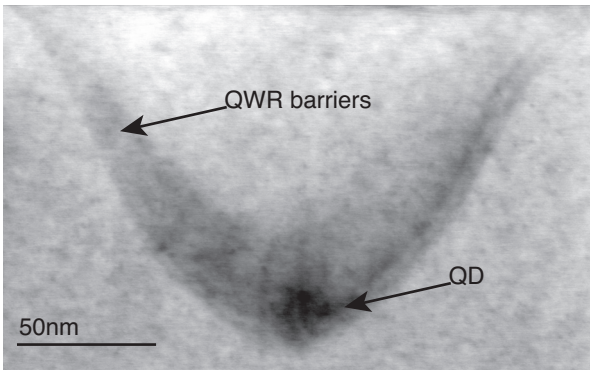

Figure 2.11 – Transmission Electron Microscope (TEM) image of a pyramidal QD (TEM imaging realized on sample 5309, with a Tecnai Osiris FEI, with an electron beam accelerated at 200kV, courtesy of T. Lagrange from the Interdisciplinary Centre for Electron Microscopy, CIME, EPFL)

A Transmission Electron Microscope (TEM) image of a pyramidal QD is shown on Fig. 2.11. Contrary to the SEM technique, TEM requires thinning the sample down to a 100nm thickness with ion beam etching. The image was acquired by collecting the electrons transmitted through the sample. With this technique, the position of each individual atom can be measured.

The variations in contrast correspond to distortions of the crystal lattice. These distortions are caused by the presence of indium atoms because InAs has a smaller lattice parameter. Black areas are thus correlated to the presence of indium and can be used to image the QD and the surrounding QWRs. On Fig. 2.11 a black 20-30nm zone corresponding to the QD is observed at the apex of the pyramid, while the grey areas correspond to the QWR barriers. Note, however, that the thickness of the QD layer is only 0.564nm. The QDs studied in Chapters 3-4 and 5 were grown with a QD layer thickness of 0.75nm and are thus expected to be thicker along the growth direction. An analysis of these TEM measurements combined with k.p simulations and PL measurement may permit an in depth understanding of the confinement of electrons and holes in such QDs grown in small pyramids as was obtained for QDs grown in larger pyramids [133].

2.2.3 Photonic crystal fabrication

The next step is the fabrication of the PhC structures aligned over the QD ensembles.

This step starts with a sequence similar to the one described in the AM fabrication section: first the deposition of an 80nm SiO_2 layer and the spinning of a PMMA A4 layer at 2000rpm followed by the EBL writing of the PhC pattern. This pattern was

aligned over the pyramid array using the alignment marks, as depicted in the sketch of Fig. 2.12(c). The quality of the alignment was assessed by writing the squared alignment pattern shown in the SEM picture of Fig. 2.12(b). These alignment patterns were written precisely at the position of large 1µm pyramids patterned together with the small pyramids, and which were positioned at the edge of the PhC area. The alignment of the PhC structures over the pyramid array was measured by comparing the distance between the center of these large pyramids (not planarized by the growth) and the center of the square alignment patterns. The PhC and their corresponding alignment patterns were written sequentially from bottom Y=0mm to top Y=4.8mm (see Fig. 2.12(c)). The measured alignment error along each directions X and Y were always better than 25nm. This value is much less than the typical variation length of optical modes in our PhCs ($\approx 100nm$). It is thus good enough to ensure the spatial matching of QDs placed near the targeted maxima of the electric field of PhC modes.

Fig. 2.12(d) is a low-magnification optical microscope picture of part of the PhC sample, in which many structures are visible. A zoom-in on PhC waveguides and cavities is given on Fig. 2.12(e-f). On the inset of Fig. 2.12(f), the position of PhC holes in an L_3 cavity relative to the QD array is indicated. The alignment better than 25nm ensures that all QDs are etched away during the ICP process except for the QD at the center of the cavity. A single QD isolated in a PhC cavity is thus obtained from this last etching step. The structure obtained constitutes an interesting implementation of on-chip cavity QED experiments. A similar method was used to fabricate a controlled number of QDs in a PhC waveguide such as the one presented on the microscope picture of Fig. 2.12(e).

The written structures were developed by a one-minute bath in MIBK:IPA 1:3 after which the PMMA mask was transferred to the SiO_2 layer through twelve minutes of RIE. PMMA was then dissolved by a five minute ultrasound bath in acetone followed by a five minutes of O_2 plasma (power: $50W$, pressure: $60mTorr$). A SEM picture of the SiO_2 pattern after these steps is shown on Fig. 2.13(a).

The SiO_2 masked pattern was then transferred onto GaAs by dry etching in an ICP system, from which we obtained arrays of 300nm deep cylindrical holes defining the PhC. A cleaved edge side-view image of such a PhC is given in Fig. 2.13(c), on which the SiO_2 layer is visible. The AlGaAs membrane was released in a 30s 10% $HF:H_2O$ bath, which also stripped away what was left of the SiO_2 mask. The final GaAs PhC pattern is shown in Fig. 2.13(b). Two side views of the slab after the membrane release are given in Fig. 2.13(d-e).

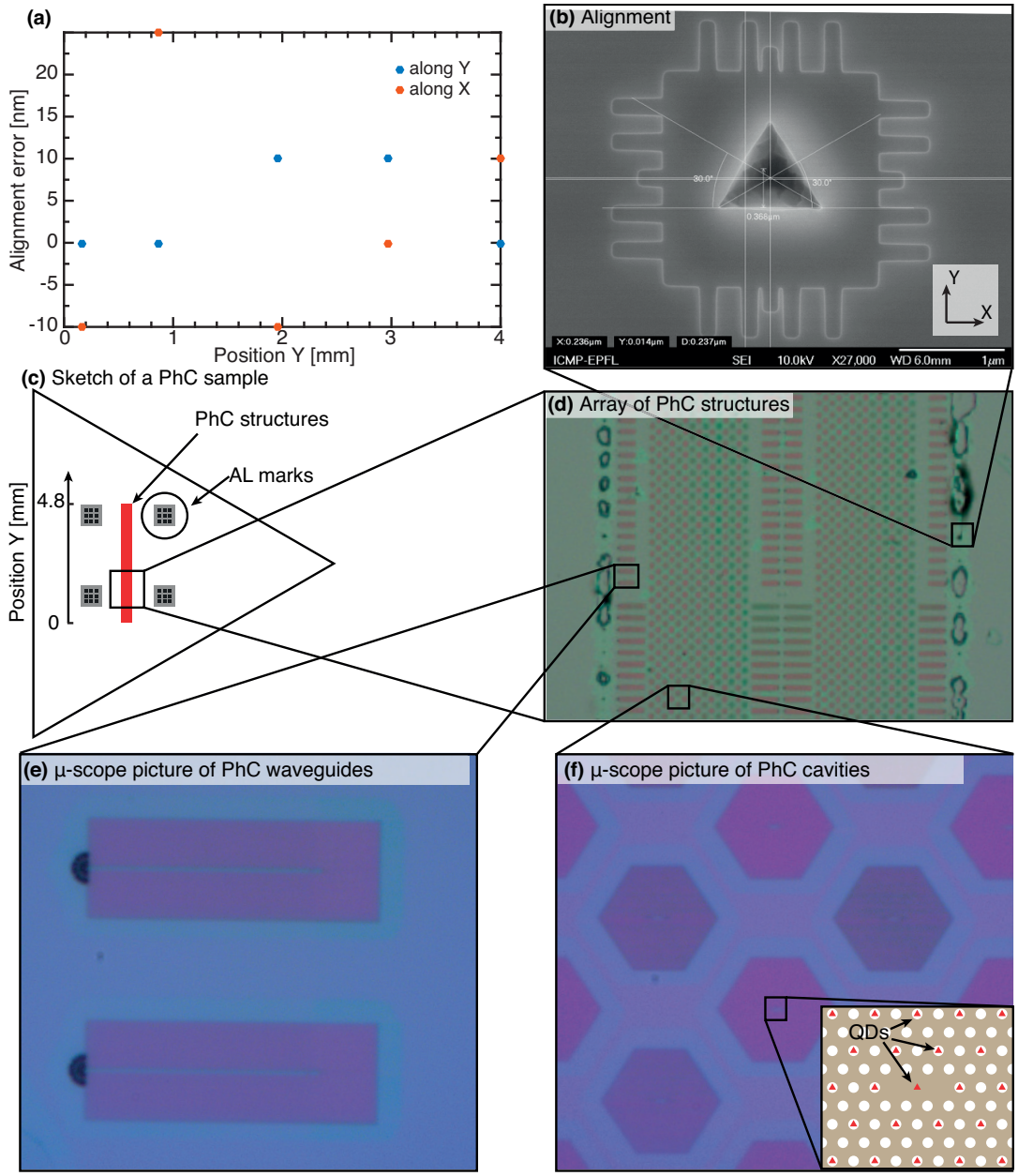

Figure 2.12 – Alignment of the PhC pattern over the QD array: (a) Measured precision of the alignment; (b) Example of an alignment test; (c) Sketch of a fabricated sample, the PhC patterns were written in the red area and aligned with the AL marks; (d) Optical microscope image of the written PhC structures (x2.5 objective); (e) Magnified microscope image of the PhC waveguide (x100 objective); (f) Magnified image of PhC cavities (x100 objective), inset shows a schematic of the PhC hole and QD positions. The microscope pictures were taken after the membrane release step. (sample 5326)

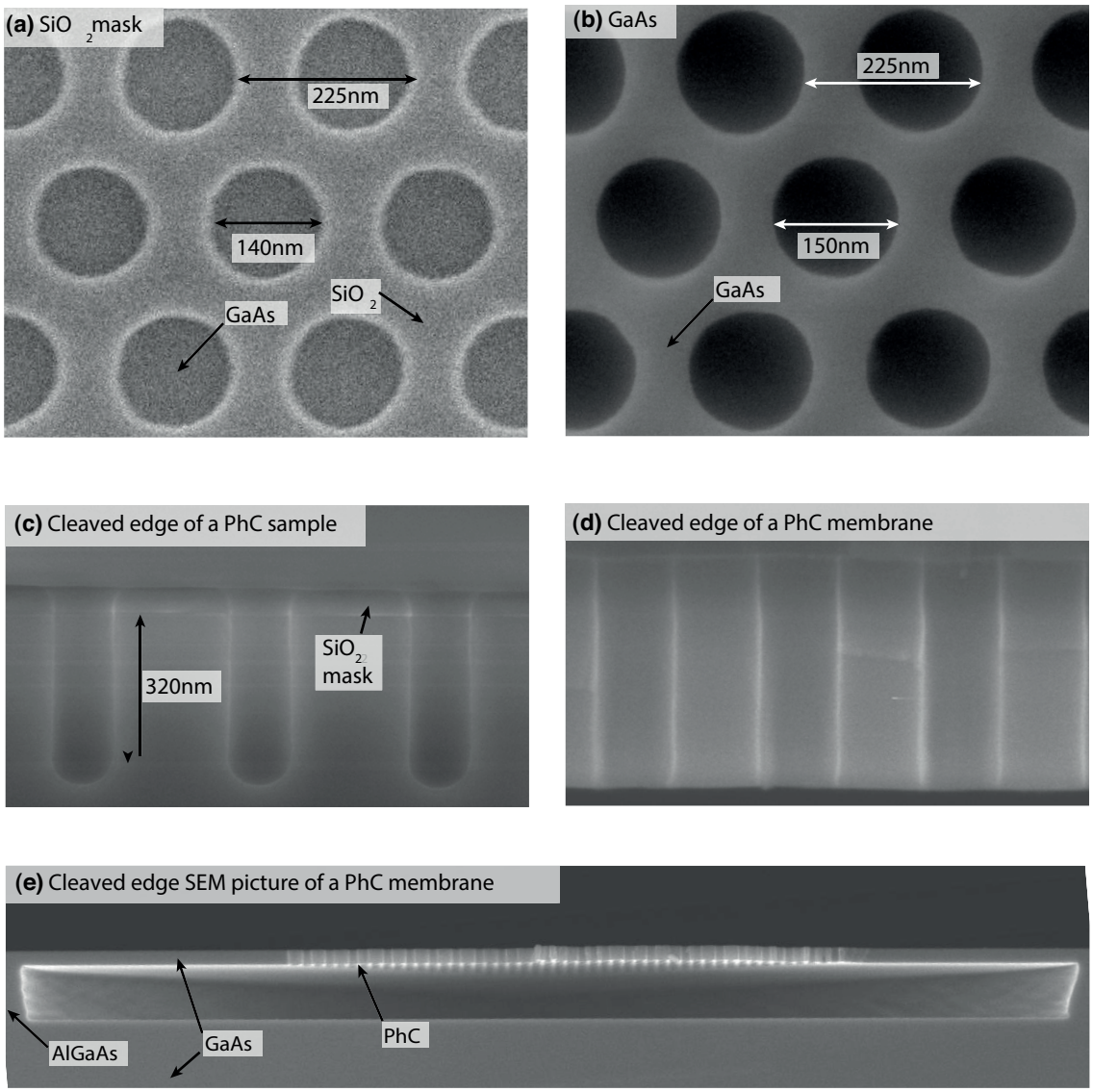

Figure 2.13 – PhC fabrication of sample 5326; (a) SEM picture of the SiO_2 mask of a PhC pattern; (b) SEM picture of a PhC pattern after the ICP etching in GaAs; (c) cleaved edge SEM picture of a PhC pattern after the ICP etching of GaAs; (d) cleaved edge SEM picture of the PhC pattern in a membrane after the membrane release; (e) cleaved edge SEM picture of a PhC structure after the membrane release.

2.2.4 Optimization of PhC structures

2.2.4.1 The impact of non-planarized QDs on L_3 Q-factors

A critical parameter of cavities used in nanophotonic is the Q-factor defined in Chapter 1. The identification of factors limiting the cavities Q-factors is usually difficult. However, the impact of different fabrication imperfections can be analyzed via 3D FDTD simulations using the software meep [124]. In previous integrations of pyramidal quantum dots in PhC cavities, the quantum dots were intentionally non-planarized in order to verify their position in the cavity via SEM measurements [58]. However, such non planarity can degrade the cavity Q-factor. The impact of non-planarized pyramids on the Q-factor of the M_0 mode in L_3 cavities is given here based on 3D-FDTD simulations. The non planarized surface of the pyramidal QD was modelled as a vacuum cylinder etched into the cavity as indicated in Fig. 2.14(a-b). Its diameter was fixed at: $D = 90nm$, and simulations were performed for a range of depth h_d from 0 to 56nm. The Q-factor was extracted using harminv, the spectrum analyzer tool integrated with meep [124]. Harminv collected the electric field at the cavity center and decomposed it into a sum of oscillating function: $e^{-i\omega t}$. The Q-factor of the target cavity mode was given by: $Q = -Re(\omega)/(2Im(\omega))$ [124].

The Q-factor dependence on h_d is indicated as blue dots in Fig. 2.14(c). The Q-factor is decreasing roughly exponentially with the defect height. For a defect height $h_d = 11nm$, the Q-factor is already decreased from 208000 down to 98000. The impact of disorder in a realistic picture needs to include other channels of losses such as absorption and other disorder related losses. In such a picture, the Q-factor can be written:

$$\frac{1}{Q} = \frac{1}{Q_l} + \frac{1}{Q_{hd}} \tag{2.8}$$

where Q_l is the Q-factor modelling all channels of losses other than the cylindrical hole, and Q_{hd} is the Q-factor of the M_0 mode including the cylindrical hole. We assumed $Q_l = 10000$. The Q-factor of the realistic L_3 cavity (with $Q_l = 10000$) is indicated as red dots in Fig. 2.14(c). A defect height $h_d = 11nm$ already causes a degradation of the Q-factor to 9000. When $h_d = 22nm$, the Q-factor drops to 6900. As a consequence, a figure of merit for reaching Q-factors beyond 10000 is to keep the non planarity of QD ensembles below 10nm.

2.2.4.2 Improving the planarity of QDs

Measurements of QD ensemble planarization prior to the PhC fabrication is therefore a prerequisite to obtain high quality PhCs. We now define the planarization as the difference between the maximal and minimal height measured on the surface.

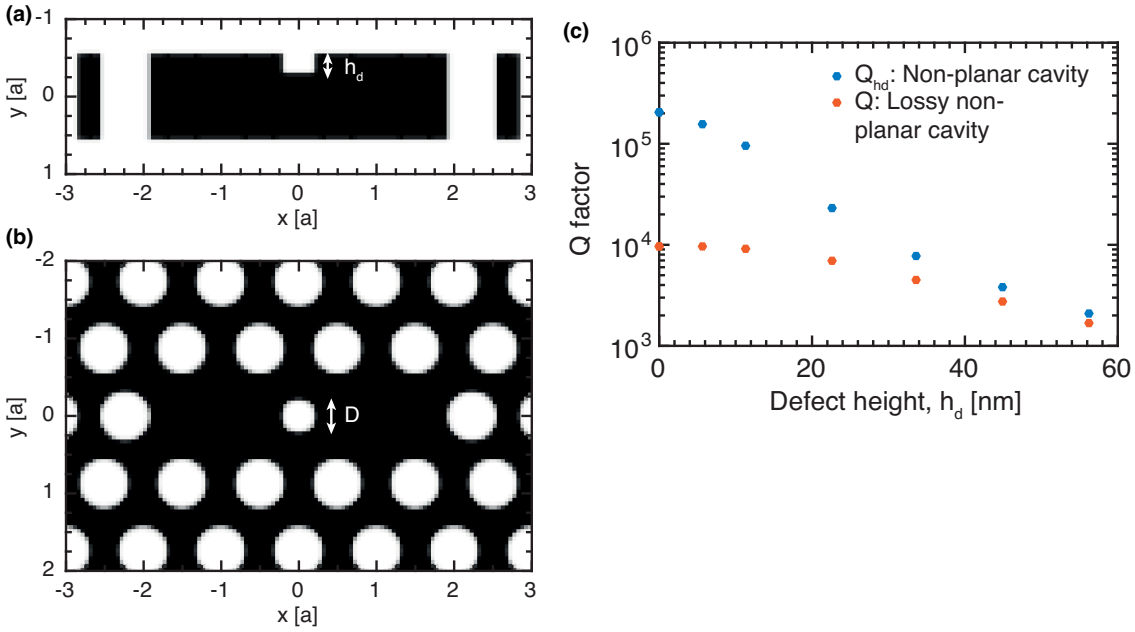

Figure 2.14 – Effect of non-planarity on the Q-factor of the M_0 mode in an L_3 cavity: (a) Side and (b) top view of the simulated cavity; (c) Q-factor of the M_0 mode in a non planar cavity with (red) and without (blue) additional fabrication and absorption related losses (parameters of the 3D FDTD simulation: n=3.46, r=67.5nm, a=225nm, th=250nm, D=90nm)

A first solution for planarization would be to use only TEGa in the cap layer. This recipe would ensure a low carbon incorporation favorable to reducing absorption by the grown GaAs material (see Section 2.3.3).For example, the surface of a QD ensemble grown with a cap made entirely of TEGa is shown in Fig. 2.15, sample: 5259. Unfortunately, TEGa growth has a small capillarity effect and the pyramidal shape is not planarized during the growth. A solution may be to grow a thicker cap layer of TEGa, such that the weaker capillarity effect of TEGa still fills in the pyramids. However, already at this step, large step bunches of about 12.5nm height are formed with the periodicity of the pyramids. Notice that such a step height corresponds to a step bunching of 44 monolayers, close to the total number of steps flowing between two rows of pyramids (which is 72).

The solution adopted to planarize the samples studied in this thesis was to grow an 8nm cap layer using TMGa as a precursor, with a V/III ratio of 942 at a temperature: T=600°C (Fig. 2.15, sample: 5326). The surface was planarized within ~ 4nm, which matches our requirements.

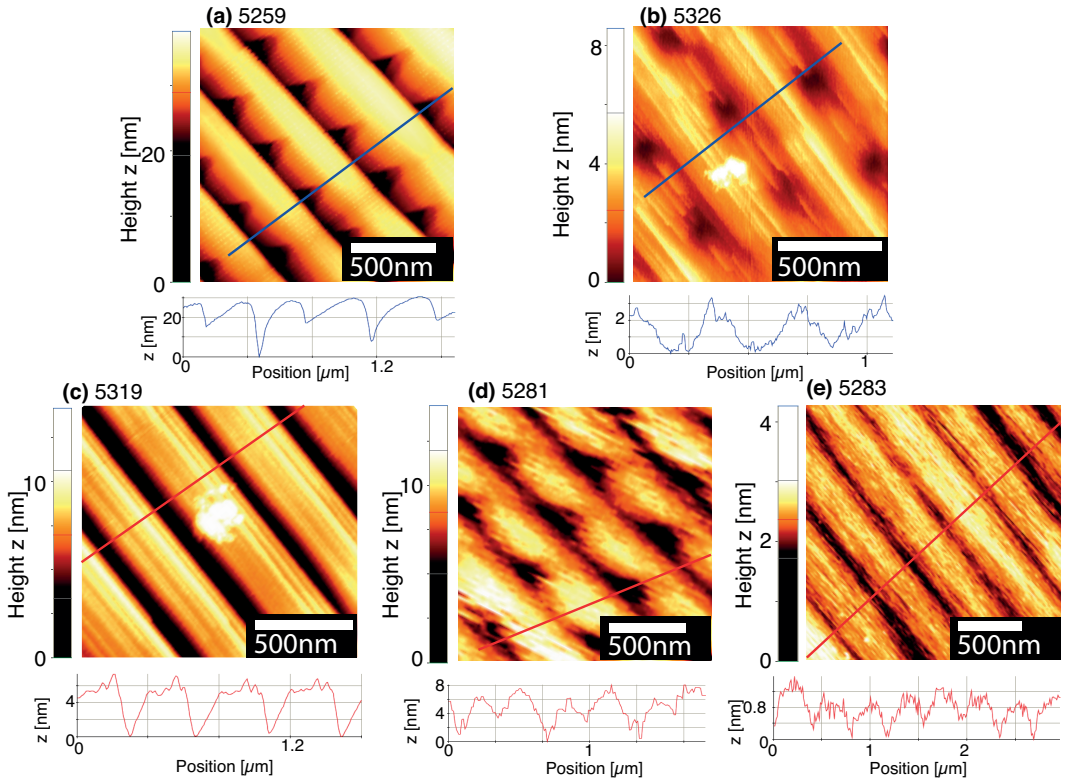

Sample	Precursor	cap thickness [nm]	V/III	cap T [°C]	Annealing
5259	TEGa	8	260	700	no
5326	TMGa	8	942	600	no
5319	TMGa	10	942	700	no
5281	TMGa	10	2643	600	no
5283	TMGa	10	2643	600	1h at 700°C

Figure 2.15 – AFM measurements on ensembles of pyramidal QDs, on sample: (a) 5259 with a pure TEGa cap; (b) 5326 with the TMGa cap used in the sample studied in Chapters 3-4-5; (c) 5319 with a 10nm TMGa cap grown at T=700°C; (d) 5281 with a TMGa cap grown with a V/III ratio of 2643; (e) 5283 with a TMGa cap grown with a V/III ratio of 2643 and a 1h annealing step at T=700°C.

However, these parameters are not optimal for TMGa growth. The incorporation of carbon is minimal at higher temperature and higher V/III ratio. Each of these degrees of freedom was tested to obtain well planarized samples. In Fig. 2.15, sample: 5319, a 10nm cap layer of TMGa was grown at 700°C with a V/III ratio of 942. However, steps of 12nm height are also formed similar to the TEGa growth (sample 5259). In Fig. 2.15, sample: 5281, a 10nm cap layer of TMGa was grown at 600°C with a V/III ratio of 2643. The obtained planarization is within ~10nm, with smaller step heights. This planarization was significantly enhanced with an additional one hour annealing step at 700°C after the growth . In this case, the obtained planarization was about

1.2nm. This last growth process is thus optimal for both low carbon incorporation and nearly perfect planarization. The GaAs material purity may be further enhanced by growing the cap only with TEGa and exploring the impact of growth parameters such as temperature, growth rate and V/III ratio to obtain satisfactory planarization.

2.3 Optical characterization of QD ensembles

Before the fabrication of PhC elements, the optical properties of pyramidal QD ensembles and PhC elements need to be assessed. This is done in a photoluminescence setup. In this section, the principles of photoluminescence are presented, followed by the presentation of the optical properties of pyramidal QD ensembles.

2.3.1 The photoluminescence setup

Photoluminescence (PL) is a process, by which a material absorbs and reemits photons. The re-emitted light spectra are usually characteristic of the material and its structure, which makes this process a simple albeit powerful tool to characterize nanostructures. It is especially useful in the case of semiconductor heterostructures; in which it can probe the optically active levels available. In the case of non-resonant photo-luminescence spectroscopy of semiconductor materials, electrons and holes are excited by a laser light above the bandgap in the bulk semiconductor as shown in Fig. 2.16(a). The created particles diffuse and are eventually absorbed by the heterostructure in which they form different excitonic complexes. Those excitons either emit phonons and decay to lower excitonic species or recombine radiatively. The emitted light spectra are then analyzed.

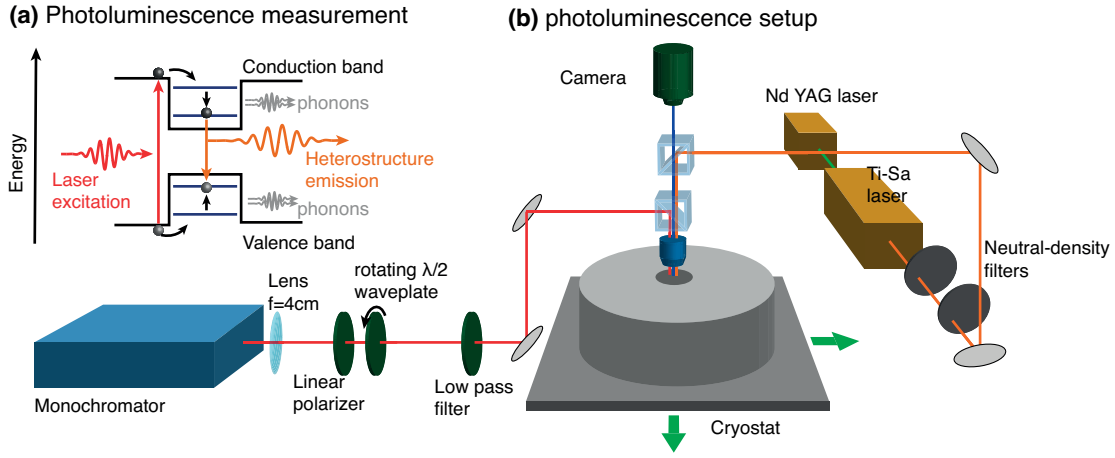

Figure 2.16 – (a) Principle of photo-luminescence spectroscopy of a semiconductor heterostructure; (b) Experimental setup for μ-photoluminescence spectroscopy

Studying the PL spectrum of a single QDs requires a high spatial resolution. It is made possible in a micro-photoluminescence setup, by a high numerical aperture (NA) microscope objective which focuses light onto a spot near the diffraction limit with a width around 1.5µm (50x magnification, NA=0.55, f=3.6mm). Electrons, holes and excitons are created by a tunable Ti-Sapphire laser (700-1000 nm, Spectra Physics Tsunami) pumped with a frequency doubled YAG laser at 532nm. The laser is tuned to photon energy above the bandgap, at 730nm wavelength. The microscope objective both focuses the beam on the structure and collects its photo-luminescence. A beam-splitter and a camera help to image the sample and focus the spot at the desired position.

The whole cryostat was translated with a position-controlled, motorized XY stage allowing to move the sample with 50nm precision and to selectively excite the structures of interest. The sample was cooled in a He flow cryostat (ST-500 made by Janis Research, or Konti-Cryostat-Mikro made by CryoVac) allowing a fine tuning of the temperature down to $5K$. The exact temperature was maintained via a closed loop control system using both the cryogenic cooling and a heating resistance placed below the cold finger on which the sample was glued.

The outgoing laser light reflected by the sample is filtered out by a low pass filter. The collected light is then focused at the entrance slit of a spectrometer. The spectrum was projected onto a nitrogen-cooled 2D Si-CCD array detector. In this thesis, two micro-photoluminescence setups were used:

- A low spectral resolution setup, equipped with time resolved photodiodes, in which the spectrometer is a 55 cm focal length Horiba Jobin Yvon Triax 550, 1200 l/mm single grating combined with a CCD (Horiba Jobin Yvon Spectrum One with 2048x512 pixels). The typical entrance slit width used all along these experiments is $100\mu m$. The achieved spectral resolution is then approximately $70\mu eV$.

- A high spectral resolution setup: where the spectrometer is a 64cm focal length Horiba Jobin Yvon FHR640 combined with a CCD (Andor iDus 416 with 2000x256 pixels) achieving a spectral resolution of 20µeV with an entrance slit width of $20\mu m$.

A linear polarizer with a vertical axis and a rotating $\lambda/2$ waveplate were introduced between the spectrometer and the cryostat to allow for polarization resolved measurements. In the Jones formalism, polarized light can be described by two amplitudes E_V, E_H and a phase ϕ relative to the vertical axis:

$$\vec{E} = \begin{pmatrix} E_H e^{i\phi} \\ E_V \end{pmatrix} \tag{2.9}$$

A passage through a half wave-plate (rotated at an angle θ with respect to the vertical direction) and the polarizer amounts to a rotation of the polarization plane of light by an angle 2θ and thus a selection of the component of vertically polarized light. By rotating the $\lambda/2$ waveplate, any linear orientation of the polarized spectra can be measured.

2.3.2 PL of arrays of QDs

2.3.2.1 QD ensembles

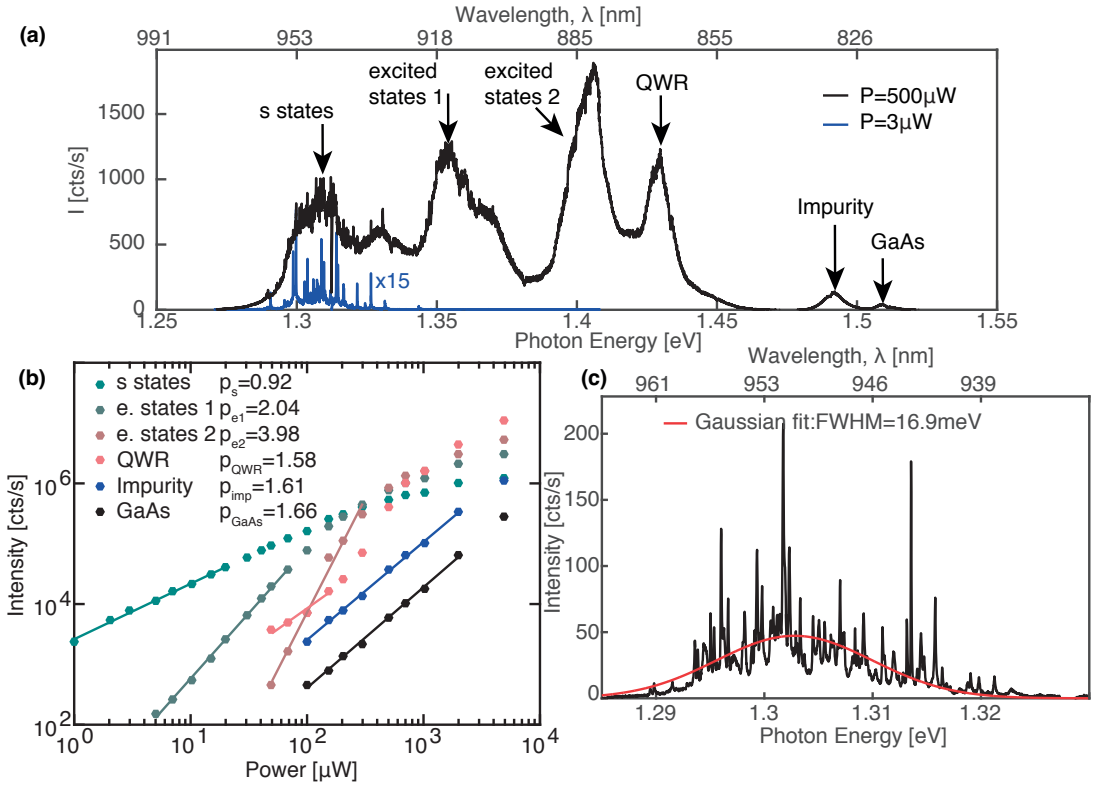

Figure 2.17 – Properties of pyramidal InGaAs/GaAs QD ensembles: (a) PL spectra of the QD ensemble with an excitation power of $P = 500\mu W$ (in black) and $P = 3\mu W$ (in blue); (b) Power dependence of the QD s states, of the excited QD states (e. states 1 or 2), of the QWR state, of the doping impurity and of GaAs; (c) Gaussian fit of a QD ensemble, (T=10K, excitation power: $P = 10\mu W$; sample 5807, the growth parameters are given in Appendix B).

PL spectra of the QD ensemble grown on the patterned GaAs membrane excited at high (P=500μW in black) and low (P=3μW in blue) excitation power are shown on Fig. 2.17(a). The laser spot size is $\approx 1.5\mu m$, the diffusion length of electrons in GaAs is limited by GaAs absorption [134] to $\approx 1\mu m$, the number of excited QDs in this setup is then ≈ 30. The low power spectrum consists of an ensemble of sharp

QD emission lines. Previous studies using TMGa-based growth have shown that such QD ensembles are composed of single QDs located in each pyramidal recess [53]. In the higher excitation power spectrum, the emission by higher QD states or QWR are observed between 1.35 to 1.45eV. The emission by GaAs at 1.52eV and a doping impurity at 1.49eV are also seen. The different QD states are identified in Fig. 2.17(b) thanks to a power dependence performed on the QD ensemble. Below saturation, the increase of the log-intensity is linear with the log-power. The slope p of each curve is given in the Figure. From the separation between each state and the slope of their power dependence, each emission was attributed to its QD or QWR state. A magnified view of the QD ensemble is shown on Fig. 2.17(c). The QD lines are approximately Gaussian-distributed. We fitted this ensemble with a Gaussian function (red line), from which we infer an approximate value for the FWHM of this ensemble ≈17meV. However, this value overestimates the true QD energy distribution because each QD exhibits several emission lines at different energies, which contributes in this "apparent" inhomogeneous broadening and because of the possible excitation of excited hole states around 1.315eV.

2.3.2.2 QD linewidths

The QD lines of four spectra of QD ensembles (collected using the $20\mu eV$ resolution PL setup) were fitted with Lorentzians to obtain the histogram of the FWHM of QD lines shown in Fig. 2.18(a). This histogram features a maximum at 50μeV, still well beyond the estimated lifetime limited linewidth of QDs (0.7μeV for a lifetime of 1ns). This histogram is well described by a skewed Gaussian, which can be interpreted as the sum of a Gaussian and an exponential random variables:

$$f(x;\mu,\sigma,\lambda,A) = A\frac{\lambda}{2}e^{\frac{\lambda}{2}(2\mu+\lambda\sigma^2-2x)}erfc\left(\frac{\mu+\lambda\sigma^2-x}{\sqrt{2}\sigma}\right), \tag{2.10}$$

Where μ is the mean of the original Gaussian distribution, σ is its standard deviation and $1/\lambda$ is the exponential decay parameter. The fit gave: $\mu = 39 \pm 4\mu eV$, $\sigma = 4.5 \pm 4\mu eV$ and $1/\lambda = 45 \pm 12\mu eV$. The mean of this distribution is: $\mu + 1/\lambda = 84\mu$eV, its standard deviation is $\sqrt{\sigma^2 + 1/\lambda^2} = 45\mu eV$. These results are substantially better than previous statistics on pyramidal QDs [109]. However, these linewidths are still larger than the best published results on site controlled QDs [49] with record linewidths as low as 6μeV. But it should be noted that this record was obtained by applying an electric field to the QDs, which can reduce the FWHM of QDs by depleting surrounding impurities from their charges. Applying an electric field may help reduce pure dephasing in our samples and lead to lifetime limited exciton linewidths.

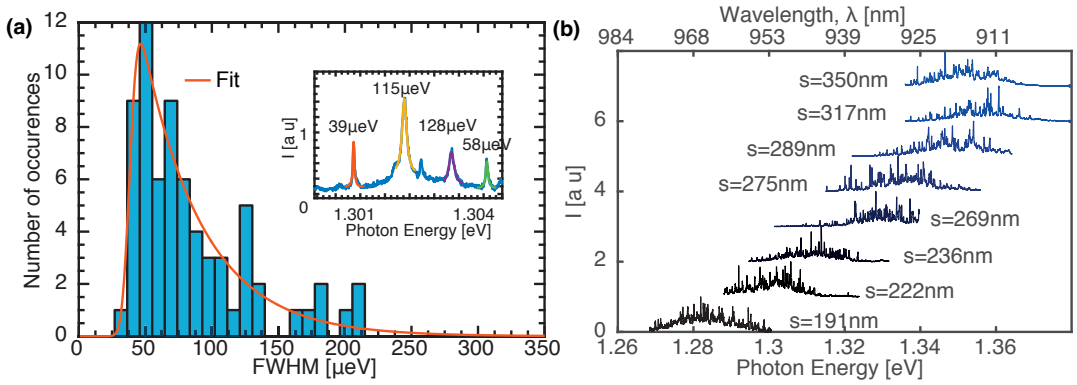

Figure 2.18 – (a) Histogram of the linewidths of excitonic lines measured on QD ensembles (T=10K, excitation power: $P = 3\mu W$); inset: example of a QD ensemble with fitted lines (sample 5326); (b) PL spectra of QD ensembles with different pyramid sizes. (T=10K, excitation power: $P = 10\mu W$; sample 5807, the growth parameters are given in Appendix B)

2.3.2.3 QD energy tunability

The emission wavelength of pyramidal QDs is tunable over a large spectral range from 850nm up to 980nm. This is realized either by changing the growth parameters such as the indium content or the QD size, or by varying the pyramidal pattern. Such pyramid size-dependent tuning was achieved by growing QDs over 8 square arrays with pyramid sizes linearly spaced between 190nm and 350nm. As the growth occurs mostly over the (111)A facet of the pyramid, the growth rate is very sensitive to the (111)A/(111)B surface ratio. Larger pyramids have a larger ratio. The same flux of precursor is distributed over a larger (111)A surface, thereby reducing the growth rate. QDs are then larger and emit at higher energies in smaller pyramids. This is evidenced in Fig. 2.18(b), where the PL spectra of the QD ensemble for each pyramid size are displayed. Using this tuning technique, narrow QD emission was obtained from 910nm to 980nm in a single sample. By controlling the size of single pyramids embedded in the otherwise uniform array, single QDs can be energy tuned as shown by Kulkova et al. [135, 65].

2.3.3 TEGa for high quality QD growth

2.3.3.1 Advantages of TEGa

One major improvement in the QD fabrication realized during this thesis is the use of TEGa as the precursor for the Ga atoms [111]. TEGa has ethyl radicals, which has deep impacts on the growth mechanism, helpful for the growth of high quality QDs:

1. TEGa is advantageous first because during TMGa growth, the carbon byproducts of the reactions leading to GaAs growth can be incorporated in the GaAs lattice

leading to doping impurities. This effect is largely mitigated by the use of ethyl radicals, which thanks to their larger size are less likely to be incorporated [136, 137]. High purity growth is a critical parameter to achieve narrow excitonic lines. Indeed, the spectral width of single excitonic lines at 10K is broadened by the pure dephasing arising as a consequence of the dynamic Stark effect caused by flickering charges, which are captured by impurities.

2. Besides, TEGa can decompose at lower temperature [138] since its larger radicals have weaker bonds. This is advantageous because the integration of QDs in a 250nm thick photonic crystal membrane limits the maximum pyramid height below 300nm, which imposes an upper limit to the growth temperature around 620°C to keep a sharp profile of the pyramid and take full advantage of the capillarity effect. On the contrary, the optimal growth temperature for TMGa based growth of GaAs on (100) oriented substrate lies around 650°C [139]. There is a tradeoff between growing high quality material and keeping a sharp profile of the pyramids when using TMGa, which is improved by the use of TEGa.

3. The growth rate of TMGa at T=650°C range varies rapidly with temperature, while it is quite stable for TEGa because of the lower temperature decomposition of TEGa [138]. Thus, TEGa is likely to improve the reproducibility of the growth. Secondly, TMGa decomposes on (111)A, but only very slowly on (111)B [140]. As a consequence, at the border of the pyramids array, the flux of precursor is higher. This leads to larger nanostructure and more confined, red-shifted QDs at the edges. On the contrary, TEGa decomposes on both (111)A and (111)B oriented surfaces [141] which may help to reduce this edge effect.

2.3.3.2 TEGa versus TMGa

The results of two growths using TEGa and TMGa are compared in Fig. 2.19(a-b), with the layer sequence indicated on the right side of each sketch. One notable difference between the two precursors is caused by growth on the (111)B facet, which is negligible with TMGa but not with TEGa.

These two growths were carried out on a pattern design with a 2.4mm square array of inverted pyramids similar to the one presented previously. The array was a triangular lattice of inverted pyramids with a 450nm pitch and a pyramid size of 250nm. PL spectra measured for different positions of the excitation spot across ensembles of pyramidal QDs grown with TMGa and TEGa are shown in Fig. 2.19(c-d). The position of the excitation spot with respect to the edge of the QD square array was scanned over the QD array as is indicated for each spectrum. The exact parameters of each growths are given in Appendix B.

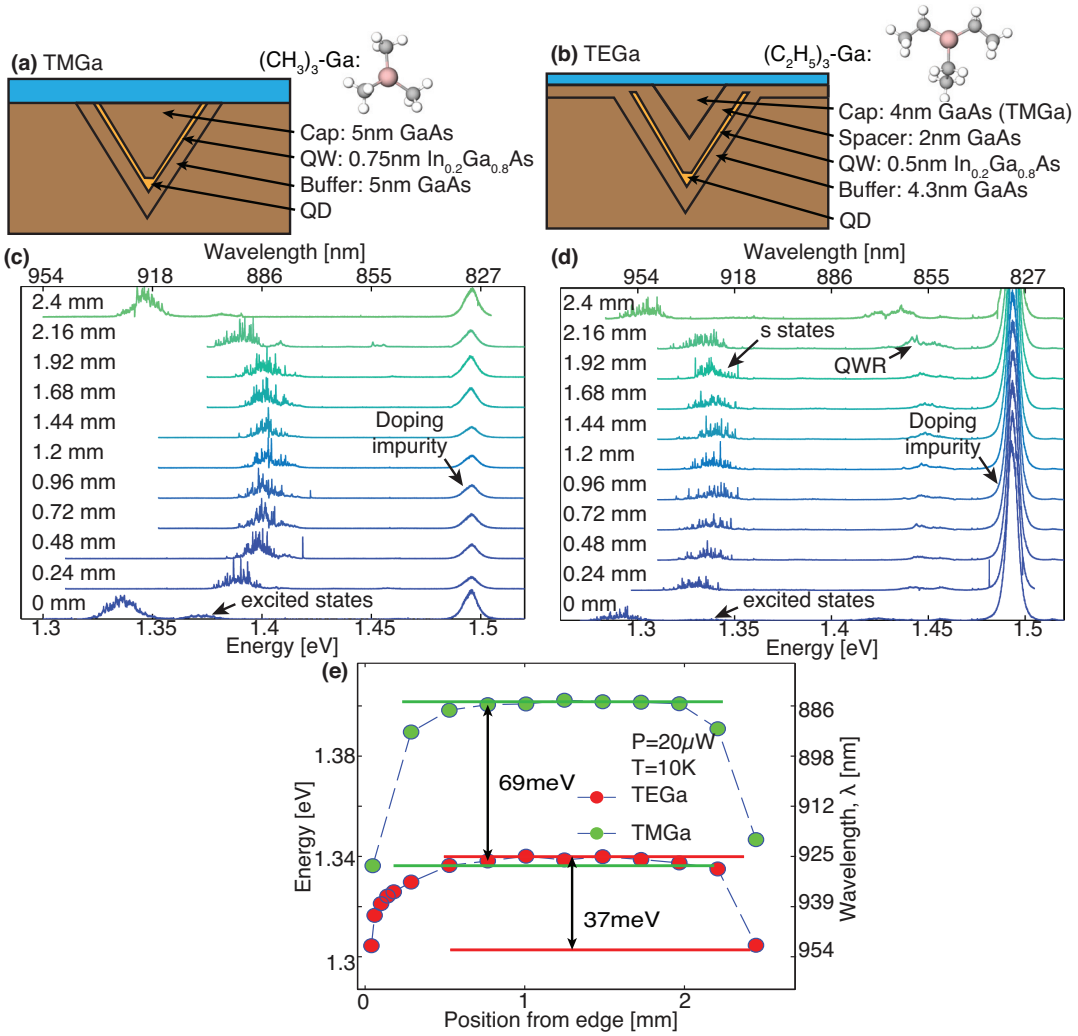

Figure 2.19 – (a) Side view sketch of a TMGa QD growth; (b) Side view sketch of a TEGa QD growth; (c-d) Photoluminescence spectra scan across an ensemble of pyramidal patterns grown with (c) TMGa and (d) TEGa (Excitation power: $P = 20\mu W$, $T = 10K$); (e) Central emission energy of s-states transitions of the QD ensembles as a function of the excitation spot distance measured from the edge of the QD array. The sample grown with TMGa precursors was number 5199; The sample grown with TEGa precursors was number 5255; (c-d-e) Reprinted from Publication [111], Copyright (2014), with permission from Elsevier.

The typical spectral signatures of QDs obtained with TMGa growth can be seen in Fig. 2.19(c). Emission from the QD s and excited states is observed, as well as the spectral signature of the acceptors incorporated in the bulk GaAs. The sample grown with TEGa, presented in Fig. 2.19(d), shows spectral features strikingly similar to those of the sample grown with TMGa: distinct QD s-state and excited states emission as well as a pronounced impurity-related emission. The energy shift between the

s-transition lines of both samples originates from the different precursors, which leads to a different InGaAs QDs thickness and composition. However, it is notable that the QD emission of the TEGa sample exhibits sharp lines up to 960nm. Indeed, the growth of high quality QDs beyond 900nm using TMGa had been a major challenge. A possible cause for this effect may be the higher purity of TEGa grown GaAs material at such low temperatures.

Fig. 2.19(e) displays the mean emission energy of the QD s-state transition as a function of the excitation laser beam position across the QD array for samples grown with TMGa and TEGa precursors. For both samples, the pyramidal arrays used for growing the QDs had similar pyramid sizes. The use of TEGa precursors reduced by 46% the spectral redshift observed at the edge of the QD array with respect to TMGa samples. This reduction of edge effects is consistent with the more efficient decomposition of TEGa on the {111}B wafer surface, causing a smaller gradient of precursors near the edge [141]. The two samples exhibited similar emission intensities with a maximum of excitonic emission peaks up to $\approx 300 cts/s$.

Prior trials to grow TEGa QDs were realized at 650°C. However, no thin lines were observed probably as a consequence of the temperature related planarization of pyramids. On the contrary growths around 600°C were shown to lead to high quality, much more reproducible growths of QD ensembles. A large number of QD growths demonstrated that QD ensembles with narrow lines are obtained over a large parameter space (with varying indium concentration, buffer and QD thickness) opening the possibility to tailor the electron and hole confinement for specific applications, and eventually to optimize the electron hole overlap. However, when the size or indium content were tuned to reach QD emission beyond 1000nm, the quality of QD ensembles degraded notably and no narrow linewidths (i.e., <100µeV) were observed. This limitation suggests a transition to a different growth mode for high In-content, maybe dominated by random nucleation similar to the Stranski-Krastanov method.

2.3.4 QD ensembles grown with triethylindium

The success of TEGa for improving the growth quality and reproducibility suggests that carbon incorporation by methyl-radicals may be the limiting factor for QD homogeneous linewidth. However, in the growth presented in Fig. 2.17(b), methyl-radicals were still used in TMIn to grow the InGaAs layer of the QD. Thus, the quality of QD ensembles in term of linewidths may be further improved by the use of triethylindium (TEIn) precursors, whose larger ethyl-radicals prevent carbon incorporation into the grown material. Besides, TEIn is decomposed at lower temperature than for TMIn. Thus, it may allow for growths at lower temperature, and ensure a better preservation of the inverted pyramidal patterns.

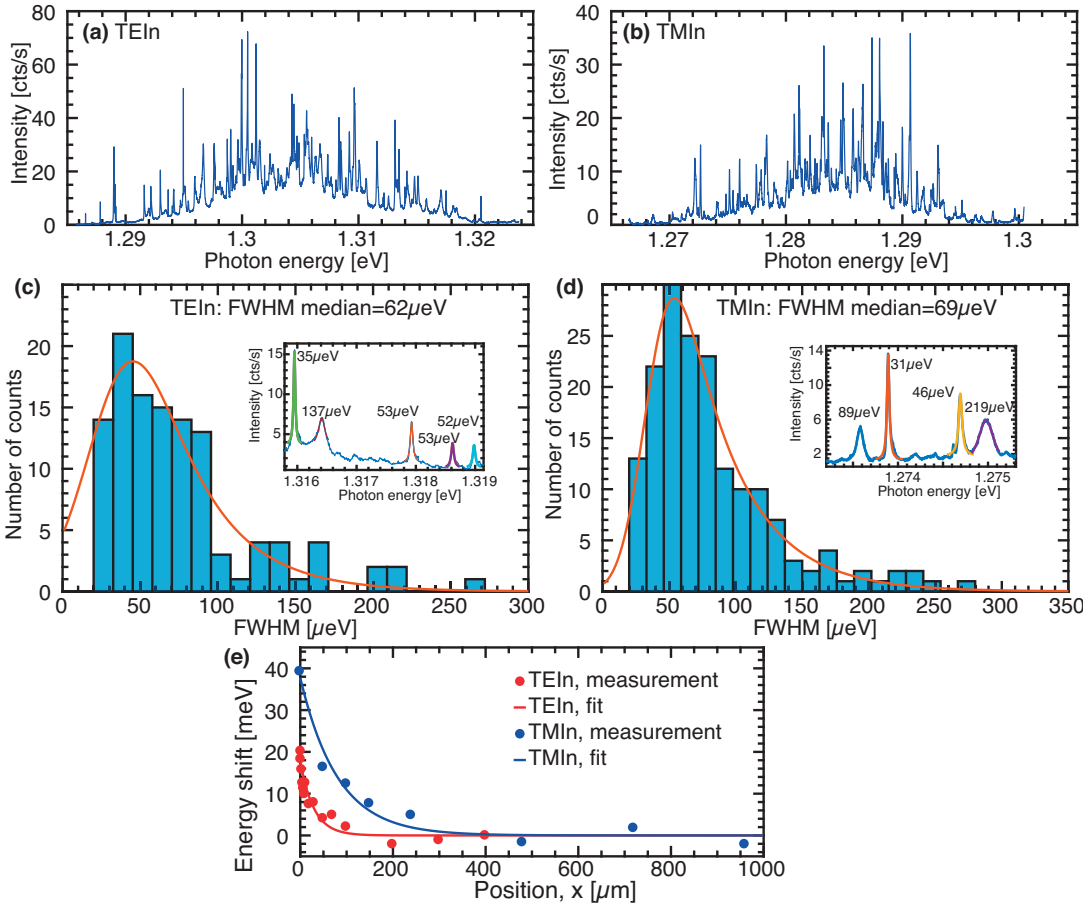

Figure 2.20 – (a) QD ensemble grown with TEIn ($P = 10\mu W$); (b) QD ensemble grown with TMIn ($P = 10\mu W$); (c) Histogram of the linewidths of excitonic lines measured on a QD ensemble grown with TEIn ($P = 7\mu W$); (d) Histogram of the linewidths of excitonic lines measured on a QD ensemble grown with TEIn ($P = 10\mu W$); (e) Energy shift of the s-states of QD ensembles near the edge of the pyramidal array: on sample 5255 grown with TMIn (blue) and 6087 grown with TEIn (red) ($P = 10\mu W$); All measurements were performed at T=10K in the $20\mu eV$ resolution PL setup; (a-c) were measured by A. Miranda on sample 6087; (b-d) were measured by A. Delgoffe on sample 5951;

A first sample grown with TEIn while keeping all other growth parameters identical as those described in 2.2.2.2 yielded a poor quality and a central emission energy of 1.23eV. In a second sample, the InGaAs thickness was reduced from from 0.75nm to 0.5nm in order to reduce the QD emission linewidth. The growth rate and In mole fractions were calibrated by A. Rudra by growing $(Ga)InAs/GaAs$ superlattice structures and fitting high resolution X-ray diffraction rocking curves with simulated curves. All thicknesses mentioned here are the nominal thicknesses that were measured on planar (100) GaAs (TEGa) and on planar (100) GaAs (TMGa).

The PL spectra obtained from the second QD ensemble thus obtained is shown in Fig. 2.20(a). For comparison, Fig. 2.20(b) displays the spectra from the best QD ensemble obtained over 18 samples grown over a timespan of 9 months all with the same recipe, described in 2.2.2.2. The two growths exhibit comparable ensemble quality and emission intensity. In each sample, all apparent QD lines from four spectra were fitted with Lorentzians. The linewidths distribution is given in the histograms displayed on Fig. 2.20(c-d). Each histogram was fitted with a skewed Gaussian. The parameters are given in the table below:

	μ [μeV]	σ [μeV]	$1/\lambda$ [μeV]	$\mu + 1/\lambda$ [μeV]
TEIn	24 ± 12	23 ± 20	37 ± 14	62 ± 32
TMIn	35 ± 3	16 ± 5	42 ± 7	78 ± 10
	$\sqrt{\sigma^2 + 1/\lambda^2}$ [μeV]	Median [μeV]	Lowest FWHM [μeV]	
TEIn	43 ± 24	62	RL ($20\mu eV$)	
TMIn	45 ± 9	69	RL($20\mu eV$)	

The two ensembles exhibit comparable emission quality, in terms of spectral linewidths, emission intensities and inhomogeneous broadening. This preliminary result is very encouraging to push further the study of TEIn based QDs, especially considering the possibility to grow high quality material at lower temperatures, thereby preserving the pyramidal pattern from step flow induced deformations.

Another notable difference between the two growths was in the spectral redshift of the s-states observed at the edge of the QD array. The central emission energy of s-states excitons from QD ensembles were obtained by scanning the PL excitation from the edge of the QD ensemble at $x = 0\mu m$ up to $x = 1000\mu m$ as in Fig. 2.19(e). The energy shifts ΔE of the s-states excitons with respect to their emission energy at the center of the sample are shown in Fig. 2.20(e). The energy shift for the sample grown with TEIn and TEGa (blue dots) is $\approx 20meV$, two times lower than that of the sample grown using TMIn and TEGa, which was itself two times lower than that of a similar sample grown with TMGa and TMIn. This reduced redshift is probably caused by the decomposition of TEIn on both (111)A and (111)B oriented surfaces. This effect was characterized by fitting this redshift with the following model:

$$\Delta E(x) = -\Delta E_0 e^{-x/L} \tag{2.11}$$

where ΔE is the energy shift of s-states, x is the laser excitation spot position with respect to the edge of the QD ensemble ΔE_0 is the maximal energy shift and L is the characteristic length of the energy shift. The parameters fitted on this distribution are shown in the table below:

	ΔE_0 $[meV]$	L $[\mu m]$
TEIn	17.7 ± 3.4	29 ± 17
TMIn	37.7 ± 6.1	81 ± 28

The use of TEIn permits a reduction of both the total energy shift and the characteristic length L. The reduction of the characteristic length for TEIn is probably caused by the lower diffusion length of TEIn precursors on the GaAs surface. These results may permit the growth of site-controlled QDs less sensitive to the presence of neighboring QDs, which would relax the constraints on the design of PhC circuits.

2.3.5 Q-factors in L_3 and L_7 cavities

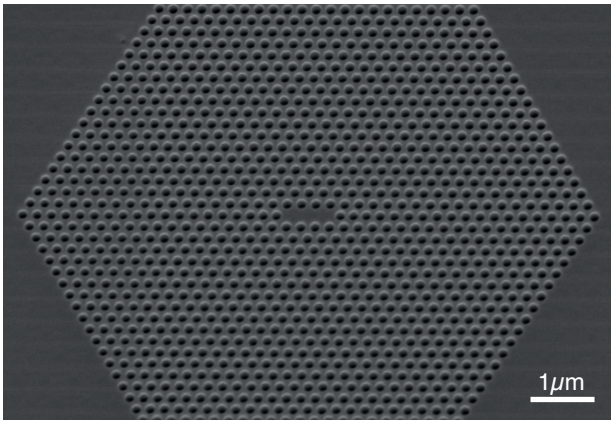

Figure 2.21 – SEM picture of an L_3 cavity

Photonic crystals are extremely sensitive to disorder. The most obvious way to assess the disorder present in a PhC structure is by SEM observation as shown on Fig. 2.21. However, SEM images may overlook other sources of quality degradation of such as absorption, surface states, small scale structural disorder or disorder below the membrane. The ultimate measurement of a PhC quality is therefore given by the optical properties of PhC structures. Small PhC cavities represent excellent landmarks for this, thanks to their narrow spectral DOS and their tiny mode volume which makes them extremely sensitive to disorder. Any imperfection will be manifested by a dramatic reduction of the cavities Q-factors.

Q-factor measurements were carried out by measuring the PL spectra of two series of L_3 cavities and L_7 cavities, with hole radii linearly spaced between 53 and 71nm. All the cavities had six holes shifted according to the design presented in Fig. 2.3(a). Each cavity was excited with a high pump laser power (P=1mW), such that the QD and QWR states emit a broad continuum exciting all photonic modes overlapping with the QDs [96]. The small density of gain material ensures that the cavity do not enter the

amplified spontaneous emission lasing regime.

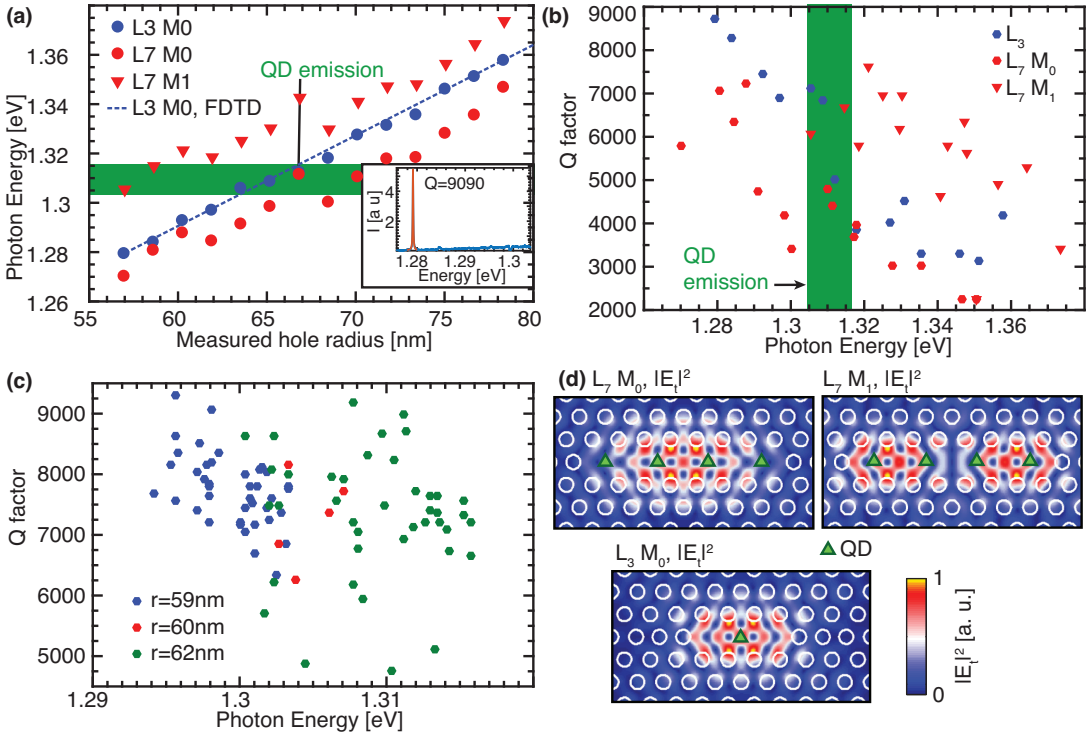

Figure 2.22 – (a) Energy of cavity modes; Inset: Lorentzian fit of the M_0 mode in an L_3 cavity; (b) Q-factors of a serie of L_3 and L_7 cavities; (c) M_0 mode Q-factors of L_3 cavities emitting near the wavelength emission of QDs with holes radii: r=59, 60, 62nm (all measurements were performed at T=10K, with a laser excitation power : P=1mW; sample 5326); (d) 3D-FDTD simulated electric field intensity in the central plane of the slab for the M_0 mode of an L_3 and the M_0 and M_1 modes of an L_7 (n=3.46, r=61nm, a=225nm, th=250nm, the white circles outline the air/GaAs interface of the etched holes).

In L_3 cavities only one QD was placed at the maximum of the in-plane electric field M_0 mode. In L_7 cavities, 4 QDs were distributed uniformly along the cavity, so that both the M_0 and M_1 mode overlapped with some of the QDs. The overlap between the QDs and the in-plane electric field intensity is depicted in Fig. 2.22(d). Each of the excited modes in the PL spectra were fitted with Lorentzians as shown in the inset of Fig. 2.22(a). The resonance energy of these modes increases linearly with the hole radius (Fig. 2.22(a)). 3D FDTD simulations of the resonance energy of the M_0 mode of L_3 cavities with PhC parameters as measured by SEM observations is shown as a dashed blue line and matches well the measured resonance energies. Besides, the energy of M_0 mode in L_3 cavities lies in between the M_0 and M_1 mode of L_7 cavities, consistently with the expected tighter confinement of the M_0 mode in the larger L_7 cavity. The standard deviation of the L_3 mode distribution is: std(E)=2.5meV

(for r=59nm). This dispersion of cavity modes may prevent the scaling of PhC devices to many cavities, which justifies efforts to tune the cavity modes after their fabrication [100].

The Q-factors of these modes is given on Fig. 2.22(b). They are much lower than their expected theoretical value (200000 for the M_0 mode in an L_3 cavity) as a result of fabrication related disorder and absorption. However, they are substantially higher than in previous works [109, 118], in which the resonant modes were much closer to the bandgap. Besides, these Q-factors are decreasing with energy. Two processes may be responsible for this decrease, first the absorption by residual doping (Urbach tails), or by electronic surface states, these absorption effects should be lower when the cavities are far detuned from the bandgap, which is a strong incentive to fabricate cavities at high wavelengths (optimally telecom wavelengths). A second effect, potentially responsible for this decrease, is that fabrication related disorder is larger for larger holes. The Q-factors of L_3 cavity modes near resonance with the QDs are given on Fig. 2.22(c), their values are between 4500 up to a maximal Q of 9200. The mean and standard deviation of the Q-factor distribution for L_3 cavities with a radius r=59nm (blue dots on Fig. 2.22(c)) is: <Q>=7750 and std(Q)=593.

2.3.6 Other PL techniques

2.3.6.1 Spectrally resolved imaging

Although PL spectroscopy is a powerful technique to analyze nanophotonic structures, it is limited to taking emission spectra, which does not make a full use of the 2D CCD detector configuration. But the PL setup can easily be modified to perform single shot, spectrally resolved imaging of linear photonic structures, which can yield a profusion of information on their properties. This is realized by replacing the 4cm focal lens before the monochromator by a 30cm one as shown in Fig. 2.23. This lens and the microscope objective constitute a microscope with a magnification given by the ratio of the two focal lengths: M=83. The structure is then imaged directly onto the vertical direction of the CCD, while wavelength is resolved onto the horizontal direction of the CCD by the monochromator. One-micron size structures are then enlarged over $83\mu m$, much larger than the $15\mu m$ size of one pixel of the CCD. The imaged length is limited by the lowest ratio D_{opt}/L in which D_{opt} is the diameter of the optical element and L is its distance to the objective. This imaged length is given by:

$$D = f\frac{D_{opt}}{L} \tag{2.12}$$

In our setup, $D \approx 30\mu m$. In this configuration, only a portion of the grating is used because of the larger focal lens at the entrance of the spectrometer which reduces the spectral resolution of this setup. We measured a resolution of $\approx 200\mu eV$.

This limitation may be overcome by the use of a smaller focal length lens at the monochromator entrance and a set of cylindrical lenses to magnify the modes only in the imaged direction.

This setup was used to perform simultaneous spectral and spatial imaging of 1D photonic structures, such as waveguides or elongated cavities. It may also be used for 2D spectral imaging. Indeed, the $100\mu m$ slit limits the imaging to a narrow 1D band of the sample. A 2D spectrally resolved picture would thus be obtained by scanning over the sample and taking spectrally resolved pictures for each 1D slice.

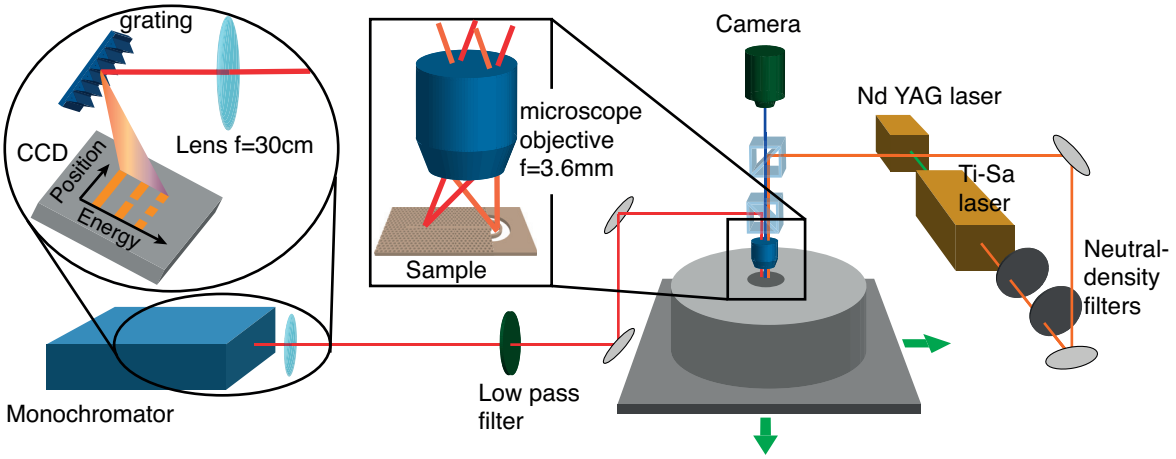

Figure 2.23 – Principles of spectrally resolved spatial imaging.

2.3.6.2 Time resolved photoluminescence

As shown in the introduction, the photonic density of modes induces variations of the exciton lifetimes through the Purcell effect. Probing the lifetimes of excitons is therefore a standard technique to infer the coupling properties of QDs to optical circuits. In this work, these lifetimes were measured in a time-resolved PL setup (TRPL).

The Ti-sapphire laser employed was operated in a mode-locked mode with an 80MHz repetition rate and emits 3ps pulses, which serve for quasi instantaneous (delta-function) excitation of the structures. Part of the excitation laser beam was directed to a fast photodiode, which served as a synchronizing pulse. A fast, sensitive avalanche photodiode (APD) was coupled to the monochromator output so as to count single photons with a detection efficiency of 15% at 950nm. The detection of an excitation laser pulse by the synchronizing photodiode started the time count in the time correlator electronics, which was stopped when the APD detected a photon.

The APDs used in this thesis were Picoquant APD τ-SPAD-FAST with 200 ps resolution. The electronics used was the Picoquant TimeHarp 260 Time-Correlated Single Photon Counting system with a 25 ps time bin width. This setup will be used in

Chapters 4 and 5 to measure the Purcell effect induced by waveguides and cavities.

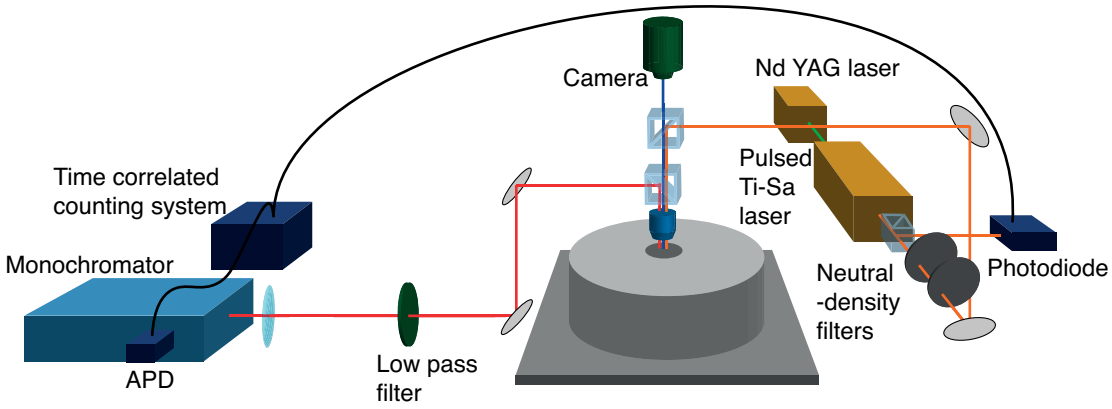

Figure 2.24 – Time resolved photoluminescence setup (TRPL).

2.3.6.3 Single photon correlations

One reason justifying the interest of QDs for quantum technologies is their emission of single photons. The very possibility to isolate single photons is a remarkable consequence of quantum mechanics. Indeed, in the 19th century, physics was divided in a seemingly fundamental dualism: matter was made of particles described by Newton's laws, while electromagnetic phenomena were described by Maxwell's equations for waves. This division was overcome in the formalism of quantum field theory in which the fundamental objects are quantum fields sharing properties of waves and particles simultaneously. Light, which was perceived as a wave, was shown to exhibit particle-like behaviors evidenced by the possibility to isolate single photons. The singleness of a particle is measured by its second order correlation function [4]:

$$g^{(2)}(\tau) = \frac{\left\langle \hat{a}^\dagger(0)\hat{a}^\dagger(\tau)\hat{a}(\tau)\hat{a}(0)\right\rangle}{\left\langle \hat{a}^\dagger\hat{a}\right\rangle^2} \tag{2.13}$$

where $\hat{a}$ is the photon annihilation operator. This quantity characterizes the probability to detect a photon at time τ, given that a photon was detected at time 0. It defines three categories of statistics for light: $g^{(2)}(0) < 1$ is the landmark of sub-poissonian statistics and anti-bunched light in which the probability of detecting a second photon immediately after the detection of a first photon is lower than one. $g^{(2)}(0) = 1$ corresponds to a poissonian statistics which is observed in laser light, while $g^{(2)}(0) > 1$ characterizes super-poissonian statistics, in which photons are bunched. The security of Quantum Key Distribution (QKD) [9] is fundamentally guaranteed by the no-cloning theorem according to which it is not possible to clone the unknown quantum state of a particle without errors. Using single photons to carry the informa-

tion is therefore a key components of many QKD schemes. Other applications such as linear optics quantum computing are based on the massive use of single photons (which should have the additional property of being indistinguishable). Therefore, building efficient single photon sources is a major challenge in quantum optics.

The second order correlations of QD emissions were measured during this thesis in a Hanbury Brown and Twiss (HBT) experiment in which the light beam collected from the QD is divided in two by a 50/50 beamsplitter (see Fig. 2.25). The light of a single QD line is filtered from other emissions by two monochromators. Single photon events are then detected by two APDs, (same type as described in section 3.7.2). One of them is starting a counter which is stopped when the second APD detects a photon.

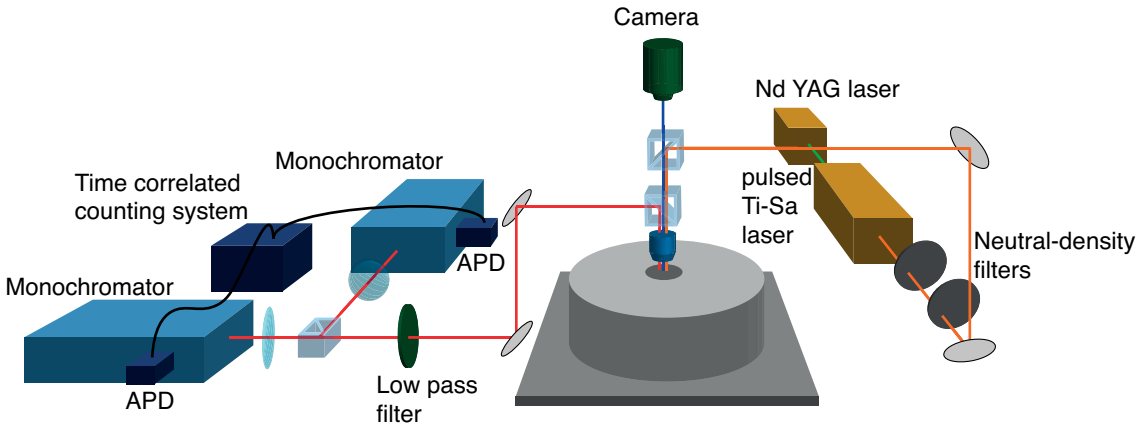

Figure 2.25 – Photon correlation setup.

Chapter summary

In this Chapter, the detailed fabrication process of the PhC-QD structures was exposed, starting from the design of experiments and associated numerical simulation techniques. The fabrication of pyramidal arrays of QDs and PhCs was then detailed. The photoluminescence properties of pyramidal QD ensembles thus fabricated featured excitonic linewidth resolution limited excitonic lines as narrow as $20\mu eV$. The use of TEGa as a precursor for Ga atoms was shown to improve the reproducibility, the available wavelength range and the average linewidths of pyramidal QD growths. Preliminary measurements on a sample grown with TEIn shows encouraging results indicating that this precursor may be useful for improving further the QD quality. The quality of PhC structures was assessed via statistics on the Q-factors of optimized L_3 cavities. Q-factors up to 9000 were observed at 970nm. Finally, the optical characterization techniques used in the next Chapters were described.

3 Effects of disorder and propagation losses in photonic crystal waveguides

A fascinating opportunity opened by PhC devices lies in the increased light-matter interaction via slowly propagating light modes appearing near the edge of waveguide bands. PhC waveguides (PhCWs) even feature the intriguing theoretical possibility to completely stop light propagation, thereby reaching an infinite interaction strength. However, this optimistic view is mitigated by the intrinsic properties of realistic implementations, which necessarily include structural disorder and inherently limit the achievable slowdown of light.

Several studies were reported on various aspects of optical disorder and mode localization in PhCWs, including the observation of Anderson-like localization close to the waveguide band edge [142, 143], the associated upper limit on the group index and propagation length [142, 144, 145, 146, 147], the group index dependence of disorder [148], the identification of dispersive, diffusive and localized regimes in the otherwise perfectly one-dimensional (1D) photonic band [149] and proposals of ways to reduce the associated optical losses [145]. The impact of optical disorder on Anderson-like mode localization in long L_n PhC cavities, essentially representing PhCWs of finite lengths, was also studied using scanning near field optical microscopy [146]. These studies reveal the detrimental impact of optical disorder on photon transport in PhCWs, similar to the well-known limitations on ballistic electron transport in one-dimensional electronic systems [150].

In this Chapter, the impact of optical disorder is investigated, first as a source of losses. A systematic analysis of Q-factors in L_n cavities is used to distinguish three main loss mechanisms: reflection losses at the L_n cavity edges, absorption and propagation scattering.

In a second part, we show how disorder affects the density of states (DOS), mode localization and slow light propagation in long L_n PhC membrane cavities incorporating site-controlled QDs. Three complementary methods are used for the identification of the photon mobility edge separating the regimes of extended and localized modes

and the diffusive edge marking the transition between diffusive and dispersive regimes. The direct spectrally resolved imaging of photonic modes permits to distinguish between localized and extended modes. Statistical measurements of the waveguide dispersion clarify the separation between the dispersive and diffusive regimes. Finally, the in-situ probing of modes by site-controlled QDs confirms this identification and demonstrates the quasi-disorderless nature of optical modes sufficiently far from the band edge and the mode distortions related to phase scattering in the diffusive regime.

3.1 L_n cavities incorporating QD light sources

3.1.1 Modes in L_n cavities

Modes in elongated cavities are commonly approximated as the product of propagating Bloch modes and an envelope function. Indeed, in analogy with Bloch waves in crystals, Bloch's theorem states that (in a 2D PhC waveguide) TE modes can be written only with the H_z component of the $\vec{H}$-field as:

$$H_z(r,\omega) = e^{ik(\omega)x} H_k(r,k) \tag{3.1}$$

Where $H_k(r)$ is the Bloch mode with a period defined by the lattice constant, $k(\omega)$ is the wavevector given by the dispersion relation of the corresponding waveguide. As the wave equation is invariant under time reversal symmetry [151], the following relationship between forward and backward propagating modes holds:

$$H_k(r,-k) = H_k(r,k)^* \tag{3.2}$$

$$\omega(-k) = \omega(k) \tag{3.3}$$

Therefore, a natural ansatz describing the modes in an elongated cavity is given by the superposition of interfering Bloch modes propagating to the left and to the right:

$$H_{L_n}(r) \propto H_k(r,k)^* e^{-ikx} + H_k(r,k) e^{ikx} \tag{3.4}$$

If we consider the periodicity of a point on the Bloch cell: $r = r_0 + ma$, where r_0 belongs to the Bloch cell and m is an integer and : $k = \pi/a(1-\epsilon)$.

$$H_{L_n}(r) \propto |H(r,k)| sin(\pi/a(1-\epsilon)(r_0+ma) + \Phi(r_0,k)) \tag{3.5}$$

$$H_{L_n}(r) \propto |H(r,k)| \cdot cos(\pi m) \cdot sin(-\pi m\epsilon + \alpha(r_0,k)) \tag{3.6}$$

Where $\Phi(r,k)$ is the phase of H_k (which is well defined almost everywhere), and α is a phase term independent of m. Each point of the resulting mode (including for example the Bloch mode maximum) will therefore have a sinusoidal envelope function with a period $1/\epsilon$. This effect arises from a beating between the Bloch mode $H_k(r,k)$ with a period a and the sinusoidal part with a period almost equal to a near the band edge. The cancellation of the field at the extremities of the cavity is ensured by a condition analogous to that of Fabry-Pérot (FP) modes: the wavevector is discretized according to: $k_p = \pi/a(1 - pa/L_{eff})$. Here, p is the number of nodes of the given mode, L_{eff} is the effective cavity length given by the sum of the real length and the "effective penetration length" into the mirrors as exposed by Lalanne et al. [152]. The period of the intensity envelope modulation is: $P = L_{eff}/p = a/(1 - k_p a/\pi)$. Although each point of the mode has this P-periodicity, the mode itself is not strictly speaking the product of a sinusoidal envelope function and the Bloch mode because of the y dependence of $\alpha(r_0,k)$, which introduces a y-dependent dephasing responsible for the zigzag shape of the modes resulting from the interference between two beams co-propagating at an angle with the waveguide. This effect is similar to a plane wave propagating between two mirrors. In this Chapter, the QDs all lie on the same y-axis: the electric field probed by the QDs is indeed the product of an a- periodic function a and a P-periodic sinusoidal envelope function.

This semi-analytical model was used to obtain the M_0 and M_4 modes in an L_{33} cavity (Fig. 3.1(a)) and compare them to the FDM computed modes as shown on Fig. 3.1(b-c). The maximal relative difference between the M_0 mode intensity computed through the two methods was better than 4.5% everywhere and better than 2.5% if we neglect the edges, which confirms the model validity. Such a model for waveguide modes has been used [153] to do semi-analytical computation of coupled modes in more complex systems. It is a good approximation to real modes everywhere except near the edges, where the analytical treatment of reflection does not reflect the intricacies of the electric field. This model will be used throughout the following Chapters to understand a number of effects occurring in waveguides and elongated cavities.

The equation predicting the analytical value of the period: $P = L_{eff}/p = a/(1 - k_p a/\pi)$ can be solved in photon energy for each value of p. The energy of each confined mode predicted by the semi-analytical model is then deduced from the W1 waveguide dispersion relation. The energy of each modes of an L_{33} predicted by the FP model is displayed on Fig. 3.1(d). A correct matching is obtained for low energy modes while it is less good for high values of p. A much better matching is obtained with $L_{eff} = 35a$ as shown on Fig. 3.1(e). From this simple method, we can infer an effective penetration length of light in the PhC $\approx 0.225\mu m$. We note this method does not exhibit a perfect matching for all modes simultaneously, which indicates a wavevector

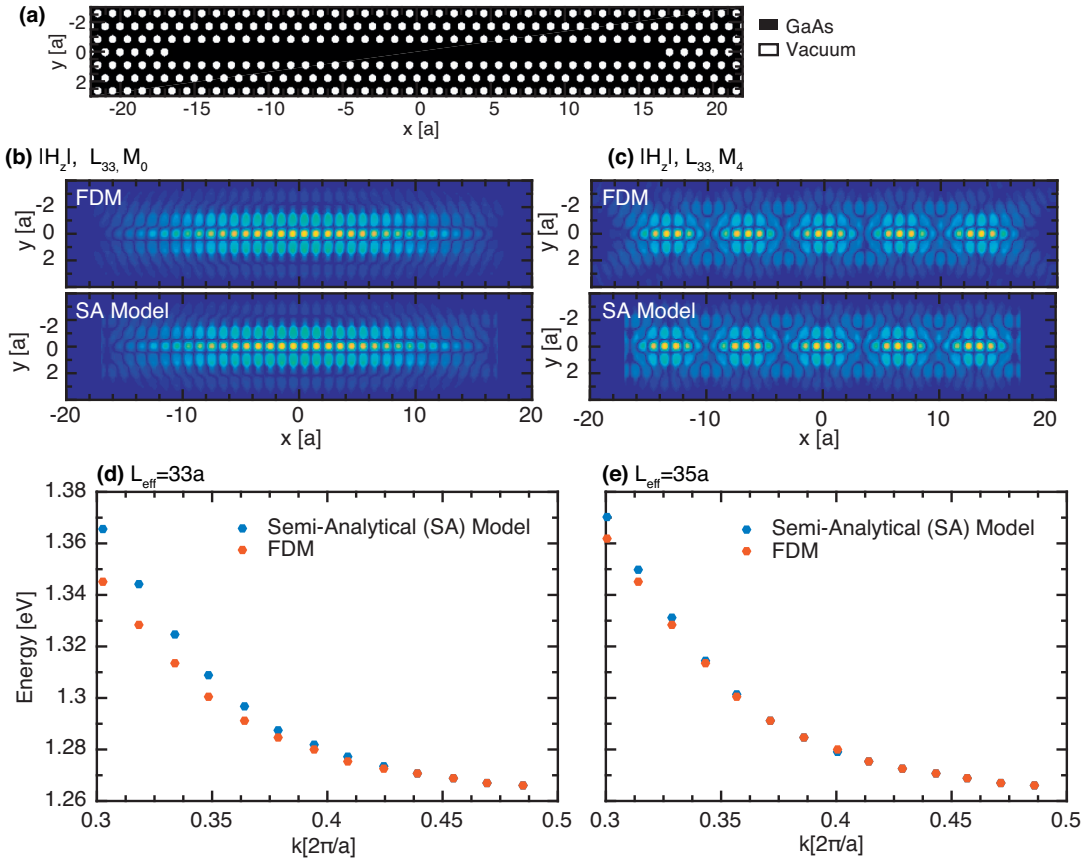

Figure 3.1 – Semi-analytical model for modes in L_n cavities: (a) Geometry of the simulated L_{33} cavity; (b) M_0 and (c) M_4 modes of the cavity computed via FDM and with the semi-analytical model; (d-e) Energy of modes in an L_{33} computed with FDM and via the semi-analytical model with (d) $L_{eff} = 33a$, (e) $L_{eff} = 35a$,

dependent penetration length. This model also yields naturally the mode wavelength separation, since two modes have a wavevector difference exactly given by π/L_{eff}.

$$\Delta\lambda = \frac{\lambda^2 \Delta\omega}{2\pi c} = \frac{\lambda^2}{2L_{eff} n_g} \tag{3.7}$$

This relation will be used in the next parts to obtain a direct measurement of n_g from the modes spacings.

3.1.2 Pyramidal QDs in a PhC wire

The structures studied in this Chapter were L_n cavities with n=3, 7, 17, 33 and 61. The PhC structures were designed using 3D FDTD such that their 1D photonic band overlaps the QD emission spectra. The PhC hole patterns were positioned on a triangular lattice with pitch a=225nm, and 15 values of hole radii were implemented,

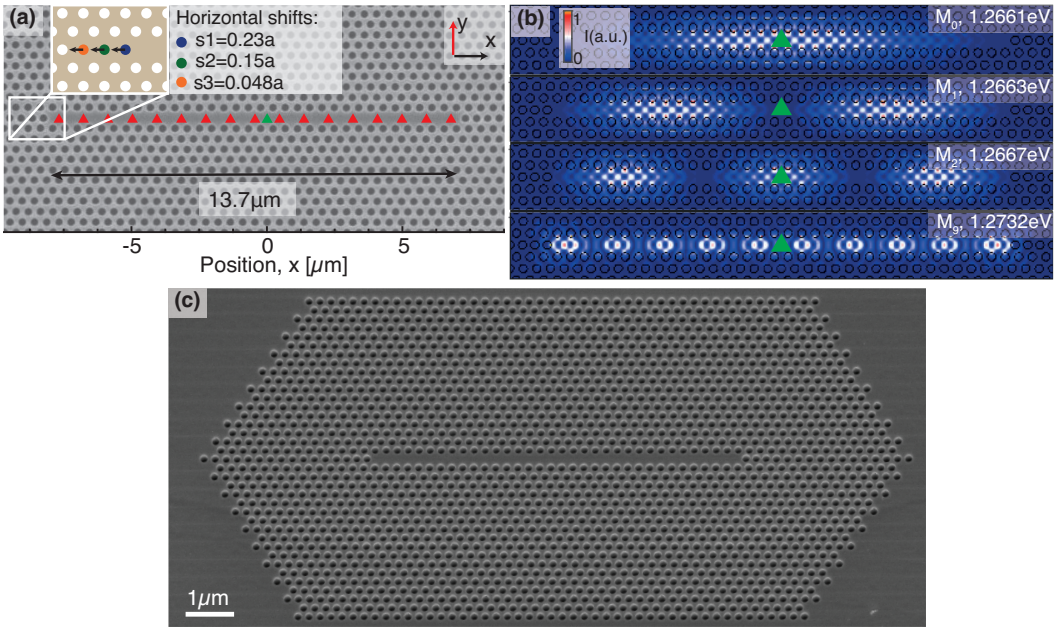

Figure 3.2 – (a) SEM picture of an L_{33} PhC cavity incorporating 16 (red triangles) or one (green triangle) embedded QDs; (b) 2D FDM calculated in-plane near field intensity patterns of the M_0, M_1, M_2 and M_9 modes of an L_{33} cavity (lattice constant: a=225nm, hole size: r=61nm, refractive index $n_{2D} = 3.13$); (c) SEM picture of an L_{33} cavity (tilted view).

(r= 57-80nm in 1.5nm steps) in order to experimentally scan the PhCW band edge across the QD emission energy. At each end of these cavities, three holes were shifted outwards along x by 0.23a, 0.15a and 0.048a. These shifts were optimized by Minkov et al. [73] to reach Q-factors of 200000 for the M_0 mode of L_3 cavities. Fig. 3.2(a) shows the design for the L_{33} cavity. On Fig. 3.2(b) the calculated near field intensity patterns of several modes of the cavity are shown, well approximated by the products of a sinusoidal envelope function and the Bloch mode of the corresponding W1 waveguide. These modes were computed using the 2D finite difference method (FDM).

The pyramidal QD layout and the PhC hole pattern were designed to yield three types of W1-based systems: L_n cavities with (n-1)/2 embedded QDs; L_n cavities with one QD; L_{61} cavities with 3QDs. The single QDs were placed at the cavity center whereas the (n-1)/2 dots were distributed uniformly along the cavities with a 0.45μm separation. The 3QDs were distributed along the L_n cavities spaced by: 20a=4.5μm. To ensure a good overlap between the QDs and cavity mode field patterns, all QDs were placed at the maxima of the in-plane electric field of the W1 waveguide Bloch mode.

3.2 Reflection and propagation losses in PhC waveguides

3.2.1 Loss measurements in PhC waveguides

A first consequence of disorder is a dramatic increase or even the appearance of losses. Strategies for minimizing propagation losses in semiconductor PhC waveguides and associated devices should consider not only inherent optical material absorption but also the impact of fabrication induced disorder and waveguide dispersion effects. Theoretical works [144, 154] investigated the impact of disorder on losses in PhC waveguide, permitting a distinction between backscattering, proportional to the overlap of the forward and backward propagating optical modes and thus roughly quadratic in n_g, while scattering to the radiation modes is only proportional to the forward propagating mode and linear in n_g. Other authors reached similar conclusions with different methods [147, 155, 156]. Mazoyer et al. [148] showed that this quadratic scaling of backscattering was valid only for very small disorder, but became super-quadratic for experimentally reasonable disorder, possibly as an indication of multiple scattering effects. However, no such simulations of scattering to the radiation modes as a function of group index were performed to our knowledge.

The true origin of loss in PhCs is often difficult to estimate in experiments. Excellent results were obtained in silicon PhC waveguides at telecommunication wavelength by comparing the transmission of waveguides of varying lengths. Losses down to 4dB/cm were demonstrated [157, 158]. Dispersion engineering permitted the reduction of losses near the band edge [159]. Finally, a confirmation of the super-linear scaling of propagation losses were measured by Kuramochi et al. [155].

Several studies also focused on GaAs, which has the significant advantage of a direct bandgap over silicon. Early results [160, 161, 162] focused on wide, multimode waveguides such as W3 or W7. Record values of 0.2dB/mm for W7 waveguides and 1.5dB/mm for W3 waveguides were observed at the cost of multimode waveguides and low photonic confinement detrimental to light-matter interaction.

More recent works concentrated on highly confined W1 single mode waveguides. Large statistical fluctuations of transmission near the band edge [154, 163] emphasized the limits of PhCW for integrated photonics, however without explicit measurements of the loss coefficients. All the previously cited results focused on PhCs operated near $1.5\mu m$, for which interband absorption losses are very low. However, most papers studying InGaAs/GaAs QDs as single photon sources in PhC waveguides are operated near 900nm, because the QD sources are easier to fabricate and the single photon detectors are more efficient. Wasley et al. [142] measured propagation losses around $1-15 mm^{-1}$ ($5-60 dB mm^{-1}$) near the band edge around 900nm, by analyzing the finesse of FP cavities of different lengths. However, the origin of propagation losses was not given.

3.2.2 A Fabry-Pérot model for losses in L_n cavities

We propose here a simple theoretical model for elucidating the different loss channels in L_n cavities followed by experimental measurements of these loss terms [114]. Losses in long linear cavities are described by two main physical effects [164]:

- The finite edge reflectivity with a reflection coefficient R.
- The propagation losses, which can result from scattering and absorption, quantified by a loss coefficient : α_p

The Q-factor in linear cavities is then straightforwardly derived from a Fabry-Pérot model [165]:

$$Q = \frac{k_0 n_g L \sqrt{R e^{-L\alpha_p}}}{1 - R e^{-L\alpha_p}} \tag{3.8}$$

In the limit $R \approx 1$ and $L\alpha_p \ll 1$, the Q-factor can be divided in two Q-factors emphasizing the two loss channels:

$$1/Q \approx 1/Q_p + 1/Q_R \tag{3.9}$$

$$Q_R = \frac{k_0 n_g L}{1 - R} \tag{3.10}$$

$$Q_p = \frac{k_0 n_g}{\alpha_p} \tag{3.11}$$

From the same Fabry-Pérot model, the free spectral range between adjacent modes is given by:

$$\Delta\lambda = \frac{\lambda^2}{2 L n_g} \tag{3.12}$$

and the finesse of the cavity is:

$$F = \frac{\Delta\lambda}{\delta\lambda} = \frac{\Delta\lambda}{\lambda} Q = \frac{\pi \sqrt{R e^{-L\alpha_p}}}{1 - R e^{-L\alpha_p}} \tag{3.13}$$

In the case of weak losses ($R \approx 1$ and $L\alpha_p \ll 1$):

$$\frac{1}{F} = \frac{1}{\pi}(1 - R + L\alpha_p) \tag{3.14}$$

The inverse of the finesse thus exhibits a linear dependence on L from which the reflection and propagation loss coefficients are straightforwardly inferred.

3.2.3 Measurement of absorption and reflection coefficients in Ln cavities

3.2.3.1 Experimental measurement of loss

These loss terms were measured using L_n cavities of different lengths (n=3-7-17-33-61) [114]. Each cavity was filled with (n-1)/2 QDs regularly spaced according to the design of Fig. 3.2(a). The FP modes in the L_n cavities were measured using a high power excitation ($P = 500\mu W$). At such a pump power, QDs emit through s, p and d transitions in the 1.3-1.33eV range, whereas the QWR barriers surrounding the QDs emit a broad continuum extending down to 1.25eV [96] thus exciting all the optical modes. Spectra measured for representative cavities of different lengths are shown in Fig. 3.3(a). On the broadband emission background of the highly excited QDs, the FP cavity modes are clearly visible which illustrates the photonic band formation as the cavity length is increased [121]. The modes intensity is enhanced near 1.32eV and 1.35eV due to the higher spectral overlap with the QD transitions. The FP modes show decreasing spacing with decreasing energy as expected for the case of an ideal L_n cavity, but show irregular spacing below a particular energy (here ~1.285eV). This feature indicates Anderson localization, as will be demonstrated next.

The Q-factors were obtained from lorentzian fits on the measured modes as indicated on the inset of Fig. 3.3(a). The resulting Q-factor distribution is shown on Fig. 3.4(a). So as to guarantee the absence of stimulated emission induced narrowing of cavity lines, the Q-factor variations with the excitation power of two modes in an L_{33} cavity are indicated on the inset of Fig. 3.4(a). No linewidth narrowing is observed, consistent with the low density of gain medium in this experiment. The group index was inferred from the measured FP mode spacing $\Delta\lambda$ in L_{61} cavities. The measured group index on one L_{61} cavity is displayed on Fig. 3.3(b) together with the 3D FDTD simulated group index. Below 1.286eV, irregular variations of group indexes indicates Anderson localized modes as will be shown next. These modes were not included in our analysis. The finesse of the FP mode is then calculated with:

$$F = \frac{\lambda Q}{2Ln_g} \tag{3.15}$$

The finesses obtained (Fig. 3.4(b)) decreases with the cavity size, which according to 3.14 is a consequence of propagation losses. The wavelength dependent propagation loss coefficients were obtained by aggregating the finesse data of Fig. 3.4(b) in 5nm wavelength bins. The wavelength dependence of $1/F$ was then fitted with equation 3.13. Note that the three (nonlinear) fits shown on Fig. 3.5(a) are close to the predicted linear relations between F and L, which indicates that the L_n cavities are in the low loss regime. Our analysis was restricted to the 900-960nm range, far enough from the band edge to avoid localized modes, which are not accurately modelled by

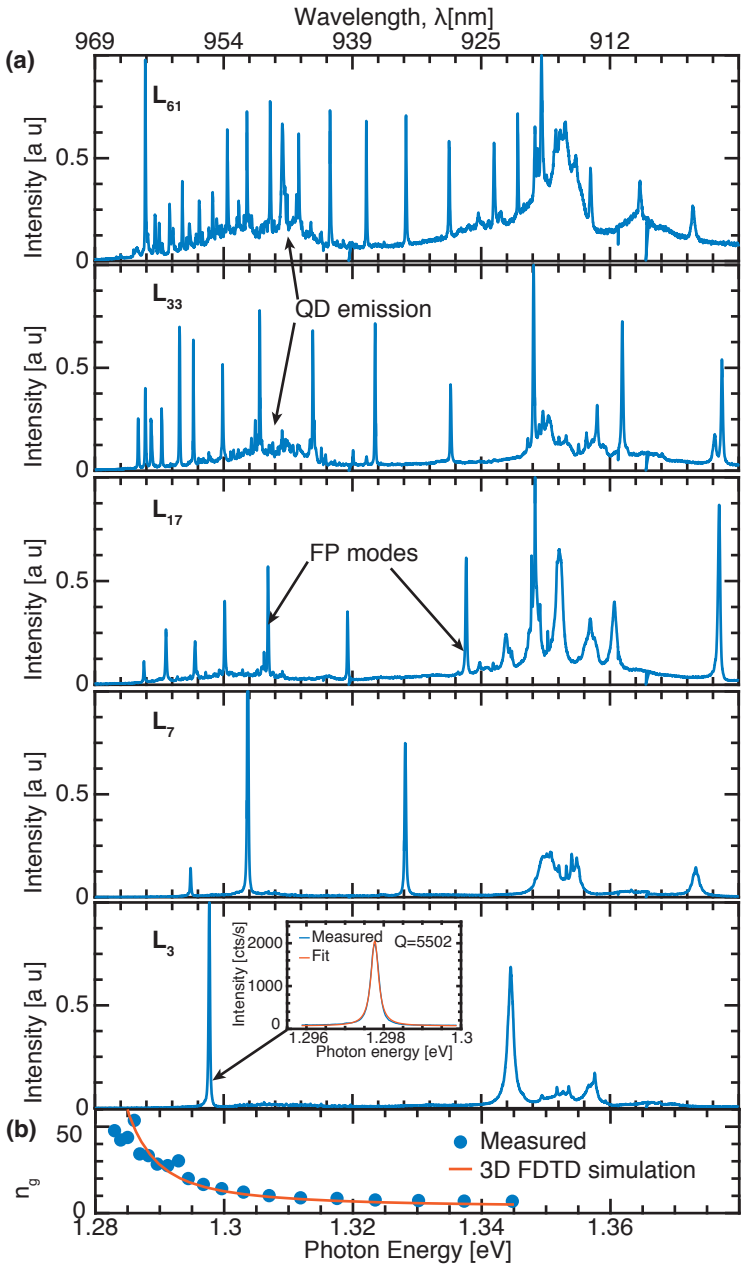

Figure 3.3 – (a) Spectra of L_n cavities of various lengths; Inset: Lorentzian fit of the M_0 mode in an L_3 cavity. The arrow points to the fitted line; (b) Measured and simulated group index in an L_{61} cavity ($P = 500\mu W$, $T = 10K$). Parameters for the 3D FDTD simulation are: $n_{3D} = 3.46$, slab thickness: $th = 250nm$, holes radius: $61nm$. The simulated curve was shifted by $14meV$ to match the band edge measured from the L_{61} cavity [114].

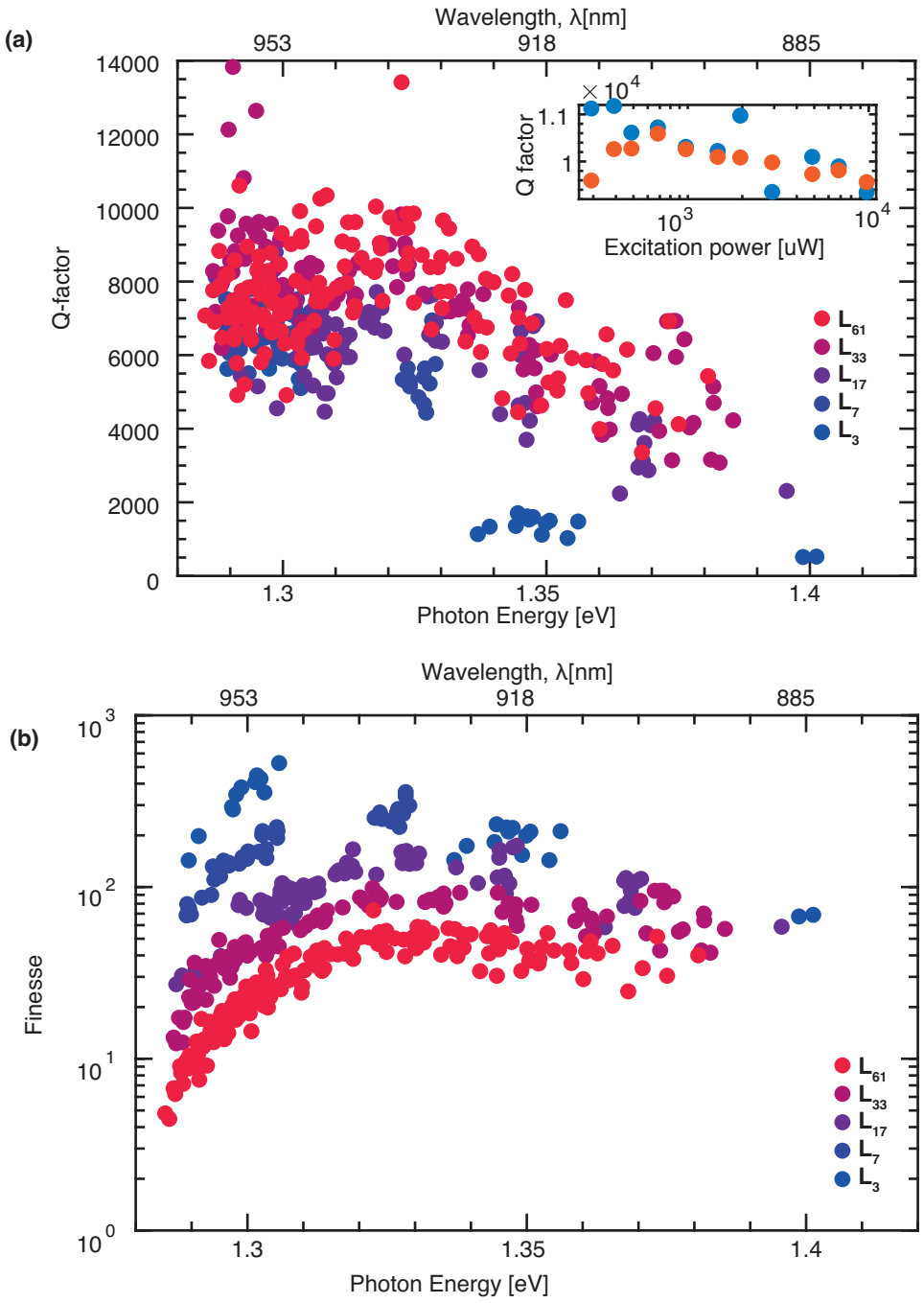

Figure 3.4 – (a) Q-factors fitted on the L_n cavities ($P = 500\mu W$, $T = 10K$, $r = 61nm$, $a = 225nm$); Inset: power dependence of the Q-factor of two modes in an L_{33} cavity; (b) Finesse obtained from the Q-factors measured on the modes of L_n cavities [114];

FP modes. The penetration length of light into the PhC inducing a slightly different effective length of PhCW was neglected in this model [152]. The extracted propagation loss coefficients α_p and the transmission parameter 1-R are displayed on Fig. 3.3(b).

3.2.3.2 Analysis of the loss channels

The extracted reflection coefficient R is constant around 99% in the whole wavelength range within the error margins, except near 950-960nm where the fit gave a value close to 100%, however with a large uncertainty. Such a reduction of reflection around 950nm is expected. Indeed, the edges of each L_n cavity were identical, and made in such a way that the Q-factor of the M_0 mode of an L_3 cavity was optimized up to ≈ 200000. As noticed by Lalanne et al. [152], in a disorderless W1 waveguide, the modes exhibit no loss and therefore the propagation losses in a disorderless L_n cavity is zero. As a consequence, optimizing the Q-factor in L_n cavities amounts to reducing the scattering loss during reflections at the edges. The reflection coefficient in these L_n cavities is therefore around 99% except in a narrow range around the wavelength of the M_0 mode of the L_3 cavity where the specific optimization reduced it to a lower value, which cannot be extrapolated precisely from the fit. The measured reflectivity R=99% is consistent with simulations of similar structures [152].

The fitted loss coefficient α_p slowly decreases from $6mm^{-1}$ ($26dB/mm$) at 910nm to $4mm^{-1}$ ($17dB/mm$) at 930nm, then increases rapidly to $17mm^{-1}$ ($74dB/mm$) at 950-960nm, closer to the photonic band edge. This increase near the band edge suggests the presence of propagation losses related to slow light. In order to unearth effects of slow light beyond a linear dependence, the propagation loss coefficient normalized by n_g is plotted on Fig. 3.5(c). The loss coefficient increase is clearly super-linear in n_g near the band edge, which cannot be explained by linear scattering propagation losses [79, 144]. Similar results were attributed to backscattering by Kuramochi et al. [155]. Indeed, backscattering is quadratic in n_g for weak disorder and can increase even faster for low enough disorder [148]. However, although backscattering is a loss term for the propagating waveguide mode (even when multiple scattering phenomena are neglected), it is not strictly speaking a loss term in L_n cavities where the standing waves are composed of both forward and backward propagating modes. Thus, if the attribution of these losses to backscattering by Kuramochi et al. [155] is valid for transmission measurements, our measurement technique using FP resonances, does not measure directly backscattering, but scattering to the radiation modes. This point does not mean that backscattering do not play any role in the propagation losses. For example, backscattering may increase the intensity of light in a portion of the PhCW, thus inducing loss increases similar to that caused by slow light. In what follows, scattering to the radiation modes will be described by a quadratic term in n_g.

The observed increased losses at shorter wavelengths suggests absorption related

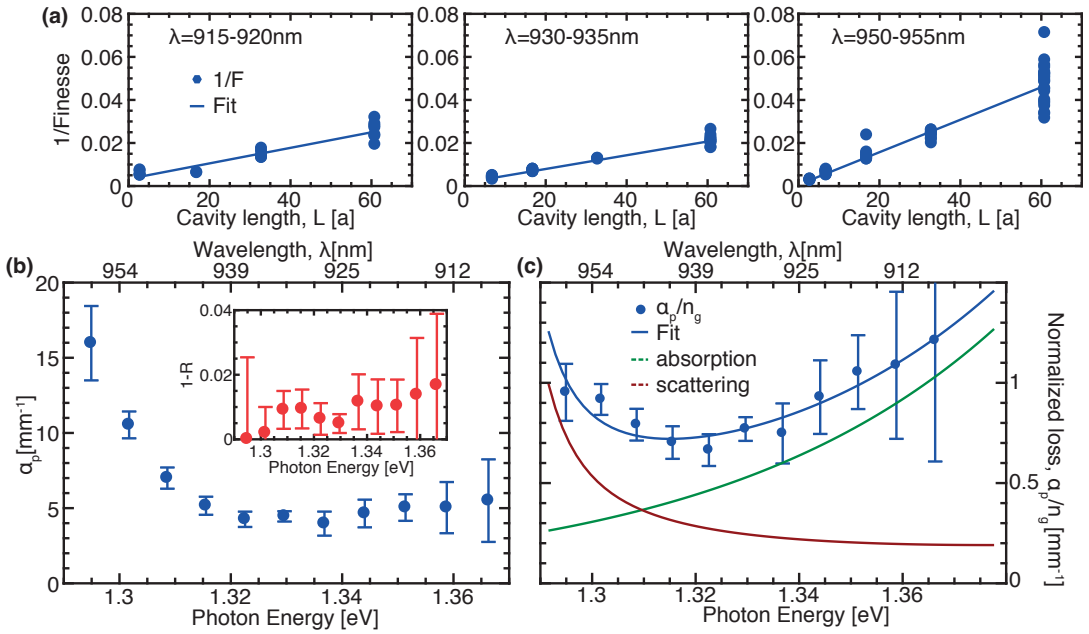

Figure 3.5 – (a) Fits of the Fabry-Pérot model on the measured finesse; (b) Propagation loss coefficient α_p; Inset: reflection coefficient at the edges extracted from the linear fit as shown in (a), (c) Fit of the loss model on α_p/n_g [114].

to the GaAs bandedge proximity, which can be described by exponential absorption tails (e.g., Urbach tails caused by lattice impurities [166]). Including these two effects, the propagation loss coefficient can be described by the following model:

$$\alpha_p = \alpha_1 e^{-(E-E_{bg})/E_a} n_g + \alpha_2 n_g^2 \tag{3.16}$$

where the first term models absorption and the second terms describes scattering to the radiation modes. E_{bg} is the photonic bandedge energy (here 968nm) and E_a is the characteristic energy for the decay of absorption far from the GaAs band edge. The fit yielded the following parameters: $\alpha_1 = 0.22 \pm 0.12 mm^{-1}$, $\alpha_2 = 0.04 \pm 0.01 mm^{-1}$, and $E_a = 55 \pm 21 meV$. This value of the Urbach parameter is larger than that measured in Si doped GaAs [134]: $E_a = 12 meV$ (density of impurities: $n = 2 \cdot 10^{18} cm^{-3}$).

The two loss mechanisms are distinguished on Fig. 3.5(c): the absorption losses dominating at high energy (green) and the scattering process dominating at low energy (dark red). This analysis confirms the interest of going to higher wavelengths for fabricating very high Q-factor cavities in GaAs materials [77].

3.2.4 Q-factors in L_n cavities

These fitted values of propagation losses are useful to determine dominant loss mechanisms in L_n PhC cavities according to the cavity mode length and energy. In the

low loss limit, the Q-factor can be divided in two Q-factors modelling the two loss channels (Eq. 3.9), from which we infer a Q-factor cavity length dependence (at a fixed photon energy):

$$Q = \frac{1}{\frac{1-R}{k_0 n_g L} + \frac{1}{Q_p}} \tag{3.17}$$

The Q-factor length dependence in the fast light regime predicted by this model is indicated on Fig. 3.5(d). The two main loss mechanisms are plotted in blue and red, based on the following measured experimental values of losses in the fast light regime (1.33eV): $\alpha_p = 5 \cdot 10^{-3} \mu m^{-1}$, $n_g = 5.5$, $\lambda = 930nm$, $R = 99\%$. The main loss mechanism is reflection losses at the edge for small cavities, and propagation losses for cavities lager than $L = 9a$. This indicates that small L_n cavities require a specific optimization of their edges to reach their optimal Q-factor as is commonly done with L_3 cavities [126]. The limit given here depends of course on the specific value of losses. However the existence of such a limit is a very general property in such elongated waveguides.

These results are also useful for the field of cavity QED. In the strong coupling regime, the strength of coupling is characterized by the coherence factor: $g/\kappa \propto Q/\sqrt{V}$, where $g \propto 1/\sqrt{V}$ is the coupling coefficient and $\kappa \propto 1/Q$ is the cavity loss coefficient. In the case of L_n cavities, since V is approximately proportional to L, the coherence factor is maximal for $L = \frac{1-R}{k_0 n_g} Q_p$. revealing an optimal length for strong coupling. However, if the PhC cavity terminations are optimized, this value is considerably reduced, although the impact of disorder on such optimized reflectors has not been investigated to our knowledge.

In the weak coupling regime, the Purcell factor is proportional to Q/V, which always decreases for longer cavities. Therefore, the Purcell factor is systematically larger in smaller cavities.

The wavelength dependence of loss channels can also be explored as outlined by the predicted L_{61} Q-factor values shown on Fig. 3.5(e). The three loss channels are distinguished through the following low loss Q-factor modelling:

$$\frac{1}{Q} = \frac{1}{Q_a} + \frac{1}{Q_{sc}} + \frac{1}{Q_R} \tag{3.18}$$

$$Q_a = \frac{k_0}{\alpha_1 e^{-(E-E_{bg})/E_a}} \tag{3.19}$$

$$Q_{sc} = \frac{k_0}{\alpha_2 n_g} \tag{3.20}$$

where Q_a, Q_{sc} and Q_R respectively model the absorption loss (in red), the propagation scattering (in dark red) and the edge scattering (in green). In such long

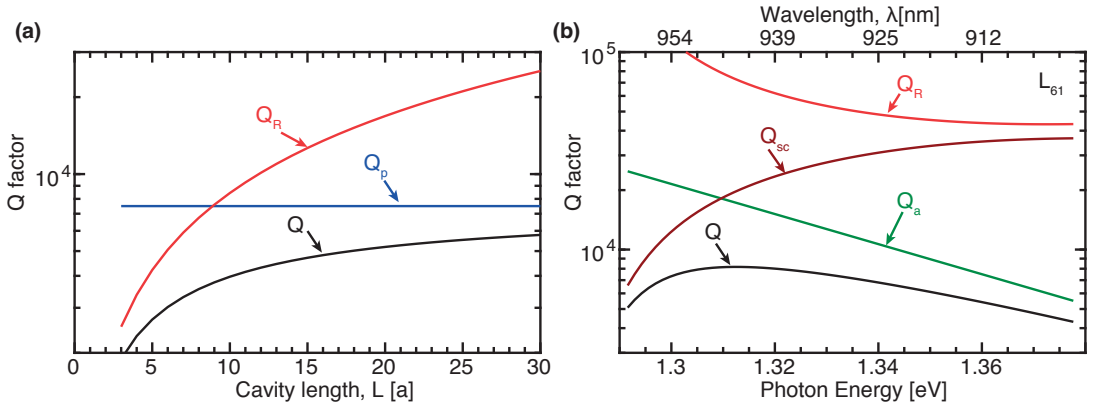

Figure 3.6 – (a) Theoretical Q-factor (black) variations with the cavity length; the red and blue curves are respectively the edge loss and the propagation loss contributions to the Q-factor ($\alpha_p = 5 \cdot 10^{-3} \mu m^{-1}$, $n_g = 5.5$, $\lambda = 930nm$, R=99%); (b) Theoretical Q-factor variation with wavelength in an L_{61} cavity ; the red green and dark red curves are respectively the edge loss, the absorption loss due to the Urbach tail and the propagation scattering contributions to the Q-factor ($\alpha_1 = 0.22 mm^{-1}$, $\alpha_2 = 0.04 mm^{-1}$, $E_a = 55meV$, R=99%)

cavities, the effect of edge scattering Q_R in red is low, although its relative importance is enhanced at larger energies. Absorption Q_a is the dominant loss mechanism at low wavelengths. Beyond 940nm the propagation scattering Q_{sc} takes over, which explains the L_{61} Q-factor maximum around 940nm observed on Fig. 3.5(b). These remarks may be of interest for the conception of nanolasers in such elongated L_n cavities [164].

These energy dependent results are also interesting for the design of smaller cavities. The M_0 mode of L_3 cavities which is often chosen for cavity QED experiments has an energy $E \approx 1.3eV$ (for the selected free space wavelength and effective index of the membrane), for which the dominating propagation loss mechanism according to our model is disorder induced scattering because of the higher group index. This hints at the possibility to reach higher Q-factors for L_3 cavities by focusing on higher order modes such as M_1. Of course, such higher order modes would need to be specifically optimized to reduce edge scattering.

Finally, the M_0 mode Q-factors in L_3 cavities presented in Chapter 2 can now be reinterpreted with more insights. In those measurements, the Q-factor increased with the PhC hole radius (Fig. 3.7). These variations can be related either to the increased absorption near the GaAs band edge or to fabrication related disorder, which may change with the hole radius. The Q-factor as predicted by Eq. 3.18 with $n_g = 11.5$ for the M_0 mode of L_3 cavities (as predicted by FDM simulation with a PhC hole radius: $r = 61nm$) is plotted together with the r/a serie of Q-factors. The model is slightly biased toward higher Q-factors, but matches well the slope of Q-factor decrease near

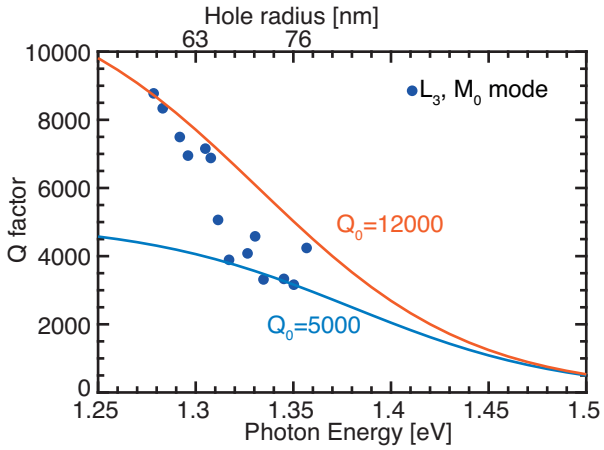

Figure 3.7 – Q-factors of an r/a serie of L_3 cavities ($\alpha_1 = 0.22mm^{-1}$, $\alpha_2 = 0.04mm^{-1}$, $E_a = 55meV$, R=100%, $n_g = 11.5$).

the GaAs band edge. According to this model, fabrication related disorder ultimately limits the Q-factor to 14000 at low energies. These results highlight the significant absorption near the band edge, which is a strong incentive to improve the quality of the grown GaAs material. Assuming that most of the impurity incorporation happens during the QD MOCVD growth, a promising possibility would be to grow the QD GaAs cap with TMGa at a larger V/III ratio which would limit unwanted carbon incorporation during the growth. As shown in Chapter 2, a good planarization (around 1-2nm) is achievable under such conditions, which may yield higher Q-factors.

3.3 Disorder effects in PhC waveguides

Disorder does not only cause losses, as emphasized in the introduction. It also dramatically distorts the shape and dispersion of modes in L_n cavities. In this part, we will investigate the influence of disorder on waveguide mode shapes and dispersion around the photonic band edge.

3.3.1 Imaging L_n cavities

3.3.1.1 Spectrally resolved imaging near the band edge

Spectrally and spatially resolved imaging of linear PhC systems using the setup described in the preceding Chapter is a powerful tool for the investigation of modes and scattering mechanisms as will be shown here. A first example of an L_{33} cavity excited at a high pump power ($P = 500\mu W$) is displayed in Fig. 3.8(a,b) (L_{33} PhC structure with 16 embedded QDs). The observed modes (M_0-M_4) exhibit sinusoidal envelope functions similar to those expected for an ideal L_{33} cavity. Comparison with the 2D-FDM calculations of an L_{33} cavity (green curves on Fig. 3.8(c)) reveal slight distortions

of the measured envelope functions due to fabrication disorder. The M_0 mode is clearly less extended than the disorderless FDM mode, indicating localization. Higher order modes reveal asymmetries between the lobes, which is also a consequence of disorder. The higher order modes (>M_4) observed extend throughout the cavity, although their number of lobes becomes increasingly difficult to discern due to the finite spatial resolution of our set up as is already clear from the M_4 mode. This first example demonstrates the possibility to image the photonic modes near the band edge (over $\approx 5meV$) using a simple PL setup, probably thanks to the disorder related out of plane scattering homogeneously distributed along the cavity. This imaging technique will serve now for the more precise study of disorder-induced effects of photonic modes.

3.3.1.2 Disorder in L_n cavities explored by spectrally resolved imaging

The simulated spectrally resolved near field patterns for an ideal L_{61} structure with homogeneous membrane and uniform PhC hole pattern is shown in Fig. 3.9(a). This picture was obtained by integrating each photonic mode along the y direction and placing the integrated component at its corresponding energy along the horizontal axis. A simulation of the mode patterns in a similar structure in which random disorder in the PhC hole radii was introduced (Fig. 3.9(b). The exact nature of disorder in our structure is unknown, however precedent studies indicated that a simple random variation of the hole radii was sufficient to capture the main physical effects of disorder [148]. In this work, disorder was simulated by varying the radius of each hole according to a gaussian random distribution. The FDM simulation parameters were: a=225nm, r=61nm, the standard deviation of the Gaussian random distribution of r was: $std(r) = 3nm$. In presence of disorder, the lowest energy modes are localized within randomly located segments of the cavity, whereas the higher energy modes (here >M_4) extend along the entire cavity length. A mobility edge placed ~5mev above the M_0 mode is observed, separating the localized and delocalized mode regimes.

Spectrally and spatially resolved images of L_{61} cavities were obtained with the imaging PL setup presented in Chapter 2, while using a cylindrical lens in the excitation path to produce an elongated excitation spot in order to ensure uniform illumination of the entire cavity length. These modes (Fig. 3.10(a-b-c)) display features similar to those of previous simulations: localized modes are confined at random locations of the cavity and the localization edge is located ~3meV above the lowest energy mode.

The similar values of the calculated and observed widths of the localized mode band suggests that the fabrication-induced disorder in our structures corresponds to strd(r) of ~3nm. Simulations with higher and lower disorder shown on Fig. 3.9(c) confirms that the spectral extension of the localized zone permits a quantification of disorder. The mobility edge indicated as a white arrow is shifted to higher energy when

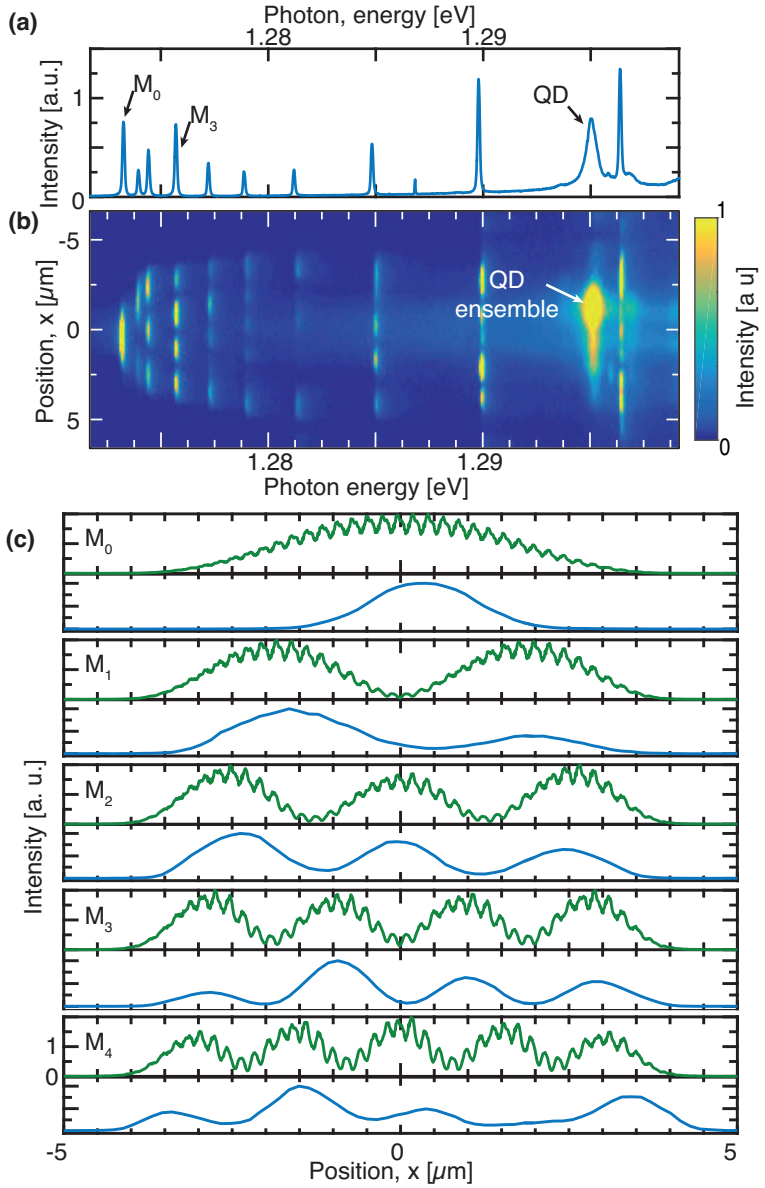

Figure 3.8 – Mode structure of an L_{33} PhC cavity excited with 16 embedded QDs. (a) PL spectrum; (b) spectrally resolved optical field (excitation power:$P = 500\mu W$, Temperature: $T = 10K$); (c) comparison between 2D FDM computed modes in an ideal (disorder-free) structure (green) and measured envelopes of the modes observed in (b) (blue). (The 2D FDM simulations were performed with the following parameters: $a = 225nm$, $r = 61nm$, $n_{2D} = 3.13$, the mode intensities were integrated along the y direction, such that only the x dependence is observed).

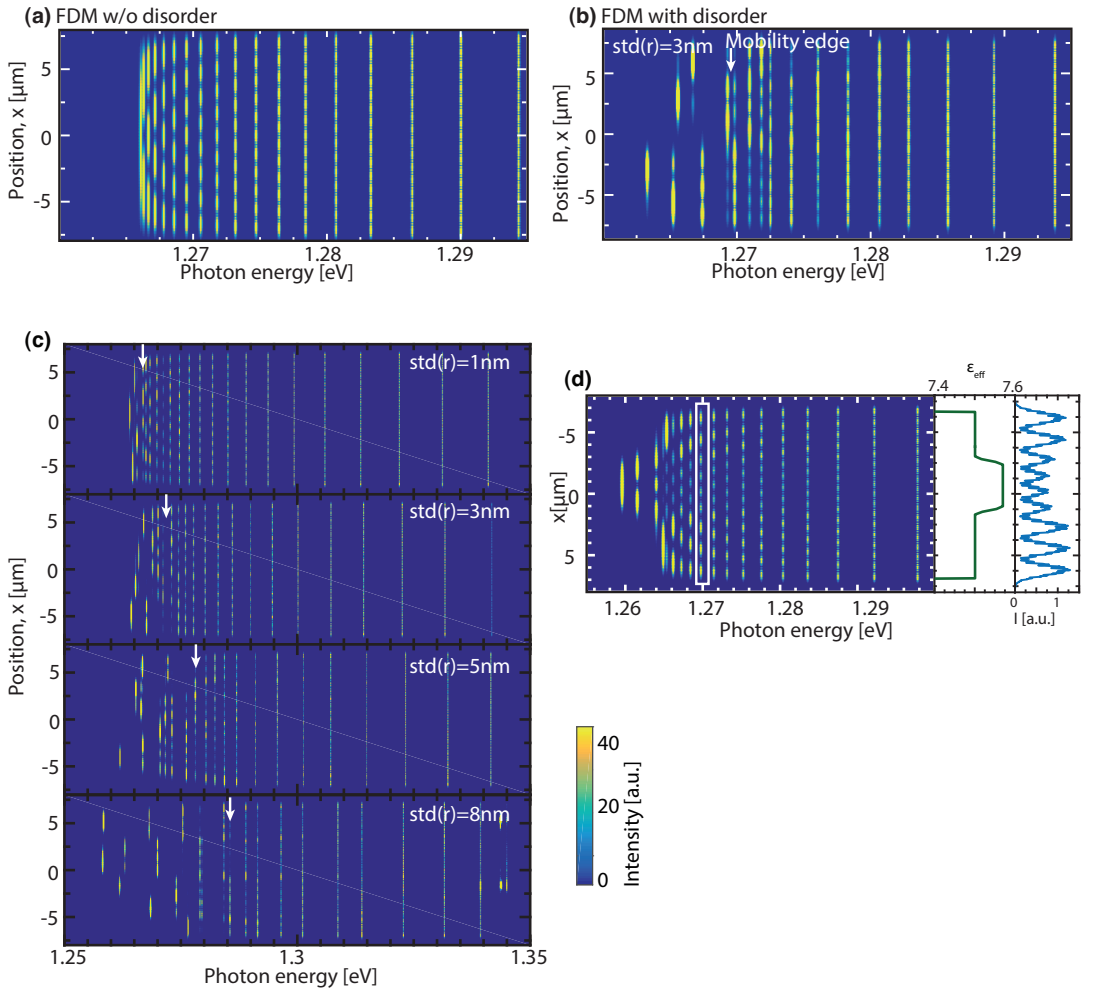

Figure 3.9 – Effect of optical disorder on L_{61} PhC cavity modes illustrated with 2D-FDM simulations of spectrally resolved mode patterns: (a) Disorder-free L_{61} cavity; (b) L_{61} cavity including random gaussian disorder; (a=225nm, r=61nm, n_{2D}=3.13, disorder implemented with: $std(r) = 3nm$); (c) L_{61} cavity with increasing random gaussian disorder; (a=225nm, r=61nm, n_{2D}=3.13, the disorder parameter is indicated on each picture, the white arrow indicates the photon mobility edge); (d) 2D-FDM simulation of an L_{61} including a long 3.8μm defect with the radius of holes next to the waveguide channel reduced to $r = 56nm$; (a=225nm, r=59nm, n_{2D}=3.13)

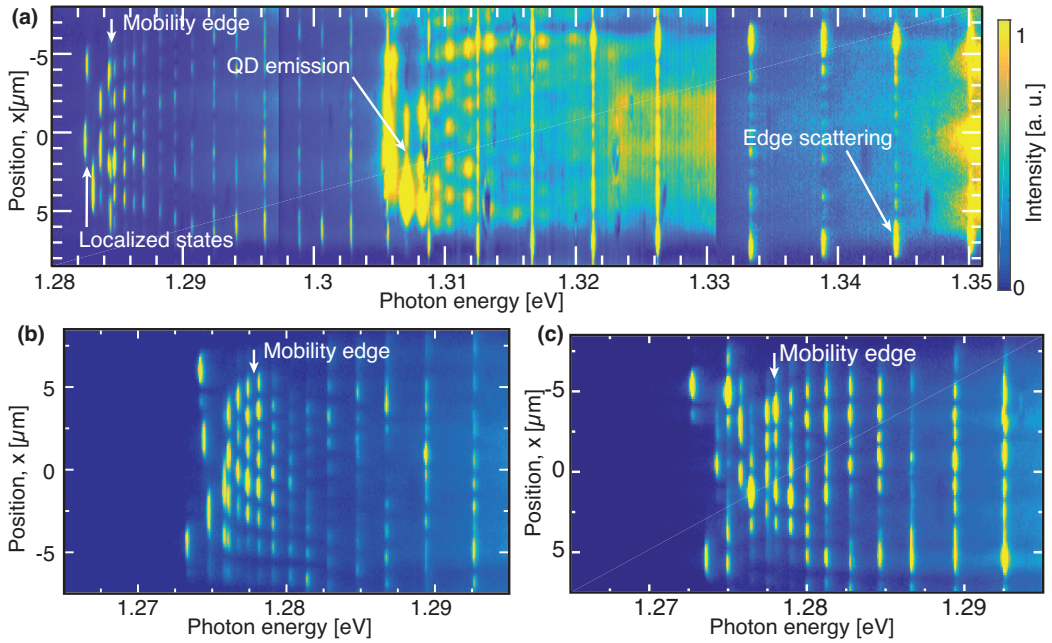

Figure 3.10 – (a-b-c) Three measured spectrally and spatially resolved image of L_{61} cavities; PhC hole radius: ($r = 61nm$ excitation power: $P = 500\mu W$, Temperature: T=10K).

disorder increases. Note that the energy shift between the calculated and measured photonic band edges in Fig. 3.9(b) and Fig. 3.10 is due to the 2D effective index approximation used in the model, which does not perfectly match real 3D cavities.

Above the mobility edge, disorder can affect the extended modes in two ways reminiscent of the 1D propagation of electron described by the Schrödinger equation [154].

A first effect is photon backscattering as illustrated by Fig. 3.9(b). At the cavity center, around 1.27eV, a scattering center leads to a higher intensity of the extended modes alternatively to the left and to the right.

The second effect is the effective index variations as illustrated by the FDM simulation shown on Fig. 3.9(d). An L_{61} cavity with $r = 59nm$, in which a $3.8\mu m$-long "defect" section was introduced, where the holes on both sides of the waveguide core had $r = 56nm$. The effective index is shown in green. In the portion with smaller effective index, the intensity is larger as a consequence of the higher group velocity, while the envelope function period is also increased by the value of k which is closer to π/a. These effects results from the energy shift of the waveguide bandstructure, itself a consequence of the effective index variations.

These two effects analogous to those observed for electrons in a 1D system can be interpreted in an energy landscape picture in which the energy is defined by the effective index [154].

3.3.1.3 Edge scattering in L_{61} cavities

The spectrally resolved image of high energy modes around 1.34eV on Fig. 3.10 shows a much higher collected intensity at the cavity edges. However, 2D-FDM simulated modes including disorder are almost indistinguishable from the disordelerless simulated cavity mode, and do not show this effect. Using 3D-FDTD, we will show that this is not a feature of the mode itself, but rather a consequence of the higher scattering at the edges in this particular cavity. The in-plane electric field of the M_{11} mode in an L_{33} was computed via 3D-FDTD (Fig. 3.11(c)). In this simulation, the PhC random gaussian disorder was implemented with $std(r) = 3nm$. Despite disorder, the mode is highly uniform, in agreement with 2D-FDM simulations of fast light modes.

The intensity collected by the lens, can be computed from the near field right above the slab [74]. This is realized by computing the angular spectrum of the electric field in a plane $\vec{E}(k_x, k_y, 0)$, obtained from the 2D Fourier transform in space of the electric field few nanometers above the slab. The electric field at any point of the upper plane can be deduced from [17]:

$$\vec{E}(x,y,z) = \int\int \vec{E}(k_x,k_y,0)e^{i(k_x x + ik_y y + k_z z)}dk_x dk_y \tag{3.21}$$

The condition $\sqrt{k_x^2+k_y^2+k_z^2} = \omega/c$ implies that the rapidly oscillating components outside the light cone defined by $\sqrt{k_x^2+k_y^2} > \omega/c$ have a imaginary k_z. These components are exponentially suppressed as the light leaves the slab. The intensity imaged by a lens collecting all the light escaping the slab is:

$$I(x,y) = \left[\int\int_{\sqrt{k_x^2+k_y^2}<\omega/c} \vec{E}(k_x,k_y,0)e^{i(k_x x + ik_y y)}dk_x dk_y\right]^2 \tag{3.22}$$

If we consider now the intensity collected by a finite apperture lens, the same equation applies, but with a smaller collection angle defined by: $\sqrt{k_x^2+k_y^2} < NA\cdot\omega/c$.

The computed collected intensity on Fig. 3.11(b) features a higher intensity at the edges similar to that measured on the three highest energy modes of Fig. 3.10. The same effect is observed on the computed escaping intensity 3.9(a), which indicates that although the mode is uniform throughout the cavity, the edge scattering is more intense than propagation scattering far from the band edge. This arises because disorder induced propagation losses increases with n_g and is therefore more important near the band edge [144]. This also indicates that the Q-factor of such modes could be optimized through a dedicated FDTD simulation of the leaky components as proposed by Nakamura et al. [72]. Indeed, the hole shifts at the edge of the L_{61} cavities corresponds to optimized hole shifts for the M_0 mode of L_3 cavities, but not for higher order modes in L_{61} cavities. In L_7 or L_3 cavities, the same effect was observed for the M_1 and other higher order modes.

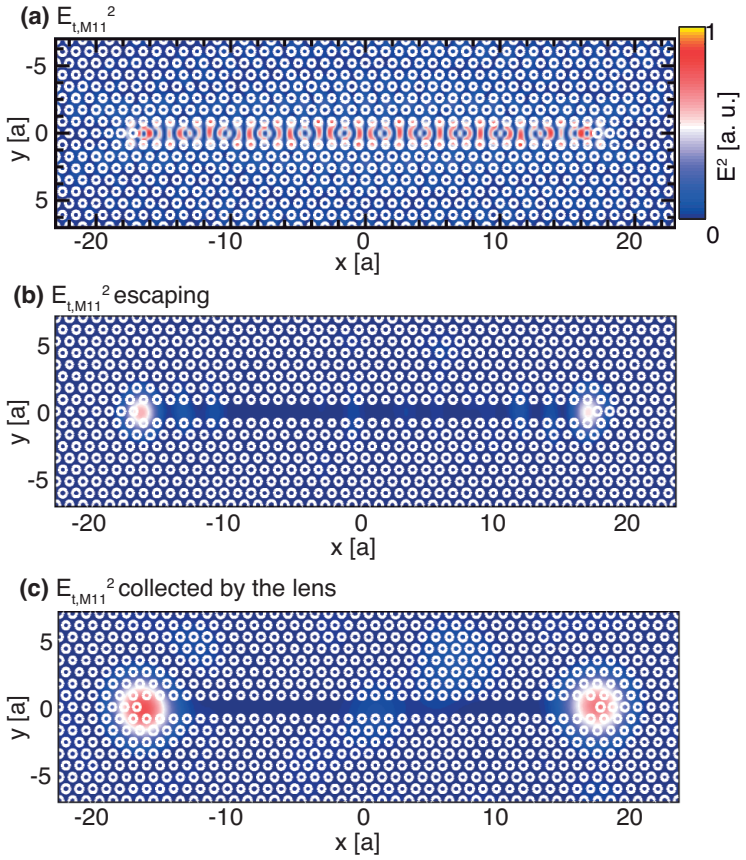

Figure 3.11 – FDTD computed in plane electric field intensity (mode M_{11} in an L_{33} cavity) of: (a) the near field. (b) the propagating waves; (c) the waves collected by the microscope objective; The simulation parameters are: $a = 225nm$, $r = 61nm$, $n = 3.46$, slab thickness: $th = 250nm$, $NA = 0.55$, disorder was included with: $std(r) = 3nm$. FDTD simulated mode M_{11} energy: 1.405eV, band edge energy: 1.273eV.

3.3.2 Waveguide dispersion in L_n cavities

Disorder can also affect the dispersion of PhC waveguides. In the absence of disorder, the waveguide modes give rise to FP resonances with wavelength spacing related to the group index by 3.7. Mode localization would yield a mode spacing that is not related to this expression but is rather determined by the random features of the localizing effective index profile [121]. In the inset of Fig. 3.12(a) we compare the simulated group index in the L_{61} structure without and with disorder.

In the absence of disorder, for this particular waveguide mode, the cavity modes spacing decreases with decreasing energy, and the group index increases indefinitely when the PhCW band edge is approached (inset of Fig. 3.12(a)). In the presence of disorder, regular slowing down of light due to the increase in the 1D PhCW density of state sustains up to n_g ~30 above which the calculated parameter n_g starts fluctuating

randomly.

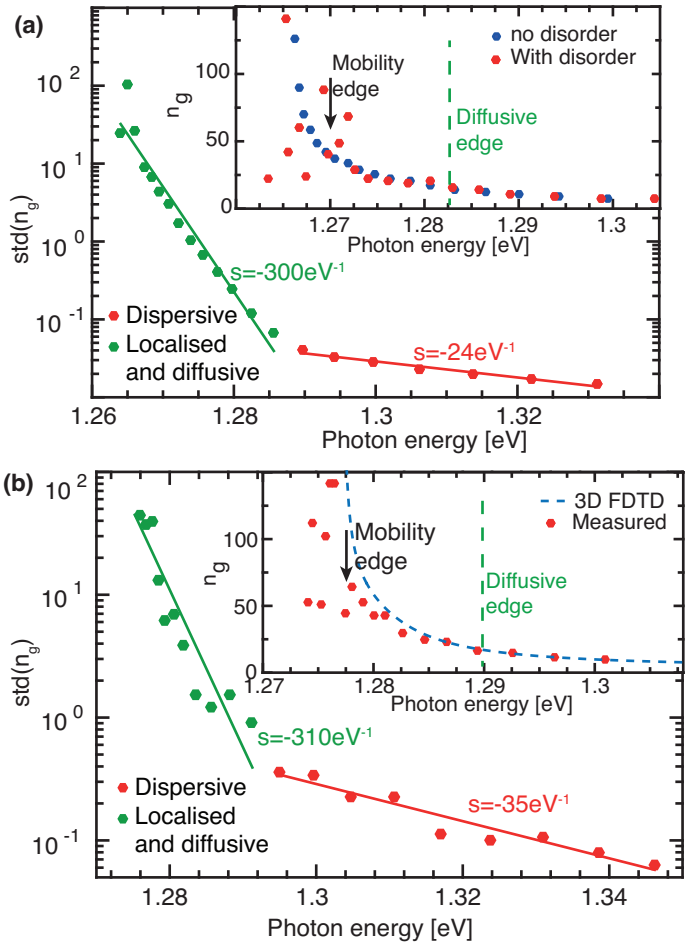

Figure 3.12 – (a) $std(n_g)$ computed by FDM over 500 simulations (a=225nm, r=61nm, n2D=3.13, $std(r) = 3nm$); Inset: Group index in an L_{61} cavity computed by 2D-FDM without disorder and with disorder ($std(r) = 3nm$); (a=225nm, r=61nm, n2D=3.13); (b) $std(n_g)$ measured with 18 similar L_{61} cavities (a=225nm, r=61nm, Excitation power: P=500μW, temperature: T=10K); inset: measured group index in an L_{61} cavity; the blue line corresponds to the group index of a perfect W1 waveguide computed via 3D FDTD ($n_{3D} = 3.4638$, a=225nm, r=61nm), blue-shifted by 9meV to fit the measurements.

This energy range corresponds to the localized and the diffusive regimes as described by L. Thomas et al. [149], while the higher energy range in which the regular increase in n_g permits the measurement of a well-defined dispersion relation is the dispersive regime. The same behavior is observed in the measured group index of a typical L_{61} structure (inset of Fig. 3.12(b)). The highest group index is limited in these structures to ≈ 30 below which n_g follows its FDTD simulated value (in blue) until fluctuations start being observed. This FDTD computation defines a theoretical band edge where the fitted group index becomes infinite. We note that the assignment of

"group indexes" at energies below those showing the regular dispersion is physically meaningless as the light does not propagate anymore according to the simple FP model from which it is measured.

In that prospect, 500 2D-FDM simulations of L_{61} with different realizations of disorder permitted the estimation of the group index standard deviation variation with energy as measured from the free spectral range of each mode. These standard deviations were plotted on Fig. 3.12(a). The energy attributed to each point is the average energy of the nth mode (labeled by increasing energy) for which the standard deviation is calculated. These variations of n_g underline two different regimes. Near the band edge, where $std(n_g)$ increases rapidly and beyond 1.288eV where this increase is much slower. This energy determines to the edge of the diffusive zone, where scattering diffuses the wavevector k, as was shown by k-space analysis of transmission in PhCW [149]. Beyond this diffusive edge, in the dispersion zone, the group index is determined by the dispersion relation.

Experimental measurements in L_{61} cavities show a similar behavior. The group index standard deviation was measured on 18 identical L_{61} cavities. To account for local variations of fabrication, each group index relation was shifted in energy such that their band edges are the same. The group index standard deviation $std(n_g)$ is plotted on Fig. 3.12(b). Similar to simulated results, $std(n_g)$ increases more steeply below $1.29eV$. These results indicate a diffusive edge 15meV above the lowest order mode. The diffusive zone located between the localized and the dispersive zones therefore spans $\approx 10meV$.

3.3.3 Site controlled QDs for probing the local density of modes

3.3.3.1 Probing photonic modes near the band edge

Fine scale features of the spatial distribution of localized and propagating modes can be analyzed in greater details by exciting optical modes with single, site-controlled QDs. Indeed, the small QD size provides an effective spatial resolution of 20nm. The precision in positioning corresponds to the precision in our alignment of the PhC hole templates with respect to the pyramidal QDs, which we confirmed to be better than 25nm. To illustrate this approach, we first repeated the spectrally resolved measurement of L_{33} cavity modes by exciting the cavity with a single pyramidal QD positioned at the cavity center. In disorderless cavity modes, the QD overlap with the antisymmetric modes is exactly zero as emphasized by the FDM simulations of Fig. 3.13(a). These simulations justify the weak intensity of these modes on the spectra and spectrally resolved image of Fig. 3.13(b-c). The still observed antisymmetric lines indicate the presence of small mode distortions near the band edge.

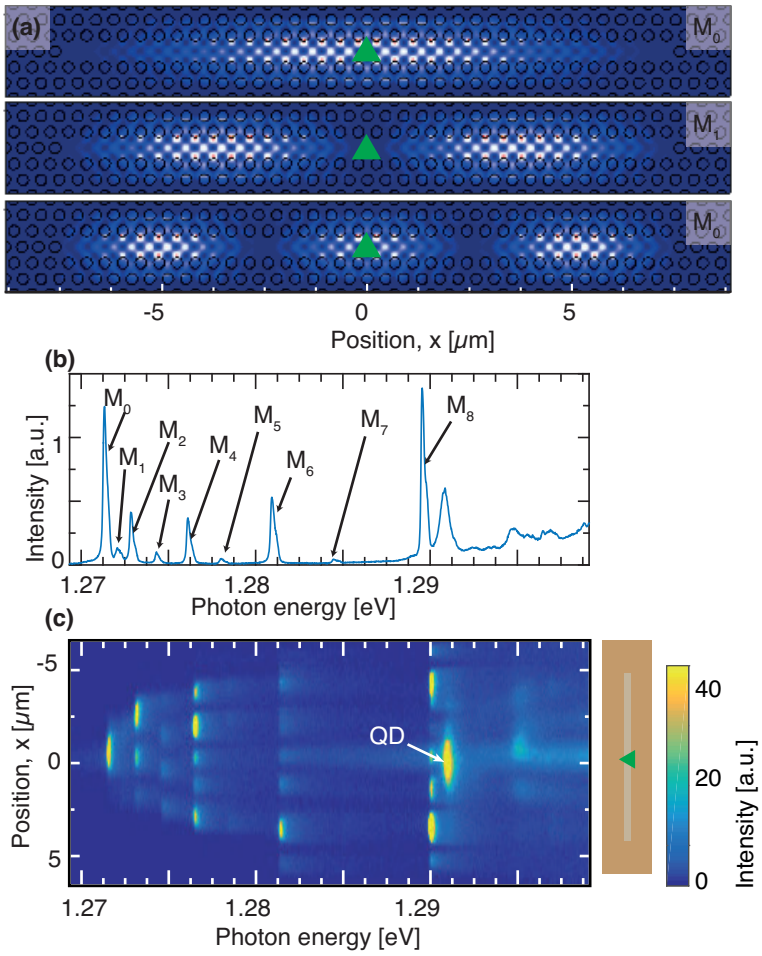

Figure 3.13 – (a) Calculated mode patterns for a disorder-free structure (2D FDM simulations with: $a = 225nm$, $r = 61nm$, $n_{2D} = 3.13$) with indication of QD position (green triangles). (b) Measured PL spectra with spectral positions of modes identified. (c) Measured spectrally resolved pattern (excitation power: $P = 500\mu W$, Temperature: $T = 10K$).

3.3.3.2 In situ probing of the diffusive and dispersive regimes

Site controlled QDs do not only show the weak mode localization in small enough L_n cavities, but also permit an alternative identification of the diffusive edge. On Fig. 3.14(a-c), the spectra obtained by exciting three isolated QDs placed at x=0, 4.5 or -4.5μm with a high pump power. This distance is sufficient to ensure the selective excitation of only one QD at a time. The mobility edge, which is typically 5meV above the lowest order mode, is shown at 1.268eV by a black arrow. As opposed to cavities with a uniform excitation, the FP modes show a modulation by an envelope function indicating variations of the QD and FP mode overlap. This assumption is validated by the 2D-FDM simulation of the normalized intensity of FP modes at the QD position in a disorderless L_{61} cavity displayed as green dots.

When the central QD is pumped (Fig. 3.14(b)), in the blue part of the spectra only modes symmetric along the x direction are excited. The antisymmetric peaks are not even visible, which simultaneously validate the excellent alignment of the PhC pattern over the QD array and the absence of distortions of FP modes. Fig. 3.14(e) shows the simulated spectra obtained by exciting a disorderless L_{61} cavity with a QD displaced from the cavity center along x by Δx. The simulation was performed via 2D FDM. The spectra were simulated by adding lorentzian lines for each simulated mode. The intensity of each lorentzian line corresponds to the overlap between the QD and the photonic mode. The QD displacement Δx induces an increase of the antisymmetric modes intensity observed on Fig. 3.14(e). The relative intensity between antisymmetric and symmetric modes in the spectra for a displacement $\Delta x = 20nm$ is already around 10 and would be visible in the experimental spectra of Fig. 3.14(b), which confirms that this structure exhibits an alignment between the PhC cavity and the QDs better than 20nm.

On the other hand, in the diffusive and localized regimes below 1.28eV, there are significant deviations between the calculated and measured mode intensities. This is also illustrated in Fig. 3.14(d), which shows the relative intensity of each FP mode when pumped by the QDs at $x = +4.5\mu m$ (left or l) or $x = -4.5\mu m$ (right or r) : $(I_l - I_r)/(I_l + I_r)$. Due to the modes symmetry, in the absence of disorder, this quantity should be exactly zero, but with disorder it may fluctuate widely. A transition from a very ordered energy range (blue part) to a disordered one (red part) is indeed observed. From these results, the diffusive edge is identified near 1.276eV, in line with the ~10meV measured previously. These measurements demonstrate that pyramidal QDs are useful as sub-wavelength, site-controlled broadband sources, which makes them ideal probes of the local DOS.

Chapter summary

In this Chapter, ensembles of QDs embedded in L_n cavities were used to study the impact of disorder on light propagation in PhC waveguides.

First, propagation losses and reflection coefficients in long L_n cavities simulating PhCWs were measured. Increasing propagation losses at shorter wavelengths were attributed to GaAs band tail absorption. A sharper increase at higher wavelength was interpreted as a sign of scattering to the radiation modes enhanced by slow light near the band edge. These results lead to a deeper understanding of the main loss channels in L_n cavities.

In a second part, the impact of disorder in PhCWs was measured via three complementary methods. Through spectrally resolved imaging of the modes, we clearly identified the mobility edge that separates the spectral zones of delocalized and lo-

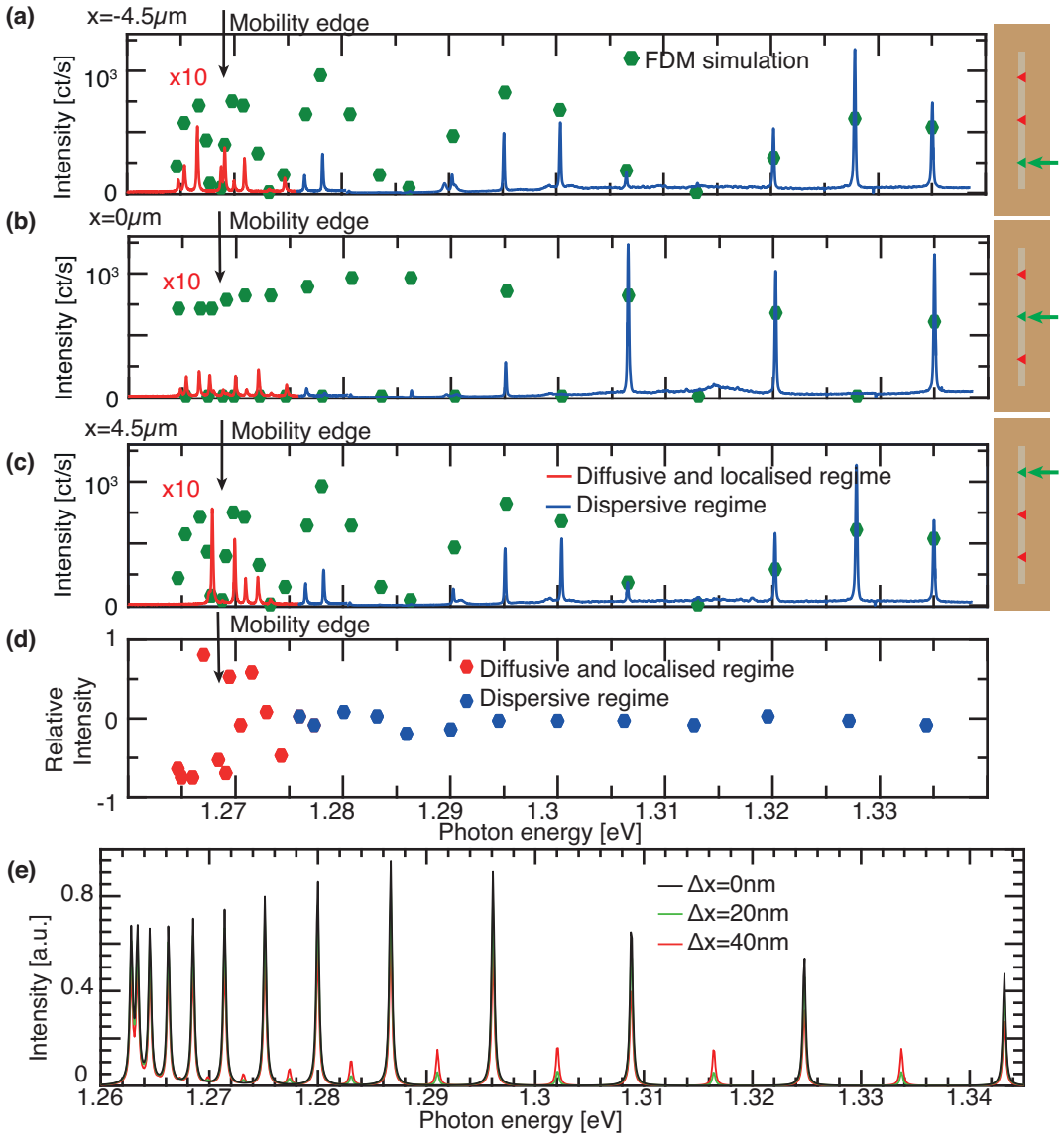

Figure 3.14 – (a-b-c) Selective excitation with single-QDs in the fast light regime in L_{61} cavities. The green circles represent the overlap between the QD and the in-plane component of the mode intensity of each mode computed with 2D FDM. The sketches on the right show the position of excited QDs as a green triangle. (excitation power: $P = 500\mu W$, Temperature: $T = 10K$, $r = 61nm$); (d) Measured relative intensity of each modes when QDs on the left or on the right are pumped: $(I_l - I_r)/(I_l + I_r)$. The black arrows indicate the limit of the mobility edge; (e) FDM simulations of spectra obtained by exciting a disorderless L_{61} cavity with a QD displaced from the cavity center along x by Δx. ($n_{2D} = 3.13$, $a = 225nm$, $r = 61nm$)

calized modes. This technique also permitted the identification of scattering at the edges of L_{61} cavities indicating insufficiently optimized reflectors. In addition, we used group index measurements and site-controlled QD excitation to identify the limit between diffusive and dispersive regimes of light propagation. The dispersive regime was characterized both by distortions of the envelop function and a highly irregular dispersion. Although photons in this spectral range can be transported across the waveguide channel, they suffer from scattering manifested by random phase variations in the wavefunction. On the contrary, selective excitation highlighted the weak disorder of modes in the dispersive regime and demonstrated the potential of site-controlled QDs for probing the local DOS in photonic structures.

More generally, these observations should be helpful in finding ways to reduce detrimental effects of photon localization and design optimal integrated photonic circuits.

4 QDs coupled to PhC waveguides

IN recent years, significant efforts were realized towards the monolithic integration of QDs in waveguides, with the objective of obtaining high efficiency on chip single photon sources. One recurrent insight guiding these efforts was the objective of obtaining on chip reproducible and deterministic single photon emission. In recent publications, Stranski-Krastanov QDs were coupled with a broadband high coupling efficiency to PhC waveguides [107, 167, 106, 105, 168, 104]. Beyond single photon sources, the recent publication of directional coupling of SK QDs in chiral waveguides [103, 102] and nonlinearity at the single photon level [101] emphasizes the potential of QDs in PhCs to fabricate on chip quantum gates. However, the analysis of such structures is complicated by the lack of control over the position of QDs. Indeed, the measured properties may not give a faithful picture of the statistical behavior of QDs in such systems [104]. Besides, the coupling relies on a probabilistic approach: it is only a proof of concept for single QDs but it cannot be scaled to many QDs and will exhibit significant statistical variations for similar structures.

Scalability and reproducibility of photonic circuits both require a good spectral and spatial matching of the QDs and the photonic modes. In this context, site-controlled QDs in waveguide offer a remarkable potential. Indeed, the spatial matching is ensured by the accurate QD positioning and the spectral matching is made possible by the broadband photonic environment of a waveguide.

In this chapter, we demonstrate the first integration of five site-controlled QDs all coupled to a waveguide and the corresponding on chip single photon transfer over macroscopic distances. Using time resolved photoluminescence (TRPL) measurements, we infer the coupling efficiency of these QDs to waveguides and give optimal conditions to reach a reproducible, broadband coupling efficiency. We then show how a short slow light section could be harnessed to increase this coupling efficiency without any manifestation of Anderson localization.

4.1 Integrating QDs in a PhC semi-waveguide

4.1.1 Design of the structure

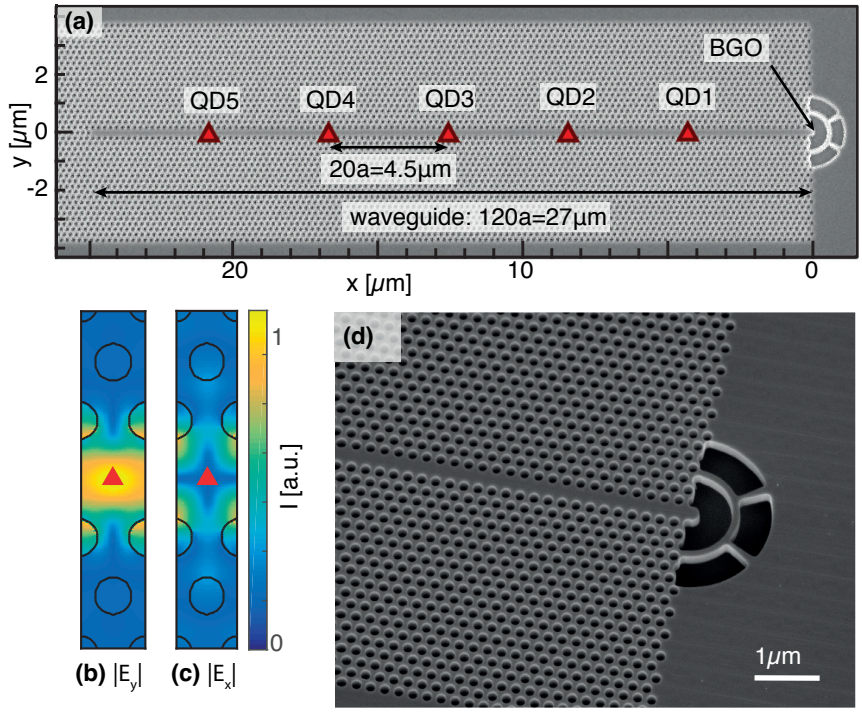

Figure 4.1 – Presentation of the integrated QD-PhC system investigated: (a) SEM image of a 27µm long semi-waveguide, the red triangles indicate the QD positions; (b, c) y and x components of the electric field amplitude of the lowest confined band in a W1 waveguide computed by 2D FDM; ($n_{eff} = 3.18$, $r = 61nm$, $a = 225nm$, $k = 0.3[2\pi/a]$); (d) SEM image of the coupler (tilted view).

The first structure studied in this chapter consists in a $27\mu m$ waveguide in which five QDs are embedded and equally spaced by $4.5\mu m$ as shown on Fig. 4.1(a). This spacing ensures that each QD can be photo-excited independently. The five QDs were placed at the maximum intensity of the y component of the Bloch mode electric field in a W1 waveguide as shown in Fig. 4.1(b-c). This position ensures an optimal coupling to the waveguide band. At the edge of these cavities, the three holes adjacent to the waveguide row were shifted respectively by 0.23a, 0.15a and 0.048a. These hole shifts were optimized by Minkov et al. [73] to ensure a high Q-factor in L_3 cavities. As exposed in the previous chapter, this reflection is optimized to be maximal at the M_0 mode energy of L_3 cavities. In this chapter the terminations are assumed to behave as a perfect reflector. The other end of the waveguide is terminated by a two-period circular Bragg grating outcoupler with a 950nm period. With such a

periodicity, this Bragg grating exhibits a vertical first diffraction order at 950nm, which is then easily collected with a microscope objective. The small number of periods ensures a broadband outcoupling and a coupling efficiency as high as 30% to our 0.55 numerical aperture objective [104].

4.1.2 A Fabry-Pérot model for QDs in a PhC semi-waveguide

4.1.2.1 Spontaneous emission rate in a Fabry-Pérot semi-waveguide

As proposed by Yao et al. [153], the emission of light by a QD in a semi-waveguide is well described by a Fabry-Pérot (FP) model with a perfect reflector (100%) on one side, an amplitude reflection coefficient r on the other side, and no propagation losses. A sketch depicting this model is given on Fig. 4.2(d). The electric field eigen-mode with a wavevector k is given by:

$$\vec{E}_k = \frac{\sqrt{a/L_{eff}}}{1 - re^{ikLeff}} \left[\vec{e}_k(\vec{x}) e^{ikx} + \vec{e}_{-k}(\vec{x}) e^{-ikx} \right] \tag{4.1}$$

where L_{eff} is the effective length of light in the photonic crystal waveguide (PhCW), and $\vec{e}_k$ is the Bloch mode in a perfect W1 waveguide with a wavevector k and with the normalization:

$$max(\epsilon(\vec{x})|\vec{e}_k(\vec{x})|^2) = 1 \tag{4.2}$$

From which we can define the mode volume V and area A:

$$\int_{cell} \epsilon(\vec{x})|\vec{e}_k(\vec{x})|^2 dV = V = aA \tag{4.3}$$

Notice that these modes are exactly similar to those studied in Chapter 3 except for the normalization condition. The Green function describing the propagation of photons in a semi-waveguide is [153]:

$$G(\vec{x}, \vec{x}', \omega) = \frac{i\omega L_n}{2v_g} \vec{E}_k(\vec{x}) \otimes \vec{E}_k^*(\vec{x}') \tag{4.4}$$

The emission rate inside the PhCW mode is then:

$$\Gamma_{wg}(r_d, \omega_d) = \frac{2\vec{d} \cdot Im(G(r_d, r_d, \omega)) \cdot \vec{d}}{\hbar\epsilon_0} \tag{4.5}$$

Where $\vec{d}$ is the QD dipole moment. The emission rate when the QD is at the maxima of the Bloch mode reads:

$$\Gamma_{wg}(r_d, \omega_d) = \frac{\omega}{\hbar\epsilon_0 v_g A} |\vec{e}_k(r_d) \cdot \vec{d}|^2 \frac{1}{(1-r)^2} \frac{1}{1 + Fsin^2(\delta/2)} sin(kr_d)^2 \tag{4.6}$$

Where $\delta = 2kL$ is the FP roundtrip phase shift, r_d is the QD position with respect to the end of the semi-waveguide and F is the coefficient of finesse:

$$F = \frac{4r}{(1-r)^2} \tag{4.7}$$

F is related to the FP modes finesse by : $\mathscr{F} = \pi / \arcsin(1/\sqrt{F})$. The Purcell factor is finally obtained:

$$P_{wg} = \frac{3}{4\pi}\frac{n_g}{n}\frac{\lambda^2}{A}|\vec{e}_k(r_d)\cdot\vec{u}_d|^2\frac{1}{(1-r)^2}\frac{1}{1+Fsin^2(\delta/2)}sin(kr_d)^2 \tag{4.8}$$

Note that in the limit $r \to 1$, the Purcell enhancement is no more broadband but consists of discrete lines similar to those of long L_n cavities studied in Chapter 3.

4.1.2.2 The local density of states in a PhC semi-waveguide

The Purcell factor defines the position and wavelength-dependent coupling rate to the waveguide mode. Its understanding is therefore crucial to the fabrication of on chip single photon sources. The first three factors: the group index, the mode area and the Bloch function were already studied in the thesis introduction (see sections 1.3.2.2 and 1.4.2). The other terms in this equation are specific to semi-waveguides and modify the local DOS affecting the coupling of QDs to semi-waveguides. The Purcell factor P_{wg} for a QD placed at the maxima of the Bloch mode electric field at a distance $r_d = 15a$ from the semi-waveguide edge is plotted on Fig. 4.2(a). The coefficient of finesse defined by the coupler reflection is in this case F=8.

Contrary to the simple picture of an infinite waveguide, the LDOS is not broadband, but rather limited to discrete emission peaks corresponding to the FP modes formed by the reflection at each edges of the waveguide as described on Fig. 4.2(f). The exact behavior of these FP modes is defined by the term $1/(1-r)^2 1/(1+4r/(1-r)^2 sin^2(\delta_1/2))$. The inter-mode spacing or free spectral range is: $\Delta\lambda = \lambda^2/(2Ln_g)$ as emphasized in previous publications[104]. The finesse of these FP resonances is: $\mathscr{F} = \pi/arcsin(1/\sqrt{F})$. Besides, these FP peaks are more intense near the band edge because of the increase in group index indicated on Fig. 4.2(b).

The FP peaks are also modulated by a spectral envelope function similar to the one obtained in the last chapter when exciting L_n cavity modes with site-controlled QDs. This spectral modulation is caused by the $|\vec{e}_k(r_d)\cdot\vec{u}_d|sin(kr_d)^2$ term, which arises from the interference between light emitted by the QD directly toward the outcoupler and light emitted in the other direction. These two waveguide modes interfere with a kr_d phase difference, as depicted on Fig. 4.2(e). The frequency period of this envelope modulation is: $\Delta\omega = v_g\pi/r_d$: it is larger near the band edge as observed on Fig. 4.2(a) and when the QD is closer to the semi-waveguide edge.

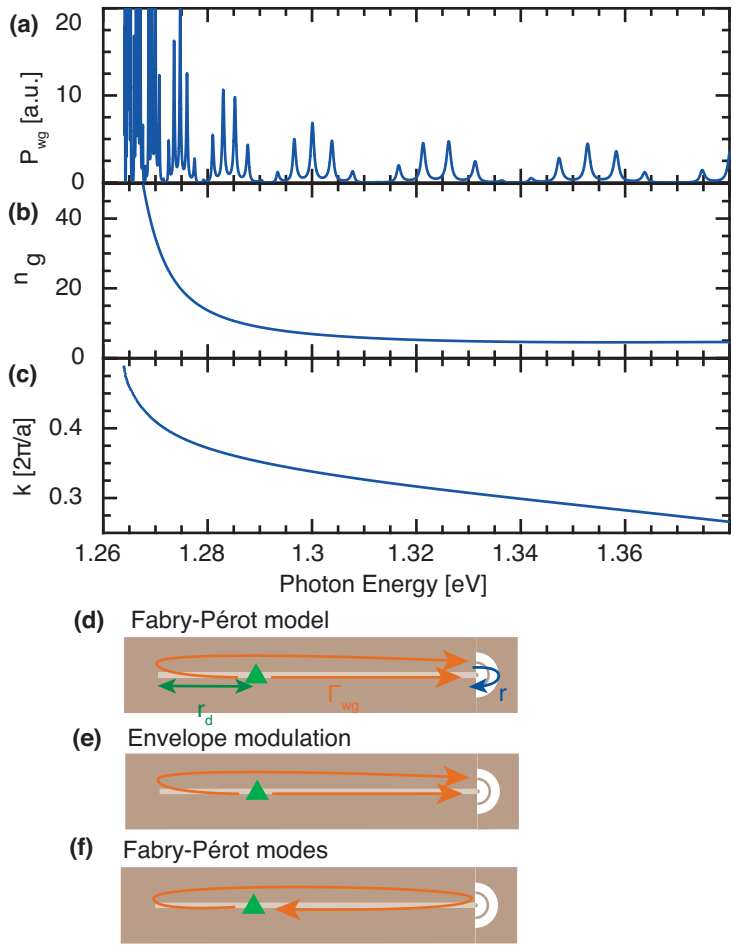

Figure 4.2 – (a) Purcell enhancement as computed from the Fabry-Pérot model, the QD to PhC edge distance is: $r_d = 15a$, the coefficient of finesse is F=8, the increase in DOS near the band edge is a result of larger group index); (b) Group index and (c) Dispersion relation in a W1 waveguide computed via 3D FDTD; (d) Sketch of the semi-waveguide model; (e-f) Sketches depicting (e) the envelope modulation and (f) the FP mode formation of the QD density of states. (the group index and dispersion relation used in all these figures were computed via 3D FDTD with the parameters: r=61nm, a=225nm, n=3.46, th=250nm)

4.2 site-controlled QDs coupled to a PhCW

In this section, the spectral properties of site-controlled QDs coupled to waveguides is analyzed. Our analysis will first concentrate on isolated QDs, then on the photonic modes in PhC waveguides. As a third step, the spectral properties of QDs coupled to semi-waveguides will be exposed.

4.2.1 Single QD properties

Although QDs show remarkable promises for on chip quantum optics applications, contrary to atoms, they are never perfectly identical because of differences in their size, composition and in the purity of the surrounding solid state matrix. These unavoidable differences are manifested through inhomogeneities of the optical spectra and resonance energies of each QD. In this context, pyramidal QDs are remarkably uniform and reproducible. Indeed, as determined by Jarlov et al. [53, 64], pyramidal QDs have the following spectral features:

- Mainly the X, XX and X^- lines are observed at low power excitation (below $5\mu W$) [133].
- The binding energy of the trion X^- , defined as: $E_{B,X-} = E_X - E_{X-}$ is around 5meV.
- The binding energy of the biexciton XX, defined as: $E_{B,XX} = 2E_X - E_{XX}$ increases with the exciton energy and can be either positive or negative.

On this basis, pyramidal QDs isolated in the PhC waveguide were studied here by means of PL spectroscopy so as to infer the properties of isolated QDs for the specific QDs used in this thesis. The PhC radii of the selected waveguides were r=75.5n, 77.5nm and 80nm, such that the PhC band edge lies near 930nm and the QDs emit in the PhC bandgap. Low power excitation spectra of 10 QDs isolated in the PhC bandgap are shown on Fig. 4.3(a). The spectral properties, inferred by Jarlov et al. [53], were used to attribute QD spectral lines to their respective confined excitons. These attributions will be confirmed later by an in depth analysis of one specific QD example. Notice that in most spectra, the X^- line is more intense than the other lines at this excitation level. We attributed this effect to a residual n-type doping of the GaAs material.

The X^- lines were fitted on 21 spectra of isolated QDs, from which we obtained the standard deviation of the QD X^- energy distribution: std(E)=5.7meV. Assuming a gaussian distribution of the trion energies, the FWHM of this distribution is 13.4meV, slightly lower than the 16.9meV fitted on the QD ensemble of the same sample in the precedent Chapter. This “artificial” broadening is caused by the non-zero binding energy between different QD lines. In larger pyramids, the record value of 1.4meV inhomogeneous broadening (individual X lines) for site-controlled QDs was achieved [54]. Such low inhomogeneous broadening, difficult to achieve with more standard techniques such as SK QDs [42], may prove crucial for the integration of several QDs in photonic circuits where tuning mechanisms (for example using the Stark effect) are usually limited to few meV [169].

The spectra of 32 QDs were obtained in a $20\mu eV$ resolution spectrometer. Each spectral line was fitted with lorentzians (inset of Fig. 4.3(b)), from which we obtained

the histogram of excitonic lines FWHM of Fig. 4.3(b). A skewed gaussian was fitted on this histogram to compare the properties of QDs before and after fabrication of the PhC and measure possible quality degradation of the excitons linewidths:

$$f(x;\mu,\sigma,\lambda,A) = A\frac{\lambda}{2}e^{\frac{\lambda}{2}(2\mu+\lambda\sigma^2-2x)}erfc\left(\frac{\mu+\lambda\sigma^2-x}{\sqrt{2}\sigma}\right), \tag{4.9}$$

The fitted parameters including the distribution mean $\mu+1/\lambda$ and its standard deviation $\sqrt{\sigma^2+1/\lambda^2}$ were:

	μ [μeV]	σ [μeV]	$1/\lambda$ [μeV]	$\mu+1/\lambda$ [μeV]
Before PhC etching	39 ± 4	4.5 ± 4	45 ± 12	84 ± 28
After PhC etching	46 ± 5	<19	58 ± 16	103 ± 42
	$\sqrt{\sigma^2+1/\lambda^2}$ [μeV]	Median [μeV]	Lowest FWHM [μeV]	
Before PhC etching	45 ± 26	71	28	
After PhC etching	58 ± 38	88	30	

As a conclusion, we observe a small degradation of the linewidths of QDs probably caused by the additional electronic surface states created by drilling the PhC holes. These surface states may be suppressed by an appropriate chemical surface treatment as was proposed in recent publications [170].

We will now focus on the analysis of one single QD isolated in the bandgap of a PhC waveguide. The vertically and horizontally polarized components of its PL spectra are shown on Fig. 4.4(a). As observed in previous studies, far detuned from any photonic modes, the QD lines are unpolarized [118]. Each line was attributed to its excitonic species according to the spectral properties inferred in [53]. The binding energies of each excitonic species (with respect to X) measured on the spectra are: $E_{B,X-} = 4.4meV$, $E_{B,XX} = -2.3meV$, $E_{B,X*} = 6.2meV$, which matches well the study of Jarlov et al. [53]. Note that the line X^* was not observed in [53], however as is shown later this transition exhibits a zero fine structure splitting. According to Kramers theorem, this feature suggests this exciton is composed of three fermions. Besides, its rather large binding energy suggests that it is an excited trion. These attributions will now be confirmed by two complementary techniques.

The first one is the excitation power dependence shown on Fig. 4.4(b). The intensity of each excitonic species transition is given as a function of the exciting power. In line with previous results [118, 53], the log of theses intensities increases linearly with the log of the power up to a saturation power where it reaches a maximum intensity. The slope of the exciton ($p_X = 0.69$) is lower than the one of the trion ($p_{X-} = 0.96$), itself lower than the one of the biexcitons ($p_{XX} = 1.99$), which confirms the attribution of these lines [109]. Besides, the saturation power of the exciton is lower than that of the biexciton, as expected because a biexciton is formed only when an exciton enters the QD while another exciton is already confined in it, which is more

probable at high excitation power.

As described in the inset of Fig. 4.4(a), the exciton consists of two bright states, splitted by the fine structure splitting (FSS) because of asymmetries of the QD confinement potential [55]. As an observable consequence, the exciton and biexciton emissions will each be composed of two orthogonally polarized lorentzians. On the contrary, the two trions do not exhibit FSS because they are made of an odd number of fermions which has to be doubly degenerate because of time reversal symmetry.

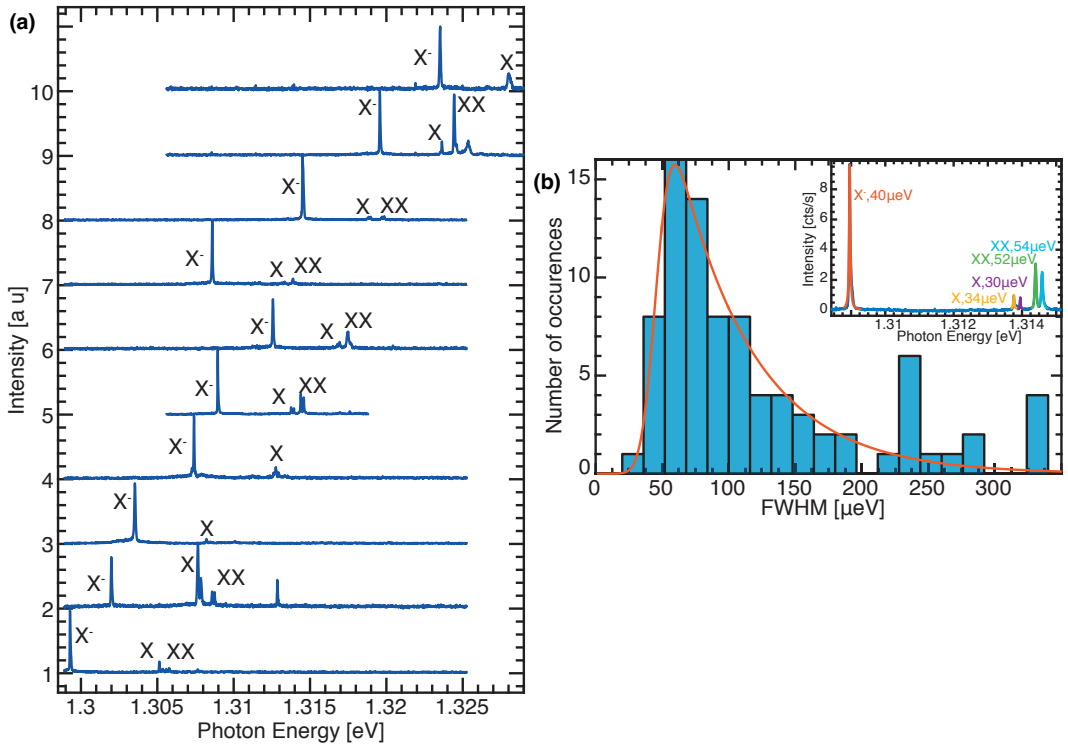

Figure 4.3 – Isolated QD properties: (a) Isolated QD PL spectra (Excitation power: P=1µW, T=10K); (b) Histogram of excitonic lines FWHM (Excitation power: P=1µW, T=10K spectral resolution : $20\mu eV$); All these measurements were performed on sample 5326 (see Appendix B) after the PhC fabrication.

The polarization-resolved measurements of each excitonic peak are displayed on Fig. 4.4(c). One QD spectrum was collected for each value of the polarization angle θ. Each excitonic line was fitted with a lorentzian. The fitted energy shift $\Delta E = < E > - E_{fitted}$ is plotted on Fig. 4.4(c) where $< E >$ is the peak energy averaged over all polarization and E_{fitted} is the fitted peak energy. As expected the trions are not polarized i. e. the peak emission energy is polarization independent. On the contrary, the emission energy of X and XX oscillates as a function of the polarization orientation. The polarization dependences were fitted with a sine function: $\Delta E \rightarrow A \cdot sin(\theta - \theta_X)$, where the FSS is given by $FSS = 2A \cdot sign(sin(\theta - \theta_X))$ [56]. The FSS fitted

on the exciton and biexciton lines are: $FSS_X = -125 \pm 9\mu eV$ and $FSS_{XX} = 145 \pm 11\mu eV$. These two values should be exactly equal as they each correspond to the energy splitting between the two bright excitons. This is indeed the case within the error-bars. The direction of polarization of these two splittings as defined in the inset of Fig. 4.4(c) are : $\theta_X = 28 \pm 2°$ and $\theta_{XX} = 121 \pm 2°$. As expected these splittings are orthogonal.

These measurements confirm the attribution of excitonic lines and the validity of the results of Jarlov et al. for TEGa-based QDs [53] emitting at longer wavelengths.

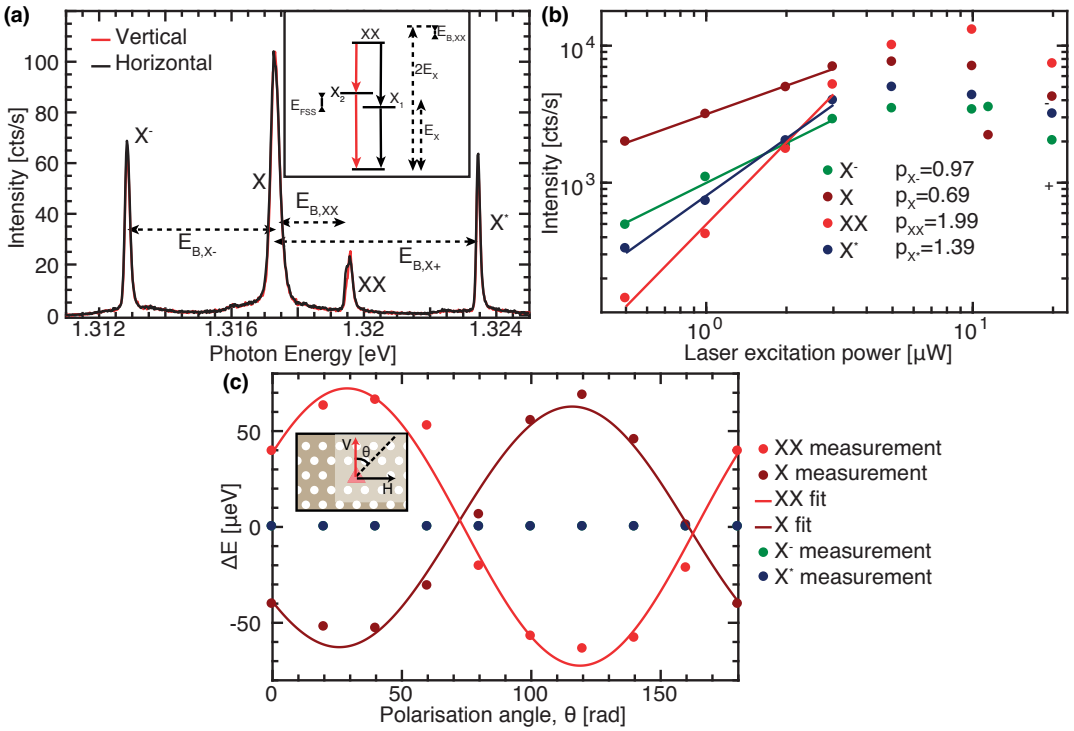

Figure 4.4 – (a) Horizontally and vertically polarized PL spectra of a single QD (Excitation power: P=2µW, T=10K); Inset: Biexciton-Exciton cascade; (b) Power dependence of each line (T=10K); (d) Polarization dependence of each line (Excitation power: P=2µW, T=10K); Inset: QD in an L_3 cavity, the arrows indicate the horizontal and vertical directions; (PhC hole radius: r=73nm).

4.2.2 Photonic modes in semi-waveguides

This section focuses on the experimental study of the photonic modes in semi-waveguides. A significant insight into the behavior of photonic modes in this system is obtained via the spectrally resolved imaging technique exposed in Chapter 2. The QD closest to the reflector of a semi-waveguide (see QD5 on Fig. 4.2(f)) was excited at high power ($P = 5mW$) for which it emits a broadband continuum [96], which is used to probe the modes of the semi-waveguide. The spectrally resolved picture is shown on Fig. 4.6(a). The excited QD is highlighted on the right as a green triangle. This QD

emits a broadband continuum, including the QWR emission tail. From 1.28eV and 1.37eV, modes propagating along the waveguide are visible due to some out-of-plane scattering. These modes then reach the coupler from which most of the light is extracted. Below the mobility edge at 1.285eV, the light does not propagate anymore because of disorder which causes Anderson-like localization of the light modes as made explicit in Chapter 3. These localized modes are observed on the spectrally resolved picture at the position of the QD between 1.27 and 1.28eV. Notice that the the localization length increases with energy as demonstrated in previous publications [171].

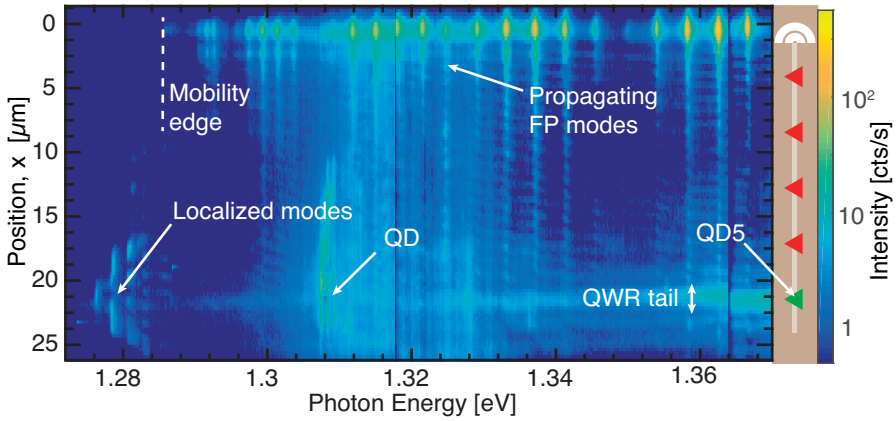

Figure 4.5 – Spectrally and spatially resolved picture of a semi-waveguide (Excitation power: P=5mW, T=10K, r=61nm, only QD5 in green in the sketch is excited).

Above the mobility edge (E>1.285eV), discrete modes are observed instead of the continuum expected in an infinite, perfect W1 waveguide. The spectra extracted from the outcoupler when exciting QD 3-4 and 5 are plotted on Fig. 4.6(a). The similarity between the Purcell factor plotted on Fig. 4.2(a) and the spectra of QD5 demonstrates both the validity of the FP model and the possibility to probe the LDOS with site-controlled QDs. These spectra feature both the predicted FP modes and the envelope modulation characteristic of excitation schemes by a point like probe. As shown in Chapter 3, PhC FP modes can be labelled by their number of lobes: the most confined mode has one lobe, the second has two lobes and mode p has p lobes. The wavevector of mode number p is: $k_p = \pi(1/a - p/L)$. As shown in section 3.1.1, the beating between the Bloch mode and the envelope function induces an spectral envelope modulation given by: $sin^2(\pi r_d p/L)$ when the QD is placed at the maxima of the Bloch mode (see Fig. 4.1(b-c)). The function $E \rightarrow sin^2(\pi r_d p(E)/L)$ is plotted in green for each positions: $r_d = 4.5\mu m$, $9\mu m$ and $13.5\mu m$, with the length of the waveguide: $L = 27\mu m$. The FP peaks modulation follows closely the predicted envelope modulation in the energy range from 1.305eV to 1.38eV which corresponds to the dispersive regime analyzed in Chapter 3. This regular periodicity is broken in

the red part of the curve, which corresponds to the diffusive regime in between the dispersive regime and the localized modes zone. Close to the mobility edge, the light spectrum extracted from the coupler do not exhibit any FP mode, but is continuous. This effect is caused by the slow-light related increase of losses near the band edge: when the free propagation distance becomes of the order of the waveguide length, the interference effect responsible for the creation of FP modes is cancelled. Note that QD3 placed at the center of the waveguide (lower spectra) excites only one mode out of two which in line with Chapter 3 demonstrates the weak disorder of waveguide modes in the dispersive regime.

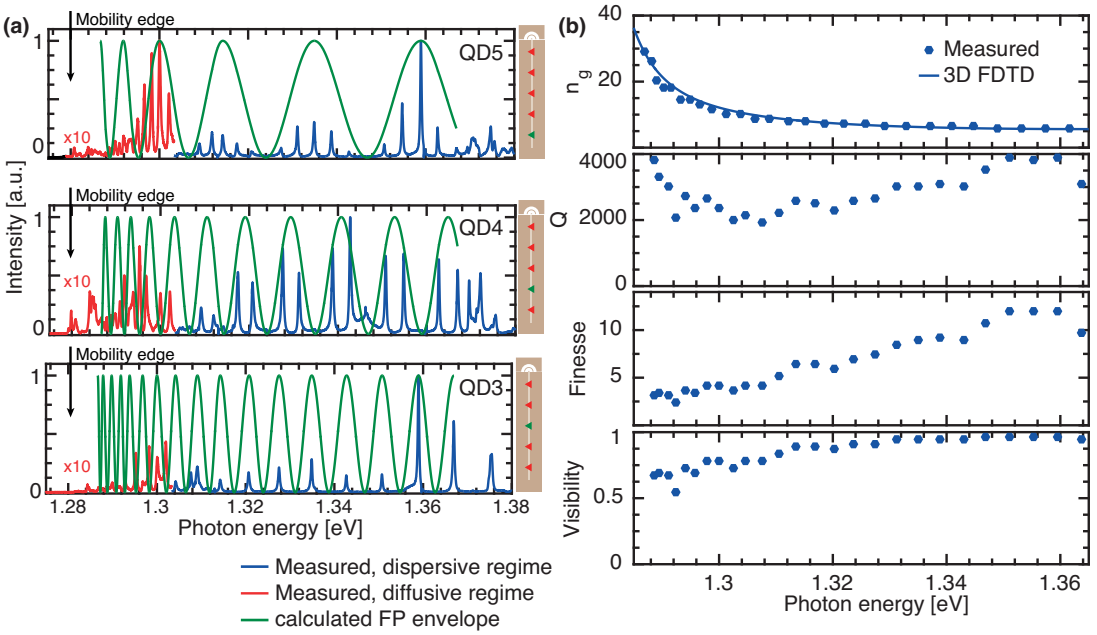

Figure 4.6 – (a) High power excitation spectra of three different QDs in the semi-waveguide (P=500uW, T=10K). The green line is the envelope modulation predicted by the FP model for semi-waveguides. It is given by: the function: $E \rightarrow sin^2(\pi xp/L)$ with the positions of the QDs: $x = 4.5\mu m$, $9\mu m$ and $13.5\mu m$ and the length of the waveguide: $L = 27\mu m$. (b) group index, Q-factor, Finesse and visibility of the FP modes (blue dots), the blue line is a 3D FDTD modeling of the group index (n=3.46 r=61nm, a=225nm, slab thickness=250nm; the simulated group index was blue shifted by 11meV to match the measured waveguide dispersion) ;

The group index of the waveguide shown in Fig. 4.6(b) is deduced from the free spectral range between FP modes (Section 3.1.1). It matches well the group index predicted by 3D FDTD simulations. The highest group index measured in this $27\mu m$ long waveguide is 30, which represents an upper bound on the slow light induced light matter interaction enhancement achievable in these waveguides (free of localization effects). The Q-factor of each FP modes given on Fig. 4.6(b) gives access to the

finesse and visibility of the modes also shown on Fig. 4.6(b), where the visibility is given by $2r/(1+r^2)$. The propagation related Q-factor Q_p of a $27\mu m$ cavity with perfect reflectors at each ends in the fast light regime ($n_g = 6$) can be predicted by the loss model exposed in section 3.2.2: $Q_p \approx 8000$. This value is close enough to the measured Q-factors to infer that between half and a quarter of the losses in these waveguides are not via the outcoupler, but rather propagation losses. However, the measured propagation loss coefficient in the fast light regime was $\alpha_p = 5 \cdot 10^{-3} \mu m^{-1}$, from which a $200\mu m$ free propagation length is inferred. Photons do propagate with weak losses through the whole waveguide. However, the high reflection coefficient of the outcoupler induces a recycling of photons which increases the proportion of propagation related losses compared to the photon extraction through the couplers. The measured Q-factor goes through a minimum near 1.3eV. The increase at lower energy is easily interpreted as a consequence of the increase in the group index. The increase of Q at high energies is less easy to explain, but may be related to a wavelength dependent reflection by the coupler. The visibility and finesse shown on Fig. 4.6(b) both decrease at low energy, because of increased loss near the band edge.

4.2.3 Single photons propagating in a PhC waveguide

In this part, we build on the properties of individual QDs and semi-waveguides discussed earlier, to study the spectral properties of QDs coupled to a semi-waveguide.

4.2.3.1 Single photon routing

Spectrally and spatially resolved imaging permit a comparison between the emission of a QD in free space and its emission through the cavity mode. Indeed, contrary to QDs in PhC cavities where the spectra of the QD and the cavity on resonance are intertwined and cannot be distinguished [172], the emission through the waveguide can be collected through the coupler, while the free space QD emission is observable directly at the QD position. The spectrally resolved picture obtained when exciting each of the 5 QDs in a PhC waveguide are shown on Fig. 4.7(a) (intensity on log scale). Each of these pictures was acquired from the same PhCW with r=58nm such that the photonic mobility edge was located at 1.285eV. The light emission from the single QDs and its collection from the coupler is visible. Some propagation scattering is also observed between the QD and the coupler. These spectrally resolved pictures demonstrate the possibility to multiplex several QDs in a single waveguide by exciting each QD separately and channelling their light to the coupler.

Fig. 4.7(b) displays the spectra emitted by QD5 through the radiation modes and through the waveguide. Each spectrum was obtained by integrating the signal on the spectrally resolved diffraction pattern over $4\mu m$ at the respective positions of the QD and the coupler. The spectra collected at the QD position (blue curve on Fig. 4.7(b))

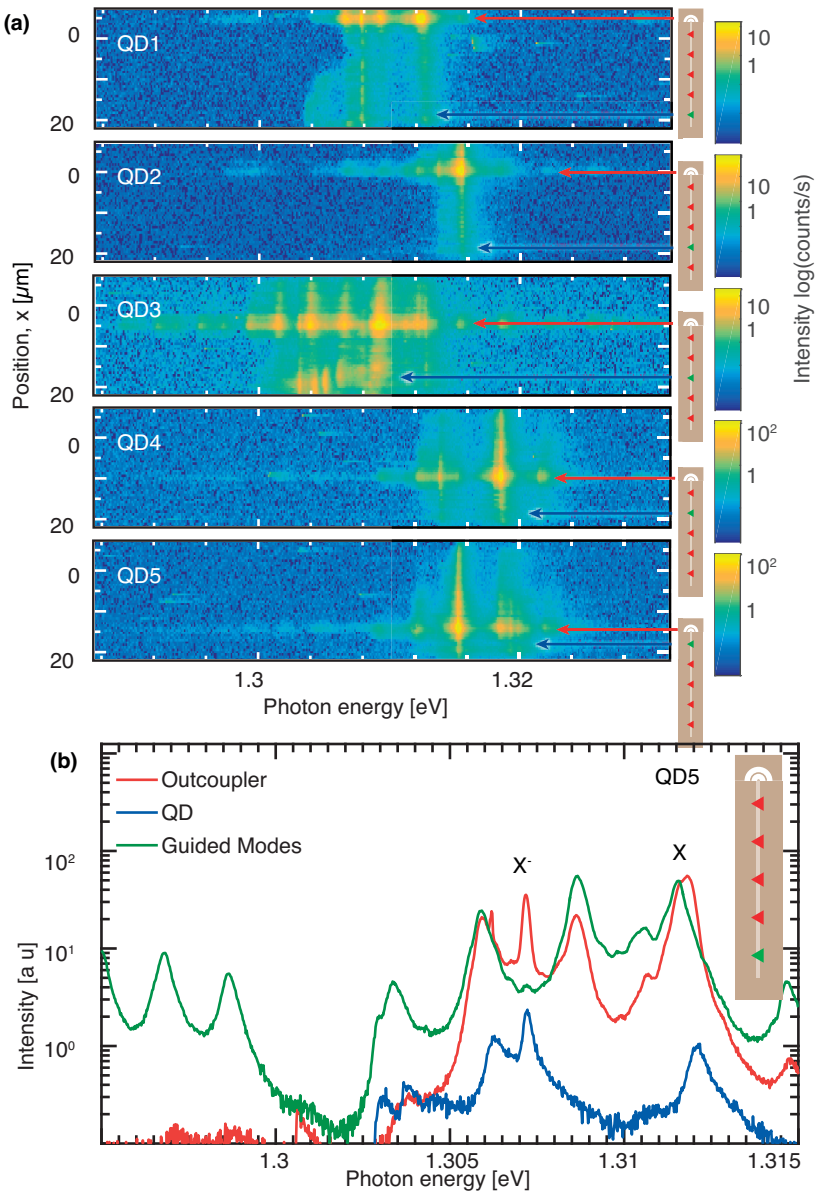

Figure 4.7 – (a) Spectrally resolved image of 5 single QDs. The red and blue arrows point to the output of the coupler and the QD; (b) Low power spectra of QD1 collected at the QD position (in blue) and at the coupler position in red ($P = 5\mu W$, $T = 10K$), and high power spectra at the coupler position (in green) ($P = 500\mu W$, $T = 10K$). These measurements were all acquired in the same waveguide with r=58nm.

has two main spectral lines distant by 5meV, which were attributed to the X and X^- excitons (see section 4.2.1). The weaker emission close to the trion line is caused by light scattering from one of the FP modes. The spectrum collected at the coupler position, in red, exhibits simultaneously the QD lines and FP lines. The attribution of FP lines is confirmed by the high power spectra collected from the coupler (in green) in which only the FP modes are visible. In analogy with QDs in cavities [172], the spectrum emitted in the waveguide is composed of lines originating from the QD emission and the nearby modes, which can be modelled using the techniques developed for single cavities [172].

The single photon emission through the waveguide modes was demonstrated using the HBT setup described in Chapter 2. The second-order autocorrelation functions for the emissions of QD5 and QD1 are given on Fig. 4.8. The measured zero-time delay after deconvolution with the APDs response was respectively: $g^{(2)}(0) = 0.092$ (QD5) and $g^{(2)}(0) = 0.16$ (QD1), which completes the demonstration of on chip single photon emission and routing over $22.5\mu m$.

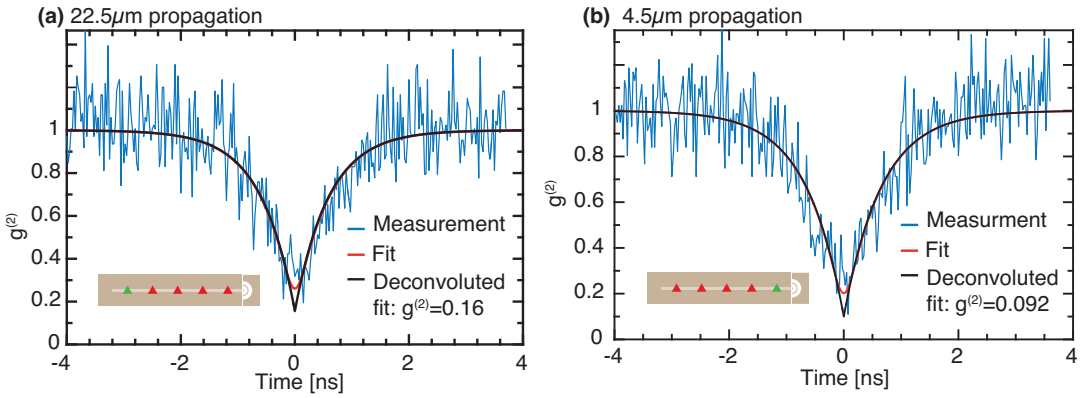

Figure 4.8 – (a) Second-order autocorrelation function for QD5 (T=4K, P=5uW); (b) for QD1 (T=4K, P=5uW); in each case, the light was collected from the outcoupler and the QD was resonant with a FP mode.

4.2.3.2 Statistics of QD coupling efficiency

The spectrally resolved images permits the comparison of QD emission into free space and into the photonic band, which is useful for characterizing the QD coupling efficiency into the PhCW mode.

The coupling of excitons to the waveguide mode was characterized by the ratio: $I_{coupler}/I_{QD}$, where $I_{coupler}$ and I_{QD} are respectively the intensities collected at the QD and the coupler positions, obtained by integrating over the QD and coupler emission energy and position range as depicted by the white rectangles on Fig. 4.9(d). This ratio was measured over the 5 QDs embedded in 11 structures with hole radii ranging from 58 to 80nm as shown on Fig.4.9(a). This hole range corresponds to a

band edge shift from 1.26eV to 1.35eV, permitting to tune the band edge through the QD emission. The dot size reflects the QD distance to the coupler. When QDs are embedded in waveguides with a hole radius below 70nm and a band edge below 1.31eV. Their intensity ratio $I_{coupler}/I_{QD}$, is large with an average around 5 and a maximal value of 8, denoting the QD emission into delocalized modes. However, these intensity ratios exhibit large fluctuations from 0.5 to 10, which originate from the discrete nature of FP modes not always matching the excitonic QD emission peaks. The presence of discrete high finesse FP modes therefore prevents obtaining a deterministic coupling of QDs into waveguides.

By contrast, much lower intensity ratios are observed when the band edge is tuned above 1.32eV, beyond the QD emission (r>72nm), which indicates the absence of guiding. The intensity ratio for these structures (r=71-80nm) decreases with the QD-coupler distance (Fig.4.9(b)). This decrease was well fitted by an exponential: $I_{coupler}/I_{QD} = Ae^{-x/\rho}$ with a characteristic length: $\rho = 7.2 \pm 0.9\mu m$. This exponential decay of coupling probably originates from evanescent waves in the PhC bandgap.

4.2.3.3 Temperature tuning of trion lines through FP modes

The coupling of QDs to a semi-waveguide was further studied by scanning a QD trion line through two FP modes. The selected PhC structure had a hole radius: r=58nm and the excited QD was QD5 at a 22.5μm distance from the coupler. At each temperature, a spectrally resolved image was acquired. The corresponding spectra acquired from the QD emission into free space (in violet) and from the coupler (in black) are plotted on Fig. 4.10(a). In these spectra the slit at the entrance of the spectrometer was left open, so as to collect all light incoming from the QD and the coupler. In this condition, the spectrally-resolved imaging setup limits the spectral resolution of the X^- line to 293μeV. Its real linewidth at T=10K measured independently is 108μeV.

In analogy with previous observations of QDs in L_3 cavities, trions or excitons can feed FP modes also out of resonance. The range of FP mode feeding (here 2meV) is larger than that expected from the mere feeding by a discrete emission line [172]. Besides, the feeding of mode FP2 by the X^- at low temperature is lower than the feeding of FP1 by X^- or the feeding of FP2 by X at higher temperatures: the FP mode feeding is increased at higher temperature, which is caused by two concurring effects.

First, pure dephasing increases with temperature. The linewidth ΔE of a trion in the PhC bandgap was measured as a function of temperature (Fig.4.10(b)). This increase is well described as a thermally activated process caused by fluctuating charges in impurities surrounding the QD:

$$\Delta E(T) = \Delta E(0) + B \cdot exp(-E_a/k_B T) \tag{4.10}$$

where E_a is the activation energy of the impurities, $\Delta E(0) = 100\mu eV$ is the $T = 0$

pure dephasing rate. The fitted activation energy is $E_a = 19meV$.

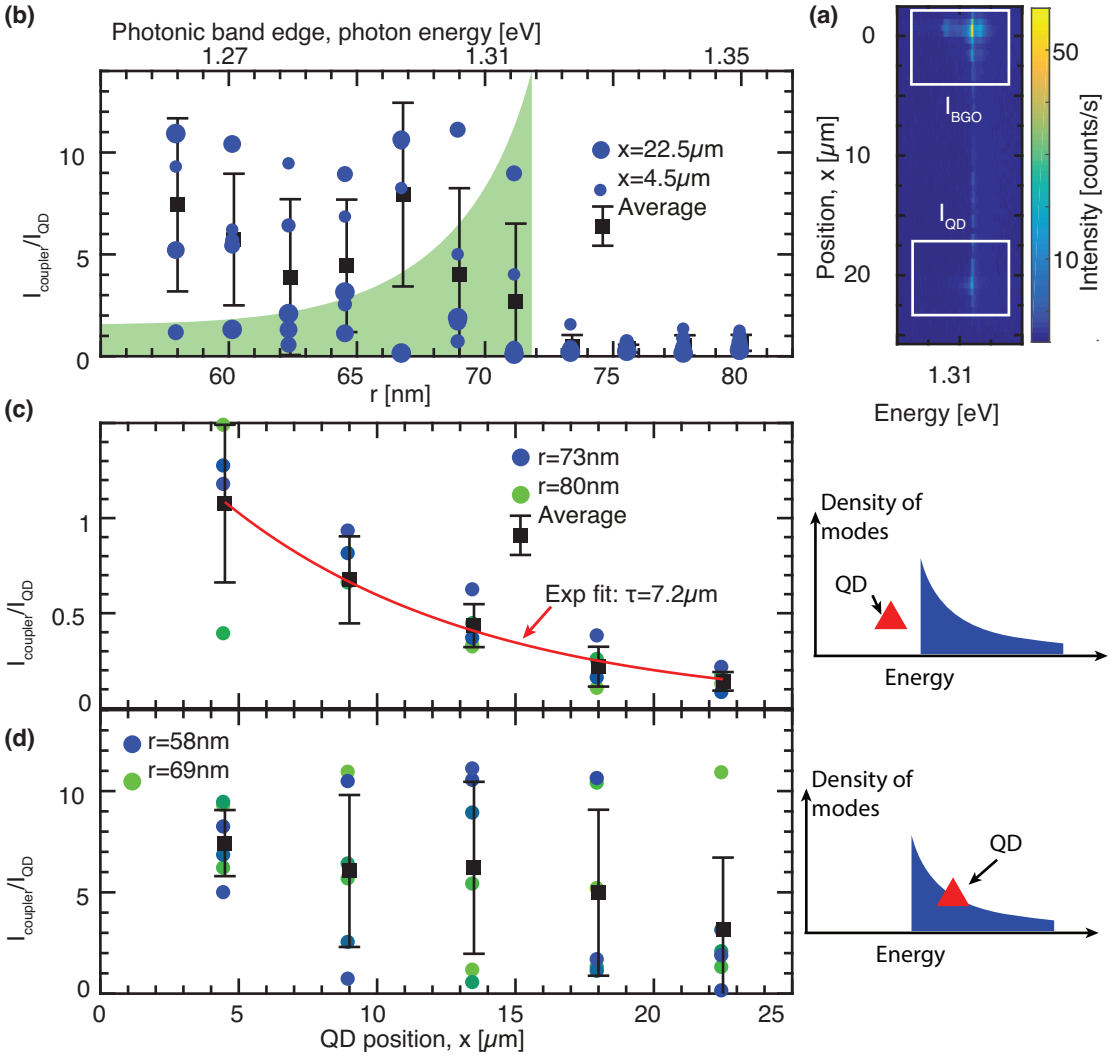

Figure 4.9 – (a) Spectrally resolved image of a single QDs, the white rectangle depicts the integration areas for $I_{coupler}$ and I_{QD}; (b) Relative intensity $I_{coupler}/I_{QD}$, the dot sizes indicate the distance between the QD and the coupler, from 4.5μm to 22.5μm; (c) Relative intensity $I_{coupler}/I_{QD}$ of QDs blue shifted with respect to the band edge; (d) Relative intensity $I_{coupler}/I_{QD}$ of QDs red shifted with respect to the band edge. ($P = 5\mu W$, $T = 10K$).

This increase of pure dephasing with temperature reduces the on-resonance feeding of FP modes at higher temperatures. However it also increases the out of resonance cavity feeding [34]. Although this phenomenon contributes to the enhanced cavity feeding, it cannot explain why the feeding of FP1 by the trion at T=30-35K is much larger than that of FP2 at lower temperatures but with similar detuning. Indeed, these

two modes exhibit a similar LDOS at the QD energy and position as was measured by high power excitation of QD5 (Fig. 4.6(a)). Besides, the QD broadening is negligible up to T=35K.

The second phenomenon explaining this temperature enhanced feeding is the phonon assisted broadband photon emission, through which a photon emission is concomitant with the emission and absorption of a longitudinal acoustic phonon [172]. This effect can be responsible for the feeding of cavity modes through several meV as is observed in this temperature dependence study. Besides, at low temperature, the emission of phonons is much more probable than the absorption, because the phonon bath is almost empty. Therefore, the phonon-enhanced FP modes feeding is higher when the modes are red-shifted than blue-shifted, which explains the low intensity of mode FP2 in the T=10-35K temperature range. Notice, that at T=60K, the feeding of mode FP2 by the exciton and of mode FP1 by the trion is much more efficient, in line with the higher population of the phonon bath.

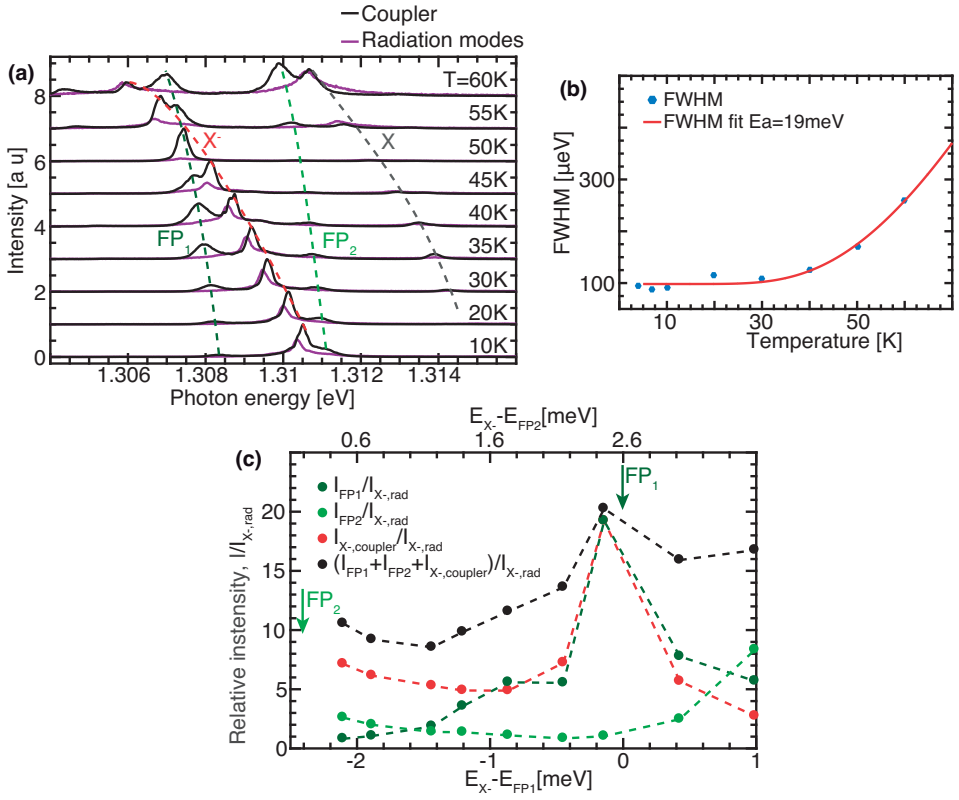

Figure 4.10 – (a) Temperature tuning of a trion through two FP modes; (b) temperature dependence of the FWHM of a trion placed in the PhC bandgap. (Excitation power: $P = 5\mu W$). The fitted parameters were: $E_a = 19meV$, $\gamma_d(0) = 100\mu eV$, $B = 6.5meV$. (c) Relative intensities of the trion and FP lorentzians throughout the temperature tuning range.($P = 5\mu W$, $T = 10K$, r=58nm)

The trion and FP mode lines measured via the coupler and the trion line measured via its free space emission were fitted with lorentzians at each temperature. The intensity ratio of the FP2 line to that of X^- collected from the radiation modes: $I_{FP2}/I_{X-,rad}$ is indicated in dark green on Fig. 4.10(c), while that of X^-: $I_{X-,coupler}/I_{X-,rad}$ is shown in red. These two ratios are clearly increased at zero detuning, which is an indication of Purcell enhanced emission [172]. A similar increase of $I_{X-,coupler}/I_{X-,rad}$ and $I_{FP1}/I_{X-,rad}$ is observed when the trion is tuned near resonance with the FP1 line, although the QD could not be tuned close enough to resonance to obtain an increase as large as with FP2. The relative intensity increase of the FP2 line at high temperature and positive detuning $E_{X-} - E_{FP1} > 0meV$ is caused by the feeding of this line by the exciton as is clear from the temperature dependence study on Fig. 4.10(a). The relative intensity of the trion line and the two FP lines: $(I_{X-,coupler} + I_{FP1} + I_{FP2})/I_{X-,rad}$ is also shown in black. Notice that the emission through FP modes strongly mitigates the emission reduction when the trion is not on resonance with the FP modes. As a last comment: the relative intensities shown here reach values almost two times higher than those given on Fig. 4.9(b). However, the relative intensities studied in this part do not take into account the emission through the radiation modes by other QD lines such as X, which explains this difference.

To conclude, phonon assisted feeding and pure dephasing enhance the out of resonance coupling and mitigate the detrimental effect of discretized FP modes for achieving the broadband coupling of QDs to waveguides. However, this advantage may also have a detrimental impact on other properties of the light emitted such as photon indistinguishability.

4.3 Coupling efficiency of QDs to semi-waveguides

4.3.1 β factors in PhCW

The most common metric for assessing the coupling efficiency is the β factor [104]:

$$\beta = \frac{\Gamma_{wg}}{\Gamma_{wg} + \Gamma_{uc}} = \frac{\Gamma_c - \Gamma_{uc}}{\Gamma_c} \tag{4.11}$$

where $\Gamma_c = \Gamma_{wg} + \Gamma_{uc}$ is the emission rate of an exciton coupled to the waveguide band, $\Gamma_{uc} = \Gamma_{rad} + \Gamma_{nr}$ is the emission rate of an exciton not coupled to the waveguide band, Γ_{wg} is the exciton emission rate into the waveguide mode, Γ_{nr} is the non-radiative exciton recombination rate and Γ_{rad} is the exciton emission rate into the radiation modes (i.e., non-waveguided modes) as depicted on Fig. 4.11(a). The β factor is usually obtained from the lifetimes of QDs in the photonic bandgap and that of QDs emitting into the PhCW band. However, lifetimes of QD ensembles in the bandgap suffer from statistical variations which translate into uncertainties of

the measured Γ_{uc}. A first source of uncertainty lies in the position of QDs in the PhCW. Indeed, the coupling to radiation modes is position and and dipole-orientation dependent, which can cause into variations of Γ_{uc} by one order of magnitude [98]. Besides, the top collection schemes used in the past [107, 105] for measuring Γ_{uc} do not guarantee that the QD is placed inside the PhCW in which the coupling to radiation modes is different [104], which may lead to overestimations of the β factor.

Thyrrestrup et al. demonstrated a beta factor value of 0.85 by temperature tuning a QD line across the photonic bandedge [106]. However, the result was made possible by the absence of Anderson localized modes caused by a significant disorder. The losses induced by such a disorder may cancel the advantage of enhanced collection.

β factors as high as 0.98 were reported by Arcari et al. [104] by measured Γ_{uc} from one single QD weakly coupled to the waveguide. This technique has the advantage of better controlling the QD position which is necessarily close to the waveguide channel. However, although variations of Γ_{uc} and β are more controlled, this method does not account for other sources of uncertainties: first, all QDs may not have the same dipole moment, which translates into uncertainties of Γ_{rad}. Secondly, QDs may exhibit statistical fluctuations of their non-radiative recombination rates Γ_{nr} as emphasized by Wang et al. [98]. In our design, the site-controlled QDs were all positioned at the same place with respect to the waveguide Bloch cell. However, statistical variations of Γ_{rad} or Γ_{nr} are still possible. A statistical measurement of Γ_{uc} is, therefore, necessary to infer the β factor with a high certainty.

4.3.2 β factors measurements with site-controlled QDs

4.3.2.1 β factor measurement robust to QD inhomogeneities

In this thesis, the average rate Γ_{uc} was estimated from time-resolved PL measurement of 18 QDs placed in W1 waveguides with r=80nm, i.e., spectrally positioned in the photonic bandgap. These 18 QDs were selected from the 25 QDs placed in 5 nominally identical PhC waveguides: only the QDs in which the trion could be unambiguously identified were analyzed. Notice that this measurement is based on the assumption that the average Γ_{uc} is weakly varying when changing the PhC hole size. Once Γ_{uc} is known, the β factor of 21 trions on resonance with the waveguide band were deduced from their time-resolved PL (TRPL) decay. These decay traces were selected out of those acquired on 47 QDs. Only structures where the trion could be unambiguously identified were measured. The lower ratio of selected QDs is caused by the more difficult identification of QD lines in the presence of FP modes. The spectrum of QDs in the bandgap were acquired by collecting the emission directly from above the QD, and that of QDs coupled to the PhCW band were collected from the coupler.

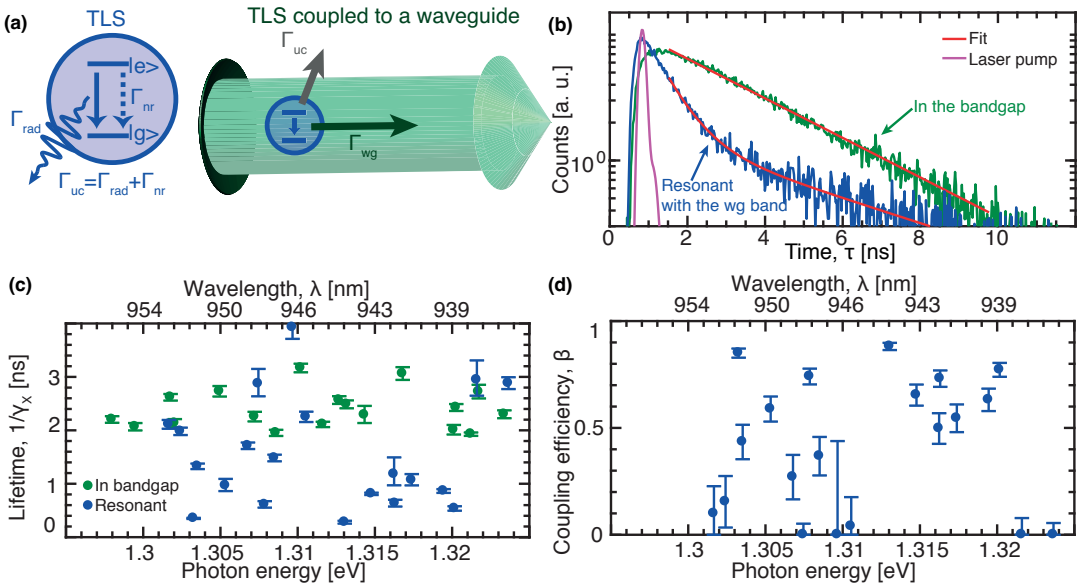

Figure 4.11 – (a) sketch of a two level system (TLS) representing the QD (left) and a TLS coupled to a semi-waveguide (right); (b) Time resolved PL of trion lines of QD5 in the bandgap (green) and on resonance with the waveguide band (blue); (c) Measured lifetimes of QDs in the bandgap (green) and on resonance with the waveguide band (blue); (d) Extracted β factors of QDs on resonance with the waveguide band ($P = 2\mu W$, T=10K)

Fig. 4.11(b) illustrates the time resolved PL trace of a trion in the bandgap (green curve) and in resonance with the PhCW band (in blue). The TRPL of the QD on resonance shows a biexponential decay. Biexponential decay is typically assumed to come from the interplay between dark and bright states in excitons. However, trions do not have dark states. Rather, the biexponential decay was interpreted as arising from the feeding of the trion states by two channels: the usual fast, phonon-assisted decay and another slow decay channel caused by the trion charge feeding by a nearby impurity [173, 112]. This model is encompassed by the following rate equations:

$$\partial_t p_{ph} = -\gamma_{ph} p_{ph} \tag{4.12}$$

$$\partial_t p_{sl} = -\gamma_{sl} p_{sl} \tag{4.13}$$

$$\partial_t p_X = -\gamma_X p_X + \gamma_{ph} p_{ph} + \gamma_{sl} p_{sl} \tag{4.14}$$

where p_{ph} is the population of excited states feeding the trion via a fast phonon assisted decay scheme with a decay rate γ_{ph}, p_{sl} and γ_{sl} the corresponding parameters for slow decay channel, and p_X is the trion population decaying at a rate γ_X, which provides the measurements of Γ_{uc} for QDs in the bandgap and of Γ_c for QDs on

resonance with the waveguide band. The solution for p_X is:

$$p_X = \frac{p_{ph}(0)\gamma_{ph}}{\gamma_X - \gamma_{ph}}(e^{-\gamma_X t} - e^{-\gamma_{ph} t}) + \frac{p_C(0)\gamma_{sl}}{\gamma_X - \gamma_{sl}}(e^{-\gamma_X t} - e^{-\gamma_{sl} t}) \tag{4.15}$$

This result yields a biexponential decay if the rise time, determined by γ_{ph}, is neglected. Exponential or biexponential decays were observed both for QDs in the bandgap and on resonance with the waveguide band. Each trion decay curve measured was fitted with either a single exponential or a biexponential. The single exponential fit for the non-resonant trace (green curve on Fig. 4.11(b)) yields the trion decay rate $\gamma_X = 0.36 \pm 0.01 ns^{-1}$, while the biexponential fit for the resonant QD (the blue curve on Fig. 4.11(b)) yields the trion decay rate $\gamma_X = 1.6 \pm 0.2 ns^{-1}$ and the slow trion feeding $\gamma_{sl} = 0.23 \pm 0.02 ns^{-1}$. The measured decay values of each of the 18 QDs in the bandgap are given on Fig. 4.11(c) as green dots and range from 1.9 to 3.2ns. Their measured average yields the average decay rate of trions in the bandgap: $\Gamma_{uc} = 0.43 ns^{-1}$, with a standard deviation of $\pm 0.06 ns^{-1}$ (or $\tau_{uc} = 2.3 \pm 0.3 ns$). The fast decay rates γ_X of each of the 21 trions are shown on Fig. 4.11(d) as blue dots. Due to the Purcell effect, the average lifetime of QDs in resonance with the waveguide band is reduced. However, some trions still exhibit lifetimes as high as the ones of uncoupled trions, confirming that some QDs have a negligible spatial or spectral overlap with the FP modes. The β factors for each QD estimated from these measurements are given on Fig. 4.11(d). The error-bars were estimated from the measured standard deviation of Γ_{uc}; We obtain values up to 0.88 ± 0.02 for $r = 54.5nm$. Although it is lower than the best reported value of $\beta = 0.98$ [104], our measurements take into account statistical variations of the QD decay rate in the bandgap, which, if not properly treated, may lead to overestimations of the β factors. The lower values of β measured here arises mainly from our rather large measured value of $\Gamma_{uc} = 0.43 ns^{-1}$ compared to that obtained in [104]: $\Gamma_{uc} = 0.098 ns^{-1}$. Note however that our measurement is comparable to that obtained in other published results: Chang et al. [93] obtained: $\Gamma_{uc} = 0.40 ns^{-1}$, Balet et al. [95] obtained: $\Gamma_{uc} = 0.28 ns^{-1}$, Luxmoore et al. [174] obtained $\Gamma_{uc} = 0.40 ns^{-1}$. The difference between our measure value of Γ_{uc}, and that obtained by Arcari et al. [104] can arise from a higher non-radiative emission rate Γ_{nr} and also possibly from the dipole moment of trions in our QDs which may not be in plane and would thus benefit less from the bandgap induced reduction of the emission rate.

4.3.3 Optimal coupling of a QD to a semi-waveguide

Using the knowledge acquired in the previous parts, an optimal design for coupling inhomogenously broadened single QDs to a semi PhC waveguide with a perfect reflectivity on one side, connected to a coupler with a reflectivity r can be inferred. First, as noted in other publications [175] the QD should be placed at the maxima of

the photonic Bloch mode.

Second, although the FP resonances may help increasing the spontaneous emission rate into the target waveguide mode, the discretization of the LDOS caused by the coupler reflection is detrimental to achieving a deterministic emission of QDs into the PhCW modes. Retrieving the broadband spectrum of a PhC waveguide requires reducing the coupler reflection r. The FP modes modulation of the waveguide-related Purcell enhancement is given by the FP modes visibility: $2r/(1+r^2)$. The visibility in blue and finesse in green of a waveguide and a semi-waveguide are plotted on Fig. 4.12(a). Obtaining a visibility of 0.5 requires a reflection coefficient $R = r^2 \approx 0.25$ in a waveguide with couplers at each ends, but only $R \approx 0.07$ in a semi-waveguide. However, in a waveguide, the QD emission is divided into the two propagation directions, which is a disadvantage for realizing on chip photon sources. Besides, the reflection from the closed edge can enhance the β factor through a positive interference effect [176]. A design for a broadband low reflection coupler restoring a broadband extraction will be exposed in Chapter 5.

A third element of optimization is the group index. In the presence of FP modes, the propagating waveguide modes are recycled several times which enhances the QD emission rate. In this context, coupling the QD to the highest group index is not necessarily a good idea, not only because more light will be lost via propagation losses after the QD emission (see Chapter 3), but also because propagation losses reduce the FP modes Q-factors. The highest achievable Purcell factor is not necessarily reached at the highest group index. This point is especially clear from the measured Q-factors of Fig. 4.6(b) where similar values of the Q-factor are obtained for both high and low values of the group index. On the contrary, if the coupler reflectivity is so low that the waveguide mode recycling is negligible, QDs are coupled only to truly propagating modes and high group indexes will enhance the Purcell factor. However, even in this case, losses after the emission may compromise the advantage of higher extraction rates.

A fourth factor that requires a precise optimization is the spatial and spectral envelope modulation of the FP modes. Notice, that this effect is completely general to semi-waveguides where it cannot be avoided even when r=1. The Purcell enhancement of a QD placed at the maximum of Bloch mode, in a W1 PhC semi-waveguide with no reflection from the coupler is given by:

$$P_{wg} = \frac{3}{4\pi}\frac{n_g}{n}\frac{\lambda^2}{A} sin((\frac{\pi}{a} - k)r_d)^2 \tag{4.16}$$

where A is the W1 mode area, n is the GaAs refractive index, n_g is the waveguide mode group index and k is its wavevector. The Purcell factor as a function of energy and QD position along the PhCW is shown on Fig. 4.12(b). It is oscillating in energy with a period $\Delta\omega = v_g\pi/r_d$ and in space with a period: $P = a/(1 - ka/\pi)$. Obtaining a

broadband and efficient coupling is obtained via a tradeoff between two opposing effects: $\Delta\omega$ is larger close to the semi-waveguide edge, but too close to the edge, the Purcell enhancement is zero because there is a destructive interference between the two counter-propagating Bloch modes. Therefore, an optimal position is between 2a and 3a, where the envelope modulation period is larger than $60meV$ ensuring a Purcell factor around 1 in this energy range. Notice that a higher Purcell effect is obtained near the band edge, although this is achieved within a lower energy range.

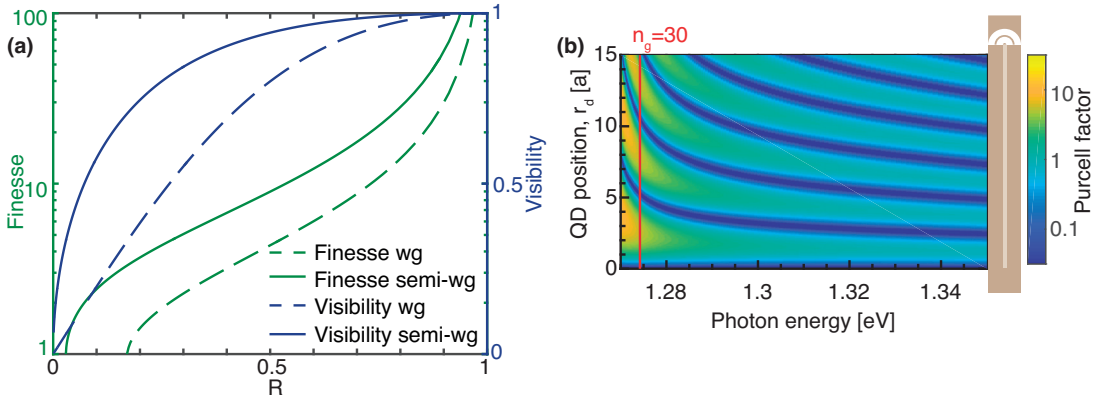

Figure 4.12 – (a) Finesse and reflectivity in a waveguide closed by couplers with intensity reflection coefficients R at each sides and a semi-waveguide closed by a perfect reflector on one side and a coupler with reflection coefficient R on the other side; (b) Purcell enhancement in a semi-waveguide (The red line indicates the disorder induced limit of light propagation: $n_g = 30$, the waveguide mode area used for this picture: $A = 0.3(n/\lambda)^2$, with n=3.46.

4.4 A short slow light section for optimal single photon collection

The possibility to slow down energy velocity of light in a waveguide has attracted a lot of attention in the past. Slow light may be used for building more compact linear optical elements like Mach-Zender interferometers [79]. Another advantage is the possibility to enhance light matter interaction. Indeed, thanks to energy conservation, light intensity in a slow light waveguide is enhanced by the slow down factor: n_g/n, which induces a similar increase in absorption and emission rates and increases by powers of n_g nonlinear effects [79].

PhCW are ideally suited for such applications, because they naturally feature slow down of light near their band edge and offer a lot of flexibility in their design [18]. The prospect of fabricating enhanced and compact optical switches or all optical light pulses storage propelled a research effort toward the design of broadband and

dispersion free slow light PhCW [81, 177, 80], or to optimize the coupling of light in and out of a slow light waveguide [178, 179, 180]. The possible applications of slow light were also studied for increasing the coupling of QDs to PhCW. Arcari et al. [104] demonstrated the slow light enhanced collection of light by using a $5\mu m$ long slow light section leading to the observation of β factors up to 0.98. This slow light section was then coupled to a fast light PhC section for optimizing extraction. In this part, the potential and limitations of slow light for extracting single photons from QDs will be exposed.

4.4.1 A short slow light section for disorder-robust light extraction

In the present work we show that light extraction can be enhanced by embedding QDs in a short slow-light segment, which mitigates the effects of fabrication disorder. The slow light segment was obtained by shifting 6 holes adjacent to the waveguide by sh, as shown on Fig. 4.13(a), such that the slow light band edge was blue shifted with respect to the fast light $17.25\mu m$ long W1 waveguide section. The slow light section was adiabatically connected to the fast light section by two holes shifted respectively by one third and two third of the slow light section hole shift. The QD was placed precisely at the maxima of the PhCW Bloch mode at the center (horizontally) of the slow light section. The fast light PhCW was connected to a Bragg grating outcoupler collecting light out of the PhCW. Six series of this structure with a hole radius r=65nm were fabricated with nine values of the shift linearly spaced between sh=3nm and 27nm. The corresponding blue shift of the photonic bandedge with respect to the fast-light waveguide (simulated by 2D FDM) goes from 5meV to 48meV.

The FDM simulated spectrally resolved image of an L_n cavity with the short slow light section described above is displayed on the upper panel of Fig. 4.13(c). The slow light effect is visible through the higher intensity of modes between 1.28 and 1.3eV in the slow light part depicted by the green line on the sketches as is clearly visible on Fig. 4.13(f). The absence of modes localized in the fast light section between 1.28 and 1.3eV suggests that the reflection coefficient between the fast and slow light section is weak. A similar simulation including random disorder is displayed on Fig. 4.13(d). As in Chapter 3, random disorder was emulated by varying the hole radii according to a random Gaussian distribution with: $std(r) = 3nm$. As shown in Chapter 3, random disorder induces Anderson localization of light around 1.265eV. However, the modes near the slow light band edge at 1.28eV are almost not distorted, which supports the claim that a sufficiently short slow light section prevents Anderson localization. On the contrary, if the slow light section is extended in length to 25a as simulated on Fig. 4.13(e), Anderson localization in the slow light section starts to be visible. Note that the maximal achievable slow light section without localization is determined by the disorder-limited minimal localization length. Hence, the determination of disorder

is crucial to design appropriately such systems. A given level of disorder imposes an upper limit on the length of the slow light section achievable without localization.

A spectrally resolved image acquired for a fabricated structure described on Fig. 4.13(a) is shown on Fig. 4.14(a). Contrary to the long uniform PhCW studied at the beginning of this Chapter, no Anderson localization is excited by the QD, which experimentally demonstrates that such a short slow light section can prevent Anderson localization in the slow light section. Besides, a larger envelope modulation in energy is obtained thanks to the QD positioning close to the waveguide reflector, which can facilitate the broadband collection of light from an inhomogenously broadened ensemble of QDs. The regularity of the spectral envelope function observed on the spectra collected from the coupler (4.13(b)) is an indication of the weak disorder guaranteed by the small size of the slow light section, even close to the bandedge.

The FDM simulated spectrally resolved image of an L_n cavity with the short slow light section described in Fig. 4.13(c) is shown on Fig. 4.15(a). As emphasized before, slow light behavior is manifested through an increase of the mode intensity in the slow light section. The ratio of the maximal intensity of the mode (defined as the squared in-plane electric field) in the slow light section I_{sl} to the maximal intensity of the mode in the fast light section I_{fl} is indicated on Fig. 4.15(b) as red dots. The "slow light enhancement factor" defined by this ratio is around 4-5 over 10meV near 1.31eV. Near the slow light band edge, this ratio is as high as 20, but was not shown to concentrate on the broad enhancement near 1.31eV. Another ratio: I_{QD}/I_{fl} is useful to characterize the slow light effect felt by the QD, where I_{QD} is the intensity of the mode at the QD position. This ratio is indicated as blue dots on Fig. 4.15(b) and features only a "slow light enhancement factor" I_{QD}/I_{fl} up to 1.5 over the broad 10meV range, which limits slow light related Purcell effect. This difference between I_{QD}/I_{fl} and I_{sl}/I_{fl} is caused by the QD positioning with respect to the waveguide edge and the related spectral envelope modulation of the FP lines.

Spectrally resolved images of fabricated structures were used to compare QD emission into free space and into the photonic band in the structures described in Section 4.4.1, with hole shifts sh going from 3nm to 27nm. The coupling to the PhCW was characterized by the ratio: $I_{coupler}/I_{QD}$, where $I_{coupler}$ and I_{QD} were respectively the intensities collected at the coupler and the QD positions and obtained by integrating over the QD and coupler emission energy and position range over the white rectangle indicated on Fig. 4.16(a-b). This ratio was measured for each of the 6 series of 11 shifts sh and is given on Fig. 4.16(c). Similar to the PhCW case, the QD transmission through the PhCW is strongly reduced when the QD emission is tuned through the slow light band edge for a shift: $sh = 15nm$. When the QD is on resonance with the slow light band (sh<15nm), the observed average ratio increases up to values as high as 17 for a shift sh=15nm. This value is larger than those obtained in the fast

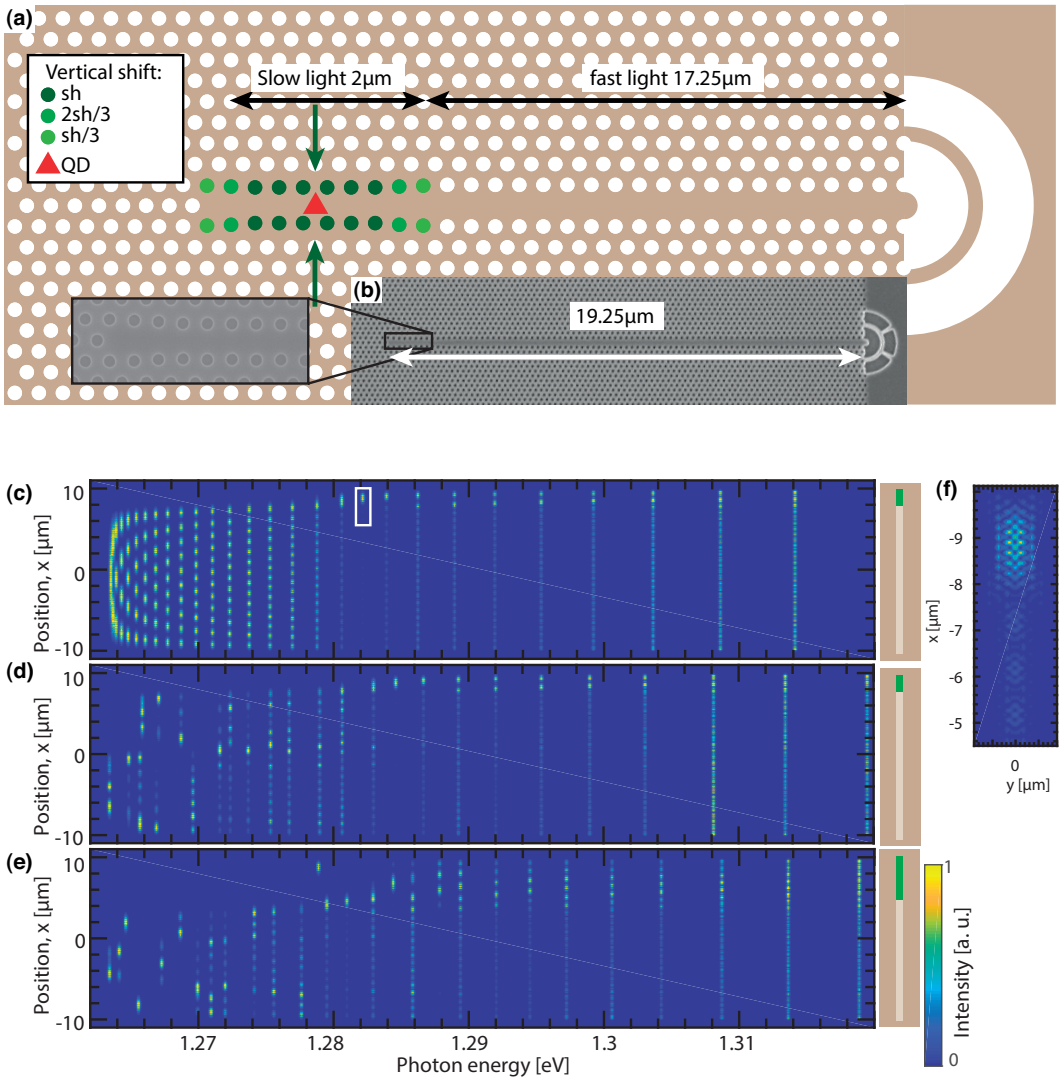

Figure 4.13 – (a) Geometry of the sample: the red triangle shows the position of the QD, the green circles represent shifted PhC holes creating a slow light region; (b) SEM image of the sample; (c-d-e) FDM simulation of a long L_n cavity including a slow light section at its upper edge; (c) 6a long slow light section without disorder; (d) 6a long slow light section with random disorder; (e) 25a long slow light section with random disorder; FDM simulation parameters a=225nm, r=61nm, shift: sh=9nm, n_{2D}=3.13. The sketches on the right depict the structure, the green stripes indicate the position and extension of the slow light section; (f) Zoom in on mode M_{18} framed with a white rectangle on Fig. 4.13(c).

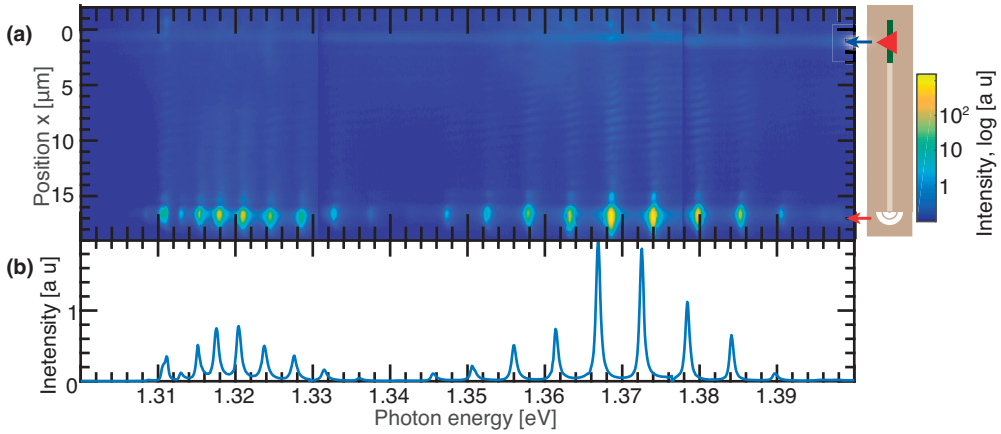

Figure 4.14 – (a) Spectrally resolved image of a fabricated structure as in Fig. 4.13(a) under a high excitation power; (b) Spectra extracted from the coupler; (slow light section shift: sh=9nm, hole radius: r=65nm, Excitation power:$P = 500\mu W$, T=10K); Credits go to T. Produit for the measurements [181]. The sketch on the right depicts the structure, the green line indicates the position and length of the slow light section.

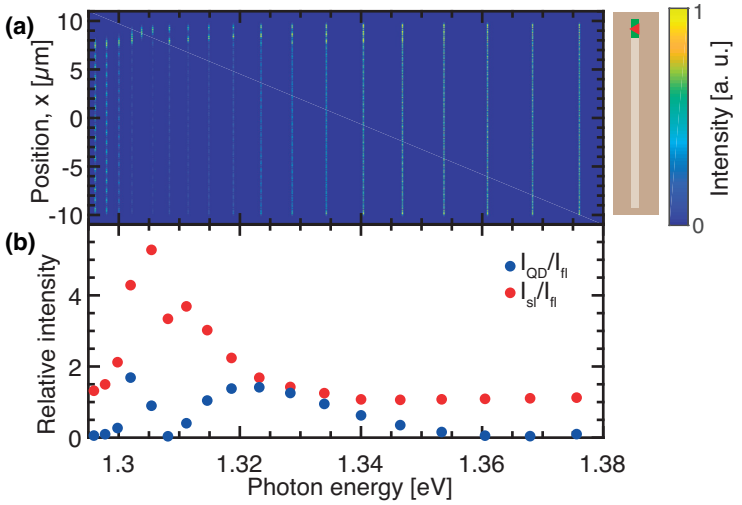

Figure 4.15 – (a) FDM simulation of a long L_n cavity including a slow light section at one of its edge; (b) slow light enhancement factors I_{QD}/I_{fl} (in red) and I_{QD}/I_{fl} (in blue); FDM simulation parameters a=225nm, r=65nm, shift: sh=9nm, n_{2D}=3.13. The sketch on the right depicts the structure, the green line indicates the position and length of the slow light section.

light PhCW (see Fig. 4.9(a)) by a factor $\approx 3-4$. One parameter impacting this value is the lower length of the slow light waveguide with respect to the fast light waveguide ($19\mu m$ compared to $27\mu m$), which can account for a factor 1.4 between the intensity ratios. If we neglect a possible shift dependent coupling to the radiation modes, this higher value of $I_{coupler}/I_{QD}$ can be explained by a combination of slow light enhancement and lower losses in the fast light section. Besides, the ratio increases from 7 (sh=3nm) up to 17 (sh=15nm) which can be attributed to a combination of slow light enhancement and increase of the envelope function as observed on Fig. 4.13(b). Moreover, for shifts larger than 15nm, the average value of the measured ratio is decreasing which is a sign of optical 'tunneling' through the 3a long slow light section separating the QD from the fast light section, in which evanescent waves emitted by the QD in the slow light channel couple to the propagating waves of the fast light section.

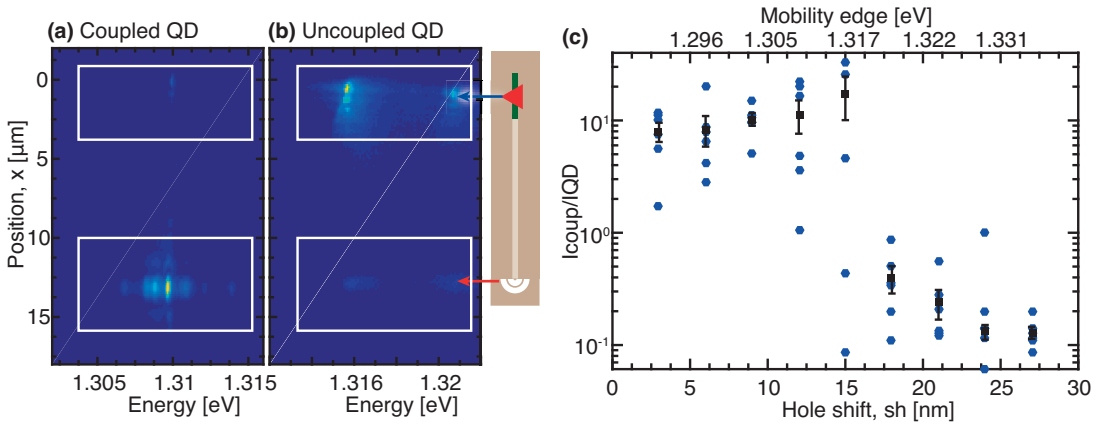

Figure 4.16 – (a-b) Examples of spectrally resolved images taken on (a) coupled (sh=6nm) and (b) uncoupled (sh=24nm) QDs. The white rectangle depicts the area over which the measured intensities I_{coup} and I_{QD} were integrated. The sketch on the right depicts the structure, the green line indicates the position and length of the slow light section. (c) Ratio of the light intensity collected at the circular Bragg grating to the intensity collected directly above the QDs (hole radius: r=65nm, $P = 2\mu W$, T=10K); The error-bars depict the standard deviation of the mean ratio estimation; Credits go to T. Produit for the measurements [181].

4.4.2 An optimal design for broadband single photon extraction

The slow light design presented before could be further improved by using a broadband slow light section [80, 182, 177], which would guarantee a efficient extraction of light from an inhomogenously broadened ensemble of QDs over a broader energy range. However, the bandwidth and group index cannot be simultaneously increased arbitrarily, but are limited by the available wavevector range in a PhC

[79]. The metric for this limitation is called the delay index bandwidth product: $n_g \Delta\omega/\omega$. Its maximum achievable value is limited by the available wavevector range to : $n_g \Delta\omega/\omega \approx c\Delta k/\omega < \lambda/2a \approx 2$. In practice, the highest simulated values of the delay bandwidth product were limited to 0.4 by the light-line ($\Delta k < 0.2$) [80].

With a design inspired by the work of Schulz et al., a flat band slow light section with n_g = 40 over 8meV was be obtained by shifting the three rows of holes [80] adjacent to the waveguide channel as displayed on Fig. 4.17(d), which produces a delay bandwidth product of 0.25, close to the value of 0.31 obtained with similar designs [183]. 3D FDTD simulations performed with the open source software Meep [124] yielded the group index and dispersion relation shown on Fig. 4.17(b-c). Fig. 4.17(a) depicts the Purcell factor predicted by equation 4.8 when the QD is placed at a distance 3a from the semi-waveguide ending in the flat band slow light PhCW. With such a design, a Purcell enhancement over 5 could be obtained over a 10meV bandwidth at the QD location. It would make possible an optimal on-chip single photon source for applications which do not require a precise tuning of each QD line, such as quantum key distribution [184].

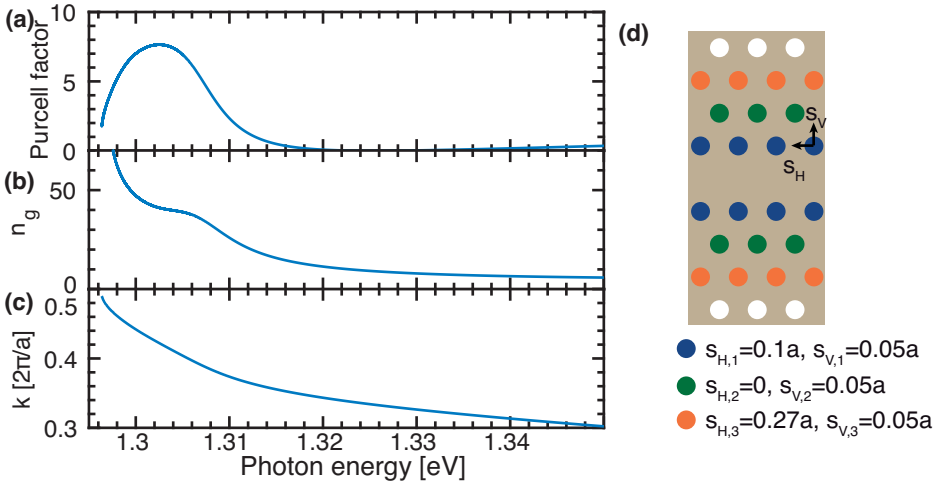

Figure 4.17 – 3D-FDTD simulation of a flat band slow light section: (a) Purcell factor predicted by Eq. 4.8 when the QD is placed at a distance 3a from the semi-waveguide reflector (coupler reflection coefficient: r=0); (b) Group index; (c) Dispersion relation; (d) Slow light PhCW design ; The FDTD simulation parameters were: PhC lattice pitch: a=225nm, hole size: r=61nm, Membrane thickness: 250nm, n=3.46.

4.5 Chapter summary

In this chapter, the first integration of a controlled number of site-controlled QDs in a semi-PhCW was demonstrated, which is an important step toward the scaling of

systems of QDs integrated in PhCs to a larger number of elements. site-controlled QDs were used as probes to investigate the local DOS of photonic modes in a PhC semi-waveguide geometry. These measurements validated the FP semi-waveguide model of these structures. Statistics on the intensity ratio of light collected from the coupler and light selected directly from the QD demonstrated the propagation of light and the detrimental impact of FP mode formation to achieve a deterministic coupling of QDs to the PhCW. The coupling efficiency was then characterized by TRPL measurements which permitted the observations of β factors up to 0.88, while taking into account the statistical variations of the QD properties.

We then showed how the use of a short slow light section can prevent the formation of Anderson-localized modes in the vicinity of the QD, and reduce propagation related losses. Finally, an optimal design was proposed for collecting light from inhomogenously broadened ensembles of QDs by using a flat band short slow light section and QDs precisely positioned to adapt to the interference effects inherent to the semi-waveguide geometry.

Although coupling QDs to an ideal PhCW mode provides in theory a broadband QD coupling, these results emphasized the significance of site-control and the necessity of a careful design to indeed benefit from these advantages. One significant issue encountered was the formation of FP modes caused by the reflection from the Bragg grating coupler. In the next chapter, an alternative design of outcoupler featuring a reduced reflection will be presented. Besides, another approach for extracting light from a QD with a cavity coupled to a waveguide will be presented.

5 QDs in L_3 cavities coupled to waveguides

In a number of quantum optics applications, each photonic component needs a precise tuning to a specific resonance frequency. In such cases, the use of broadband photonic environments is no more advantageous and other designs with narrow band high Purcell enhancement factors are preferred. A natural design for these applications is made of a QD embedded inside a small volume cavity, itself coupled to a waveguide. The cavity guarantees a strong Purcell enhancement of the QD decay, while the waveguide is used for photon collection.

The photonic modes in such systems were studied using coupled mode theory by Waks et al. [185] who highlighted the non-lorentzian spectra of cavities coupled to PhC waveguides near the band edge. Some geometric configurations were shown to optimize the cavity to PhCW coupling [186]. A green function approach was used to describe both strong and weak coupling in these systems [187, 153].

Experimental demonstrations include the demonstration of QD emission through a cavity coupled to a waveguide and then up to another cavity [188], while experimentally observing the correlations between the emission of the two cavities. β factors as high as 0.98 were reported in this work. In a different configuration, the coupling of two degenerate modes from an H_1 cavity to different waveguides [189] opened promising possibilities such as QD spin state readout or single photon optical switch. Schwagmann et al. [190] demonstrated light emission by a QD in an L_3 cavity and then in a PhCW, however without measuring the coupling efficiencies between each components.

In all these works, the given coupling factors between the cavity and the waveguide were deduced from FDTD calculations instead of measurements. Besides, the coupling between the QD and the cavity is usually deduced by comparing the lifetime of a QD in resonance with the cavity to that of another QD placed in the PhC bandgap. However, this methodology neglects possible fluctuations of exciton lifetime caused by different positions or different intrinsic QD properties. This uncertainty

may significantly alter the estimated values of β.

In this chapter, we first demonstrate an alternative design for a Bragg grating coupler which reduces the back reflection and the formation of FP modes into the PhCW. This design is used in a second part in which a QD embedded inside a cavity coupled to a PhCW is studied. This coupler design removes the need for a precise tuning between FP modes and the cavity mode to observe a cavity-waveguide coupling. We first show the existence of a cavity to waveguide coupling which optimizes the coupling efficiency of photons to the waveguide. We then demonstrate the emission of QDs to waveguide modes through a cavity [191]. The coupling coefficient of cavities to waveguides is measured by a statistical analysis of Q-factors. The QD-to-cavity coupling efficiency is finally measured in one specific structure by temperature tuning the QD through the cavity mode. From these measurements, we infer a global coupling efficiency close to the optimal value achievable within our fabrication limitations.

5.1 Low reflection output couplers

5.1.1 Reflection in PhC waveguides

Reflections from each PhCW ends induce to the formation of FP modes. The resulting frequency modulation of the waveguide density of modes also affects the coupling mechanism of cavities to waveguides [153]. Besides, due to random disorder, the energy of cavities is randomly distributed with a standard deviation (in our structures) typically around 2-3meV, which is also the order of magnitude of the FP modes separation in a $15\mu m$ waveguide. We can therefore expect the coupling coefficient to be randomly distributed with variations at least as large as the the visibility of FP modes. This randomness in the coupling coefficient can be mitigated if the waveguide DOS is smoothed by a reduction of the output coupler reflection. Such low reflection couplers would also be highly beneficial to achieving a deterministic photon collection from inhomogeneously broadened ensembles of QDs by broadband waveguides as proposed in chapter 4.

The coupler design used in previous chapters and initially proposed by Faraon et al. [192] is broadband [104] and has a relatively high collection efficiency of 30%. It is versatile and does not require a system-specific optimization. However, as was already observed in Chapter 4, this coupler exhibits a significant reflection coefficient for the simple reason that this Bragg grating coupler is also a Bragg grating reflector. Other coupler geometries were proposed in the literature. Thomas et al. [193] proposed to use one dimensional grating to access modes below the light line; however, this design was more intended as an imaging method than an efficient coupler. Tsai et al. [194] proposed a Perturbative Photonic Crystal Waveguide Coupler based on local modifications of the PhC holes to match a target gaussian outcoupled mode and

demonstrated a coupling efficiency ≈ 30%. However, no experimental demonstrations were presented. Besides, this work focused on a waveguide mode close to the band edge and therefore susceptible to be affected by disorder. Hamel et al. [195] proposed and experimentally demonstrated a PhC outcoupler based on band folding, with a reflection coefficient around R=10% and an extraction efficiency up to 30%, however at the cost of a long out-coupling section (larger than 30a) and with a bandwidth restricted to $\approx 10meV$. Another approach adopted by Tran et al. [196] was to collect light directly from the PhCW side. Reflection is reduced by using an adiabatic mode adapter consisting in a tip termination. This approach was experimentally demonstrated [104, 196] and exhibits simultaneously a broadband, large coupling efficiency and a low reflection coefficient of R=1.7%. However, this side collection geometry requires a more complex experimental setup as it prevents using the same microscope objective for excitation and collection.

The adiabatic coupler geometry described at the beginning of this chapter combines the advantages of the out of plane coupler proposed by Faraon et al. [192] and that of the in plane mode adapter [196]. This is achieved thanks to the adiabatic termination tip inserted between the coupler and the waveguide as shown on the SEM picture of Fig. 5.1(b). For clarity, this structure will be called "adiabatic coupler" as opposed to the more common coupler geometry shown on Fig. 5.1(a), which will be named "circular coupler".

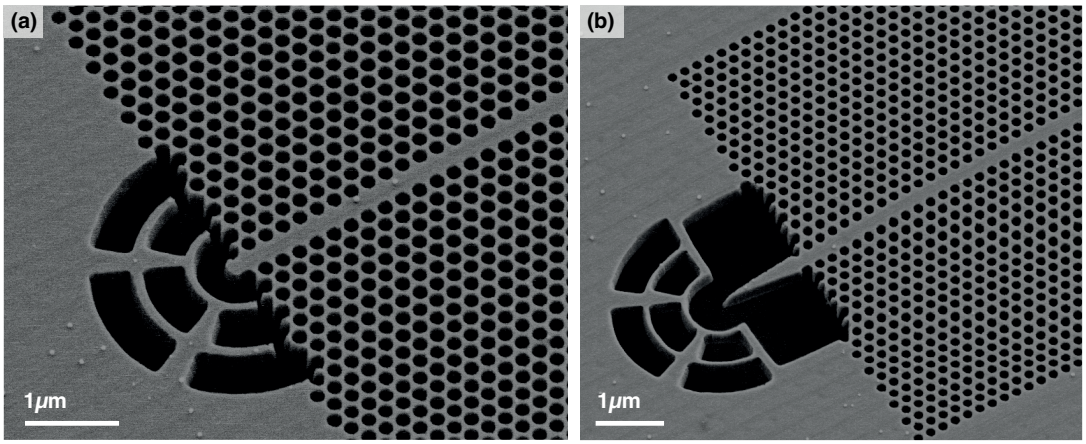

Figure 5.1 – (a) SEM picture of a circular coupler; (b) SEM picture of an adiabatic coupler. Both couplers are coupled to a W1 PhC membrane waveguide.

5.1.2 Low reflection adiabatic coupler

5.1.2.1 Simulated Fabry-Pérot modes formed by coupler reflection

The reflection of these adiabatic couplers were numerically simulated using the FDTD software meep [124]. The simulated couplers were adiabatic couplers with adiabatic

tip lengths of respectively 0.5, 1, 1.5 and 2μm and a circular coupler. The simulated volume was enclosed with perfectly matched layers (pml). As pmls are known to be unreliable absorbers for PhCW modes [123] we did not directly try to measure the reflection. Instead, the simulation were applied to a waveguide (a=225nm, r=0.3a, membrane thickness: th=250nm, n=3.4653) with the coupler ending on one side and a PhC reflector on the other side as shown on Fig. 5.2(a). The waveguide length was: 28a. A Gaussian-pulse dipole source was placed at the W1 PhCW Bloch mode maximum closest to the waveguide reflector. Its emission energy was centered on 1.37eV with a broadband pulse linewidth of 1eV

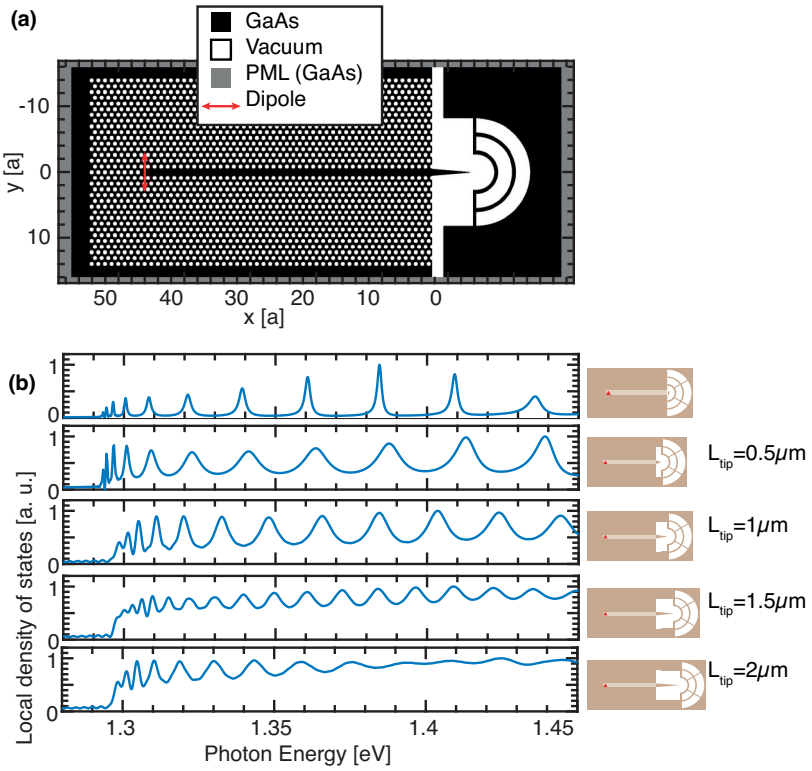

Figure 5.2 – (a) Geometry of the LDOS FDTD simulation the LDOS was simulated at the location specified by the red arrow indicating the dipole source position; (b) FDTD simulation of different coupler designs using meep, with from top to bottom: a circular coupler, an adiabatic coupler, with a tip length of 0.5μm, 1μm, 1.5μm and 2μm. (simulation parameters: a=225nm, r=61nm, slab thickness: th=250nm, n=3.46)

The simulation ran for a time Na/c (where N is an integer) while the local density of states (LDOS) was extracted from the discrete Fourier transform of the field measured at the source position indicated by a red arrow on Fig. 5.2(a). The FDTD simulation time was 2000c/a for the adiabatic coupler with a tip length between 1 and 2μm. In simulations with lower tip lengths and the circular coupler, the DOS computation did

not completely converge and required a longer simulation time of 7000a/c (adiabatic coupler with a 0.5μm tip length) and 20000a/c (circular coupler). The FP modulation is clearly visible on each of the computed LDOS of Fig. 5.2(b) with a free spectral range decreasing near the PhC band edge at 1.3eV. The finesse of the FP modes for the adiabatic coupler is indeed lower than that of the circular coupler. Besides, it decreases with the adiabaticity of the coupler i.e. the coupler tip length. This adiabatic coupler geometry therefore appears to be a reliable solution for reducing back-reflection.

5.1.2.2 Measured Fabry-Pérot modes formed by coupler reflection

This effect was experimentally assessed by fabricating structures similar to the simulated ones: with an adiabatic coupler including tip lengths of respectively 0.5, 1, 1.5 and 2μm, and with a circular coupler. The only difference was the larger waveguide length of 70a. This structure was fabricated in a different sample albeit with the exact same fabrication parameters as those described in chapter 2 for the membrane (250nm thick GaAs membrane), the QD growth and the PhC pattern. The QD was positioned at a distance a from the PhC reflector, similar to the position shown on Fig. 5.2(a) for the dipole source.

Two spectrally resolved pictures for each of these structures were obtained using a monochromator slit width of 100μm (see section 2.3.7.1 in Chapter 2). One such spectrally resolved pictures for each design are shown on Fig. 5.3(a-b-c) and Fig. 5.4(a-b). In these pictures, the continuum of QWR emission is clearly visible at $x = 0\mu m$ position, while the FP spectra was collected at $x = 15\mu m$. The spectra shown below each picture were obtained by integrating the light intensity over 4μm above the coupler position. In line with simulations, the FP visibility is maximal for the circular coupler and decreases as the tip length increases up to 1.5μm. The 2μm tip length features larger FP modes visibility, which may have been caused by distortion in the tip cantilever due to its weight. These measurements give a picture fully consistent with the simulated DOS, which confirms the possibility of reducing back-reflection from coupler by inserting an adiabatic taper at the waveguide output.

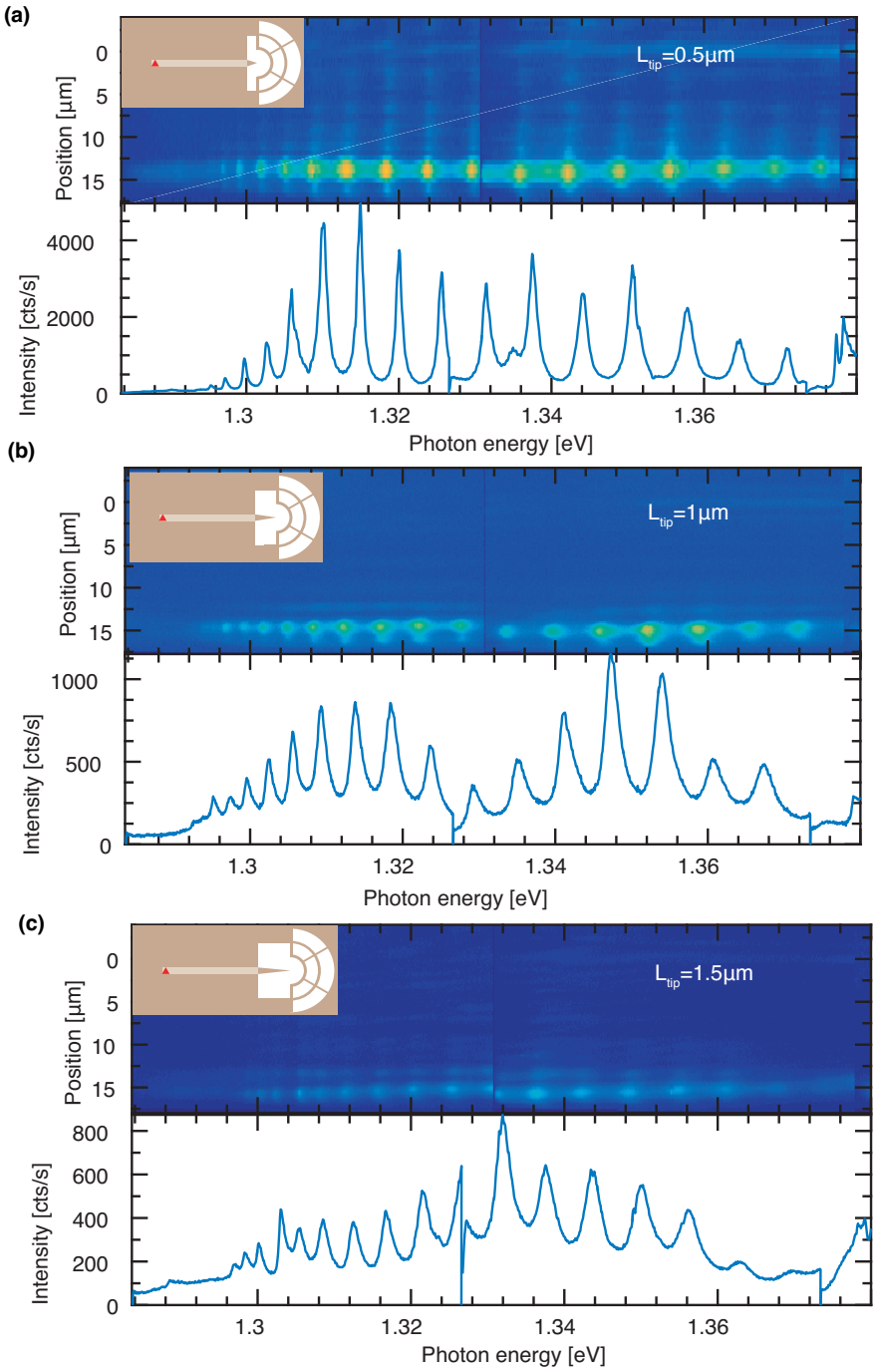

Figure 5.3 – Spectrally resolved picture and spectra in an adiabatic coupler, with a tip length of: (a) $0.5\mu m$, (b) $1\mu m$, (c) $1.5\mu m$; Excitation power: $P = 500\mu W$, T=10K. The QD position is depicted as a red triangle in the sketches.

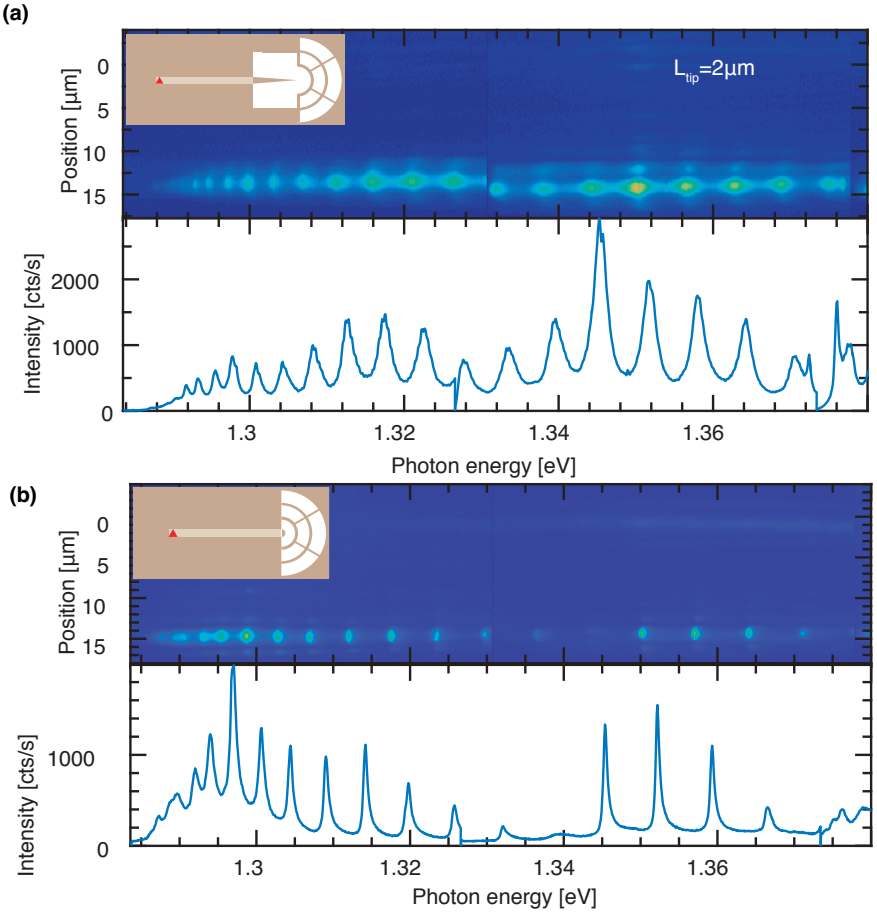

Figure 5.4 – (a) Spectrally resolved picture and spectra in an adiabatic coupler, with a tip length of $2\mu m$; (b) Spectrally resolved picture and spectra of a circular coupler (as described in [192]); Excitation power: $P = 500\mu W$, T=10K. The QD position is depicted as a red triangle in the sketches.

5.1.2.3 Reflection in adiabatic and circular couplers

These observations can be made more quantitative by measuring the coupler reflection on the spectra of Fig. 5.3(a-b-c) and Fig. 5.4(a-b). The finesse shown on Fig. 5.5(a) for each measured structures was computed as the ratio of the free spectral range and the FWHM fitted on each FP peak. These measurements quantitatively confirm the decrease of finesse induced by the adiabatic tip, as well as the decrease of finesse with increased taper length up to taper lengths of $1.5\mu m$. The finesse values measured on L_{61} cavities in the fast light regime were around 30, much larger than those measured in the 66a long structures studied in this part. We can therefore safely assume that propagation losses are negligible in these structures (see section 3.2.3.1). Within this approximation, the intensity reflection coefficient is straightforwardly deduced from the measured FP Finesse (if we assume that losses on the PhC reflector

edge are negligible) [165]:

$$\mathscr{F} = \frac{\pi}{2arcsin(\frac{1-\sqrt{R}}{2R^{1/4}})}. \tag{5.1}$$

The measured reflection coefficients are given on Fig. 5.5(c) and can be compared to the simulated ones extracted from the FDTD LDOS simulations of Fig. 5.3(f). The results are similar within a 20% error margin, with a reduction of the reflection coefficient from 0.4-0.5 down to below 0.1 in adiabatic structures with $1.5\mu m$ tip lengths, which is sufficient to ensure an FP peak visibility (shown on Fig. 5.5(b)) down to 0.5-0.7.

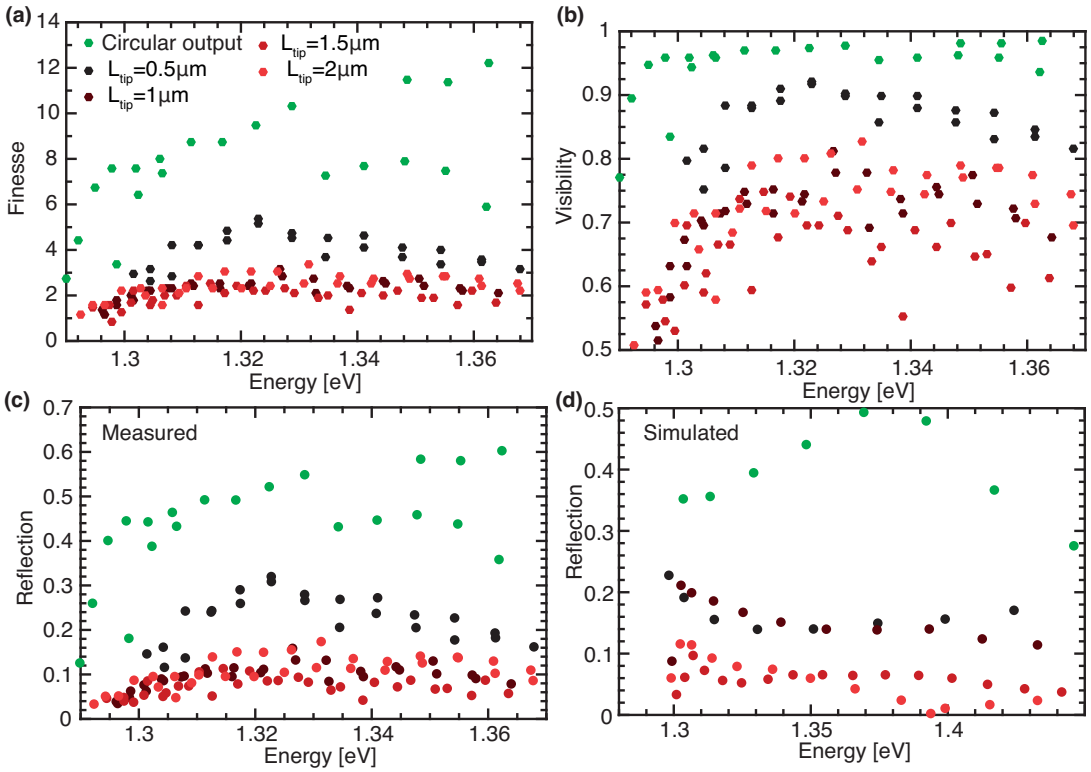

Figure 5.5 – (a) Finesse, (b) Visibility, (c) Reflection coefficient R as measured from the FP tips on the structures of Fig. 5.3(a-b-c) and Fig. 5.4(a-b) (d) Reflection coefficient extracted from the LDOS numerical simulations of Fig. 5.2(b).

We can therefore expect modulations in the Purcell factor of QDs in PhCW related to the FP mode formation by 50-70%. In the same way, the reduction of FP modes visibility can reduce the fluctuations of the coupling between cavities and waveguides as will be shown in Section 5.2.2.2. Besides, if such an adiabatic coupler was combined with an optimal slow light geometry as described in Chapter 4, it may enable the fabrication of truly broadband efficient coupling of site-controlled QDs to PhC

waveguides.

The reflectivities obtained here are similar to the simulated values in the alternative design by Hamel et al. [195] of R=10% over 10meV however, the design proposed here is easier to design and is more broadband (70meV). These values are larger than the reflection coefficient R=1.7% measured with an adiabatic tip [196]. But the design proposed here is intended to couple light out of the PhC plane contrary to the design by Tran et al.

5.1.3 Coupling efficiency

The adiabatic couplers discussed, therefore, do feature lower reflection into the PhCW mode. However, as we will show, they suffer from lower coupling efficiency to small NA objectives than circular couplers. The coupling efficiencies of a circular and an adiabatic coupler with $L_{tip} = 1.5\mu m$ were obtained via numerical simulations performed with the software meep. The two simulated structures are displayed on Fig. 5.6(a-b). In each simulation, a continuous wave y-dipole with a wavelength $\lambda = 950nm$ is placed at the center of a $12\mu m$ PhCW open at its left end and terminated on the right by the coupler. The chosen length was large enough to ensure that evanescent modes excited by the dipole have decayed before the light reaches the couplers. In each simulation, the whole space was surrounded with a $0.225\mu m$ pml except along the x-axis, where the pml width was $0.45\mu m$.

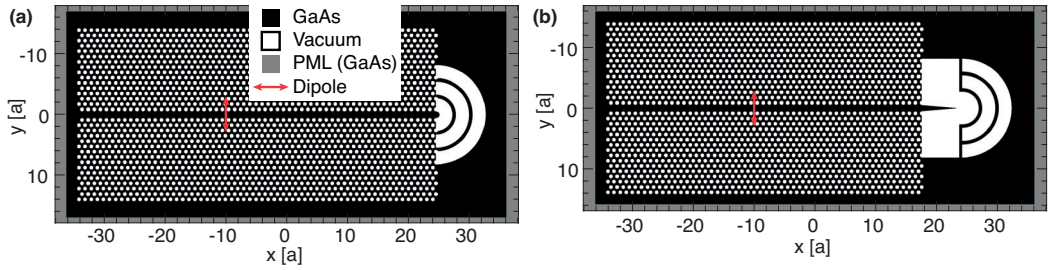

Figure 5.6 – Structures for FDTD simulation of an outcoupler and a dipole in a W1 waveguide: (a) Circular coupler; (b) adiabatic coupler. The simulation parameters were: a=225nm, r=61nm, slab thickness: th=250nm, n=3.4653.

The simulation lasted 2000a/c after which the field was in a steady state as confirmed by the constant amplitude of the electric field sinusoidal oscillations within an error of 3%. The simulated near fields are given on Fig. 5.7(a)-(d). As exposed in chapter 3, the field coupled to a microscope objective can be computed by filtering the collected angular expansion of the electric field in the plane right above the slab: $\vec{E}(k_x, k_y, t)$ by the collection angle. Once this filtered electric field is transformed back to real space by an inverse Fourier transform, the leaky components of the electric field can be imaged.

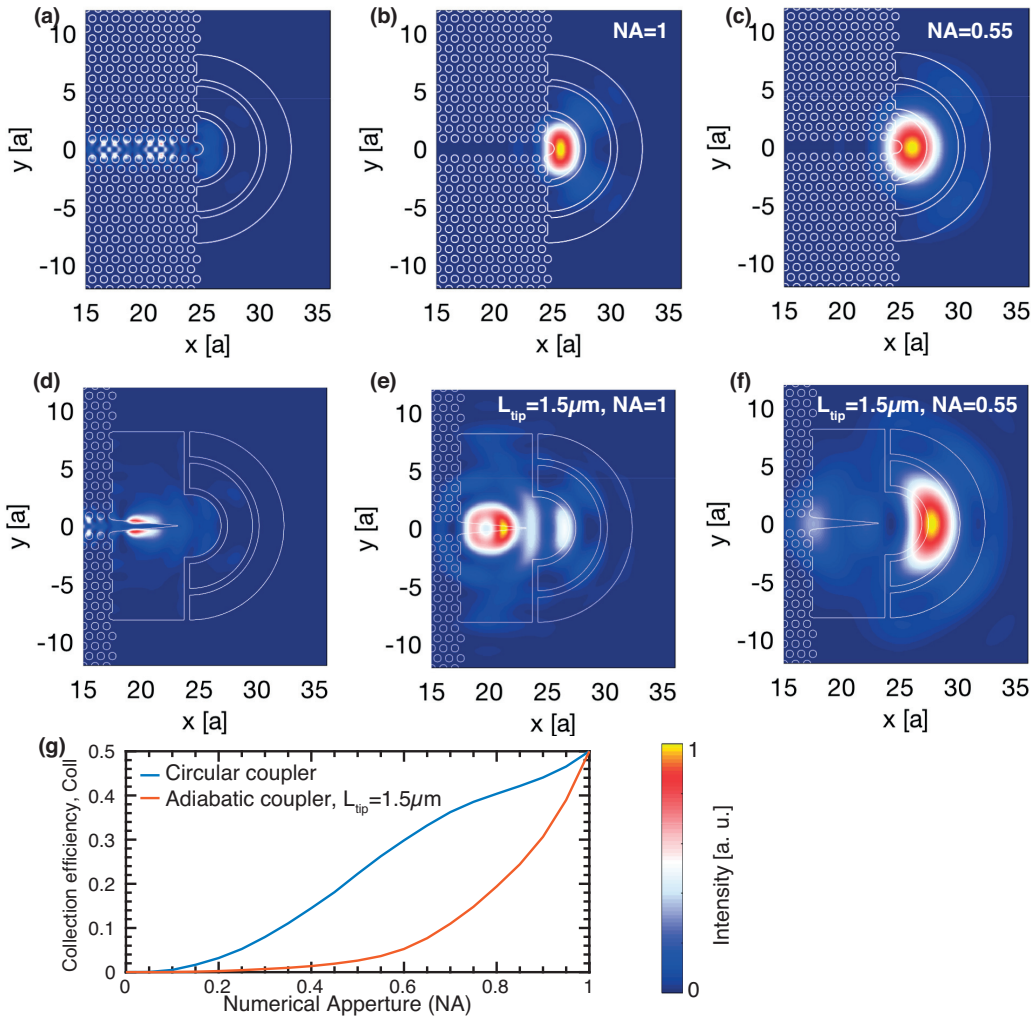

Figure 5.7 – Continuous wave FDTD modeling of couplers: (a) Near field intensity above the slab in a circular coupler; (b) Radiation modes escaping from a circular coupler; (c) Radiation modes collected by a NA=0.55 objective above a circular coupler; (d) Near field intensity above the slab in an adiabatic coupler; (e) Radiation modes escaping from an adiabatic coupler; (f) Radiation modes collected by a NA=0.55 objective above an adiabatic coupler; (g) Collection efficiency of the couplers (n=3.46, a=225nm, r=61nm, slab thickness=250nm, the wavelength of the continuous wave source in the simulations was $\lambda = 950nm$)

The result is then integrated over one oscillation time period, and we obtain the intensity image collected by the lens:

$$I_{coll}(x,y,NA) = \int_P \left[\mathscr{IF}_t(t_{lens}(k_x,k_y,NA)\cdot\mathscr{F}_t(E_i(x,y,t)))\right]^2 dt \tag{5.2}$$

where $t_{lens}(k_x,k_y,NA) = 1$ when $\sqrt{k_x^2+k_y^2} < NA\cdot\omega/c$ and zero otherwise. The

near field patterns, radiation modes pattern and collected radiation modes pattern are indicated for each coupler on Fig. 5.7(a-f). Such visualization of the leaky components permits to distinguish between the different sources of light, which is useful for the analysis of photonic structures. Notice the oscillations of the waveguide envelope function on Fig. 5.7(a) indicating reflection from the coupler. The coupling efficiency is then obtained by integrating the light intensity escaping the slab, and that collected by the microscope objective. The collection efficiency for each coupler is defined by:

$$Coll(NA) = \frac{\int I_{coll}(x, y, NA)dS}{\int I_{coll}(x, y, 1)dS} \tag{5.3}$$

This parameter is shown on Fig. 5.7(g). Note that in z-symmetric PhC devices, the collection efficiency is necessarily lower than 0.5 because half the intensity is lost downward. The values obtained for the circular coupler (in blue): $Coll(NA = 0.65) = 0.33$ and $Coll(NA = 0.82) = 0.40$ are slightly higher than those computed by Arcari et al. [104]: $Coll(NA = 0.65) = 0.23$ and $Coll(NA = 0.82) = 0.34$, as a result of slightly different parameters in our design. The adiabatic coupler on the contrary features a much lower coupling efficiency to conventional NA objectives, with $Coll(NA = 0.65) = 0.08$ and $Coll(NA = 0.82) = 0.19$. This indicates that adiabatic couplers scatters a more significant fraction of light with a low angle with respect to the slab plane contrary to the circular coupler. This low coupling efficiency found its explanation by visualizing the collected intensities for varying values of the numerical aperture depicted on Fig. 5.7(b-c-e-f). The picture collected from the circular coupler by the microscope objective (Fig. 5.7(c)) displays features similar to that of the radiation modes (Fig. 5.7(b)), albeit with a lower resolution causing the broadening of the collected spot. On the contrary, the radiation mode picture and that collected by the microscope objective from the adiabatic coupler displays very different features. Most of the intensity escaping the adiabatic coupler originates from the adiabatic tip as is clear from Fig. 5.7(e). However, the NA=0.55 collects mostly light scattered by the Bragg grating as observed on Fig. 5.7(f). The interpretation of this low coupling efficiency is therefore clear. As simulated by Arcari et al. [104], adiabatic tips scatter light with a relatively broad angle. Only the fraction of light incident on the Bragg grating is efficiently outcoupled. A significant fraction of it is emitted above or below the grating. This fraction can only be collected by a very large NA objective. These results clarify the limits of this adiabatic coupler design, which displays broadband outcoupling and low reflection, but also suffers from low collection efficiency by narrow NA objectives.

5.2 Site-controlled QD placed in a cavity coupled to a PhCW

5.2.1 Optimal photon extraction from a QD placed in a cavity coupled to a waveguide

Obviously, in a system made of a QD coupled to a waveguide through a cavity mode, there is a tradeoff between long optical confinement times and efficient light extraction. In this subsection, we will present a model giving mathematical substantiality to this intuition.

The exciton emission rate into the bulk GaAs is usually divided into a radiative emission rate: Γ_{rad} and a non-radiative emission rate Γ_{nc}. Once placed in a PhC cavity, the radiative emission rate is modified via the Purcell effect. The presence of the PhC bandgap leads to a reduction of this radiative emission rate: $\Gamma_{rad}^{bg} = F_p^{bg}\Gamma_{rad}$, where F_p^{bg} is the Purcell emission factor into all modes other than the target cavity mode. The presence of a cavity mode near resonance with the exciton emission opens another decay channel: $\Gamma_{rad}^{cm} = F_p^{cm}\Gamma_{rad}$ as shown on Fig. 5.8(c). F_p^{cm} is the Purcell emission factor into the target cavity mode. F_p^{cm} depends on the intrinsic cavity emission rate: γ_{cm} depicted on Fig. 5.8(b). The total exciton emission rate is then: $\Gamma_{uc} + \Gamma_{rad}^{cm}$, where the exciton loss rate is: $\Gamma_{uc} = \Gamma_{nc} + \Gamma_{rad}^{bg}$ as depicted on Fig. 5.8(a). Γ_{uc} depends on the exact position and dipole orientation of the exciton. It also depends on the photonic environment. Coupling the cavity to the PhCW opens another decay channel for the cavity mode as depicted by the sketch of the complete QD-cavity-waveguide system shown on Fig. 5.8(e). This decay to the PhCW, is characterized by the cavity-to-waveguide coupling rate: κ.

In experimental realizations, almost all these parameters are limited by fabrication imperfections. They can be statistically assessed, and most parameters suggest an obvious optimum for realizing single photon sources. The intrinsic cavity emission rate γ_c and QD loss rate Γ_{uc} should be as small as possible. The QD emission rate inside the isolated cavity Γ_{rad}^{cm} should be as large as possible (although this value is limited ultimately by the advent of the strong coupling regime). The cavity to waveguide coupling rate κ on the contrary is a free parameter, easily controlled by varying the cavity to waveguide distance (or refractive index barrier). Besides, when κ is very large, the extraction into the waveguide is efficient, but the cavity is weakly confined and the Purcell effect is reduced. When κ is very small, no light is extracted from the cavity, and the extraction from the QD to the waveguide is reduced. As sketched before, this tentative argument suggests there is an optimum for photon extraction in such systems.

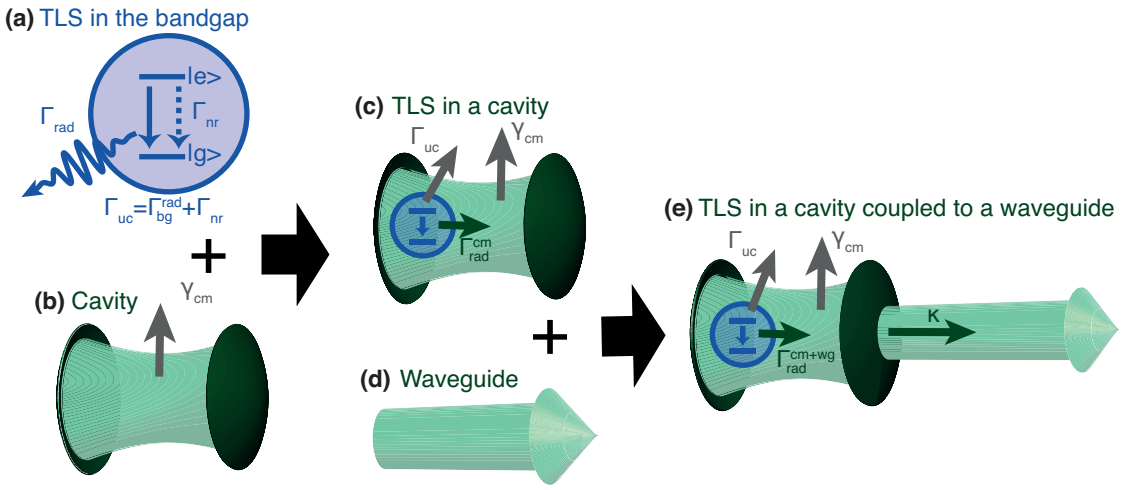

Figure 5.8 – Sketch of the model: (a) Two level system (TLS) placed in the PhC bandgap; (b) Isolated cavity; (c) TLS interacting with a cavity in the weak coupling regime; (d) Waveguide; (e) TLS interacting with a cavity coupled to a waveguide.

This point is made more rigorous using an approach based on a paper by Yao et al. [153], which adopts a Green function formalism to describe a system made of a QD in a cavity coupled to a Fabry-Pérot PhC waveguide. In this framework, the spontaneous emission rate of the QD into the cavity mode, when it is coupled to the waveguide (Fig. 5.8(e)) is given by:

$$\Gamma_{rad}^{cm+wg} = \frac{2Im(\vec{d}\cdot G(r_d,r_d).\vec{d})}{\hbar\epsilon_0} \tag{5.4}$$

$$= \frac{2|\vec{d}\cdot\vec{E}_c(r_d)|^2\omega_{cm}}{\hbar\epsilon_0(\kappa+\gamma_{cm})} \tag{5.5}$$

where $\vec{d}$ is the exciton dipole momentum and G is the Green function [153] of the coupled cavity-waveguide system, $\vec{E}_c(r_d)$ is the electric field amplitude of the cavity mode at the QD position, ω_{cm} is the cavity resonance angular frequency. This emission rate can be expressed using the set of parameters proposed before:

$$\Gamma_{rad}^{cm+wg} = \Gamma_{rad}^{cm}\frac{\gamma_{cm}}{(\kappa+\gamma_{cm})} \tag{5.6}$$

where Γ_{cav} is the spontaneous emission rate in the uncoupled cavity. This expression for the on resonance spontaneous emission rate has an obvious interpretation. It is exactly similar to the emission rate in an isolated cavity except for the cavity emission rate, which has to include the two decay channels: κ and γ_{cm}. The beta

factor, i.e. the QD emission efficiency into the composite cavity mode is then obtained as:

$$\beta = \frac{\Gamma_{rad}^{cm+wg}}{\Gamma_{rad}^{cm+wg} + \Gamma_{uc}} = \frac{1}{1 + \Gamma_{uc}/\Gamma_{rad}^{cm}(\kappa/\gamma_{cm} + 1)} \tag{5.7}$$

Defining the QD loss ratio as: $r_{loss} = \Gamma_{uc}/\Gamma_{rad}^{cm}$, β can be rewritten as:

$$\beta = \frac{1}{1 + r_{loss}(\kappa/\gamma_{cm} + 1)} \tag{5.8}$$

The cavity to waveguide coupling efficiency is defined as:

$$\gamma = \frac{\kappa}{\kappa + \gamma_{cm}} \tag{5.9}$$

In which case, the the total coupling efficiency of a single QD to the waveguide mode is:

$$\epsilon = \gamma\beta \tag{5.10}$$

This total coupling efficiency is non-monotonous and is maximized for:

$$\kappa_{opt} = \gamma_{cm}\sqrt{1 + 1/r_{loss}} \tag{5.11}$$

Note that the optimal value for κ is always higher than γ_{cm}. When $\kappa = \kappa_{opt}$, the coupling efficiency becomes:

$$\epsilon_{opt} = 2r_{loss} + 1 - 2r_{loss}\sqrt{1 + 1/r_{loss}} \tag{5.12}$$

The three coupling efficiencies: γ_{opt}, β_{opt} and ϵ_{opt} when $\kappa = \kappa_{opt}$ only depend on r_{loss}. They are displayed on Fig. 5.9.

We can distinguish two regimes of coupling: first when the QD losses are high: $r_{loss} \gg 1$, the optimum is found when the cavity loss rate is equally distributed between the two decay channels : $\kappa \approx \gamma_{cm}$ (which implies $\gamma_{opt} \approx 0.5$) and the highest possible efficiency is:

$$\epsilon_{opt} \approx \frac{1}{4r_{loss}} \tag{5.13}$$

In the second regime, the losses are small: $r_{loss} \ll 1$, in which case, the optimal κ is: $\kappa \approx \gamma_{cm}/\sqrt{r_{loss}}$ and ϵ_{opt} can be expanded to the first order:

$$\epsilon_{opt} \approx 1 - 2\sqrt{r_{loss}} \tag{5.14}$$

In this case, the losses are equally distributed between the QD losses Γ_{uc} and the cavity losses γ_{cm}. The optimal values for β_{opt} and γ_{opt} are: $\beta_{opt} \approx \gamma_{opt} \approx 1 - \sqrt{r_{loss}}$. Note that this model and the optimum derived applies equally well to any alternative experimental realization of a TLS coupled to a cavity itself coupled to a waveguide.

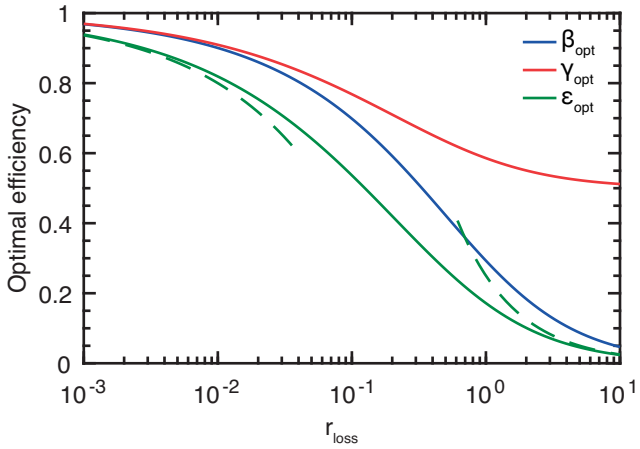

Figure 5.9 – Optimal coupling efficiencies β_{opt}, γ_{opt} and ϵ_{opt}; the dashed green lines represent the first order expansions on ϵ_{opt} for large and low values of r_{loss}.

5.2.2 Design of a QD-cavity-waveguide system

The system theoretically studied in the precedent part will now be experimentally demonstrated and analyzed.

5.2.2.1 Fabricated structures

The design adopted in this chapter for realizing on chip single photon sources consists of an L_3 cavity where one QD (the TLS) is integrated at the maximum of the isolated cavity optical field to ensure a maximum Purcell enhancement (Fig. 5.10(a)). This cavity was optimized by Minkov et al. [73] to obtain a theoretical Q-factors of 200000. In this specific design, three holes were shifted outwards along the x direction by 0.23a, 0.15a and 0.048a as indicated on the inset of Fig. 5.10(a). The L_3 cavity was side-coupled to a W1 waveguide, terminated by a PhC reflector at one end (with the same hole shifts than the L_3 cavity: 0.23a, 0.15a and 0.048a) and by the adiabatic coupler at the other end. The cavity was located adjacent to the closed edge of the semi-waveguide, which as we will show is essential in guaranteeing the deterministic coupling from the cavity to the PhCW.

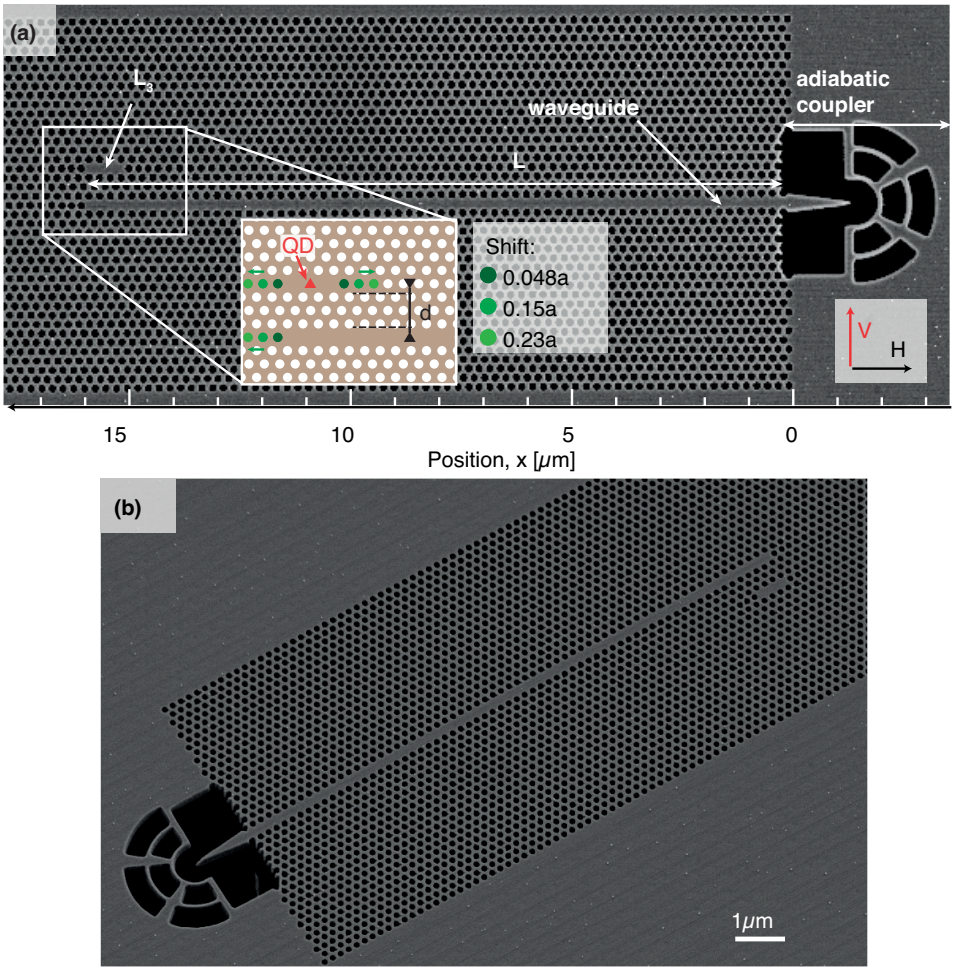

Figure 5.10 – (a) Scanning electron micrograph of the cavity-waveguide structure; inset: schematic illustration of the design of the system; the red triangle indicates QD position; (b) scanning electron microscope image of the cavity-waveguide structure.

A new membrane sample, dedicated to this experiment, was fabricated with exactly the same parameters as described in Chapter 2 for the membrane fabrication (250nm thick GaAs membrane) and the QD growth. The exact same experimental procedure was used to etch the PhC pattern except for the SiO_2 thickness of the ICP mask which was 100nm, and the ICP etching time which was 400s. An alignment between the site controlled QDs and the PhC pattern better than 30nm was measured using the technique exposed in Chapter 2.

The fabricated sample contained cavities with 4 different cavity to waveguide distances d_p corresponding to: p=1-3-5 and 7 holes. The waveguide distance will be referred in this work as $d_p = \sqrt{3}p/2$ where p is the number of holes separating the cavity from the PhCW channel (see Fig. 5.10 for exact configuration). Because of the narrow linewidths of the cavity modes, and the larger inhomogeneous broadening of

QDs ($\approx 13meV$), coupling QDs to the optical field relied on the fabrication of six series of 15 structures for each value of p in which the radii were linearly spaced between 43 and 58nm, which ensured a scanning of the cavity modes across the QD emission energy.

5.2.2.2 Theory of cavity to semi-waveguide coupling

The correct design of a cavity-waveguide system requires an understanding of the coupling mechanism controlling the emission by the cavity into the waveguide mode. The coupling rate between a cavity and a semi-waveguide κ was studied by Yao et al. [153] who proposed an analytical expression based on perturbation theory:

$$\kappa = \frac{1}{1+r^2-2r\cdot cos(2kL)}\frac{a\omega}{v_g}|V_{kc}| \tag{5.15}$$

where r is the amplitude reflection coefficient of the adiabatic coupler, L is the waveguide length, v_g is the waveguide group velocity, a is the PhC lattice parameter and $|V_{kc}|$ is proportional to the overlap between the cavity and the semi-waveguide (isolated) electric field at the cavity frequency.

This expression yields significant insights into how the coupling between a cavity and a waveguide is best achieved. First, the Fabry Pérot resonances of the waveguide modulates the coupling rate κ by a factor: $(1+r)^2/(1-r)^2$ which can be $\approx 2-3$ with the adiabatic couplers we are using, and ≈ 30 for circular couplers. This coupling rate increases with n_g and with the overlap between the cavity and waveguide mode. As both, the cavity and waveguide mode fields decrease exponentially in the PhC regions, the coupling rate also decreases with the cavity to waveguide distance.

The FP modes that were extensively studied in Chapter 3 exhibit sinusoidal envelope modulations of the order of $1.5\mu m$ at the M_0 cavity mode energy. These spatial modulations may affect the reproducibility of the cavity-to-waveguide coupling rate as the cavity overlap with the FP mode may be exactly cancelled by this spatial envelope modulation effect modelled by the V_{kc} coefficient. An alternative but equivalent analysis of this effect is obtained by observing that the cavity couples simultaneously to the two counter-propagating Bloch modes. One of the modes is then reflected by the semi-waveguide reflector and interferes with the other Bloch mode. When the interference is perfectly destructive, the coupling rate from the cavity to the waveguide is cancelled. This effect takes place even in a perfectly open semi-waveguide with zero reflection coefficient from the output coupler. Note that using this effect, a local variation of the refractive index (through carrier injection for example [197]) may represent an efficient method to achieve a dynamic control over the coupling between the cavity and the waveguide.

This issue is solved in the design adopted in this study where the cavity is placed near the semi-waveguide ending, where there is always a maximum of the FP mode.

On the contrary, when the cavity is placed closer to the semi-waveguide center, the disorder induced fluctuations of the cavity energy prevents the achievement of a reproducible cavity to waveguide coupling. As a conclusion, a broadband coupling of the cavity to the waveguide mode in realistic disordered PhC systems requires placing the cavity near the end of the semi-waveguide and limiting unwanted reflections from the coupler. These two conditions are realized in the design presented on Fig. 5.10(a).

5.2.2.3 FDFD simulations of the cavity-waveguide coupling rate κ

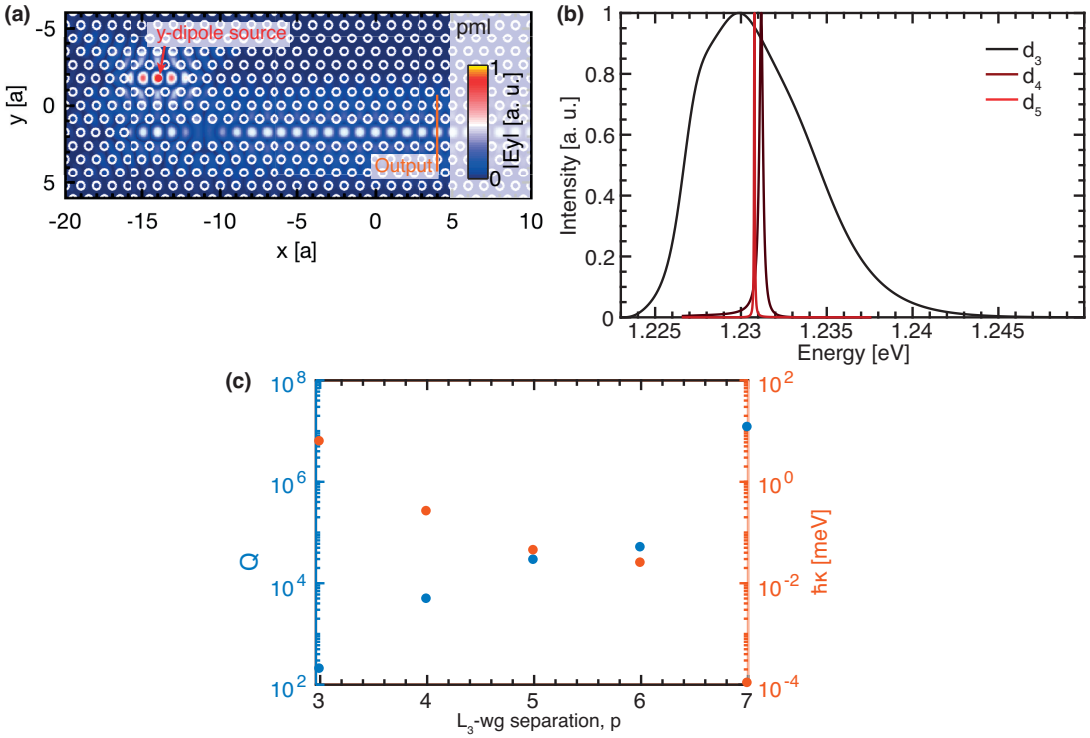

Figure 5.11 – FDFD simulation of L_3 cavities side coupled to a W1 semi-waveguide: (a) $|E_y|$ component of the propagating electric field (Dipole source emission energy: $E = 1.23eV$), the red dot indicate the position of the y-dipole source on resonance with the cavity mode; (b) Spectra obtained for the simulations of 3, 4 and 5 hole distances between the cavity and the waveguide; (c) 2D-FDFD simulated Q-factors (in blue) and coupling rates $\hbar\kappa$ (in red). (Parameters of the FDFD simulation: r=55nm, a=225nm, $n_{2D} = 3.17$, pml parameters: $\sigma = 0.01$, pml length: 30a on the x>0 edge)

The coupling rates κ in our design were simulated using 2D FDFD [120]. A y-dipole was placed at the maxima of the cavity field, emitting light at a frequency which was scanned through the cavity mode frequency: one simulation was performed for each frequency within a frequency range overlapping the energy of the cavity mode. The structure was surrounded by pml layers with a width of 1a, except on the waveguide

output, where the pml size was 30a. An example of such a simulation is given in Fig. 5.11(a), where the L_3 cavity mode decaying inside the waveguide is clearly seen. For each simulation the output power through the orange line was recorded, through which the DOS at the position of the QD could be obtained [18].

The normalized results of such simulations (Fig. 5.11(b)) show the broadening of cavity modes, when d_p decreases as predicted by coupled mode theory [153, 185]. The cavity mode is blue-shifted from p=3 to p=4 as expected from a reduction of the cavity confinement. For p>4, the cavity shift with p was non-monotonous possibly because of insufficiently converged simulations (note that the variations observed here correspond to $\approx 3 \cdot 10^{-4} \times$ the cavity energy).

The Q-factors of these coupled cavities increases roughly exponentially with p as shown on Fig. 5.11(c). This increase is equivalent to an exponential decrease of the cavities coupling rates κ. This dependence is consistent with coupled mode theory [153, 185] according to which the coupling rate is given by the overlap of the waveguide and the cavity field. Indeed, the cavity and the waveguide field decay exponentially in the PhC region due to the absence of guided modes. The resulting exponential decrease of their overlap with d_p induces the exponential decrease of $\kappa$and increase of Q.

5.2.3 Coupling the cavity to the waveguide – the γ factor

We will now demonstrate the emission of photons from a QD into a cavity mode and then into a waveguide and measure all related experimental parameters in two step: a first step will focus on the coupling between cavities and waveguides measured by γ. In the second part, the coupling between a QD and a cavity characterized by β will be measured.

5.2.3.1 Direct imaging of the guided light

The effect of coupling a cavity to a waveguide mode was observed first through spectrally resolved imaging. The photonic structure was probed by high power excitation of isolated QDs ($P = 1000\mu W$), thereby exciting all cavity modes overlapping the QDs thanks to the broad QWR emission [96]. Three representative examples of such spectrally resolved pictures are given on Fig. 5.12(a), on which the emission by the cavity and the adiabatic coupler are distinguished. The collection intensity ratio between the light collected from the coupler and light collected directly from the cavity increases while p decreases as is expected from the increased coupling.

This effect is characterized statistically on Fig. 5.12(b). The ratio of light intensity collected from the adiabatic coupler to light intensity collected from the cavity is plotted for the three values of p (and for hole radius between 45 and 47nm). As expected, this ratio is larger for smaller values of p. The average ratios are 12.8 ± 0.5

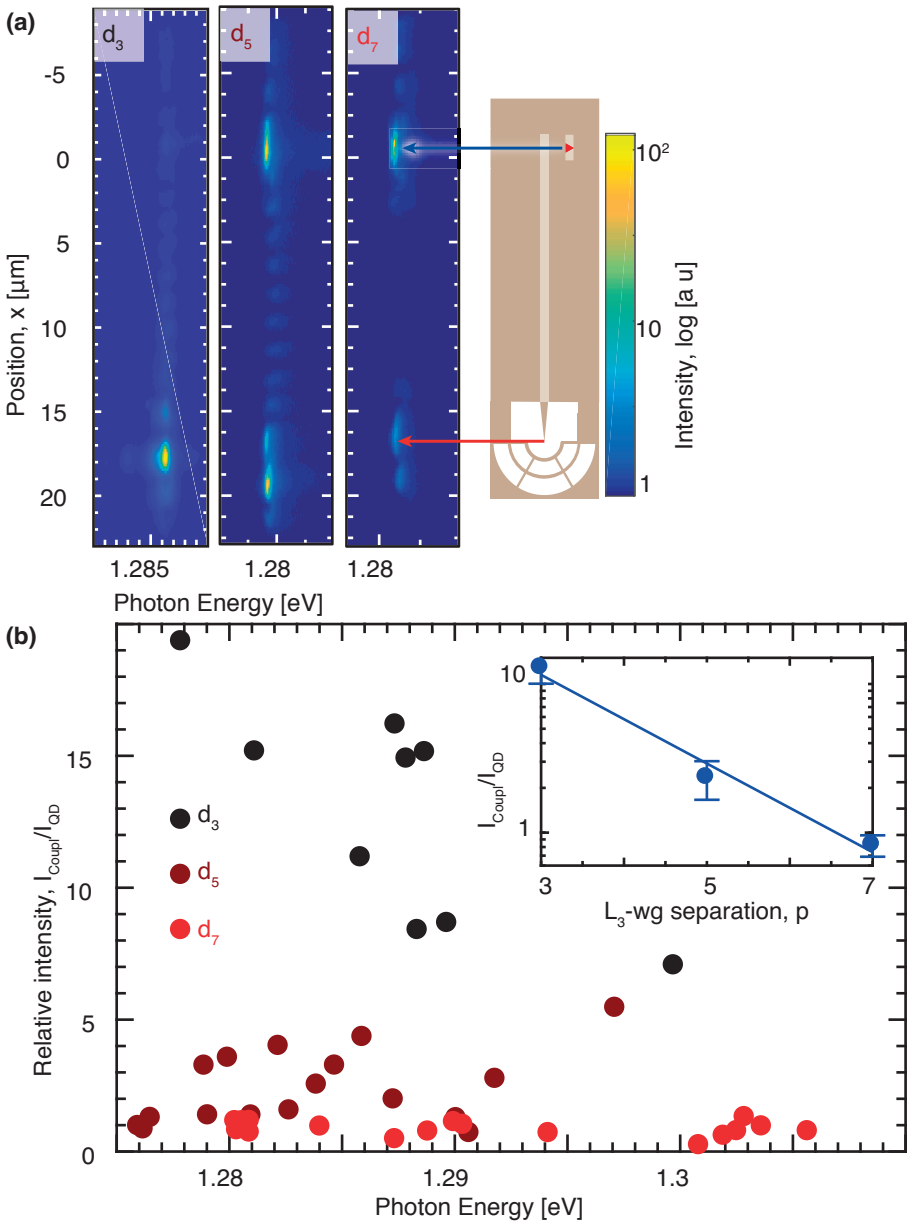

Figure 5.12 – (a) Three spectrally resolved pictures of a system of one cavity coupled to a semi-waveguide (P = 1000μW, T=10K, spectrometer slit width: 100μm, hole radii: 45nm); (b) Ratio of the light intensity collected from the coupler and from the cavity (P = 1000μW, T=10K, slit width: 100μm, hole radii: 45-47nm), for different separations d, no significant fluctuations of the relative intensities were observed in this range of radii. Inset: average of I_{coupl}/I_{QD} for all values measured in (b). The blue line is a linear fit; the error-bars indicate the 95% confidence interval on the average values.

for p=3, 2.2 ± 0.1 for p=5 and 0.82 ± 0.02 for p=7, indicating an increase of emission into the cavity mode for lower p (the error-bars are the 95% confidence interval of the average ratio). No significant fluctuations of the relative intensities were observed for similar cavity-waveguide separations in this narrow range of radii.

The average intensity ratio is given in the inset of Fig. 5.12(b) as a function of p. The error-bars represent the 95% confidence interval for the average ratios. The decrease of coupling is reasonably well fitted by an exponential reduction of the ratio with p (inset of Fig. 5.12(b)): $I_{coupl}/I_{QD} = 89.1 \cdot 10^{-0.298p}$, which is similar to the exponential decrease of coupling simulated on Fig. 5.11(d).

These results prove the emission of light by the QD into the cavity and then through the waveguide. They also demonstrate the impact of increased coupling on the intensity emitted through the waveguide. However, although this technique demonstrates the existence of coupling, it does not allow for a measurement of the coupling rate without an additionnal and complex modelling of the cavity-waveguide structure. Indeed, although 3D FDTD modelling and spectrally resolved measurements may allow for an estimation of the intensity of emissions from the cavity to the waveguide and into the radiation modes. The cavity and QD emissions are difficult to separate experimentally and may affect the reliability of such a method. We will therefore focus on an alternative technique based on cavity loss measurements for measuring the coupling rate κ.

5.2.3.2 Measurement of the coupling rate κ

The energy and Q-factors of M_0 modes in the L_3 cavities were measured for each fabricated (composite) structure by exciting the QD with a high power excitation and by fitting a lorentzian on each cavity line. Five additional series with only one isolated L_3 cavity were also measured with the same method. The spectra were collected directly from above the cavities for the 6 series of structures with p=5 or 7 and the isolated L_3 cavities. When p=3, the cavity emission above the slab was too low and the spectra were collected from the adiabatic coupler.

Fig. 5.14(a) shows examples of these spectra on which signs of coupling are already apparent from the increased cavity Q-factors (from 3700 to 8000) when the distance to the waveguide increases. The variations of the cavities energy with the hole radius is given on Fig. 5.14(b). The resonances are redshifted with increasing p in line with FDFD simulations. However, the observed redhift $\approx 10meV$ between the isolated L_3 and coupled structures with p=3 contrary to pthe expected blue shift, which suggests that this effect is related to fabrication fluctuations of hole sizes at different zones of the sample.

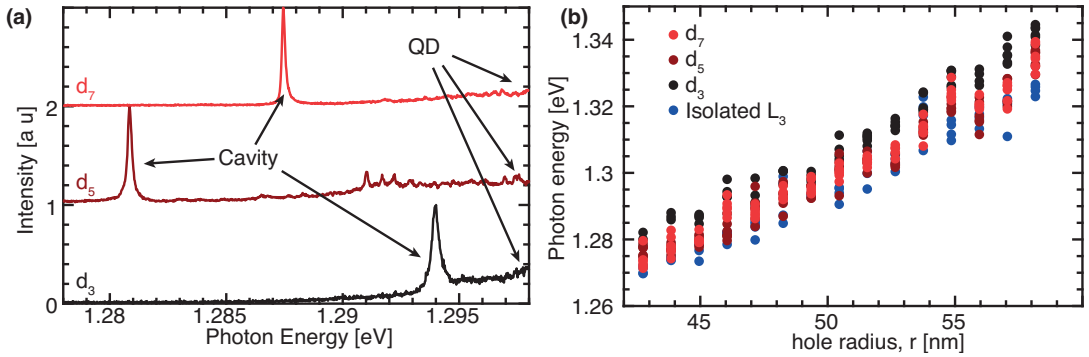

Figure 5.13 – Experimental study of M_0 modes in L_3 cavities coupled to waveguides: (a) Three high power spectra of cavities coupled to waveguides (r=46nm); (b) Energy emission of L_3 cavities (T=10K, $P = 1000\mu W$).

The Q-factors of each measured spectra were extracted from the lorentzian fits as shown on Fig. 5.14(a). The Q-factors of isolated cavities are decreasing with increasing hole radius as was already observed in Chapter 2. As expected from FDFD simulations, the average Q-factor at a given hole size is increasing with p and is maximal for isolated L_3 cavities. For each value of p, the Q-factor dependence on the PhC hole radius was fitted with a 2^{nd} order polynomial. The result of each fit is indicated as a solid line on Fig. 5.14(a). The 95% confidence interval of the average Q value for each type of structure is depicted as shaded areas. When the average fitted Q-factor between different types of structures is separated by more than their respective 95% confidence interval, the Q-factor separation is statistically significant, which is the case in the radii range: r=43-55nm. In this range, the observed Q-factor differences indicate an effect of coupling.

In the regime of coupled mode theory, the Q-factor of a loaded cavity is given by:

$$\frac{1}{Q_{cm+wg}} = \frac{1}{Q_{cm}} + \frac{1}{Q_{wg}} = \hbar(\kappa + \gamma_{cm})/E_{cm} \tag{5.16}$$

where Q_{cm+wg} is the Q-factor of the cavity mode coupled to the PhCW (red and black lines on Fig. 5.14(a)), $Q_{cm} = E_{cm}/(\hbar\gamma_{cm})$ is the Q-factor of the isolated cavity mode (blue line on Fig. 5.14(a)), $Q_{wg} = E_{cm}/(\hbar\kappa)$ models the coupling to the waveguide, and E_{cm} is the cavity energy. The measured values of Q_{cm+wg} then yields an estimation for $\hbar\kappa$. The average coupling rate thus estimated is plotted on Fig. 5.14(b). Its value ranges between $\approx 0.1-1meV$ for p=3 and $\approx 0.05-0.3meV$ for p=5, and is $< 0.2meV$ for p=7, although in this last case, the fitted average Q-factors Q_{cm+wg} (red line) and Q_{cm} (blue line) are too close for a precise estimation of the coupling rate except in the r=43-47nm range. 2D-FDFD simulation of these structures with r=55nm (shown on Fig. 5.11) yielded $\hbar\kappa = 6.1meV$ for p=3, $\hbar\kappa = 44\mu eV$ for p=5 and $\hbar\kappa = 0.11\mu eV$ for p=7. Although the range of values measured for p=5 and 7 match

those simulated, the one simulated for p=3 is around one order of magnitude larger than the measured value, possibly because 2D simulations are not precise enough. These measurements also demonstrate a decrease of κ when the PhC hole radius increases for p=3. This probably arises from the lower confinement of PhC modes when the PhC hole radius increases, which induces an increased overlap the cavity and waveguide modes.

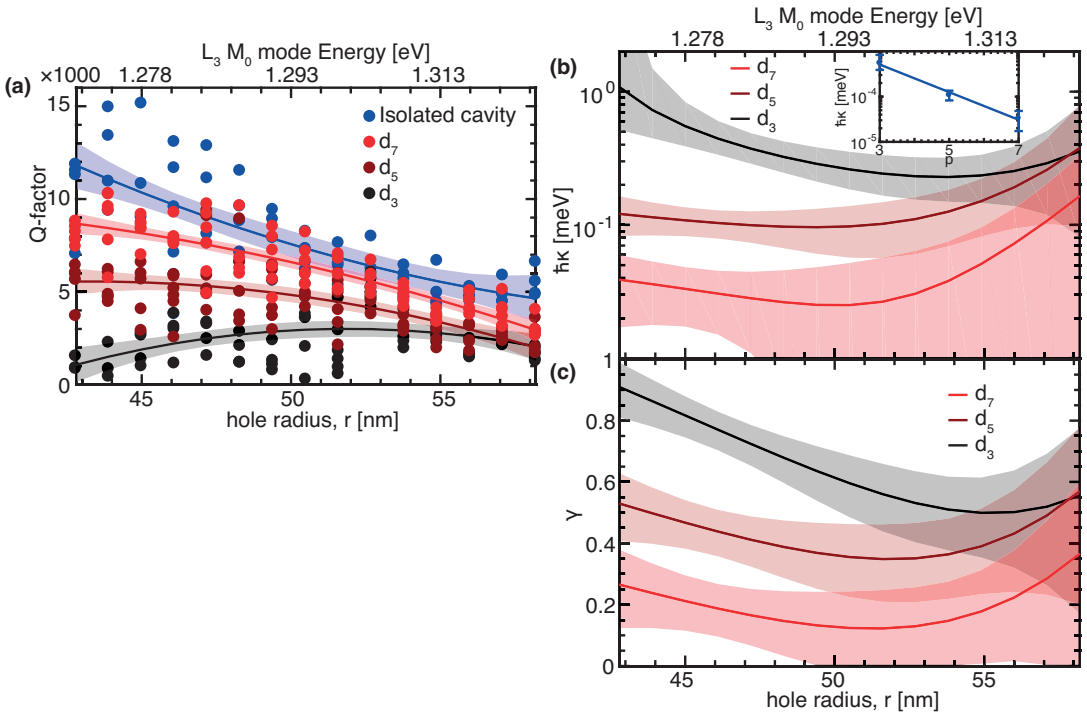

Figure 5.14 – Experimental study of M_0 modes in L_3 cavities coupled to waveguide: (a) Measured (dots) and fitted (lines) Q-factors (the lines are 2^{nd} order polynomial fits on the Q-factor distributions); (b) coupling rates $\hbar\kappa$ estimated from the Q-factors distribution; inset: coupling rate $\hbar\kappa$ dependence on p and exponential fit (r=45nm); (c) coupling efficiency estimated from the Q-factor distribution (T=10K, $P = 1000\mu W$); in figures (a-b-c), the error-bars are the fitted 95% confidence interval on the average value of Q, κ and γ.

The decay of $\hbar\kappa$ was fitted with an exponential decay (Inset of Fig. 5.14(b)) yielding the following decay parameters: $\hbar\kappa(p) = 4.2 \cdot 10^{-0.305p} meV$. Note that the exponent 0.305 is close to the one obtained via direct imaging of outcoupled light on structures with similar radius, which was 0.298. On the contrary, the coefficient obtained from an exponential fit on the simulated coupling rates (Fig. 5.11) is 1.05, i.e. much larger. This difference may originate from an increase of the attenuation length of confined modes into the PhC induced by disorder, in line with previous results from simulations [198]. This increased attenuation length of confined modes would then increase the overlap

of the cavity and waveguide modes and the coupling rate for large values of p.

The transmission efficiency from the cavity to the waveguide, represented by the parameter γ, is then extracted on Fig. 5.14(c) from the measured values of κ and γ_{cm}. A cavity-waveguide separation of p=3 permits a large transmission up to 0.9 (r=43nm), and is thus our preferred choice for efficient single photon collection. Larger cavity-waveguide separations would be interesting for structures in which unloaded cavities exhibit larger Q-factors.

5.2.4 Coupling the QD to the cavity – the β factor

We will now concentrate on one single QD-cavity-waveguide structure in order to estimate the QD-cavity-waveguide coupling parameters. The knowledge acquired in the last subsections will allow for a complete characterization of this structure and an estimation of the total coupling efficiency ϵ.

5.2.4.1 The cavity to waveguide coupling efficiency

In this perspective, one structure was selected with p=3 and r=51nm. The relatively small cavity to PhCW distance was chosen so as to ensure a large collection of the cavity emission by the waveguide. The cavity Q-factor obtained by fitting a lorentzian line on the cavity mode was: $Q_{cm+wg} = 2040$. The average Q-factor of an isolated L_3 cavity with the same PhC hole radius is $Q_{cm} = 6840 \pm 3780$ (This is the 95% confidence interval of the Q-factor distribution. It was obtained from the polynomial fit on the isolated cavity Q-factor distribution). The coupling rate deduced from the loaded cavity Q-factor Q_{cm+wg} and the average Q-factors of similar isolated L_3 cavities Q_{cm} is: $\hbar\kappa = 464$ (95% confidence interval: $227\mu eV - 533\mu eV$) and the cavity to waveguide coupling efficiency: $\gamma = 0.71$ (95% confidence interval: $0.35 - 0.81$).

5.2.4.2 Tuning a trion through a cavity mode

The QD to cavity coupling efficiency β can be obtained by comparing the exciton decay rate on resonance with the cavity mode $\Gamma_{cm+wg} + \Gamma_{uc}$ to that of the same QD far detuned from the same cavity mode Γ_{uc}, which was achieved by tuning the trion line of this QD, in and out of resonance with the cavity mode. The polarization resolved spectra of this structure are shown on Fig. 5.16(a). The cavity M_0 mode is almost entirely vertically polarized in line with FDTD simulations [109]. From their binding energies, power dependences and polarization splitting, three of the four QD lines observed in this spectra were attributed respectively to the neutral exciton, the trion and the biexciton. The line indicated X^* may be an excited hole state exciton [133].

In line with previous studies, the trion is co-polarized by the cavity [172]. The trion-cavity detuning was controlled by varying the sample temperature. The spectra obtained for each temperature are shown on Fig. 5.16(c). Notice that these spectra

were collected from the adiabatic coupler. In this geometry, only the light emitted through the cavity mode is collected, contrary to similar temperature dependence studies [172] performed on an isolated cavity, where the QD and cavity spectra are mixed. The observation of the QD line for detunings as large as 1.5meV is therefore a property of the cavity spectrum itself and the exciton-cavity coupling mechanisms, manifesting the pure dephasing and phonon assisted feeding of the cavity mode by the QD.

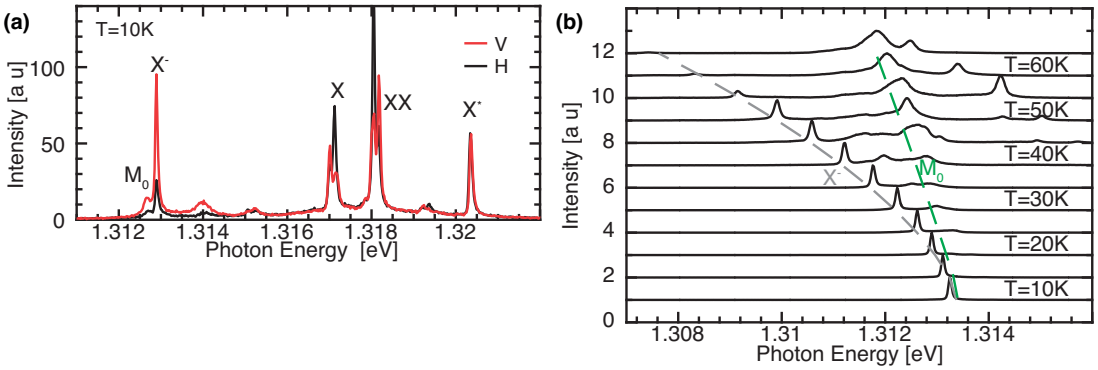

Figure 5.15 – (a) Polarisation resolved spectra of a QD in an L_3 cavity coupled to a waveguide ($P = 5\mu W$, T=10K, p=3, r=51nm); (b) Temperature dependence of the spectra acquired from the coupler ($P = 5\mu W$);

5.2.4.3 TRPL measurement of the β factor

The TRPL of the trion line was measured for each temperature. Three representative examples of these decay curves are given on Fig. 5.16(a). As expected from the Purcell effect, the decay rate is much shorter on resonance with the cavity mode. The model proposed for trion biexponential decay described in Chapter 4 is also applicable to this trion decay. The same notations are used with two decay rates: γ_X the fast decay rate corresponding to the trion intrinsic decay rate and γ_{sl} the slow decay rate resulting from the slow feeding of charge by a neighboring impurity. The observed decay is biexponential on resonance (Fig. 5.16(a)). For detunings beyond 1.5meV, the weaker intensity of the decay curve and did not permit to distinguish two decays. Only a single exponential decay was fitted to obtain γ_X. Each fit was deconvoluted with the APD response time (200ps). The fitted decay rates are shown on Fig. 5.16(c).

The decay rate temperature dependence was fitted with the following model [96]:

$$\gamma_X = \Gamma_{rad}^{cm+wg}(T) + \Gamma_{uc}(T) \tag{5.17}$$

where the trion emission rate into the loaded cavity is:

$$\Gamma_{rad}^{cm+wg}(T) = \frac{F_p}{\tau_0}\frac{1}{2}\frac{(\gamma_{cm+wg}+\gamma_d)\gamma_{cm+wg}}{(\gamma_{cm+wg}+\gamma_d)^2+(2\Delta E)^2} f \tag{5.18}$$

Here, $\gamma_d = 60\mu eV$ is the trion pure dephasing effective relaxation term, which was obtained from a lorentzian fit on the trion line, $\gamma_{cm+wg} = E_{cm}/(\hbar Q_{cm+wg})$ is the loaded cavity decay rate, and ΔE is the QD cavity detuning. The temperature dependent uncoupled emission rate Γ_{uc} was measured by means of TRPL on the trion of a different QD tuned in the PhC bandgap and is shown on Fig. 5.16(b). This decay rate does not change with temperature up to 40K, until the decay rate starts increasing in a way suggesting a thermally activated process possibly caused by additionnal phonon decay channels or thermally activated nearby impurities in which the trion may decay non-radiatively. This effect was described through the following empirical model:

$$\Gamma_{uc}(T) = A + Be^{-\frac{E_a}{k_B T}} \tag{5.19}$$

where the first term corresponds to the temperature independent part of the decay and the second term includes an additionnal thermally activated decay channel. A fit of the temperature dependent decay of Fig. 5.16(b) yielded the following values: $A = 0.22 \pm 0.03 ns^{-1}$, $E_a = 22 \pm 10 meV$ and $B < 29 ns^{-1}$.

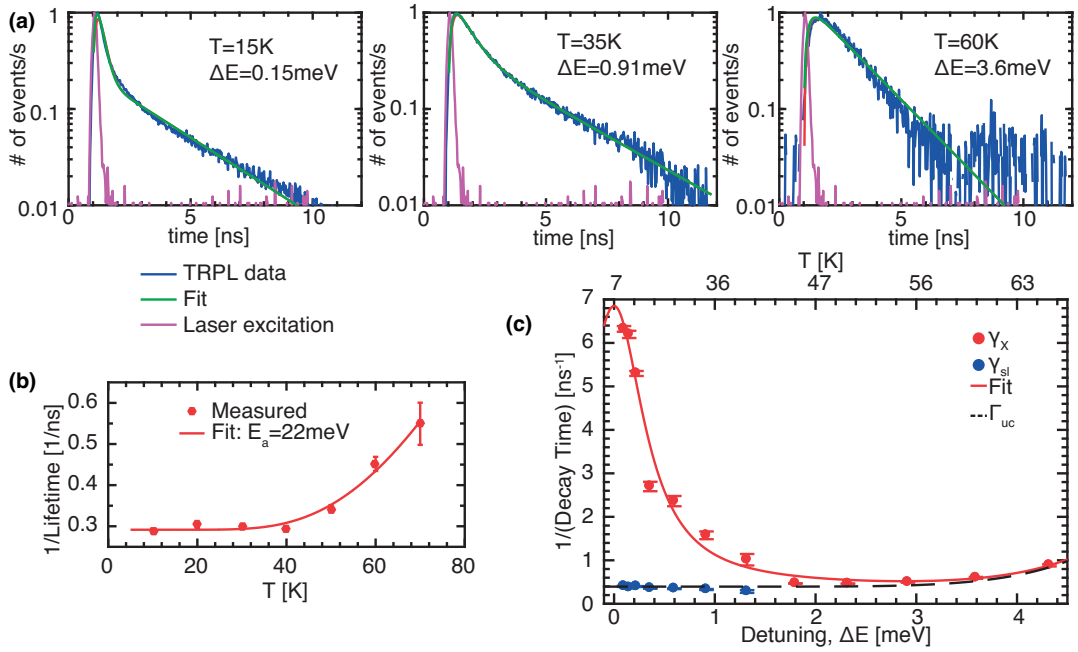

Figure 5.16 – (a) Measured and fitted TRPL decay curves of the trion line for different detunings ΔE; (b) temperature variations of the TRPL decay rates of the X^- transition in a QD placed in the PhC bandgap (r=65nm, Excitation power: $P = 5\mu W$); (c) TRPL decay rates of the X^- transition for different detuning between the X^- and the cavity mode lines (structure with d=3a, r=51nm). The corresponding temperatures are shown on the upper axis. See text for the definition of fitted curves.

The measured γ_X values were fitted with the model shown on Eq. 5.17 (red line on Fig. 5.16(c)). From the fit, we extracted $F_p/\tau_0 = 14.3 \pm 2.0 ns^{-1}$. A Purcell factor value: $F_p = 17$ or $F_p = 34$ is then estimated from two typical emission lifetimes measured on trions placed in the bulk material: $\tau_0 = 1.2ns$ or $\tau_0 = 2.4ns$ [109]. A statistical characterization of the emission from trions would be needed for an accurate assessment of F_p. Only upper bounds of the other fit parameters could be obtained: $A < 0.85 ns^{-1}$ and $B < 138 \cdot 10^6 ns^{-1}$, $E_a < 560 meV$.

Notice that the Purcell factor expected for an in plane TLS placed at the maximum electric field of an L_3 cavity with this value of Q and a mode volume: $V = (\lambda/n)^3$ is $F_p = 151$. However, the probable light-hole nature of s-states holes in our system (see Appendix A) reduces this theoretical Purcell factor to $F_p = 63$. Besides, a misalignment up to 30nm was observed for these structures which can cause a reduction of the overlap between the in plane electric field intensity and the QD by a factor f=0.6. The minimum theoretical Purcell factor expected from these measurements is therefore 38. An additional aspect that may affect the observed reduction of the trion lifetime on resonance is the presence of non-radiative decay, for which we can only give an upper bound given by the lowest trion decay rate measured: $\Gamma_{nr} < 0.46 ns^{-1}$.

Although the fit does not permit a precise estimation for Γ_{uc}, a conservative estimate can be extrapolated from the minimal measured value of γ_X: $\Gamma_{uc} = 0.46 ns^{-1}$. Notice that this value is close to the slow decay rates γ_{sl} measured for detunings $\Delta E < 1.2 meV$. Thus, a possibility is that this value is limited by the slow QD feeding and not by the intrinsic trion decay rate. This value for Γ_{uc} therefore constitutes only an upper bound of the true uncoupled decay rate Γ_{uc}.

The QD to cavity coupling efficiency extrapolated from these lifetime measurements is $\beta = 0.93$. The cavity to waveguide coupling efficiency measured previously is: $\gamma = 0.71$ (95% confidence interval: $0.35 - 0.81$). The total coupling efficiency is thus: $\epsilon = 0.67$. This value is already close to the optimum, however, it can be slightly improved by an adjustment of the coupling rate, using the model described previously. Indeed, the intrinsic cavity decay rate (out-of-plane) is: $\gamma_{cm} = 192 \mu eV$ and the loss ratio: $r_{loss} = 0.021$. The optimal coupling rate is therefore: $\kappa = \gamma_{cm}\sqrt{1 + 1/r_{loss}} = 1300 \mu eV$. With this value of the coupling coefficient, the QD to cavity coupling efficiency β is reduced from 0.93 to 0.86 to reach a larger cavity to waveguide coupling efficiency γ which increases from 0.71 to 0.87. The total coupling efficiency ϵ is then improved from 0.67 to 0.75. The experimental values of each parameters and the values corresponding to the theoretical optimum are given in Table 5.1. Note that only the parameters dependent upon κ are modified in the optimal scheme. The coupling rate κ could be tuned continuously for exemple by shrinking or enlarging the size of holes in between the cavity and waveguide so as to tune the overlap between their modes.

	Measured	Optimal
$\Gamma_{uc}\ [ns^{-1}]$	0.46	0.46
$\Gamma_{rad}^{cm}\ [ns^{-1}]$	22	22
r_{loss}	0.021	0.021
$\Gamma_{rad}^{cm+wg}\ [ns^{-1}]$	6.4	19.5
β	0.93	0.86
$\hbar\gamma_{cm}\ [\mu eV]$	192	192
$\hbar\kappa\ [\mu eV]$	464	1300
γ	0.71	0.87
ϵ	0.66	0.75

Table 5.1 – Summary of measured and optimal parameters in the structure studied in this subsection.

5.2.4.4 Single photon emission

The autocorrelation function $g^{(2)}(\tau)$ of the trion presented on Fig. 5.15 (p=3, r=51nm) was measured in a Hanbury Brown and Twiss setup. The light was extracted directly from the coupler. A zero time delay autocorrelation value of $g^{(2)}(0) = 0.45$ was measured after deconvolution with the instrument response time (200ps) as shown on Fig. 5.17(b).

The autocorrelation of the trion line from a different structure is given on Fig. 5.17(a). This QD was placed in an L_3 cavity, itself coupled to a PhCW, with a cavity-waveguide distance of p=1. The small cavity-waveguide distance induces a broadband cavity-waveguide coupling. In such structures, the QD lines are coupled without any need of energy tuning, which facilitates the extraction of high QD intensities useful for correlation measurements. The zero time delay autocorrelation value measured was: $g^{(2)}(0) = 0.18$.

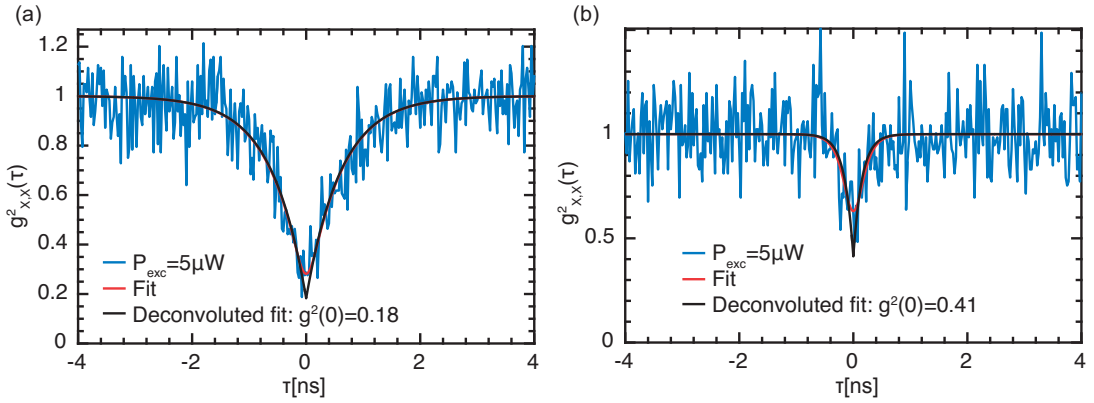

Figure 5.17 – Autocorrelation function of a QD coupled to a waveguide through an L_3 cavity with a cavity to waveguide separation: (a) p=1 ($T = 7K$, $P = 10\mu W$); (b) p=3 ($T = 20K$, $P = 5\mu W$), in each case, the light was collected from the adiabatic coupler

5.3 Chapter summary

This chapter focused on the study of a system made of one QD placed in a cavity coupled to a waveguide. A first part concentrated on the design of an out-of-plane coupler with low and broadband reflection characteristics. The insertion of an adiabatic tip termination between a PhCW and a Bragg grating permitted a reduction of the reflection coefficient from ≈ 0.5 to ≈ 0.1 . This reduced reflection coefficient induces a reduction of the FP modes visibility in a system made of an adiabatic coupler and a semi-waveguide. The reduced visibility of the resulting FP modes is useful to ensure a coupling of cavities to PhCWs resilient to random fluctuations of the cavity energy.

In a second part, we showed that the cavity-waveguide coupling rate could be controlled to maximize the global collection efficiency ϵ from the QD into the PhCW. We demonstrated an experimental realization of this model made by a QD placed in an L_3 cavity coupled to a PhCW, itself terminated by an adiabatic coupler. First evidences of cavity-waveguide coupling were obtained by spectrally and spatially resolved imaging. The coupling rate κ and efficiency γ were measured via a statistical analysis of Q-factors of L_3 cavities coupled and not coupled to PhCWs. Finally, the coupling efficiency from the QD to the cavity $\beta = 0.93$, the coupling efficiency from the cavity to the waveguide: $\gamma = 0.71$ and the the total coupling efficiency $\epsilon = 0.67$ in one structure were obtained. We showed that in this specific structure, a higher global coupling efficiency could be obtained by using a specific coupling rate κ.

These results represent the first demonstration of a site controlled QD integrated in a PhC circuit beyond simple cavities or waveguides and will be useful to the design of future devices. The system presented here may represent an optimal choice for on chip linear optical quantum computing [21].

6 Conclusion and outlook

This thesis focused on the coupling between site-controlled QDs, PhC cavities and waveguides. We used InGaAs/GaAs QDs fabricated using MOCVD growth on arrays of inverted pyramids. The deterministic formation of QDs inside the pyramids permits the integration of well controlled number of QDs in PhC circuits with a precision accuracy around 20nm. These QDs were used throughout this thesis both as broadband point like sources for probing the local density of states in PhCs and as emitters of single photons with the aim of realizing efficient on-chip single photon sources.

In Chapter 2, the experimental methods and techniques used to simulate, fabricate and characterize our devices were described. As a first step the methodology and numerical simulation methods used to design the systems studied in this thesis were described. The nanofabrication techniques and the fabrication steps relevant to our technology were then detailed. The QD ensembles thus fabricated were characterized by means of micro PL spectroscopy. In the course of this thesis, the introduction of a new growth recipe using TEGa instead of TMGa [113] permitted a dramatic improvement of the reproducibility, quality and available wavelength range of pyramidal QD growths. QD lines limited by the resolution of our setup ($20\mu eV$) were observed and the QD s-state emission wavelength could be tuned continuously from 860 to 980nm, while keeping a good quality of the QD ensembles.

However, despite these improvements, a major limitation preventing the use of pyramidal QDs for quantum optics applications is their broadened linewidths. Improving the cleaning process prior to growth and increasing the deoxydation time, may reduce the excitons homogeneous broadening. Another possibility is to use TEIn as a precursor for indium and reduce the carbon incorporation due to the methyl radicals of TMIn. A first growth showed encouraging results in this perspective. Another possibility for improving the QD quality would be to deplete the GaAs lattice impurities from their flickering charges by applying an electric field over the QD [49]. This may bring the optical linewidth of pyramidal QDs even closer to the limit imposed by their

lifetime and would permit to overcome the yet statistical methods in fabricating QDs in PhCs experiments, which would be an essential step for the realization of systems of several QDs interacting in a PhC. One last solution for improving the optical quality of pyramidal QD emission would be based on the resonant excitation of QDs which has been essential for the demonstration of on quantum gates [199] and efficient indistinguishable single photon sources [66]. However, resonant excitation of QDs in PhCs present specific challenges to filter out the laser light which can be scattered into the PhC modes. Another possibility opened by the large degree of freedom offered by the pyramidal QD fabrication technique would be to tailor the QD confinement potential to optimize the electron and hole overlap of excitons confined in the QDs and thus obtain larger dipole strengths.

Finally, the quality of PhC fabrication was assessed by measuring the quality factors of L_3 and L_7 cavities. The possibility to grow QDs at larger wavelengths than was available before permitted to obtain quality factor of M_0 modes in L_3 cavities up to 10000 for the sample presented in Chapters 2-3 and 4 and up to 15000 for the sample presented in Chapter 5, improving on the 1000-4000 values obtained below $\lambda = 900nm$ in previous works [125, 112]. Note that these cavities were fabricated on (111) substrates which is unconventional in the field. The improvement of PhC quality was explained in Chapter 3 as arising from the reduced absorption from GaAs band tail caused by lattice impurities. In that context, the growth of higher purity QD caps may increase further the Q-factors obtained. Another more ambitious objective would be to grow InGaAsP pyramidal QDs in an InP matrix. Indeed, in such heterostructures, the reduction of lattice mismatch may permit the growth of more deeply confined QDs. This advantage may permit the fabrication of telecom wavelength site-controlled QDs with deeply confined excitons, which would reduce the semiconductor band edge related absorption. The PhC quality may also vastly benefit from recent results indicating that surface treatments can reduce the detrimental impact of surface states, both on the cavities Q-factor and on the QD dynamics [200, 170]. The continuous improvements of QDs and PhC cavities Q-factors quality brings us closer to achieving strong coupling with site-controlled QDs, which if combined with the proper tuning mechanisms [100] would constitute an essential building block for scalable on-chip quantum circuits.

A second part of this work focused on the impact of disorder on the losses, density of states, mode localization and dispersion in long linear PhC cavities. Comparison of the finesse in L_n cavities of various lengths permitted to unveil the contribution to losses by absorption, propagation scattering and scattering at the edges [114]. The spectrally resolved mode imaging technique exposed in this thesis permitted the observation of Anderson localized modes and the observation of scattering at the L_n cavity edges indicating that these modes may reach higher Q-factors by a

specific optimization of the edge reflection. Statistical measurement on the dispersion relation of L_{61} cavities pinpointed the boundary between diffusive and dispersive light propagation regimes [201]. The site-controlled QDs were then used as broadband point like light emitters for selective mode excitation and to probe in-situ the impact of disorder. This lead to a second way of identifying the diffusive edge for photon transport, below which phase scattering distorts the optical modes. This in-situ probing permitted a direct measurement of the mode distortion in both regimes, thus highlighting the weak disorder observed in the dispersive regime. These observations strongly support the necessity to use PhCW in the dispersive regime for light transport.

A third part of this thesis was dedicated to studying QDs in PhCs as on-chip sources of single photons using two alternative designs: either QDs directly integrated in PhC waveguides (Chapter 4) or QDs integrated in cavities coupled to PhC waveguides (Chapter 5).

Chapter 4 described a system of five site-controlled QDs integrated in a PhC waveguide [202]. Spectrally resolved imaging lead to the demonstration of on-chip single photon transfer over macroscopic distances. Statistics on the intensity of light coupled to the PhCW compared to that collected out of plane evidenced the effect of the photonic bandgap and the detrimental impact of Fabry-Pérot modes induced by the high coupler reflection to achieve broadband, deterministic coupling of QDs to PhCW. Coupling efficiencies of QDs to PhCW modes up to $\beta = 0.88$ were measured using TRPL measurements. These measurements were realized by taking into account the statistical variations between different QDs, thereby suppressing uncertainties of previous results [104]. We showed that an optimal location of QDs for reproducible broadband high coupling efficiency is near the end of the PhC reflector. In a last part, a short slow light section permitted a reduction of absorption related losses and simultaneously prevented Anderson localization at the QD position. Finally, an optimal design for fabricating reproducible efficient on-chip single photon sources was proposed using a short slow light section. Such a design may prove useful for applications like quantum key distribution in which the precise tuning of each QD is not a strict requirement.

Chapter 5 presented an alternative design for fabricating single photon sources, where a single QD was embedded in a cavity itself coupled to a PhC waveguide [191]. Since the formation of FP modes is detrimental to the reproducible coupling of cavities to PhCW, a first part focused on the demonstration of a low back-reflection outcoupler. A reduction of the FP modes finesse from 8 to 2 was ensured by the insertion of an adiabatic extraction tip in between the PhCW and the Bragg grating coupler. In a second step, we demonstrated the existence of a cavity-to-waveguide coupling which optimizes the coupling efficiency of single photons to the waveguide. The coupling efficiency of the cavity to the waveguide γ was then characterized statistically from

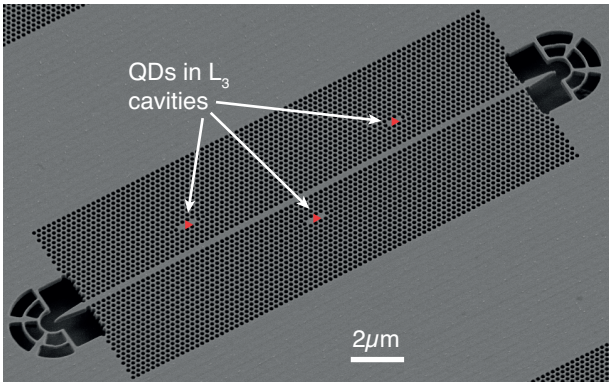

Figure 6.1 – Scanning electron micrograph of a system of three QDs in L_3 cavities all coupled to the same PhCW. The red triangles indicate the positions of each QD.

the variations in Q-factors induced by the presence of the waveguide. Coupling efficiencies up to $\gamma = 0.9$ were observed. In a last step, the coupling efficiency of one single QD to a cavity β was measured as $\beta = 0.93$, and a coupling efficiency from the cavity to the waveguide $\gamma = 0.71$, from which we inferred a global coupling efficiency from the QD to the waveguide of $\epsilon = 0.67$ close to its optimal value. The model described in this chapter indicates that this value could be further improved up to $\epsilon = 0.75$ if the coupling between the cavity and the PhCW was suitably tuned.

This design is optimal for technologies where a precise tuning of the emission energy is required such as quantum computing [7]. Note also that the QD extraction rate in a PhC cavity is usually assumed to be limited by the advent of the strong coupling regime. However, an interesting deisgn for overcoming this limit would consist in a QD placed in an energy tunable PhC cavity coupled to a waveguide, where the QD emits at an energy just below the PhCW band edge. A very bright source of single photon may in this case be obtained by alternatively tuning the cavity on resonance with the QD during a half of a Rabi oscillation and then on resonance with the waveguide for efficient photon extraction. With such a dynamically modulated cavity, the optimal single photon extraction rate evidenced in Chapter 5 could be overcome.

A natural extension of the works presented in this thesis would be the demonstration of non-linear effects induced by single QD in the continuity of the efforts of Javadi et al. [101]. An optimal design for increasing the nonlinearity may be via QDs embedded in cavities side-coupled to a PhCW similar to the structure shown on Fig. 6.1.

Another promising avenue for on-chip quantum photonics is chiral quantum optics [102], in which directional emission of QDs is made possible by a specific design of the PhCW and by the presence of a magnetic field breaking the time reversal symmetry [103]. Chiral effects are very sensitive to the QD location. Hence site-

controlled QDs may unlock the full potential of this new field of research.

A QD dipole moment orientation

One significant parameter of exciton-light interaction is the orientation of the excitons dipole moment, which determines the coupling strength to photonic modes. An in plane dipole moment orientation of the s-state excitonic emission was measured in AlGaAs/GaAs pyramidal QDs [203] grown in $3-4\mu m$ pyramids via cleaved edge PL measurements. However, QDs grown in smaller pyramids may exhibit significant differences in their shape and accordingly in their dipole moment orientation.

The dipole moment orientation is determined by the squared dipolar matrix element for optical transitions exposed in the introduction chapter. The dipole moment orientation is controlled by the nature of holes confined in the QD [203]. Depending on the shape of QDs and within a first approximation, holes are a linear combination of light and heavy hole bands. These holes are distinguished by their angular momentum along the quantization axis (in this case the z-axis): $J_z = \pm 3/2$ for heavy holes and $J_z = \pm 1/2$ for light holes. If the QD exhibit shape anisotropies (such as a strong confinement along the z-direction), this degeneracy can be lifted. The hole states are then a mixture of heavy and light holes. When the QD emission is isotropic in terms of linear polarization in the z-direction, the light intensity emitted in the x direction is [203]:

$$I = \begin{pmatrix} I_y \\ I_z \end{pmatrix} \propto \begin{pmatrix} \frac{1}{2}|J_{|3/2|}|^2 + \frac{1}{6}|J_{|1/2|}|^2 \\ \frac{2}{3}|J_{|1/2|}|^2 \end{pmatrix} \tag{A.1}$$

where the two components are respectively the fraction of light linearly polarized along the y and z direction and:

$$|J_{|m|}|^2 = \sum |< F_h|F_e >|^2 \tag{A.2}$$

This sum is performed over all available spin orientations and F_e and F_h are respectively the electron and hole envelope wave functions.

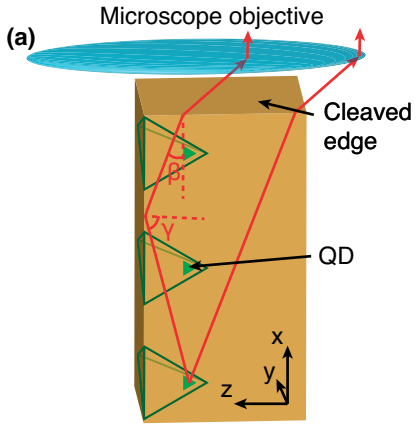

Figure A.1 – Sketch of the side view PL spectroscopy on a cleaved ensemble of pyramidal QDs.

Clearly, heavy holes transitions are more favorable to ensuring a strong interaction with quasi-TE PhC modes in which the electric field at the slab center is polarized in plane. However, in the general case, holes are a mixture of each hole specie. This mixing can be measured via the degree of linear polarization defined as:

$$DOLP = \frac{I_y - I_z}{I_y + I_z} \tag{A.3}$$

The DOLP of pyramidal QD was measured by PL from the x-oriented surface of a cleaved sample in which pyramidal QD ensembles were grown as depicted on Fig. A.1. A technical difficulty in applying this method to QD ensembles is that some excited QDs may be situated deep into the GaAs sample (low values of x). The light emitted by such a QD is reflected on the z-oriented growth interface on which a partial reflection may affect the final measured polarization. However, in GaAs, light emitted by the QDs is collected by the NA=0.55 microscope objective up to an angle of $\beta = 9°$. The incident angle of the collected light on the growth interface is therefore above $\beta = 81°$. All light collected by the microscope objective undergoes total internal reflection on the growth interface, which therefore does not affect the intensity of collected light polarized along the z and y-directions. Thus a cleaved edge polarization resolved PL gives a faithful measurement of the intrinsic QD emission properties.

The measured linear polarization spectra of two QD ensembles along the y and z directions are given on Fig. A.2(a-b). On Fig. A.2(a), the QD ensemble was grown with a QD layer thickness of 0.75nm and on Fig. A.2(b) it was 0.564nm. The z-oriented intensity is large which is indicative of a high light-hole content of the excitons. The valence band mixing defined as the fraction of heavy holes in the hole is measured from the DOLP as:

$$HH = \frac{|J_{|3/2|}|^2}{|J_{|1/2|}|^2 + |J_{|3/2|}|^2} = \frac{3 + 5 \cdot DOLP}{6 + 2 \cdot DOLP} \tag{A.4}$$

In the ensembles observed here, the average DOLP is -0.49 (0.75nm QD layer thickness) and -0.47 (0.564nm QD layer thickness). These numbers are very close to the lowest DOLP attained with pure light holes: DOLP=-3/5. The valence band mixing estimated from these DOLP is: HH=0.11 (0.75nm QD layer thickness) and HH=0.13 (0.564nm QD layer thickness). As will be shown in Chapter 2, the most intense QD lines in the pyramidal QD ensembles, excited at low powers, studied in this thesis are usually trions because of a residual n-doping. A reasonable assumption is therefore that the spectra of Fig. A.2(a-b) are mainly composed of trion lines. With this assumption, the orientation of the dipole moment of a trion line can be estimated using a simple model in which the transition is ensured by a circular dipole in plane and a z oriented dipole component [22]:

$$p_x = p \begin{pmatrix} \frac{sin(\alpha)}{\sqrt{2}} \\ i\frac{sin(\alpha)}{\sqrt{2}} \\ cos(\alpha) \end{pmatrix} \tag{A.5}$$

where α is a parameter controlling the vertical QD emission. In which case, the intensity collected by the objective for each polarization orientation is:

$$I = \begin{pmatrix} I_y \\ I_z \end{pmatrix} \propto \begin{pmatrix} sin^2(\alpha) \\ 2cos^2(\alpha) \end{pmatrix} \tag{A.6}$$

Using this model, the dipole orientation α is:

$$\alpha = arccos(\sqrt{\frac{1 - DOLP}{3 + DOLP}}) \tag{A.7}$$

From the measured DOLP, the angle of dipole moment can be inferred: $\alpha = 39.6°$ (0.75nm QD layer thickness) and $\alpha = 40.3°$ (0.564nm QD layer thickness). Thus, the in-plane component of the dipole moment of trion lines may be enhanced by a factor almost three if structural changes in the QD shape force the QD dipole moment to be in the growth plane. This would also ensure a heavy hole nature of the s-state holes. The valence band mixing of s-state can be controlled by the confinement potential of QDs [204]: a QD confinement more elongated in the z-direction than in the growth direction favors light s-state holes, while if the QD is more elongated in the growth plane, the hole s-states are heavy. Thus, these measurements suggests that the QDs studied in this thesis are elongated in the z-direction. Besides, these results also suggests that an in-plane dipole moment of trions could be obtained with thinner QDs as was demonstrated in [204].

Notice that some QD lines (for example at E=1.293eV on Fig. A.2(a)) exhibit a polarization dependent splitting. This indicates the presence of two lines: one polarized in plane and the other polarized along the z-direction. Similar effects were observed in larger pyramidal QDs [57] and were attributed to the fine structure splitting of excitons. These observations indicate that a more precise analysis of side view PL on isolated QDs would be needed for an accurate assessment of the excitonic species orientation.

The same measurements were carried out on sample 6087 grown using TEIn and are shown on Fig. A.2(b-c). The DOLP obtained in this sample was -0.11, indicating a larger valence band mixing, with HH=0.43 and a dipole moment of trions more in plane: with $\alpha = 35°$, which corresponds to an increase of the dipole strength and correspondingly of the coupling strength to optical modes g, by a factor 1.4. A polarization resolved spectra was aquired by exciting the QD ensemble at a larger power ($P = 50\mu W$) at the same position (Fig. A.2(b)). An increased DOLP is observed near 1.325eV, which indicates the presence of excited states with a larger valence band mixing HH. A precise measurement of HH for these states is rendered diffcult by the overlap between the emission from each exciton ensemble. By growing thinner QDs, a crossing between these two hole states may be observed. The obtained s-state emission may in this case be almost perfectly in plane.

Further measurements on isolated QDs are required to provide a more precise picture of the composition of each single exciton line as was done in the past with QDs grown in larger pyramids [203].

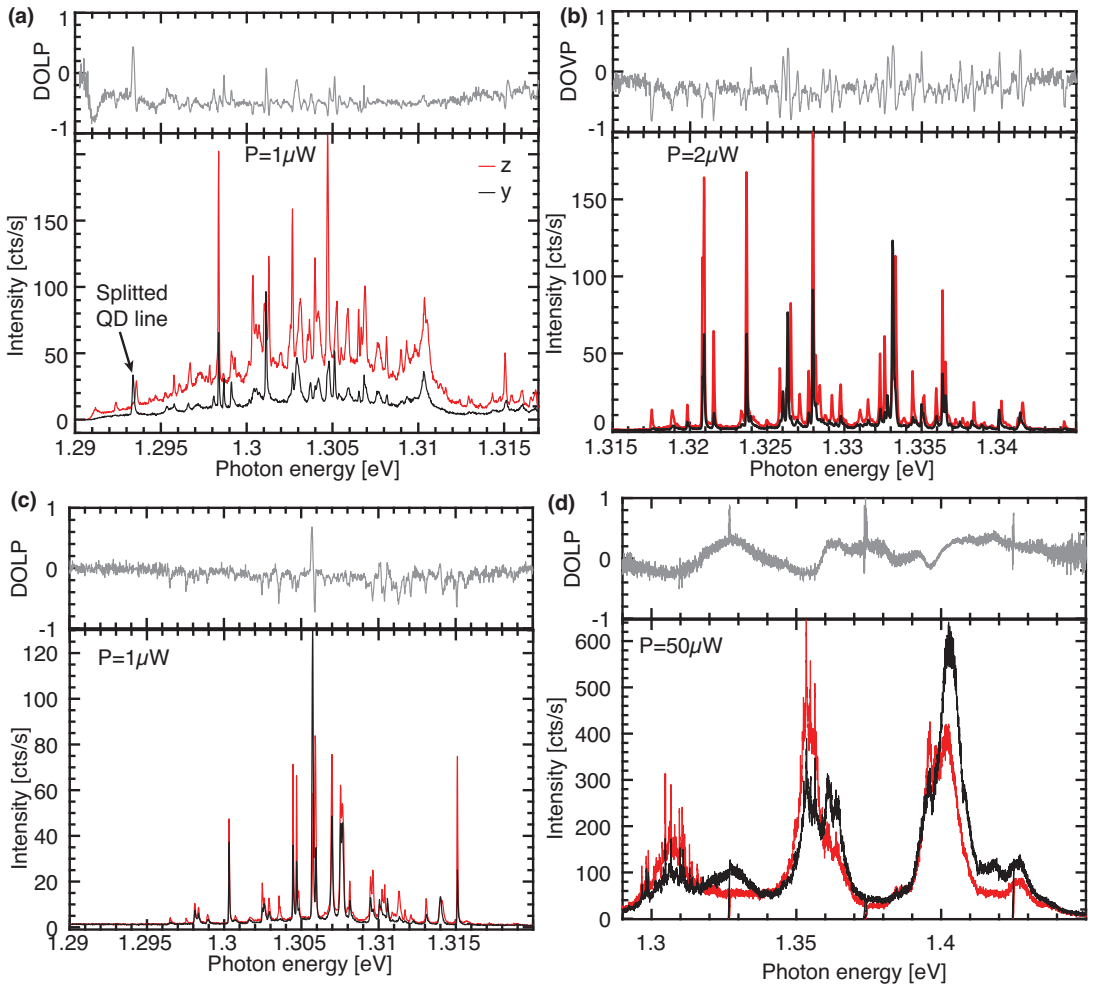

Figure A.2 – Polarization resolved PL of a QD ensemble measured in a cleaved edge configuration: (a) Sample 5564 grown with TMIn (excitation power: $P = 1\mu W$, QD layer thickness: 0.75nm); (b) Sample 5309 grown with TMIn (excitation power: $P = 2\mu W$, QD layer thickness: 0.564nm); (b) Sample 6087 grown with TEIn (excitation power: $P = 1\mu W$); (c) Sample 6087 grown with TEIn (excitation power: $P = 50\mu W$); (all measurements were carried out at T=10K, the growth parameters are given in Appendix B).

B MOCVD growth parameters

In this appendix, the parameters used for MOCVD growth of the samples studied in this work are presented. These growths were all carried out in an Aixtron 200 operated by Dr. A. Rudra. The indium content (In %) corresponds to the partial pressure of indium with respect to that of gallium. The thicknesses and growth rates shown here were calibrated on (100) oriented GaAs surface. The grown thicknesses can change significantly on non-planar surfaces such as the inverted pyramids presented in this thesis. The temperatures shown here were measured and stabilized with a thermocouple integrated with the substrate holder. The V/III ratio corresponds to the ratio of flow rate of group V elements by the flow rate of group III elements. The sequence of layers is as follows: A deoxydation step (Deox) without growth, one or two buffer layers of GaAs a QD layer and one or two cap layers.

Samples used to compare growth with TEGa and TMGa (Chapter 2)

Sample 5199

Layer	Material	Precursor	In %	Thickness [nm]	Growth rate [nm/s]	T[°C]	V/III
Deox	-	-	-	-	-	570	Max
Buffer 1	GaAs	TMGa		1.3	0.0082	570-590	3505
Buffer 2	GaAs	TMGa		4.29	0.0082	600	3505
QD	InGaAs	TEGa/TMIn	25	0.68	0.0109	600	2530
Cap	GaAs	TMGa		3.25	0.0082	600	3505

Sample 5255

Layer	Material	Precursor	In %	Thickness [nm]	Growth rate [nm/s]	T[°C]	V/III
Deox	-	-	-	-	-	600	Max
Buffer	GaAs	TEGa		5	0.005	600	260
QD	InGaAs	TEGa/TMIn	25	0.68	0.011	600	244
Cap	GaAs	TEGa		2	0.005	600	260
Cap	GaAs	TMGa		8	0.009	600	2643

Sample used for TEM measurement (Chapter 2)

Sample 5309

Layer	Material	Precursor	In %	Thickness [nm]	Growth rate [nm/s]	T[°C]	V/III
Deox	-	-	-	-	-	600	Max
Buffer	GaAs	TEGa		5	0.005	600	260
QD	InGaAs	TEGa/TMIn	30	0.564	0.0112	600	244
Cap	GaAs	TEGa		2	0.005	600	260
Cap	GaAs	TMGa		8	0.009	600	942

Sample used to infer the impact of variable pyramid sizes (Chapter 2)

Sample 5807

Layer	Material	Precursor	In %	Thickness [nm]	Growth rate [nm/s]	T[°C]	V/III
Deox	-	-	-	-	-	600	Max
Buffer	GaAs	TEGa		5	0.005	600	260
QD	InGaAs	TEGa/TMIn	25	0.75	0.011	600	246
Cap	GaAs	TEGa		2	0.005	600	260
Cap	GaAs	TMGa		8	0.009	600	942

Samples used to compare growth with TEIn and TMIn (Chapter 2)

Sample 5951

Layer	Material	Precursor	In %	Thickness [nm]	Growth rate [nm/s]	T[°C]	V/III
Deox	-	-	-	-	-	600	Max
Buffer	GaAs	TEGa		5	0.005	600	260
QD	InGaAs	TEGa/TMIn	25	0.75	0.011	600	246
Cap	GaAs	TEGa		2	0.005	600	260
Cap	GaAs	TMGa		8	0.009	600	942

Sample 6087

Layer	Material	Precursor	In %	Thickness [nm]	Growth rate [nm/s]	T[°C]	V/III
Deox	-	-	-	-	-	600	Max
Buffer	GaAs	TEGa		5	0.005	600	260
QD	InGaAs	TEGa/TEIn	25	0.5	0.011	600	246
Cap	GaAs	TEGa		2	0.005	600	260
Cap	GaAs	TMGa		8	0.009	600	942

Sample used to measure the excitons dipole momentum (Appendix A)

Sample 5309

Layer	Material	Precursor	In %	Thickness [nm]	Growth rate [nm/s]	T[°C]	V/III
Deox	-	-	-	-	-	600	Max
Buffer	GaAs	TEGa		5	0.005	600	260
QD	InGaAs	TEGa/TMIn	30	0.564	0.0112	600	244
Cap	GaAs	TEGa		2	0.005	600	260
Cap	GaAs	TMGa		8	0.009	600	942

Sample 5564

Layer	Material	Precursor	In %	Thickness [nm]	Growth rate [nm/s]	T[°C]	V/III
Deox	-	-	-	-	-	600	Max
Buffer	GaAs	TEGa		5	0.005	600	260
QD	InGaAs	TEGa/TMIn	25	0.75	0.011	600	246
Cap	GaAs	TEGa		2	0.005	600	260
Cap	GaAs	TMGa		8	0.009	600	942
Cap	GaAs	TEGa		2000	0.24	600	2

Samples used for AFM measurements (Chapter 2)

Sample 5259

Layer	Material	Precursor	In %	Thickness [nm]	Growth rate [nm/s]	T[°C]	V/III
Deox	-	-	-	-	-	600	Max
Buffer	GaAs	TEGa		5	0.005	600	260
QD	InGaAs	TEGa/TMIn	25	0.68	0.011	600	244
Cap	GaAs	TEGa		2	0.005	600	260
Cap	GaAs	TEGa		8	0.009	700	260

Sample 5255

Layer	Material	Precursor	In %	Thickness [nm]	Growth rate [nm/s]	T[°C]	V/III
Deox	-	-	-	-	-	600	Max
Buffer	GaAs	TEGa		5	0.005	600	260
QD	InGaAs	TEGa/TMIn	25	0.68	0.011	600	246
Cap	GaAs	TEGa		2	0.005	600	260
Cap	GaAs	TMGa		8	0.009	600	2643

Sample 5281

Layer	Material	Precursor	In %	Thickness [nm]	Growth rate [nm/s]	T[°C]	V/III
Deox	-	-	-	-	-	600	Max
Buffer	GaAs	TEGa		5	0.005	600	260
QD	InGaAs	TEGa/TMIn	18	0.68	0.011	600	246
Cap	GaAs	TEGa		2	0.005	600	260
Cap	GaAs	TMGa		10	0.009	600	2643

Sample 5283

Layer	Material	Precursor	In %	Thickness [nm]	Growth rate [nm/s]	T[°C]	V/III
Deox	-	-	-	-	-	600	Max
Buffer	GaAs	TEGa		5	0.005	600	260
QD	InGaAs	TEGa/TMIn	18	0.75	0.011	600	246
Cap	GaAs	TEGa		2	0.005	600	260
Cap	GaAs	TMGa		10	0.009	600	2643

Sample 5319

Layer	Material	Precursor	In %	Thickness [nm]	Growth rate [nm/s]	T[°C]	V/III
Deox	-	-	-	-	-	600	Max
Buffer	GaAs	TEGa		5	0.005	600	260
QD	InGaAs	TEGa/TMIn	25	0.75	0.011	600	246
Cap	GaAs	TEGa		2	0.005	600	260
Cap	GaAs	TMGa		10	0.009	600	942
Annealing						700	88

Membrane samples used for fabrication of QDs integrated in PhC waveguides and cavities

Sample 5326 (or D7wTa6-2B) **(Chapter 3 and 4)**

Layer	Material	Precursor	In %	Thickness [nm]	Growth rate [nm/s]	T[°C]	V/III
Deox	-	-	-	-	-	600	Max
Buffer	GaAs	TEGa		5	0.005	600	260
QD	InGaAs	TEGa/TMIn	25	0.75	0.011	600	246
Cap	GaAs	TEGa		2	0.005	600	260
Cap	GaAs	TMGa		10	0.009	600	942

Sample 5327 (or D7wTa6-6B) **(Chapter 5)**

Layer	Material	Precursor	In %	Thickness [nm]	Growth rate [nm/s]	T[°C]	V/III
Deox	-	-	-	-	-	600	Max
Buffer	GaAs	TEGa		5	0.005	600	260
QD	InGaAs	TEGa/TMIn	25	0.75	0.011	600	246
Cap	GaAs	TEGa		2	0.005	600	260
Cap	GaAs	TMGa		10	0.009	600	942

C Contributions

The author, B. Rigal, did all the data analysis presented in this thesis and all the optical measurements except for those presented in subsection 2.3.4 (measurements by A. Miranda and A. Delgoffe), section 3.2 (measurements by K. Joanesarson) and section 4.4 (measurements by T. Produit). The author did all the FDTD and 2D-FDM modelling with a matlab code written by K. F. Karlsson and using the open software meep. The author wrote the matlab FDFD code and did all FDFD simulations presented in this thesis. The work was partly supported by the French RENATECH network: A. Arnoult did MBE growth of the (111)B GaAs/AlGaAs membrane wafers employed. The samples presented in this thesis were fabricated by the author in collaboration with B. Dwir, A. Rudra, A. Lyasota, I. Kulkova and A. Miranda. All e-beam writings were carried out by B. Dwir. All MOCVD growths and X-ray characterizations were performed by A. Rudra. The author did all the other steps of the clean room fabrication process on samples 5326, 5327, except for the ICP etching of PhCs and its optimization. The ICP optimization and etching on samples 5326 was performed by I. Kulkova with the help of A. Lyasota. The ICP optimization and etching on samples 5327 was performed by A. Miranda with the help of A. Lyasota. The author did all steps of fabrication except e-beam writing and MOCVD growth on samples 5255, 5259, 5281, 5283, 5319, 5564. The clean room fabrication of samples 5807, 5951 and 6087 was carried out by A. Miranda and that of sample 5199 by A. Lyasota. Professor E. Kapon supervised the work presented in this thesis.

D Publications and conferences

Journal publications

- Rigal, B., C. Jarlov, A. Rudra, P. Gallo, A. Lyasota, B. Dwir, and E. Kapon. "Site-Controlled InGaAs/GaAs Pyramidal Quantum Dots Grown by MOVPE on Patterned Substrates Using Triethylgallium." Journal of Crystal Growth, Proceedings of the Seventeenth International Conference on Metalorganic Vapor Phase Epitaxy, 414 (2015): 187–91. https://doi.org/10.1016/j.jcrysgro.2014.11.007.

- Rigal, B., C. Jarlov, P. Gallo, B. Dwir, A. Rudra, M. Calic, and E. Kapon. "Site-Controlled Quantum Dots Coupled to a Photonic Crystal Molecule." Applied Physics Letters 107, no. 14 (2015): 141103. https://doi.org/10.1063/1.4932228.

- I. V. Kulkova, A. Lyasota, C. Jarlov, B. Rigal, A. Rudra, B. Dwir, and E. Kapon. "Emission Wavelength Control of Ordered Arrays of InGaAs/GaAs Quantum Dots." Journal of Crystal Growth, (2016)

- B. Rigal, K. Joanesarson, A. Lyasota, C. Jarlov, B. Dwir, A. Rudra, I. Kulkova, and E. Kapon. "Propagation Losses in Photonic Crystal Waveguides: Effects of Band Tail Absorption and Waveguide Dispersion." Optics Express 25, no. 23 (2017): 28908–13. https://doi.org/10.1364/OE.25.028908.

- B. Rigal, D. Drahi, C. Jarlov, B. Dwir, A. Rudra, I. Kulkova, A. Lyasota, and E. Kapon. "Probing Disorder and Mode Localization in Photonic Crystal Cavities Using Site-Controlled Quantum Dots", Journal of Applied Physics, in print (2018).

- B. Rigal, B. Dwir, A. Rudra, I. Kulkova, A. Lyasota, and E. Kapon. "Single Photon Extraction and Propagation in Photonic Crystal Waveguides Incorporating Site-Controlled Quantum Dots." Applied Physics Letters, in print (2018).

- B. Rigal, A. Miranda, B. Dwir, A. Rudra, A. Lyasota, and E. Kapon, “Site-controlled quantum dots integrated with coupled cavity-waveguide systems for efficient single photon extraction and routing.” Optica, Manuscript submitted for publication (2018).

Conference presentations

- P. Gallo, B. Dwir, C. Jarlov, A. Lyasota, B. Rigal, A. Rudra and E. Kapon, “Site-controlled InGaAs/GaAs pyramidal quantum dots grown by OMVPE on patterned substrates using triethylgallium”, ICMOVPE 2014 17th European Workshop on Metalorganic Vapour Phase Epitaxy, Switzerland, Lausanne, 13-19 July, (Contributed, Poster)

- B. Rigal, C. Jarlov, B. Dwir, A. Rudra, P. Gallo, M. Calic, A. Lyasota and E. Kapon« Integration of site-controlled quantum dots in a photonic molecule », PIERS 2015, Prague, Czech republic, 6-9 july (Contributed, Oral)

- J. R. de Lasson, B. Rigal, E. Kapon, J. Mørk, and N. Gregersen. “Design of Slow and Fast Light Photonic Crystal Waveguides for Single-Photon Emission Using a Bloch Mode Expansion Technique.” PIERS 2015: Session 2A3 FocusSession. SC3: Single Photonics: Integrated Optics for On-Chip Manipulation of Single Photons, 2015.

- B. Rigal, J. R. de Lasson, C. Jarlov, B. Dwir, A. Rudra, A. Lyasota, I. Kulkova, N. Gregersen, J. Mørk, and E. Kapon. “Site-Controlled Quantum Dots Coupled to a Photonic Crystal Waveguide.” META 2016, Malaga, Spain, 25-28 july, (Contributed Poster)

- B. Rigal, C. Jarlov, B. Dwir, I. Kulkova, A. Lyasota, and E. Kapon. “On-Chip Single Photon Transfer with Site-Controlled Quantum Dots Coupled to Photonic Crystal Waveguides.” SAT2s.4, Nanometa 2017, Seefeld, January 4, (Contributed Oral)

- B. Rigal, T. Produit, A. Miranda, A. Lyasota, C. Jarlov, B. Dwir, A. Rudra, A. Delgoffe, and E. Kapon, “Efficient on chip single photon sources using slow light and site controlled QDs” PIERS 2017, St Petersburg, Russia, 22-25 May (Contributed, Oral)

Bibliography

[1] Peter W. Atkins and Ronald S. Friedman. *Molecular quantum mechanics*. Oxford university press, 2011.

[2] John Stewart Bell. *Speakable and Unspeakable in Quantum Mechanics: Collected papers on quantum philosophy*. Cambridge university press, 2004.

[3] Jonathan P. Dowling and Gerard J. Milburn. Quantum technology: the second quantum revolution. *Philosophical Transactions of the Royal Society of London A: Mathematical, Physical and Engineering Sciences*, 361(1809):1655–1674, 2003.

[4] Claude Cohen-Tannoudji, Bernard Diu, and Franck Laloë. *Mécanique quantique*. Centre de Publications Universitaire, Téhéran, 1986.

[5] Alain Aspect, Jean Dalibard, and Gérard Roger. Experimental test of Bell's inequalities using time-varying analyzers. *Physical review letters*, 49(25):1804, 1982.

[6] Richard P. Feynman. Simulating physics with computers. *International Journal of Theoretical Physics*, 21(6-7):467–488, June 1982.

[7] David Deutsch. Quantum theory, the Church-Turing principle and the universal quantum computer. *Proceedings of the Royal Society of London. A. Mathematical and Physical Sciences*, 400(1818):97–117, 1985.

[8] Peter W. Shor. Polynomial-time algorithms for prime factorization and discrete logarithms on a quantum computer. *SIAM review*, 41(2):303–332, 1999.

[9] Hoi-Kwong Lo, Marcos Curty, and Kiyoshi Tamaki. Secure quantum key distribution. *Nature Photonics*, 8(8):595–604, August 2014.

[10] J. Abadie, B. P. Abbott, R. Abbott, T. D. Abbott, M. Abernathy, C. Adams, R. Adhikari, C. Affeldt, B. Allen, G. S. Allen, and others. A gravitational wave observatory operating beyond the quantum shot-noise limit. *Nature Physics*, 7(12):962–965, 2011.

[11] Vittorio Giovannetti, Seth Lloyd, and Lorenzo Maccone. Advances in quantum metrology. *Nature photonics*, 5(4):222–229, 2011.

[12] Ph Goy, J. M. Raimond, M. Gross, and S. Haroche. Observation of cavity-enhanced single-atom spontaneous emission. *Physical review letters*, 50(24):1903, 1983.

[13] R. J. Thompson, G. Rempe, and H. J. Kimble. Observation of normal-mode splitting for an atom in an optical cavity. *Physical Review Letters*, 68(8):1132, 1992.

[14] J. McKeever, A. Boca, A. D. Boozer, R. Miller, J. R. Buck, A. Kuzmich, and H. J. Kimble. Deterministic generation of single photons from one atom trapped in a cavity. *Science*, 303(5666):1992–1994, 2004.

[15] A. A. Houck, D. I. Schuster, J. M. Gambetta, J. A. Schreier, B. R. Johnson, J. M. Chow, L. Frunzio, J. Majer, M. H. Devoret, S. M. Girvin, and R. J. Schoelkopf. Generating single microwave photons in a circuit. *Nature*, 449(7160):328–331, September 2007.

[16] M. H. Devoret and R. J. Schoelkopf. Superconducting Circuits for Quantum Information: An Outlook. *Science*, 339(6124):1169–1174, March 2013.

[17] Lukas Novotny and Bert Hecht. *Principles of nano-optics*. Cambridge university press, 2012.

[18] John D. Joannopoulos, Steven G. Johnson, Joshua N. Winn, and Robert D. Meade. *Photonic crystals: molding the flow of light*. Princeton university press, 2011.

[19] D. E. Chang, Anders Søndberg Sørensen, P. R. Hemmer, and M. D. Lukin. Quantum optics with surface plasmons. *Physical review letters*, 97(5):053002, 2006.

[20] Susumu Noda, Masayuki Fujita, and Takashi Asano. Spontaneous-emission control by photonic crystals and nanocavities. *Nature photonics*, 1(8):449–458, 2007.

[21] Pieter Kok, William J. Munro, Kae Nemoto, Timothy C. Ralph, Jonathan P. Dowling, and G. J. Milburn. Linear optical quantum computing with photonic qubits. *Reviews of Modern Physics*, 79(1):135, 2007.

[22] Oliver Gywat, Hubert J. Krenner, and Jesse Berezovsky. *Spins in optically active quantum dots*. Wiley. com, 2009.

[23] Philippe Guyot-Sionnest. Colloidal quantum dots. *Comptes Rendus Physique*, 9(8):777–787, 2008.

[24] Michael S. Shur. *Handbook series on semiconductor parameters*, volume 1. World Scientific, 1996.

[25] Simon M. Sze and Kwok K. Ng. *Physics of semiconductor devices*. Wiley. com, 2006.

[26] Lok C. Lew Yan Voon and Morten Willatzen. *The k p Method : electronic properties of semiconductors*. Springer, Berlin, 2009.

[27] Peter Lodahl, Sahand Mahmoodian, and Søren Stobbe. Interfacing single photons and single quantum dots with photonic nanostructures. *Reviews of Modern Physics*, 87(2):347, 2015.

[28] Craig Pryor. Eight-band calculations of strained InAs/GaAs quantum dots compared with one-, four-, and six-band approximations. *Physical Review B*, 57(12):7190, 1998.

[29] H. A. Kramers. HA Kramers Proc. roy. Acad. Amsterdam, 32 (1929). In *Proc. Roy. Acad. Amsterdam*, volume 33, page 959, 1930.

[30] Hartmut Haug and S. Stephan W. Koch. *Quantum theory of the optical and electronic properties of semiconductors*. World scientific, 2009.

[31] Z. Hens. Can the oscillator strength of the quantum dot bandgap transition exceed unity? *Chemical Physics Letters*, 463(4–6):391–395, October 2008.

[32] V. Türck, S. Rodt, O. Stier, R. Heitz, R. Engelhardt, U. W. Pohl, D. Bimberg, and R. Steingrüber. Effect of random field fluctuations on excitonic transitions of individual CdSe quantum dots. *Physical Review B*, 61(15):9944, 2000.

[33] Andreas Naesby, Troels Suhr, Philip Trøst Kristensen, and Jesper Mørk. Influence of pure dephasing on emission spectra from single photon sources. *Physical Review A*, 78(4):045802, 2008.

[34] Alexia Auffèves, Jean-Michel Gérard, and Jean-Philippe Poizat. Pure emitter dephasing: A resource for advanced solid-state single-photon sources. *Physical Review A*, 79(5):053838, May 2009.

[35] Thomas Grange, Gaston Hornecker, David Hunger, Jean-Philippe Poizat, Jean-Michel Gérard, Pascale Senellart, and Alexia Auffèves. Cavity-funneled generation of indistinguishable single photons from strongly dissipative quantum emitters. *Physical review letters*, 114(19):193601, 2015.

[36] Ivan Favero, Alice Berthelot, Guillaume Cassabois, Christophe Voisin, Claude Delalande, Ph Roussignol, Robson Ferreira, and Jean-Michel Gérard. Temperature dependence of the zero-phonon linewidth in quantum dots: An effect of the fluctuating environment. *Physical Review B*, 75(7):073308, 2007.

[37] E. A. Muljarov and R. Zimmermann. Dephasing in quantum dots: Quadratic coupling to acoustic phonons. *Physical review letters*, 93(23):237401, 2004.

[38] K. Leosson, Dan Birkedal, Ingibjörg Magnúsdóttir, W. Langbein, and Jørn Märcher Hvam. Homogeneous linewidth of self-assembled III–V quantum dots observed in single-dot photoluminescence. *Physica E: Low-dimensional Systems and Nanostructures*, 17:1–6, 2003.

[39] I. Favero, Guillaume Cassabois, R. Ferreira, D. Darson, C. Voisin, J. Tignon, C. Delalande, G. Bastard, Ph Roussignol, and J. M. Gérard. Acoustic phonon sidebands in the emission line of single InAs/GaAs quantum dots. *Physical Review B*, 68(23):233301, 2003.

[40] A. Zrenner, L. V. Butov, M. Hagn, G. Abstreiter, G. Böhm, and G. Weimann. Quantum dots formed by interface fluctuations in AlAs/GaAs coupled quantum well structures. *Physical review letters*, 72(21):3382, 1994.

[41] I. N. Stranski and L. Von Krastanow. Abhandlungen der Mathematisch-Naturwissenschaftlichen Klasse. *Akademie der Wissenschaften und der Literatur in Mainz*, 146:797, 1939.

[42] D. Leonard, M. Krishnamurthy, C. M. Reaves, Steven P. DenBaars, and Pierre M. Petroff. Direct formation of quantum-sized dots from uniform coherent islands of InGaAs on GaAs surfaces. *Applied Physics Letters*, 63(23):3203–3205, 1993.

[43] Susanna M. Thon, Matthew T. Rakher, Hyochul Kim, Jan Gudat, William T. M. Irvine, Pierre M. Petroff, and Dirk Bouwmeester. Strong coupling through optical positioning of a quantum dot in a photonic crystal cavity. *Applied Physics Letters*, 94(11):111115, March 2009.

[44] J. Tommila, A. Tukiainen, J. Viheriälä, A. Schramm, T. Hakkarainen, A. Aho, P. Stenberg, M. Dumitrescu, and M. Guina. Nanoimprint lithography patterned GaAs templates for site-controlled InAs quantum dots. *Journal of Crystal Growth*, 323(1):183–186, 2011.

[45] Jesús Herranz, Lukasz Wewior, Benito Alén, David Fuster, Luisa González, and Yolanda González. Role of re-growth interface preparation process for spectral line-width reduction of single InAs site-controlled quantum dots. *Nanotechnology*, 26(19):195301, 2015.

[46] C. Schneider, A. Huggenberger, T. Sünner, T. Heindel, M. Strauß, S. Göpfert, P. Weinmann, S. Reitzenstein, L Worschech, M. Kamp, S. Höfling, and A. Forchel. Single site-controlled In(Ga)As/GaAs quantum dots: growth, properties and device integration. *Nanotechnology*, 20(43):434012, 2009.

[47] Stephane Faure, Masao Nishioka, Satomi Ishida, Denis Guimard, and Yasuhiko Arakawa. Metal organic chemical vapor deposition growth of high spectral quality site-controlled InAs quantum dots using in situ patterning. *Applied Physics Express*, 4(11):112001, 2011.

[48] A. Huggenberger, S. Heckelmann, C. Schneider, S. Höfling, S. Reitzenstein, L. Worschech, M. Kamp, and A. Forchel. Narrow spectral linewidth from single site-controlled In (Ga) As quantum dots with high uniformity. *Applied Physics Letters*, 98(13):131104, 2011.

[49] Michael K. Yakes, Lily Yang, Allan S. Bracker, Timothy M. Sweeney, Peter G. Brereton, Mijin Kim, Chul Soo Kim, Patrick M. Vora, Doewon Park, Samuel G. Carter, and Daniel Gammon. Leveraging Crystal Anisotropy for Deterministic Growth of InAs Quantum Dots with Narrow Optical Linewidths. *Nano Letters*, 13(10):4870–4875, October 2013.

[50] Juan Márquez, Lutz Geelhaar, and Karl Jacobi. Atomically resolved structure of InAs quantum dots. *Applied Physics Letters*, 78(16):2309–2311, 2001.

[51] Ducommun. *Semiconductor Quantum Dots grown in inverted pyramids*. PhD thesis, EPFL, 2001.

[52] M. Merano, S. Sonderegger, A. Crottini, S. Collin, P. Renucci, E. Pelucchi, A. Malko, M. H. Baier, E. Kapon, B. Deveaud, and others. Probing carrier dynamics in nanostructures by picosecond cathodoluminescence. *Nature*, 438(7067):479–482, 2005.

[53] C. Jarlov, P. Gallo, M. Calic, B. Dwir, A. Rudra, and E. Kapon. Bound and anti-bound biexciton in site-controlled pyramidal GaInAs/GaAs quantum dots. *Applied Physics Letters*, 101(19):191101–191101, 2012.

[54] Arun Mohan, Pascal Gallo, Marco Felici, Benjamin Dwir, Alok Rudra, Jerome Faist, and Eli Kapon. Record-Low Inhomogeneous Broadening of Site-Controlled Quantum Dots for Nanophotonics. *Small*, 6(12):1268–1272, June 2010.

[55] M. A. Dupertuis, K. F. Karlsson, D. Y. Oberli, E. Pelucchi, A. Rudra, P. O. Holtz, and E. Kapon. Symmetries and the Polarized Optical Spectra of Exciton Complexes in Quantum Dots. *Physical Review Letters*, 107(12):127403, September 2011.

[56] L. O. Mereni, O. Marquardt, G. Juska, V. Dimastrodonato, E. P. O'Reilly, and E. Pelucchi. Fine-structure splitting in large-pitch pyramidal quantum dots. *Physical Review B*, 85(15):155453, 2012.

[57] K. F. Karlsson, M. A. Dupertuis, D. Y. Oberli, E. Pelucchi, A. Rudra, P. O. Holtz, and E. Kapon. Fine structure of exciton complexes in high-symmetry quantum dots: Effects of symmetry breaking and symmetry elevation. *Physical Review B*, 81(16):161307, April 2010.

[58] Pascal Gallo, M. Felici, B. Dwir, K. A. Atlasov, K. F. Karlsson, A. Rudra, A. Mohan, G. Biasiol, L. Sorba, and E. Kapon. Integration of site-controlled pyramidal quantum dots and photonic crystal membrane cavities. *Applied Physics Letters*, 92(26):263101–263101, 2008.

[59] Igor Aharonovich, Dirk Englund, and Milos Toth. Solid-state single-photon emitters. *Nature Photonics*, 10(10):631–641, 2016.

[60] Mark J. Holmes, Kihyun Choi, Satoshi Kako, Munetaka Arita, and Yasuhiko Arakawa. Room-Temperature Triggered Single Photon Emission from a III-Nitride Site-Controlled Nanowire Quantum Dot. *Nano Letters*, 14(2):982–986, February 2014.

[61] F. Ding, R. Singh, J. D. Plumhof, T. Zander, V. Křápek, Y. H. Chen, M. Benyoucef, V. Zwiller, K. Dörr, G. Bester, A. Rastelli, and O. G. Schmidt. Tuning the Exciton Binding Energies in Single Self-Assembled InGaAs/GaAs Quantum Dots by Piezoelectric-Induced Biaxial Stress. *Physical Review Letters*, 104(6):067405, February 2010.

[62] Anthony J. Bennett, Raj B. Patel, Joanna Skiba-Szymanska, Christine A. Nicoll, Ian Farrer, David A. Ritchie, and Andrew J. Shields. Giant Stark effect in the emission of single semiconductor quantum dots. *Applied Physics Letters*, 97(3):031104, July 2010.

[63] Hyochul Kim, Deepak Sridharan, Thomas C. Shen, Glenn S. Solomon, and Edo Waks. Strong coupling between two quantum dots and a photonic crystal cavity using magnetic field tuning. *Optics Express*, 19(3):2589, January 2011.

[64] M. H. Baier, S. Watanabe, E. Pelucchi, and E. Kapon. High uniformity of site-controlled pyramidal quantum dots grown on prepatterned substrates. *Applied physics letters*, 84(11):1943–1945, 2004.

[65] Irina V. Kulkova, Alexey Lyasota, Clément Jarlov, Bruno Rigal, Alok Rudra, Benjamin Dwir, and Eli Kapon. Emission wavelength control of ordered arrays of InGaAs/GaAs quantum dots. *Journal of Crystal Growth*, 464:69–74, April 2017.

[66] O. Gazzano, S. Michaelis De Vasconcellos, C. Arnold, A. Nowak, E. Galopin, I. Sagnes, L. Lanco, A. Lemaître, and P. Senellart. Bright solid-state sources of indistinguishable single photons. *Nature communications*, 4:1425, 2013.

[67] Eli Yablonovitch. Inhibited spontaneous emission in solid-state physics and electronics. *Physical review letters*, 58(20):2059–2062, 1987.

[68] Sajeev John and Jian Wang. Quantum electrodynamics near a photonic band gap: Photon bound states and dressed atoms. *Physical review letters*, 64(20):2418–2421, 1990.

[69] T. F. Krauss, R. M. D. L. Rue, and S. Brand. Two-dimensional photonic-bandgap structures operating at near-infrared wavelengths. *Nature*, 383(6602):699–702, 1996.

[70] E. Yablonovitch and K. M. Leung. Hope for photonic bandgaps. *Nature*, 351(6324):278–278, 1991.

[71] Dennis W. Prather. *Photonic Crystals, Theory, Applications and Fabrication*, volume 68. John Wiley & Sons, 2009.

[72] Tatsuya Nakamura, Yasushi Takahashi, Yoshinori Tanaka, Takashi Asano, and Susumu Noda. Improvement in the quality factors for photonic crystal nanocavities via visualization of the leaky components. *Optics Express*, 24(9):9541, May 2016.

[73] Momchil Minkov and Vincenzo Savona. Design-specific global optimization of a variety of photonic crystal cavities. In *CLEO: 2014*, OSA Technical Digest (online), page JTu4A.92. Optical Society of America, June 2014.

[74] Jelena Vuckovic, Marko Loncar, Hideo Mabuchi, and Axel Scherer. Optimization of the Q factor in photonic crystal microcavities. *Quantum Electronics, IEEE Journal of*, 38(7):850–856, 2002.

[75] Ph. Lalanne, S. Mias, and J. Hugonin. Two physical mechanisms for boosting the quality factor to cavity volume ratio of photonic crystal microcavities. *Optics Express*, 12(3):458–467, February 2004.

[76] Yoshihiro Akahane, Takashi Asano, Bong-Shik Song, and Susumu Noda. High-Q photonic nanocavity in a two-dimensional photonic crystal. *Nature*, 425(6961):944–7, 2003.

[77] Sylvain Combrié, Alfredo De Rossi, Quynh Vy Tran, and Henri Benisty. GaAs photonic crystal cavity with ultrahigh Q: microwatt nonlinearity at 1.55 μm. *Optics Letters*, 33(16):1908–1910, August 2008.

[78] Hiroshi Sekoguchi, Yasushi Takahashi, Takashi Asano, and Susumu Noda. Photonic crystal nanocavity with a Q-factor of˜ 9 million. *Optics Express*, 22(1):916–924, 2014.

[79] T. F. Krauss. Slow light in photonic crystal waveguides. *Journal of Physics D: Applied Physics*, 40(9):2666, May 2007.

[80] S. A. Schulz, L. O'Faolain, D. M. Beggs, T. P. White, A. Melloni, and T. F. Krauss. Dispersion engineered slow light in photonic crystals: a comparison. *Journal of Optics*, 12(10):104004, October 2010.

[81] Shousaku Kubo, Daisuke Mori, and Toshihiko Baba. Low-group-velocity and low-dispersion slow light in photonic crystal waveguides. *Optics letters*, 32(20):2981–2983, 2007.

[82] Herbert Walther, Benjamin TH Varcoe, Berthold-Georg Englert, and Thomas Becker. Cavity quantum electrodynamics. *Reports on Progress in Physics*, 69(5):1325, 2006.

[83] Jelena Vučković and Yoshihisa Yamamoto. Photonic crystal microcavities for cavity quantum electrodynamics with a single quantum dot. *Applied Physics Letters*, 82(15):2374–2376, 2003.

[84] Bruce W. Shore and Peter L. Knight. The jaynes-cummings model. *Journal of Modern Optics*, 40(7):1195–1238, 1993.

[85] H. J. Carmichael, R. J. Brecha, M. G. Raizen, H. J. Kimble, and P. R. Rice. Subnatural linewidth averaging for coupled atomic and cavity-mode oscillators. *Physical Review A*, 40(10):5516, 1989.

[86] Alexia Auffèves, Benjamin Besga, Jean-Michel Gérard, and Jean-Philippe Poizat. Spontaneous emission spectrum of a two-level atom in a very-high-Q cavity. *Physical Review A*, 77(6):063833, 2008.

[87] Tomoyuki Yoshie, Axel Scherer, J. Hendrickson, G. Khitrova, H. M. Gibbs, G. Rupper, C. Ell, O. B. Shchekin, and D. G. Deppe. Vacuum Rabi splitting with a single quantum dot in a photonic crystal nanocavity. *Nature*, 432(7014):200–203, 2004.

[88] J. áP Reithmaier, G. Sek, A. Löffler, C. Hofmann, S. Kuhn, S. Reitzenstein, L. V. Keldysh, V. D. Kulakovskii, T. L. Reinecke, and A. Forchel. Strong coupling in a single quantum dot-semiconductor microcavity system. Technical report, NAVAL RESEARCH LAB WASHINGTON DC, 2004.

[89] Ryuichi Ohta, Yasutomo Ota, Masahiro Nomura, Naoto Kumagai, Satomi Ishida, Satoshi Iwamoto, and Yasuhiko Arakawa. Strong coupling between a photonic crystal nanobeam cavity and a single quantum dot. *Applied Physics Letters*, 98(17):173104, 2011.

[90] Dirk Englund, Arka Majumdar, Andrei Faraon, Mitsuru Toishi, Nick Stoltz, Pierre Petroff, and Jelena Vučković. Resonant Excitation of a Quantum Dot Strongly Coupled to a Photonic Crystal Nanocavity. *Physical Review Letters*, 104(7):073904, February 2010.

[91] Kevin Hennessy, Antonio Badolato, M. Winger, D. Gerace, Mete Atatüre, S. Gulde, S. Fält, Evelyn L. Hu, and A. Imamoğlu. Quantum nature of a strongly coupled single quantum dot–cavity system. *Nature*, 445(7130):896–899, 2007.

[92] Edward M. Purcell. Spontaneous emission probabilities at radio frequencies. *Physical Review*, 69:681, 1946.

[93] Wen-Hao Chang, Wen-Yen Chen, Hsiang-Szu Chang, Tung-Po Hsieh, Jen-Inn Chyi, and Tzu-Min Hsu. Efficient single-photon sources based on low-density quantum dots in photonic-crystal nanocavities. *Physical review letters*, 96(11):117401, 2006.

[94] D. G. Gevaux, A. J. Bennett, R. M. Stevenson, A. J. Shields, P. Atkinson, J. Griffiths, D. Anderson, G. A. C. Jones, and D. A. Ritchie. Enhancement and suppression of spontaneous emission by temperature tuning InAs quantum dots to photonic crystal cavities. *Applied physics letters*, 88(13):131101, 2006.

[95] L. Balet, M. Francardi, A. Gerardino, N. Chauvin, B. Alloing, C. Zinoni, C. Monat, L. H. Li, N. Le Thomas, R. Houdré, and others. Enhanced spontaneous emission rate from single InAs quantum dots in a photonic crystal nanocavity at telecom wavelengths. *Applied Physics Letters*, 91(12):123115, 2007.

[96] C. Jarlov, A. Lyasota, L. Ferrier, P. Gallo, B. Dwir, A. Rudra, and E. Kapon. Exciton dynamics in a site-controlled quantum dot coupled to a photonic crystal cavity. *Applied Physics Letters*, 107(19):191101, November 2015.

[97] Alistair Brash, Feng Liu, John O'Hara, Luis Martins, Rikki J. Coles, Catherine L. Phillips, Ben Royall, Christopher Bentham, Igor E. Itskevich, Luke Wilson, Maurice S. Skolnick, and Mark Fox. Bright and Coherent On-Chip Single Photons from a Very High Purcell Factor Photonic Crystal Cavity. In *Conference on Lasers and Electro-Optics (2017), paper FTu4E.5*, page FTu4E.5. Optical Society of America, May 2017.

[98] Qin Wang, Søren Stobbe, and Peter Lodahl. Mapping the Local Density of Optical States of a Photonic Crystal with Single Quantum Dots. *Physical Review Letters*, 107(16):167404, October 2011.

[99] V. S. C. Manga Rao and S. Hughes. Single Quantum Dot Spontaneous Emission in a Finite-Size Photonic Crystal Waveguide: Proposal for an Efficient "On Chip" Single Photon Gun. *Physical Review Letters*, 99(19):193901, November 2007.

[100] Christof P. Dietrich, Andrea Fiore, Mark G. Thompson, Martin Kamp, and Sven Höfling. GaAs integrated quantum photonics: Towards compact and multi-functional quantum photonic integrated circuits. *Laser & Photonics Reviews*, 10(6):857–857, November 2016.

[101] A. Javadi, I. Söllner, M. Arcari, S. Lindskov Hansen, L. Midolo, S. Mahmoodian, G. Kiršanskė, T. Pregnolato, E. H. Lee, J. D. Song, S. Stobbe, and P. Lodahl. Single-photon non-linear optics with a quantum dot in a waveguide. *Nature Communications*, 6:ncomms9655, October 2015.

[102] Peter Lodahl, Sahand Mahmoodian, Søren Stobbe, Arno Rauschenbeutel, Philipp Schneeweiss, Jürgen Volz, Hannes Pichler, and Peter Zoller. Chiral quantum optics. *Nature*, 541(7638):473–480, January 2017.

[103] Immo Söllner, Sahand Mahmoodian, Sofie Lindskov Hansen, Leonardo Midolo, Alisa Javadi, Gabija Kiršanskė, Tommaso Pregnolato, Haitham El-Ella, Eun Hye Lee, Jin Dong Song, and others. Deterministic photon–emitter coupling in chiral photonic circuits. *Nature nanotechnology*, 10(9):775–778, 2015.

[104] M. Arcari, I. Söllner, A. Javadi, S. Lindskov Hansen, S. Mahmoodian, J. Liu, H. Thyrrestrup, E. H. Lee, J. D. Song, S. Stobbe, and P. Lodahl. Near-Unity Coupling Efficiency of a Quantum Emitter to a Photonic Crystal Waveguide. *Physical Review Letters*, 113(9):093603, August 2014.

[105] Thang Ba Hoang, Johannes Beetz, Leonardo Midolo, Matthias Skacel, Matthias Lermer, Martin Kamp, Sven Höfling, Laurent Balet, Nicolas Chauvin, and Andrea Fiore. Enhanced spontaneous emission from quantum dots in short photonic crystal waveguides. *Applied Physics Letters*, 100(6):061122, 2012.

[106] Henri Thyrrestrup, Luca Sapienza, and Peter Lodahl. Extraction of the β-factor for single quantum dots coupled to a photonic crystal waveguide. *Applied Physics Letters*, 96(23):231106, June 2010.

[107] T. Lund-Hansen, S. Stobbe, B. Julsgaard, H. Thyrrestrup, T. Sünner, M. Kamp, A. Forchel, and P. Lodahl. Experimental Realization of Highly Efficient Broadband Coupling of Single Quantum Dots to a Photonic Crystal Waveguide. *Physical Review Letters*, 101(11):113903, September 2008.

[108] M. Calic, C. Jarlov, P. Gallo, B. Dwir, A. Rudra, and E. Kapon. Deterministic radiative coupling of two semiconductor quantum dots to the optical mode of a photonic crystal nanocavity. *Scientific Reports*, 7:4100, 2017.

[109] Clément William Tendaï Jarlov. Cavity quantum electrodynamics with systems of site-controlled quantum dots and photonic crystal cavities. 2016.

[110] C. Jarlov, K. A. Atlasov, L. Ferrier, M. Calic, P. Gallo, A. Rudra, B. Dwir, and E. Kapon. 1d and 2d arrays of coupled photonic crystal cavities with a site-controlled quantum wire light source. *Optics Express*, 21(25):31082–31091, December 2013.

[111] B. Rigal, C. Jarlov, P. Gallo, B. Dwir, A. Rudra, M. Calic, and E. Kapon. Site-controlled quantum dots coupled to a photonic crystal molecule. *Applied Physics Letters*, 107(14):141103, October 2015.

[112] Alexey Lyasota. Interaction between site-controlled quantum dot systems and photonic cavity structures. 2017.

[113] B. Rigal, C. Jarlov, A. Rudra, P. Gallo, A. Lyasota, B. Dwir, and E. Kapon. Site-controlled InGaAs/GaAs pyramidal quantum dots grown by MOVPE on patterned substrates using triethylgallium. *Journal of Crystal Growth*, 414:187–191, March 2015.

[114] B. Rigal, K. Joanesarson, A. Lyasota, C. Jarlov, B. Dwir, A. Rudra, I. Kulkova, and E. Kapon. Propagation losses in photonic crystal waveguides: effects of band tail absorption and waveguide dispersion. *Optics Express*, 25(23):28908–28913, November 2017.

[115] Arno Hartmann, Yann Ducommun, Laurent Loubies, Klaus Leifer, and Eli Kapon. Structure and photoluminescence of single AlGaAs/GaAs quantum dots grown in inverted tetrahedral pyramids. *Applied physics letters*, 73(16):2322–2324, 1998.

[116] M. H. Baier, E. Pelucchi, E. Kapon, S. Varoutsis, M. Gallart, I. Robert-Philip, and I. Abram. Single photon emission from site-controlled pyramidal quantum dots. *Applied physics letters*, 84(5):648–650, 2004.

[117] Alessandro Surrente, Marco Felici, Pascal Gallo, Benjamin Dwir, Alok Rudra, Giorgio Biasiol, L. Sorba, and Elyahou Kapon. Ordered systems of site-controlled pyramidal quantum dots incorporated in photonic crystal cavities. *Nanotechnology*, 22(46):465203, 2011.

[118] Milan Calic. *Cavity Quantum Electrodynamics with Site-Controlled Pyramidal Quantum Dots in Photonic Crystal Cavities*. PhD thesis, EPFL, 2013.

[119] Ranojoy Bose, Deepak Sridharan, Hyochul Kim, Glenn S. Solomon, and Edo Waks. Low-Photon-Number Optical Switching with a Single Quantum Dot Coupled to a Photonic Crystal Cavity. *Physical Review Letters*, 108(22):227402, May 2012.

[120] Raymond C. Rumpf. Simple implementation of arbitrarily shaped total-field/scattered-field regions in finite-difference frequency-domain. *Progress In Electromagnetics Research B*, 36:221–248, 2012.

[121] Kirill A. Atlasov, Marco Felici, Karl Fredrik Karlsson, Pascal Gallo, Alok Rudra, Benjamin Dwir, and Eli Kapon. 1d photonic band formation and photon localization in finite-size photonic-crystal waveguides. *Optics Express*, 18(1):117, January 2010.

[122] Kane Yee. Numerical solution of initial boundary value problems involving maxwell's equations in isotropic media. *IEEE Transactions on Antennas and Propagation*, 14(3):302–307, May 1966.

[123] Allen Taflove and Susan C. Hagness. *Computational electrodynamics*. Artech house, 2005.

[124] Ardavan F. Oskooi, David Roundy, Mihai Ibanescu, Peter Bermel, John D. Joannopoulos, and Steven G. Johnson. MEEP: A flexible free-software package for electromagnetic simulations by the FDTD method. *Computer Physics Communications*, 181(3):687–702, 2010.

[125] Milan Calic, Pascal Gallo, M. Felici, K. A. Atlasov, B. Dwir, A. Rudra, G. Biasiol, L. Sorba, G. Tarel, and V. Savona. Phonon-mediated coupling of InGaAs/-GaAs quantum-dot excitons to photonic crystal cavities. *Physical review letters*, 106(22):227402, 2011.

[126] Momchil Minkov and Vincenzo Savona. Automated optimization of photonic crystal slab cavities. *Scientific Reports*, 4, May 2014.

[127] Dirk Englund, Ilya Fushman, and Jelena Vuckovic. General recipe for designing photonic crystal cavities. *Optics Express*, 13(16):5961–5975, August 2005.

[128] Po Dong, Wei Qian, Shirong Liao, Hong Liang, Cheng-Chih Kung, Ning-Ning Feng, Roshanak Shafiiha, Joan Fong, Dazeng Feng, Ashok V. Krishnamoorthy, and Mehdi Asghari. Low loss shallow-ridge silicon waveguides. *Optics Express*, 18(14):14474–14479, July 2010.

[129] VSC Manga Rao and Stephen Hughes. Single quantum-dot Purcell factor and β factor in a photonic crystal waveguide. *Physical Review B*, 75(20):205437, 2007.

[130] Toshihiko Baba. Slow light in photonic crystals. *Nature photonics*, 2(8):465–473, 2008.

[131] F. Alimenti, P. Mezzanotte, L. Roselli, and R. Sorrentino. Modal Absorption in the Fdtd Method: A Critical Review. *International Journal of Numerical Modelling: Electronic Networks, Devices and Fields*, 10(4):245–264, July 1997.

[132] G. Binnig, C. F. Quate, and Ch. Gerber. Atomic Force Microscope. *Physical Review Letters*, 56(9):930–933, March 1986.

[133] K. Fredrik Karlsson, Daniel Y. Oberli, Marc-André Dupertuis, Valentina Troncale, Marcin Byszewski, Emanuele Pelucchi, Alok Rudra, Per-Olof Holtz, and E. Kapon. Spectral signatures of high-symmetry quantum dots and effects of symmetry breaking. *New Journal of Physics*, 17(10):103017, 2015.

[134] Marius Grundmann. *Physics of Semiconductors*, volume 11. Springer, 2010.

[135] Alessandro Surrente, Romain Carron, Pascal Gallo, Alok Rudra, Benjamin Dwir, and Eli Kapon. Self-formation of hexagonal nanotemplates for growth of pyramidal quantum dots by metalorganic vapor phase epitaxy on patterned substrates. *Nano Research*, 9(11):3279–3290, November 2016.

[136] T. F. Kuech and R. Potemski. Reduction of background doping in metalorganic vapor phase epitaxy of GaAs using triethylgallium at low reactor pressures. *Applied physics letters*, 47(8):821–823, 1985.

[137] R. Bhat, P. O'Connor, H. Temkin, R. Dingle, and V. G. Keramidas. Acceptor incorporation in high-purity OMCVD grown GaAs using trimethyl and triethyl gallium sources. In *Gallium arsenide and related compounds, 1981: contributed papers from the Ninth International Symposium on Gallium Arsenide and Related Compounds held at Oiso, Japan, 20-23 September 1981*, page 101. CRC Press, 1982.

[138] Peter W. Lee, Thomas R. Omstead, Donald R. McKenna, and Klavs F. Jensen. In situ mass spectroscopy and thermogravimetric studies of GaAs MOCVD

gas phase and surface reactions. *Journal of Crystal Growth*, 85(1–2):165–174, November 1987.

[139] Gerald B. Stringfellow. *Organometallic vapor-phase epitaxy: theory and practice*. Academic Press, 1999.

[140] E. Pelucchi, S. Watanabe, Klaus Leifer, Q. Zhu, B. Dwir, P. De Los Rios, and E. Kapon. Mechanisms of quantum dot energy engineering by metalorganic vapor phase epitaxy on patterned nonplanar substrates. *Nano letters*, 7(5):1282–1285, 2007.

[141] Toshio Nishida and Naoki Kobayashi. Step-Free Surface Grown on GaAs (111)B Substrate by Local Metalorganic Vapor Phase Epitaxy. *Japanese Journal of Applied Physics*, 36(3S):1690, March 1997.

[142] N. A. Wasley, I. J. Luxmoore, R. J. Coles, E. Clarke, A. M. Fox, and M. S. Skolnick. Disorder-limited photon propagation and Anderson-localization in photonic crystal waveguides. *Applied Physics Letters*, 101(5):051116, July 2012.

[143] P. D. García, S. Smolka, S. Stobbe, and P. Lodahl. Density of states controls Anderson localization in disordered photonic crystal waveguides. *Physical Review B*, 82(16):165103, October 2010.

[144] S. Hughes, L. Ramunno, Jeff F. Young, and J. E. Sipe. Extrinsic optical scattering loss in photonic crystal waveguides: role of fabrication disorder and photon group velocity. *Physical review letters*, 94(3):033903, 2005.

[145] D. P. Fussell, S. Hughes, and M. M. Dignam. Influence of fabrication disorder on the optical properties of coupled-cavity photonic crystal waveguides. *Physical Review B*, 78(14):144201, October 2008.

[146] S. R. Huisman, G. Ctistis, S. Stobbe, A. P. Mosk, J. L. Herek, A. Lagendijk, P. Lodahl, W. L. Vos, and P. W. H. Pinkse. Measurement of a band-edge tail in the density of states of a photonic-crystal waveguide. *Physical Review B*, 86(15):155154, October 2012.

[147] B. Wang, S. Mazoyer, J. P. Hugonin, and P. Lalanne. Backscattering in monomode periodic waveguides. *Physical Review B*, 78(24):245108, December 2008.

[148] Simon Mazoyer, Jean-Paul Hugonin, and Philippe Lalanne. Disorder-induced multiple scattering in photonic-crystal waveguides. *Physical review letters*, 103(6):063903, 2009.

[149] N. Le Thomas, H. Zhang, J. Jágerská, V. Zabelin, R. Houdré, I. Sagnes, and A. Talneau. Light transport regimes in slow light photonic crystal waveguides. *Physical Review B*, 80(12):125332, September 2009.

[150] C. W. J. Beenakker and Henk van Houten. Quantum transport in semiconductor nanostructures. *Solid state physics*, 44(1):228, 1991.

[151] Kazuaki Sakoda. *Optical properties of photonic crystals*, volume 80. Springer Science & Business Media, 2004.

[152] Philippe Lalanne, Christophe Sauvan, and Jean Paul Hugonin. Photon confinement in photonic crystal nanocavities. *Laser & Photonics Reviews*, 2(6):514–526, 2008.

[153] Peijun Yao and S. Hughes. Controlled cavity QED and single-photon emission using a photonic-crystal waveguide cavity system. *Physical Review B*, 80(16):165128, October 2009.

[154] Mark Patterson, Stephen Hughes, Sylvain Combrié, N.-V.-Quynh Tran, Alfredo De Rossi, Renaud Gabet, and Yves Jaouën. Disorder-induced coherent scattering in slow-light photonic crystal waveguides. *Physical review letters*, 102(25):253903, 2009.

[155] Eiichi Kuramochi, Masaya Notomi, S. Hughes, Akihiko Shinya, T. Watanabe, and L. Ramunno. Disorder-induced scattering loss of line-defect waveguides in photonic crystal slabs. *Physical Review B*, 72(16):161318, 2005.

[156] Weiwei Song, Ryan A. Integlia, and Wei Jiang. Slow light loss due to roughness in photonic crystal waveguides: An analytic approach. *Physical Review B*, 82(23):235306, December 2010.

[157] Eric Dulkeith, Sharee J. McNab, and Yurii A. Vlasov. Mapping the optical properties of slab-type two-dimensional photonic crystal waveguides. *Physical Review B*, 72(11):115102, 2005.

[158] L. O'Faolain, X. Yuan, D. Mcintyre, S. Thoms, H. Chong, R. M. D. La Rue, and T. F. Krauss. Low-loss propagation in photonic crystal waveguides. *Electronics Letters*, 42(25):1454–1455, December 2006.

[159] L. O'Faolain, S. A. Schulz, D. M. Beggs, T. P. White, M. Spasenović, L. Kuipers, F. Morichetti, A. Melloni, S. Mazoyer, J. P. Hugonin, P. Lalanne, and T. F. Krauss. Loss engineered slow light waveguides. *Optics Express*, 18(26):27627–27638, December 2010.

[160] C. J. M. Smith, H. Benisty, S. Olivier, M. Rattier, C. Weisbuch, T. F. Krauss, R. M. De La Rue, R. Houdré, and U. Oesterle. Low-loss channel waveguides with two-dimensional photonic crystal boundaries. *Applied Physics Letters*, 77(18):2813–2815, October 2000.

[161] A. Talneau, L. Le Gouezigou, and N. Bouadma. Quantitative measurement of low propagation losses at 1.55 μm on planar photonic crystal waveguides. *Optics Letters*, 26(16):1259–1261, August 2001.

[162] M. Mulot, S. Anand, M. Swillo, M. Qiu, B. Jaskorzynska, and A. Talneau. Low-loss InP-based photonic-crystal waveguides etched with Ar/Cl2 chemically assisted ion beam etching. *Journal of Vacuum Science & Technology B: Microelectronics and Nanometer Structures Processing, Measurement, and Phenomena*, 21(2):900–903, March 2003.

[163] S. Mazoyer, P. Lalanne, J.C. Rodier, J.P. Hugonin, M. Spasenović, L. Kuipers, D.M. Beggs, and T.F. Krauss. Statistical fluctuations of transmission in slow light photonic-crystal waveguides. *Optics Express*, 18(14):14654, July 2010.

[164] Weiqi Xue, Yi Yu, Luisa Ottaviano, Yaohui Chen, Elizaveta Semenova, Kresten Yvind, and Jesper Mork. Threshold characteristics of slow-light photonic crystal lasers. *Physical review letters*, 116(6):063901, 2016.

[165] Anthony E. Siegman. Lasers university science books. *Mill Valley, CA*, 37:462–466, 1986.

[166] John D. Dow and David Redfield. Toward a Unified Theory of Urbach's Rule and Exponential Absorption Edges. *Physical Review B*, 5(2):594–610, January 1972.

[167] S. J. Dewhurst, D. Granados, D. J. P. Ellis, A. J. Bennett, R. B. Patel, I. Farrer, D. Anderson, G. a. C. Jones, D. A. Ritchie, and A. J. Shields. Slow-light-enhanced single quantum dot emission in a unidirectional photonic crystal waveguide. *Applied Physics Letters*, 96(3):031109, January 2010.

[168] A. Laucht, S. Pütz, T. Günthner, N. Hauke, R. Saive, S. Frédérick, M. Bichler, M.-C. Amann, A. W. Holleitner, M. Kaniber, and others. A waveguide-coupled on-chip single-photon source. *Physical Review X*, 2(1):011014, 2012.

[169] A. K. Nowak, S. L. Portalupi, V. Giesz, O. Gazzano, C. Dal Savio, P.-F. Braun, K. Karrai, C. Arnold, L. Lanco, I. Sagnes, and others. Deterministic and electrically tunable bright single-photon source. *Nature communications*, 5, 2014.

[170] Biswarup Guha, Felix Marsault, Fabian Cadiz, Laurence Morgenroth, Vladimir Ulin, Vladimir Berkovitz, Aristide Lemaître, Carmen Gomez, Alberto Amo, Sylvain Combrié, Bruno Gérard, Giuseppe Leo, and Ivan Favero. Surface-enhanced gallium arsenide photonic resonator with quality factor of six million. *Optica*, 4(2):218–221, February 2017.

[171] Marko Spasenović, Daryl M. Beggs, Philippe Lalanne, Thomas F. Krauss, and L. Kuipers. Measuring the spatial extent of individual localized photonic states. *Physical Review B*, 86(15):155153, October 2012.

[172] C. Jarlov, É. Wodey, A. Lyasota, M. Calic, P. Gallo, B. Dwir, A. Rudra, and E. Kapon. Effect of Pure Dephasing and Phonon Scattering on the Coupling of Semiconductor Quantum Dots to Optical Cavities. *Physical Review Letters*, 117(7):076801, August 2016.

[173] M. Feucker, R. Seguin, S. Rodt, A. Hoffmann, and D. Bimberg. Decay dynamics of neutral and charged excitonic complexes in single InAs/GaAs quantum dots. *Applied Physics Letters*, 92(6):063116, February 2008.

[174] I. J. Luxmoore, R. Toro, O. Del Pozo-Zamudio, N. A. Wasley, E. A. Chekhovich, A. M. Sanchez, R. Beanland, A. M. Fox, M. S. Skolnick, H. Y. Liu, and A. I. Tartakovskii. III–V quantum light source and cavity-QED on Silicon. *Scientific Reports*, 3:1239, February 2013.

[175] S. Hughes. Enhanced single-photon emission from quantum dots in photonic crystal waveguides and nanocavities. *Optics letters*, 29(22):2659–2661, 2004.

[176] G. Lecamp, P. Lalanne, and J. P. Hugonin. Very large spontaneous-emission β factors in photonic-crystal waveguides. *Physical review letters*, 99(2):023902, 2007.

[177] A. Yu Petrov and M. Eich. Zero dispersion at small group velocities in photonic crystal waveguides. *Applied Physics Letters*, 85(21):4866–4868, November 2004.

[178] T. P. White, L. C. Botten, C. Martijn de Sterke, K. B. Dossou, and R. C. McPhedran. Efficient slow-light coupling in a photonic crystal waveguide without transition region. *Optics Letters*, 33(22):2644–2646, November 2008.

[179] C. Martijn de Sterke, K. B. Dossou, T. P. White, L. C. Botten, and R. C. McPhedran. Efficient coupling into slow light photonic crystal waveguide without transition region: role of evanescent modes. *Optics Express*, 17(20):17338–17343, September 2009.

[180] J. P. Hugonin, P. Lalanne, T. P. White, and T. F. Krauss. Coupling into slow-mode photonic crystal waveguides. *Optics Letters*, 32(18):2638–2640, September 2007.

[181] Thomas Produit. *Site-controlled pyramidal quantum dots in a slow light photonic crystal waveguide geometry*. PhD thesis, EPFL, 2017.

[182] Ran Hao, Eric Cassan, Xavier Le Roux, Dingshan Gao, Van Do Khanh, Laurent Vivien, Delphine Marris-Morini, and Xinliang Zhang. Improvement of delay-bandwidth product in photonic crystal slow-light waveguides. *Optics Express*, 18(16):16309, August 2010.

[183] Juntao Li, Thomas P. White, Liam O'Faolain, Alvaro Gomez-Iglesias, and Thomas F. Krauss. Systematic design of flat band slow light in photonic crystal waveguides. *Optics Express*, 16(9):6227–6232, April 2008.

[184] R. M. Stevenson, R. M. Thompson, A. J. Shields, I. Farrer, B. E. Kardynal, D. A. Ritchie, and M. Pepper. Quantum dots as a photon source for passive quantum key encoding. *Physical Review B*, 66(8):081302, August 2002.

[185] Edo Waks and Jelena Vuckovic. Coupled mode theory for photonic crystal cavity-waveguide interaction. *Optics Express*, 13(13):5064–5073, June 2005.

[186] Andrei Faraon, Edo Waks, Dirk Englund, Ilya Fushman, and Jelena Vučković. Efficient photonic crystal cavity-waveguide couplers. *Applied Physics Letters*, 90(7):073102, February 2007.

[187] S. Hughes and H. Kamada. Single-quantum-dot strong coupling in a semiconductor photonic crystal nanocavity side coupled to a waveguide. *Physical Review B*, 70(19):195313, 2004.

[188] Dirk Englund, Andrei Faraon, Bingyang Zhang, Yoshihisa Yamamoto, and Jelena Vučković. Generation and transfer of single photons on a photonic crystal chip. *Optics Express*, 15(9):5550–5558, April 2007.

[189] R. J. Coles, N. Prtljaga, B. Royall, I. J. Luxmoore, A. M. Fox, and M. S. Skolnick. Waveguide-coupled photonic crystal cavity for quantum dot spin readout. *Optics Express*, 22(3):2376–2385, February 2014.

[190] Andre Schwagmann, Sokratis Kalliakos, David JP Ellis, Ian Farrer, Jonathan P. Griffiths, Geb AC Jones, David A. Ritchie, and Andrew J. Shields. In-plane single-photon emission from a L3 cavity coupled to a photonic crystal waveguide. *Optics express*, 20(27):28614–28624, 2012.

[191] Bruno Rigal, Alessio Miranda, Benjamin Dwir, Alok Rudra, Alexey Lyasota, and Elyahou Kapon. Site-controlled quantum dots integrated with coupled cavity-waveguide systems for efficient single photon extraction and routing. *Optica*, Manuscript submitted for publication, 2018.

[192] Andrei Faraon, Ilya Fushman, Dirk Englund, Nick Stoltz, Pierre Petroff, and Jelena Vuckovic. Dipole induced transparency in waveguide coupled photonic crystal cavities. *Optics express*, 16(16):12154–12162, 2008.

[193] N. Le Thomas, R. Houdré, L. H. Frandsen, J. Fage-Pedersen, A. V. Lavrinenko, and P. I. Borel. Grating-assisted superresolution of slow waves in Fourier space. *Physical Review B*, 76(3):035103, July 2007.

[194] Cheng-Chia Tsai, Jacob Mower, and Dirk Englund. Directional free-space coupling from photonic crystal waveguides. *Optics Express*, 19(21):20586–20596, October 2011.

[195] P. Hamel, P. Grinberg, C. Sauvan, P. Lalanne, A. Baron, A.M. Yacomotti, I. Sagnes, F. Raineri, K. Bencheikh, and J.A. Levenson. Coupling light into a slow-light photonic-crystal waveguide from a free-space normally-incident beam. *Optics Express*, 21(13):15144, July 2013.

[196] Quynh Vy Tran, Sylvain Combrié, Pierre Colman, and Alfredo De Rossi. Photonic crystal membrane waveguides with low insertion losses. *Applied Physics Letters*, 95(6):061105, August 2009.

[197] Ilya Fushman, Edo Waks, Dirk Englund, Nick Stoltz, Pierre Petroff, and Jelena Vučković. Ultrafast nonlinear optical tuning of photonic crystal cavities. *Applied Physics Letters*, 90(9):091118, February 2007.

[198] M. A. Kaliteevski, D. M. Beggs, S. Brand, R. A. Abram, and V. V. Nikolaev. Stability of the photonic band gap in the presence of disorder. *Physical Review B*, 73(3):033106, January 2006.

[199] Y. Kodriano, I. Schwartz, E. Poem, Y. Benny, R. Presman, T. A. Truong, P. M. Petroff, and D. Gershoni. Complete control of a matter qubit using a single picosecond laser pulse. *Physical Review B*, 85(24):241304, 2012.

[200] Gregory Moille, Sylvain Combrié, Laurence Morgenroth, Gaëlle Lehoucq, François Neuilly, Bowen Hu, Didier Decoster, and Alfredo de Rossi. Integrated all-optical switch with 10 ps time resolution enabled by ALD. *Laser & Photonics Reviews*, 10(3):409–419, May 2016.

[201] B. Rigal, D. Drahi, C. Jarlov, B. Dwir, A. Rudra, I. Kulkova, A. Lyasota, and E. Kapon. Probing disorder and mode localization in photonic crystal cavities using site-controlled quantum dots. *Journal of applied physics*, Imprint, 2018.

[202] Bruno Rigal, Benjamin Dwir, Alok Rudra, Irina Kulkova, Alexey Lyasota, and Elyahou Kapon. Single Photon Extraction and Propagation in Photonic Crystal Waveguides Incorporating Site-Controlled Quantum Dots. *Applied Physics Letters*, Imprint, 2018.

[203] K. F. Karlsson, V. Troncale, D. Y. Oberli, A. Malko, E. Pelucchi, A. Rudra, and E. Kapon. Optical polarization anisotropy and hole states in pyramidal quantum dots. *Applied Physics Letters*, 89(25):251113, December 2006.

[204] V. Troncale, K. F. Karlsson, E. Pelucchi, A. Rudra, and E. Kapon. Control of valence band states in pyramidal quantum dot-in-dot semiconductor heterostructures. *Applied Physics Letters*, 91(24):241909, December 2007.

Bruno Rigal

26 year old, single, French, permit B
31 Bd de Grancy
1006 Lausanne
+41 762889850
bruno.rigal@epfl.ch

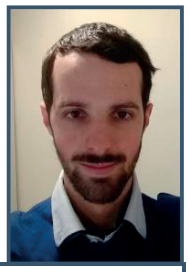

- Master degree at Ecole Polytechnique and EPFL PhD in physics
- Excellent analytical and synthetic thinking
- Strong background in physics and mathematics

Education

2014 - 2018 **PhD in physics in the Laboratory of Physics of Nanostructures** Design, simulation, fabrication and optical characterisation of photonic crystal circuits with site-controlled quantum dots to realize efficient single photon sources: a key component in quantum cryptography and quantum computing.

2012 - 2014 **Ecole Polytechnique Fédérale de Lausanne (EPFL)** Master of Physics: Semiconductors and Optoelectronic devices, Quantum Field Theory, Statistical Physics, Quantum Optics, Optics, Solid State Physics.

2009 - 2012 **Ecole Polytechnique, Paris Tech** Solid states physics, nuclear physics, Laser and Quantum Optics, Integrated Circuits design. Relativity, Quantum physics, Fourier analysis and dynamical systems, hydrodynamics, Continuum mechanics.

2007 - 2009 **Aux Lazaristes** Preparation for national competitive entrance exams to leading french "grandes écoles", specializing in mathematics. Admitted to ENS Ulm.

Professional experience

Autumn 2013 **Laboratory of Physics of Nanostructures** (EPFL), 4 months master project in which I demonstrated the mutual coupling of two site controlled quantum dots to a photonic molecule.

End of 2012 **Laboratory of Quantum Optoelectronics** (EPFL), one day per week on a project of enhanced slow light absorption in a photonic crystal slot waveguide.

Spring 2012 **University of Oxford**, 4 months internship on the optimization of optical pumping and on the effects of imperfect optical pumping to design a room temperature quantum memory in a hollow core fiber. I was awarded the **research internship prize**.

Spring 2011 **Laboratory of Thermonuclear Plasmas** at the National Commission of Nuclear Energy of Chile. I worked as a technician manufacturing electrical devices.

Languages

French	Mother tongue.
English	Pratique professionnelle, stage de 4 mois à Oxford, Doctorat de 4 ans dans un environnement multiculturel, avec l'anglais pour langue commune.
Spanish	Beginner, One month internship in a Spanish speaking Chilean laboratory.

Computer skills

Languages	Matlab (data analysis, FDFD and FDTD simulation tools), python, Latex.
Softwares	Illustrator, Meep (FDTD software)

Activités extra-professionnelles

Ski hiking, running, judo.
Scout leader in a unit of 30 scouts.